Control system for an unmanned aerial manipulator interacting with the environment based on a generalized model

Car, Marko

University of Zagreb

FACULTY OF ELECTRICAL ENGINEERING AND COMPUTING

Marko Car

CONTROL SYSTEM FOR AN UNMANNED AERIAL MANIPULATOR INTERACTING WITH THE ENVIRONMENT BASED ON A GENERALIZED MODEL

DOCTORAL THESIS

Zagreb, 2023

University of Zagreb

FACULTY OF ELECTRICAL ENGINEERING AND COMPUTING

Marko Car

CONTROL SYSTEM FOR AN UNMANNED AERIAL MANIPULATOR INTERACTING WITH THE ENVIRONMENT BASED ON A GENERALIZED MODEL

DOCTORAL THESIS

Supervisors:
Professor Stjepan Bogdan, PhD
Professor Mirko Kovac, PhD

Zagreb, 2023

Sveučilište u Zagrebu
FAKULTET ELEKTROTEHNIKE I RAČUNARSTVA

Marko Car

SUSTAV UPRAVLJANJA BESPILOTNIM ZRAČNIM MANIPULATOROM U INTERAKCIJI S OKOLINOM ZASNOVAN NA POOPĆENOM MODELU

DOKTORSKI RAD

Mentori:
Prof. dr. sc. Stjepan Bogdan
Prof. dr. sc. Mirko Kovac

Zagreb, 2023.

DOCTORAL THESIS is written at the University of Zagreb, Faculty of Electrical Engineering and Computing, Department of Control and Computer Engineering.

Supervisors: Professor Stjepan Bogdan, PhD and Professor Mirko Kovac, PhD

Doctoral thesis has 143 pages

Dissertation No.:

About the Supervisors

Professor Stjepan Bogdan, PhD

Stjepan Bogdan graduated, and got master and PhD degrees in the field of electrical engineering at the University of Zagreb, Faculty of Electrical Engineering and Computing (FER). Since June 1991, he has been working at the Department of Automation and Computer Engineering of FER. He spent the school year 1996/97 as a visiting researcher at the Automation and Robotics Research Institute, University of Texas at Arlington. In December 2016, he was elected to the position of full professor in a permanent position. From October 2022, he holds the position of vice dean for research and innovation at FER.

As a researcher, he participated in a dozen development research projects financed by the industry. He was the principal investigator of 2 projects financed by the Ministry of Education, Culture, Sports, Science and Technology, 1 project financed by the HRZZ, 2 bilateral Chinese-Croatian projects, 1 project financed by the Air Force Office of Scientific Research and 1 NATO SpS project. He participated in the research on 3 EU FP7 projects (ACROSS, EC-SAFEMOBIL, EuRoC), 7 H2020 projects (subCULTron, ENDORSE, CROBOHUB, ACROSS, RoboCom++, ENCORE, AeroWind), was the leader of the work package of the EU FP7-FET project (ASSISI_bf). He currently participates in the work of 2 Obzor2020 projects (Watch-Plant, AerialCore), 4 ESIF projects (EKOKOMVOZ, HEKTOR, ASAP, VirtUAV), was the coordinator of the Obzor2020 project (AeRoTwin), and currently coordinates the ObzorEurope project AeroSTREAM. He has published 4 books, more than 50 journal papers and more than 160 papers in international conference proceedings in the field of intelligent control systems, multi-agent systems and autonomous drones.

Prof. Bogdan is a member of professional associations IEEE and KoREMA. He was the vice-president of the Croatian Society for Robotics and the president of the CS23 section of the Croatian IEEE section. He participates in dozens of program committees of scientific conferences and is a member of the editorial boards and reviewer of several scientific journals. Performs the function of editor-associate in 5 scientific journals. In 1993, he received the "Josip Lončar" silver plaque from FER for a particularly distinguished master's thesis, and in 2000 he received the award of the Association of University Teachers as the best young scientist. In 2013, he received the Science Award, awarded by the FER Faculty Council, in 2015, he received the Fran Bošnjaković Award, awarded by the University of Zagreb, and in 2021, he received the "Josip Lončar" gold plaque, awarded by the FER Faculty Council for scientific contribution in the field of autonomous systems, with an emphasis on the development of heterogeneous robotic systems.

Professor Mirko Kovac, PhD

Prof. Mirko Kovac is Director of the Aerial Robotics Laboratory at Imperial College London and the Head of the Materials and Technology Centre of Robotics at the Empa Material Science Institute in Switzerland. His research focusses on the development of novel, biologically inspired flying robots for distributed sensing in air and water and on autonomous robotic construction for digital infrastructure systems. Prof. Kovac's particular specialisation is in robot design, fluid-structure interaction and multi-modal robot mobility. He is internationally known as an emerging leader in bio-inspired aerial robotics. He is winner of several awards and the author of over 50 articles on mobile robotics that have been published in major journals, including Science, IEEE Transactions and Science Robotics. Prof. Kovac regularly advises industry, investment funds and government on robotic research strategy is holder of the prestigious Royal Society Wolfson Fellowship.

Before his appointment in London, he was post-doctoral researcher at the Harvard Microrobotics Laboratory as part of the Wyss Institute for Biologically Inspired Engineering at Harvard University in Cambridge, USA. He obtained his PhD with the Laboratory of Intelligent Systems at the Swiss Federal Institute of Technology in Lausanne (EPFL). He received his M.S. degree in Mechanical Engineering from the Swiss Federal Institute of Technology in Zurich (ETHZ) in 2005. During his studies he was research associate with the University of California in Berkeley USA, RIETER Automotive Switzerland, the WARTSILA Diesel Technology Division in Switzerland, and CISERV in Singapore.

Since 2006, he has presented his work at numerous international conferences and has won several best paper and best presentation awards. He has also delivered and been invited to more than 60 keynote lectures at research institutions world-wide.

O mentoru

Prof. dr. sc. Stjepan Bogdan

Stjepan Bogdan diplomirao je, magistrirao i doktorirao u polju elektrotehnike na Sveučilištu u Zagrebu Fakultetu elektrotehnike i računarstva (FER).

Od lipnja 1991. godine radi na Zavodu za automatiku i računalno inženjerstvo FER-a. Školsku godinu 1996/97 proveo je kao gostujući istraživač na Automation and Robotics Research Institute, Univesrity of Texas at Arlington. U prosincu 2016. godine izabran je u zvanje redovitog profesora u trajnom zvanju. Od listopada 2022. godine obnaša funkciju prodekana za istraživanje i inovacije FER-a.

Kao istraživač sudjelovao je u desetak razvojno istraživačkih projekata financiranih od strane industrije. Bio je voditelj 2 projekta financiranih od strane MZO-a, 1 projekta financiranog od strane HRZZ-a, 2 bilateralno Kinesko-Hrvatska projekta, 1 projekta financiranog od strane Air Force Office of Scientific Research te 1 NATO SpS projekta. Sudjelovao je u radu 3 EU FP7 projekta (ACROSS, EC-SAFEMOBIL, EuRoC), 5 H2020 projekata (subCULTron, ENDORSE, CROBOHUB, ACROSS, RoboCom++), bio je voditelj radnog paketa EU FP7-FET projekta (ASSISI_bf). Trenutno sudjeluje u radu 4 Obzor2020 projekta (WatchPlant, ENCORE, AeroWind, AerialCore), 4 ESIF projekta (EKOKOMVOZ, HEKTOR, ASAP, VirtUAV), bio je koordinator Obzor2020 projekta (AeRoTwin), a trenutno koordinira ObzorEurope projekt AeroSTREAM. Objavio je 4 knjige, više od 50 radova u časopisima i više od 160 radova u zbornicima međunarodnih konferencija u području inteligentnog upravljanja sustavima, višeagentskih sustava i autonomnih bespilotnih letjelica.

Prof. Bogdan član je stručnih udruga IEEE i KoREMA. Bio je potpredsjednik Hrvatskog društva za robotiku i predsjednik odjela CS23 hrvatske sekcije IEEE. Sudjeluje u više desetaka programskih odbora znanstvenih konferencija i član je uređivačkih odbora i recenzent više znanstvenih časopisa. Obavlja funkciju urednika-suradnika u 5 znanstvenih časopisa. Godine 1993. Primio je srebrnu plaketu „Josip Lončar“ FER-a za posebno istaknuti magistarski rad, a 2000. godine primio je nagradu Društva sveučilišnih nastavnika kao najbolji mladi znanstvenik. 2013. godine primio je nagradu Znanost koju mu je dodijelilo Fakultetsko vijeće FER-a, 2015. godine primio je nagradu Fran Bošnjaković koju dodjeljuje Sveučilište u Zagrebu, a 2021. godine primio je zlatnu plaketu „Josip Lončar“, koju dodijeljuje Fakultetsko vijeće FER-a, za znanstveni doprinos u području autonomnih sustava, s naglaskom na razvoj heterogenih robotskih sustava.

Prof. dr. sc. Mirko Kovac

Profesor Mirko Kovač je direktor Laboratorija za bespilotne letjelice na Imperial Collegeu u Londonu i voditelj Centra za materijale i tehnologiju u robotici Instituta za znanost o materijalima Empa u Švicarskoj. Njegovo istraživanje usmjereno je na razvoj novih, biološki inspiriranih letjelica za distribuirano osjetilno istraživanje u zraku i vodi te na autonomnu robotsku konstrukciju za digitalne infrastrukturne sustave. Profesor Kovač se posebno specijalizirao za dizajn robota, interakciju fluida i struktura, te višemodalnu pokretljivost robota. Međunarodno je poznat kao budući lider u bio-inspiriranoj zračnoj robotici. Osvojio je nekoliko nagrada i autor je preko 50 članaka o mobilnoj robotici koji su objavljeni u vodećim časopisima, uključujući Science, IEEE Transactions i Science Robotics. Profesor Kovač redovito savjetuje industriju, investicijske fondove i vlade o strategiji robotičkog istraživanja i dobitnik je prestižne Wolfson Fellowship nagrade Kraljevskog društva.

Prije nego što je došao u London, bio je postdoktorski istraživač u laboratoriju za mikrorobotiku Harvarda kao dio Wyss Institute for Biologically Inspired Engineering na Sveučilištu Harvard u Cambridgeu, SAD. Doktorirao je u Laboratoriju za inteligentne sustave na Švicarskom federalnom institutu za tehnologiju u Lausanni (EPFL). Diplomirao je strojarstvo na Švicarskom federalnom institutu za tehnologiju u Zürichu (ETHZ) 2005. godine. Tijekom studija bio je istraživački suradnik na Sveučilištu u Kaliforniji u Berkeleyju, SAD, RIETER Automotive Switzerland, WARTSILA Diesel Technology Division u Švicarskoj i CISERV-u u Singapuru.

Od 2006. godine predstavio je svoj rad na brojnim međunarodnim konferencijama i osvojio nekoliko nagrada za najbolji rad i najbolju prezentaciju. Također je održao i bio pozvan na više od 60 predavanja na institucijama za istraživanje diljem svijeta.

Acknowledgements

I would like to express my deepest gratitude to my mentor, prof. Stjepan Bogdan, whose guidance and mentorship have been invaluable throughout my academic journey. His wisdom, support and belief in my capabilities have been instrumental in shaping my research and personal growth. I am also deeply indebted to prof. Matko Orsag. Without his guidance, dedicated supervision and expert insights, this accomplishment would not have been possible. I extend my heartfelt thanks to prof. Zdenko Kovačić, the head of the Laboratory of Robotics and Intelligent Control Systems (LARICS), for providing me with the opportunity to work in such an innovative and inspiring research environment.

To my colleagues at LARICS, I am grateful for your acceptance, company and the collaborative spirit that made my time at work enjoyable and productive. Special thanks go to my friends in the lab—Marsela, Barbara, Antun, Jurica, Lovro, Frano, Tomislav and Goran - for their support, both academically and personally. A huge thanks to my friends outside the lab for their support, patience, motivation and comfort during the challenging times of my PhD journey.

My deepest thanks go to my parents and sister for their unconditional love, encouragement, and belief in me. Lastly, I want to express my profound gratitude to my wife, Marsela, and our beloved Medo, for their support, understanding, and sacrifices. Your love, patience, and belief in me have been my driving force, and I am immensely grateful for your presence in my life.

This journey would not have been possible without the collective support and encouragement of all these wonderful individuals, and I am deeply thankful for their contributions to my academic and personal growth.

Zagreb, July 12 2023.

Abstract

This thesis develops a control framework for a generalized unmanned aerial vehicle (UAV), enabling full 6 DoF control of the vehicle, as well as stable execution of contact based tasks, such as environment manipulation, contact based inspection or transport of fragile payload. The generalized UAV model developed within this thesis considers three different control modalities, namely the classical rotor thrust amplitude, rotor thrust direction, and centroid variation actuators. A unified non-linear model is derived for a vehicle with these actuator systems, regardless of their hardware implementation details and other parameters. The model also has a capability of generalization to vehicles with any subset of the considered actuation systems, by parametrization or fixing of the unused controlled variables to a fixed value. The developed generalized model is used for extensive analysis of the influence of different mechanical and dynamic parameters of UAV hardware components on the UAV dynamics. The analysis included Bode analysis, root locus and Hurwitz stability analysis. The analysis results can be used in the procedure of a custom UAV design, depending on the system requirements.

Several control concepts are proposed in this thesis, based on the linearized version of the derived nonlinear UAV model, that unify the different actuation systems, and enable stable 6 DoF control depending on the UAV task. The attitude control is based on the classical approach using rotor magnitude variation. UAV position controllers are developed using rotor thrust direction variation, and a combination of rotor thrust direction variation with centroid variation. The combination is based on a mid-ranging controller in a control scheme known as Valve Position Control (VPC). In the VPC scheme, one actuation system is considered as a fast-response actuator (small valve) that compensates the disturbances and responds to reference changes. The other actuation system is considered a slow-response actuator (the large valve), that enables returning of the fast valve to the mid of it's working range. In this thesis, rotor thrust direction variation is considered as the fast actuation system, and the centroid variation is considered as the slow one in UAV position control.

Fully actuated UAV control in all 6 degrees of freedom enables development of more elaborate and complex controllers. In this thesis an impedance controller is developed for stable interaction of an unmanned aerial manipulator with the environment. The controller is based on the classical impedance control, but relaxes its requirements for accurate environment modelling. Namely, relying on precise environment position estimate, the controller is equipped with an adaptation mechanism that enables simultaneous estimation of environment stiffness, and precise force reference tracking. The adaptation mechanism is derived using Lyapunov stability criteria. This controller enables precise and compliant execution of complex tasks that involve robotic interaction with the environment, as the results of experimental validation on different robotics platforms show in this thesis.

The following original scientific contribution is achieved with this thesis:

- A generalized unmanned aerial manipulator model unifying actuation concepts based on centre of mass variation, rotor thrust direction and amplitude,
- Unmanned aerial manipulator control method based on the generalized model,
- Impedance control system for stable interaction of unmanned aerial manipulator with the environment based on the generalized model.

Keywords: Unmanned Aerial Vehicle (UAV), Impedance Control, Adaptive Control, Aerial Manipulation, Valve Position Control, Mathematical Modeling

Sažetak

SUSTAV UPRAVLJANJA BESPILOTNIM ZRAČNIM MANIPULATOROM U INTERAKCIJI S OKOLINOM ZASNOVAN NA POOPĆENOM MODELU

Svijet bespilotnih letjelica bio je privlačan kako široj javnosti tako i znanstvenoj zajednici od samih njihovih početaka. U samim počecima bespilotne letjelice su se uglavnom koristile u vojne svrhe kao alternativa za letjelice s ljudskom posadom u svrhu izviđanje. Danas su pronašle svoje mjesto u raznim primjenama, od vojne znanstvene fantastike do široke primjene u znanosti, industriji i svakodnevnim aplikacijama zahvaljujući razvoju algoritama za kontrolu te smanjenju veličine i cijene. U svijetu bespilotnih letjelica, kvadrokopteri se izdvajaju kao najpopularnija platforma zbog svoje sposobnosti vertikalnog polijetanja i slijetanja, okretnosti, jednostavnosti izrade i održavanja. Mogu se koristiti kako u civilnim tako i u vojnim aplikacijama, kao pojedinačna vozila ili u timovima više vozila. U usporedbi s drugim bespilotnim letjelicama, imaju neosporne prednosti zahvaljujući svojoj sposobnosti lebdenja, mogućnosti leta kako u zatvorenim tako i na otvorenim prostorima te svojoj sposobnosti letenja pri niskim brzinama.

Područje primjene bespilotnih letjelica raste iz dana u dan. Najčešća primjena je u filmskoj i fotografskoj industriji, a često se koriste i u misijama traganja i spašavanja, gašenju požara i nadzoru granica. S rastom ljudske civilizacije i povećanjem broja građevina i infrastrukture, održavanje postaje sve veći problem. Prirodne katastrofe poput potresa ili poplava, kao i nepovoljni vremenski uvjeti kao što su promjene temperature, susnježica i kiša, mogu prouzročiti strukturalna oštećenja na zgradama, mostovima itd. Bez adekvatnog pregleda i održavanja, manja oštećenja i manji problemi na kraju mogu dovesti do razornih katastrofa. Iz tog razloga, održavanje infrastrukture ključno je za sprječavanje oštećenja putem detekcije i popravka. Trenutačno se ovi zadaci uglavnom izvode ručno od strane stručnih radnika koji su obučeni za rad na visokim nadmorskim visinama. Ovakav ljudski rad je opasan, skup i vremenski zahtjevan. Upotreba bespilotnih letjelica mogla bi prevladati ove probleme, no osiguranje stabilne kontrole i sigurnosti ovih robota još uvijek je izazov.

Neki jednostavni zadaci, koje mi ljudi odrađujemo svakodnevno, poput uzimanja i odlaganja predmeta, umetanje predmeta ili okretanja ventila, već su unutar mogućnosti bespilotnih letjelica. Iako su ovi zadaci jednostavni za ljude, mogu biti izazovni za robote. Za rješavanje takvih zadataka, bespilotne letjelice su često opremljene robotskim rukama. Vrste robotskih ruku mogu varirati, od jednostavnih s jednim stupnjem slobode do složenijih robotskih ruku. Krutost u robotskoj ruci i propagacija kontaktnih sila prilikom interakcije s okolinom mogu uzrokovati nestabilan kontakt s okolinom i rezultirati oštećenjem okoline ili robota. Upravo to predstavlja glavnu motivaciju za primjenu suptilnijih pristupa pri interakciji s okolinom. Ova

disertacija ima za cilj razviti upravljanje bespilotnim zračnim manipulatorom kako bi se osigurao stabilan kontakt između robota i okoline, uzimajući u obzir informacije o okolini putem senzora za mjerenje sile i momenta.

Stabilna interakcija bespilotnog manipulatora s okolinom može se postići putem različitih principa upravljanja. Najčešći i široko korišten princip upravljanje temelji se na varijaciji brzine vrtnje rotora. No osim klasičnog pristupa, postoje i napredniji principi upravljanja. Jedan takav pricip temelji se na nagibu rotora, što omogućuje kontrolu svih 6 stupnjeva slobode bespilotne letjelice. Drugi pristup je kontrola variranjem centra mase letjelice. Takav pristup omogućava korištenje tereta kako bi se pomoglo stabilizirati tijelo bespilotne letjelice. Mogućnost upotrebe teretea kao mehanizma upravljanja, umjesto kao smetnje, moglo bi pomoći poboljšati ukupnu izvedbu bespilotnog manipulatora. S tim ciljem, razvijen je općeniti model bespilotnog zračnog manipulatora koji objedinjuje koncepte upravljanja temeljene na varijaciji centra mase, varijaciji smjera potiska i varijaciji amplitude potiska. U okviru ovog istraživanja, razvijena je općenita metoda upravljanja temeljena na izvedenom modelu bespilotnog zračnog manipulatora i provijerena za različite koncepte upravljanja.

Ova disertacija je organizirana u osam poglavlja. Prvo poglavlje disertacije daje uvod u temu kroz motivaciju i pregled područja istraživanja. Također se definiraju znanstveni doprinosi disertacije i hipoteze istraživanja. Drugo poglavlje opisuje razmatrane principe upravljanja bespilotnom letjelicom dok treće poglavlje razvija općeniti model bespilotnog zračnog manipulatora na temelju tih načela, uključujući i nelinearnu i linearnu verziju modela. U četvrtom poglavlju opisuju se metode projektiranja i izrade bespilotnog zračnog manipulatora koji služi kao eksperimentalna letjelica na kojoj se testiraju sva tri principa upravljanja, varijacija centra mase, promijena smjera potiska i promjena brzine vrtnje rotora. Provode se analize utjecaja raznih statičkih i dinamičkih parametara na ponašanje sustava. Peto poglavlje razvija jedinstvenu metodu kontrole primjenjivu na općeniti model. Šesto poglavlje bavi se razvojem adaptivnog algoritma za upravljanjem impedancijom bespilotne letjelice kako bi se osigurala stabilna interakcija robota s nepoznatim okolišem. Eksperimentalni rezultati prikazani su u sedmom poglavlju, a zaključci su navedeni u posljednjem poglavlju. Potom je izložen popis literature korištene u disertaciji. Glavni doprinosi disertacije su izloženi i opisani u nastavku poglavlja.

#1P OOPĆENI MODEL BESPILOTNOG ZRAČNOG MANIPULATORA KOJI OBJEDINJUJE AKTUACIJU POMICANJEM CENTRA MASE TE PROMJENOM SMJERA I IZNOSA POTISKA ROTORA.

Ovom disertacijom se predlaže općeniti model bespilotnog zračnog manipulatora koji objedinjuje tri različita principa upravljanja, tj. klasično upravljanje varijacijom amplitude potiska rotora, varijacijom smjera potiska rotora i varijacijom centra mase. Kao proširenje klasičnog upravljanja korištenjem varijacije amplitude potiska rotora, ovaj pristup omogućava razvoj potpuno aktuiranih bespilotnih letjelica, odnosno kontrolu svih 6 stupnjeva slobode. Ovo je posebno važno u složenim situacijama koje uključuju suradnju više bespilotnih robota, interakciju bespilotnih robota s okolinom ili prijevoz opasnih ili krhkih tereta. Općenitost modela također je primjenjiva na druge vrste bespilotnih letjelica, jednostavno fiksiranjem ili postavljanjem određenih varijabilnih parametara na nulu.

Općeniti model je lineariziran kako bi se klasični alati za analizu linearnih sustava mogli primijeniti za verifikaciju stabilnosti i odabir optimalnih parametara pri dizajniranju stvarnih bespilotnih sustava. Nadalje, regulatori su podešavani na temelju dobivenih linearnih aproksimacijskih modela. Niz eksperimentalnih pokusa potvrdio je preciznost i praktičnu relevantnost razvijenog modela usporedbom teoretskih očekivanja s eksperimentalnim ponašanjem stvarne robotske platforme.

#2M ETODA UPRAVLJANJA BESPILOTNIM ZRAČNIM MANIPULATOROM ZASNOVANA NA POOPĆENOM MODELU.

Razvijeni općeniti model omogućio je dizajniranje novih principa upravljanja bespilotnom letjelicom koje inkorporiraju različite principe aktuacije u stabilnu kontrolu vozila. Ovaj značajan napredak u području robotike omogućava razvoj inovativnih bespilotnih sustava sposobnih za širok spektar primjena. U disertaciji su predstavljene različite metode koje se oslanjaju na sve ili neke od mogućih principa upravljanja.

Jedan od ključnih doprinosa teze je razvoj regulatora položaja bespilotnog manipulatora temeljenog na različitim principima aktuacije. To su promijena amplitude potiska rotora i promijena smjera potiska rotora. Ovaj inovativni pristup omogućava precizno upravljanje položajem bespilotnih vozila, što je od ključne važnosti u različitim situacijama, uključujući zadatke u kojima je potrebna kolaboracija između više bespilotnih sustava, interakciju s okolišem ili prijevoz osjetljivih tereta. Ovaj razvijeni princip kontrole uspješno je eksperimentalno potvrđen kako u slobodnom letu, tako i u interakciji s okolinom, što ukazuje na njegovu praktičnu primjenjivost.

Osim toga, razvijen je i kontroler položaja koji uključuje sva tri principa aktuacije, temeljen na shemi VPC metodi upravljanja. Ovdje se jedan od sustava aktuacije smatra bržim sustavom, dok se drugi smatra sporijim sustavom, omogućavajući dinamično prilagođavanje uvjetima u

stvarnom vremenu. Ova inovativna strategija omogućava bolje iskorištavanje mogućnosti bespilotne letjelice i manipulatora, čime se povećava fleksibilnost u različitim scenarijima primjene.

Regulacija orijentacije, iako temeljena samo na varijaciji amplitude potiska rotora u ovom kontekstu, otvara vrata za teorijski razvoj naprednih strategija kontrole orijentacije. Razvijeni općeniti model u teoriji omogućava primjenu naprednih metoda upravljanja kao što je modelsko prediktivno upravljanje. Ovo može rezultirati poboljšanjem kontrole orijentacije vozila uzimajući u obzir dodatne parametre kao što su promijena centra mase i varijacija smjera potiska rotora. Ova mogućnost ostaje otvorena za buduće istraživanje i razvoj.

Osim navedenih strategija upravljanja, diseminacija također istražuje dodatne aspekte upravljanja vozilom, uključujući učinkovitu distribuciju tereta između komponenata vozila te obradu referenci za poziciju. Ovaj sveobuhvatni pristup rezultira boljom prilagodljivošću i učinkovitošću u različitim scenarijima primjene, čime se unapređuje područje bespilotnih sustava i robotike. Sve navedeno doprinosi razvoju naprednih i višenamjenskih bespilotnih sustava za buduće izazove i zadatke.

#3S USTAV UPRAVLJANJA IMPEDANCIJOM BESPILOTNOG ZRAČNOG MANIPULATORA ZA STABILNU INTERAKCIJU S OKOLINOM ZASNOVAN NA POOPĆENOM MODELU.

Konačni rezultat teze je adaptivna kontrolna strategija impedancije koja omogućuje stabilnu interakciju robotskog manipulatora s okolišem bez obzira na nesigurnosti okoline. Drugim riječima, čak i uz nepoznatu preciznu poziciju okoline i nepoznatu krutost okoline, robot je sposoban postići željene referentne sile na stabilan način. Prilagodba se temelji na online procjeni krutosti okoline na temelju mjerenih signala sile. Adaptivni regulator impedancije određuje referencu pozicije robota, koje će ga voditi prema postizanju željene referentne sile.

Osim adaptivnog regulatora impedancije, općeg modela vozila i stabilnih regulatora položaja i orijentacije, ova disertacija također predlaže strategiju za upravljanje položajem bespilotne letjelice i robotskog manipulatora kako bi se učinkovito raspodijelio teret između komponenata sustava. Naime, ovisno o konfiguraciji bespilotne letjelice i manipulatora, jedna ili druga komponenta je u boljoj poziciji za rekonfiguraciju, promjenu svoje pozicije ili apliciranje potrebne sile na okoliš. Ovaj inovativni pristup omogućava bolju prilagodljivost i učinkovitost u različitim scenarijima primjene, što rješava pitanje problema inverzne kinematike s više sustava djelovanja.

Uz to, razvijeni adaptivni pristup impedanciji testiran je na nekoliko eksperimentalnih testnih postrojenja. To uključuje samostalni robotski manipulator,koji je testiran u laboratorijskim uvijetima. Također, primijenjen je na bespilotnom zračnom manipulatoru, gdje je željena interakcija s okolišem uspješno ostvarena s bespilotnom letjelicom uz potpunu kontrolu svih 6 stupnjeva slobode. Ovaj uspjeh potvrđuje praktičnu primjenjivost razvijenih strategija kontrole

u stvarnim okruženjima i doprinosi napretku u području bespilotnih sustava i robotike.

Ključne riječi: bespilotne letjelice, podatno upravljanje, adaptivno upravljanje, VPC upravljanje, zračna manipulacija, matematičko modeliranje

Contents

CHAPTER 1

Introduction

The world of unmanned aerial vehicles (UAVs) has been attractive to both general public and research community since its inception. In the beginning, the UAVs were mainly used for military applications as alternative to recon manned aerial vehicles. Nowadays, these vehicles have found their way from military science fiction to wide usage in science, industry and every day applications thanks to the development of control algorithms and reductions in size and price. Among all used UAV platforms, quadrotors stand out as the most popular platform due to their vertical take-off and landing (VTOL) capability, maneuverability, simplicity of construction and maintenance [1]. They can be used both in civil and military applications, as individual vehicles or in teams of multiple vehicles. Compared to other UAVs, they have unquestionable advantages thanks to their ability to hover, the possibility of indoor and outdoor flight, and their low speed flight capability.

The number of different UAV deployment scenarios is steadily increasing. The most common application is in filming and photography industry, and they are very often used in search and rescue missions, firefighting and border surveillance. With the growth of human civilization and the accompanying increase in buildings and infrastructure, maintenance is becoming an ever-increasing problem. Natural disasters such as earthquakes or floods, as well as adverse weather conditions including temperature changes, sleet, and rain, can cause structural damage to the buildings, bridges etc. Without proper inspection and maintenance small damages and minor problems can eventually lead to devastating disasters. For this reason, infrastructure maintenance is critical to preventing damage through detection and repair. Currently, these tasks are mainly done manually by skilled workers who are trained to work at high altitudes. This kind of human labor is dangerous, expensive, and time-consuming. The use of robots could overcome these problems, but ensuring stable control and safety of these robots is still

a challenge. Numerous scientific studies accelerated the development of UAV maneuverability, yielding more stable and aggressive attitude controllers [2], and motion planners ensuring obstacle avoidance [3]. These results have greatly contributed to the UAV deployment in situations and environments that would be dangerous for humans. They are already being used in inspections of wind turbines [4, 5, 6], transmission lines [7], gas refineries [8, 9] and bridges [10, 11]. The snapshots from this researches are shown on Fig. 1.1. Furthermore, different UAV designs are being developed, in order to enable their active involvement in solving practical tasks in hard-to-reach places, such as fixing screws on bridges. Adding a manipulator to the UAV structure, resulting in an unmanned aerial manipulator, opens many possibilities for solving complex tasks that require interaction with the environment.

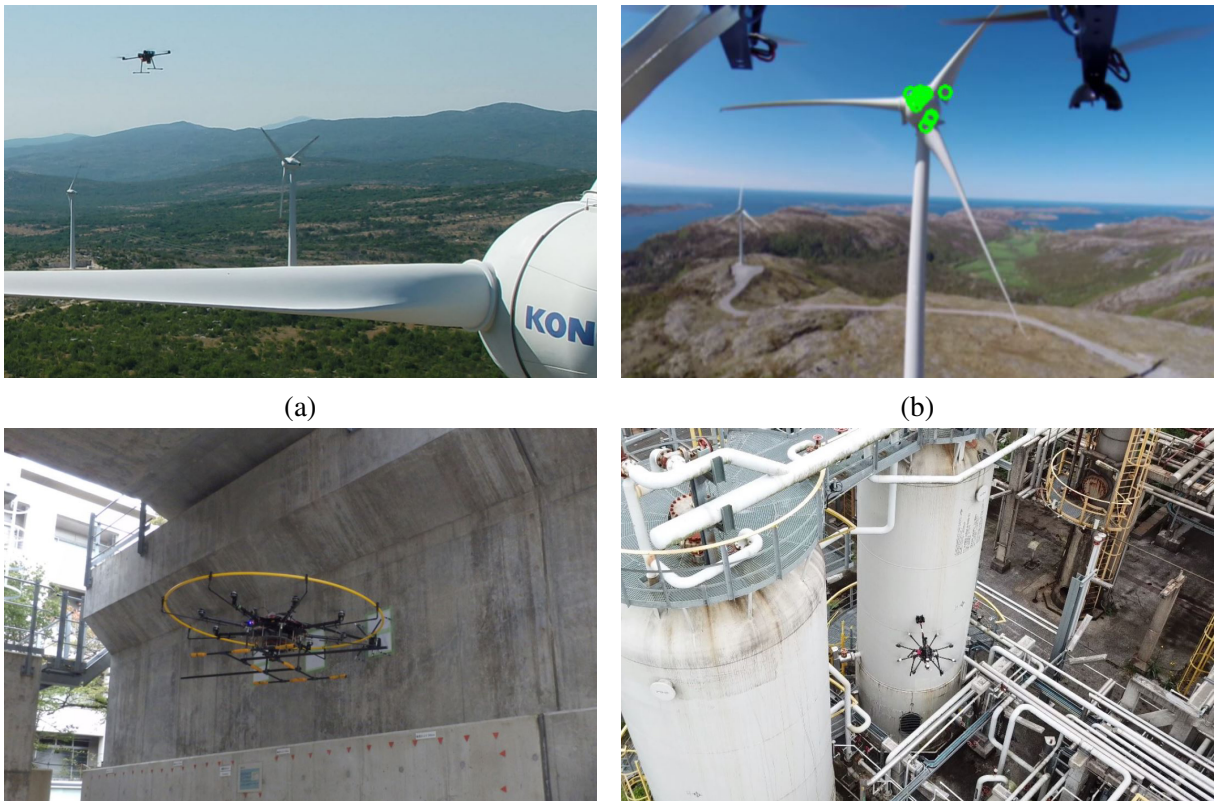

(a) (b)

(c) (d)

Figure 1.1: Snapshots from researches where UAV is used in situations and environments dangerous for humans. In a) authors presented LiDAR-equipped UAV performing semi-autonomous wind-turbine blade inspection [6], in b) the autonomous machine vision module for UAV navigation for wind turbines inspection is developed [5], c) shows UAV in bridge inspection task [10] , and d) shows aerial robotic manipulator that provides physical contact inspection with unprecedented capabilities for oil and gas inspection industry [9]

Some simple, everyday tasks for humans, like pick-and place, peg-in-hole and valve turning are already within the capabilities of aerial manipulators. Although these tasks are simple for humans, they can be challenging for robots. To solve a contact-based task, UAVs are often equipped with a manipulator arm. Types of manipulators can vary from single Degree of

Freedom (DOF) [12, 13] to multi DOF grippers [14]. Some examples of such missions include valve turning [15], opening and closing a cupboard drawer [16], or surface cleaning [17], which can be seen on Fig. 1.2. Rigidity in the manipulator and the propagation of contact forces when interacting with the environment can cause unstable contact with environment and result in crashes. This presents the main motivation for deployment of more delicate approaches when interacting with the environment. This research aims to develop a control system for stable contact between an unmanned aerial manipulator and the environment by taking into account the information about the environment through a force-torque sensing apparatus.

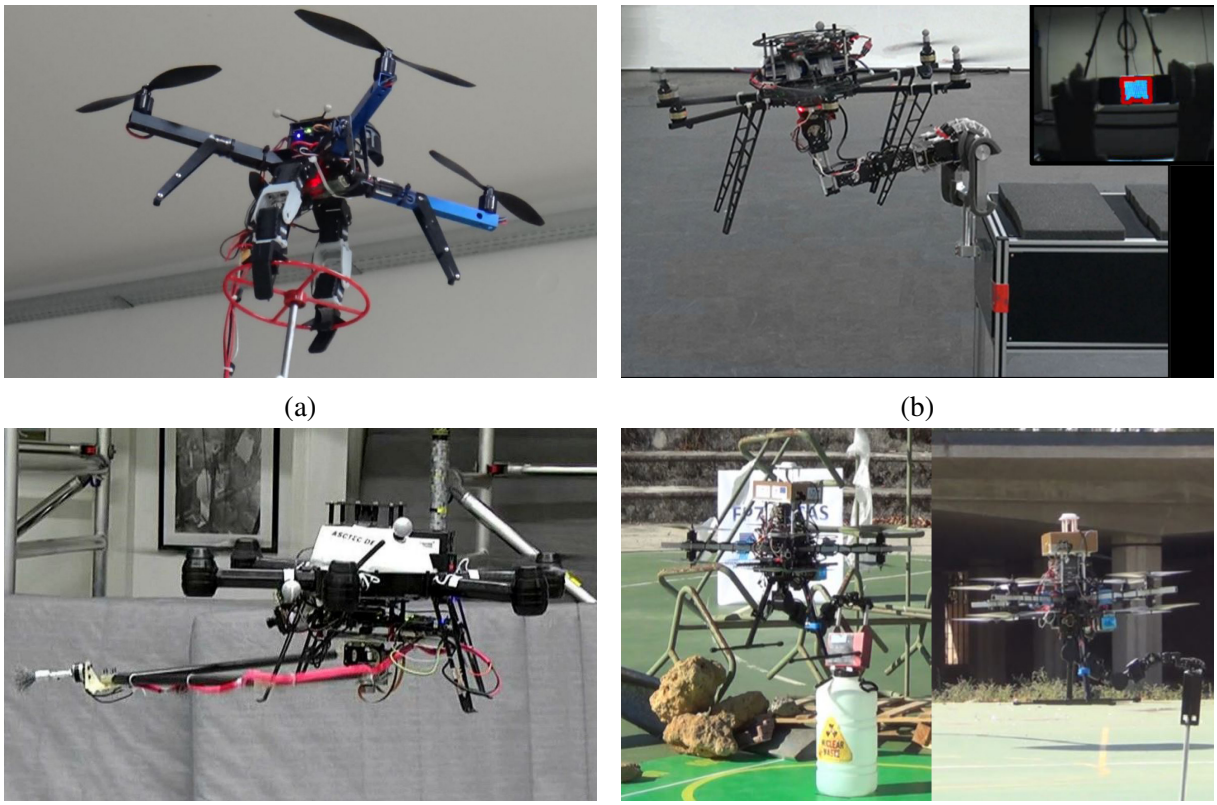

(a) (b)

(c) (d)

Figure 1.2: The figure shows various aerial manipulators in action. In a) authors used dual arm manipulator to turn valve [15], in b) a single arm manipulator is used to open and close an unknown drawer [16], in c) a parallel aerial manipulator is presented [17], and in d) design, analyze and test the behaviour of first-order CLIK (Closed-Loop Inverse Kinematics) manipulator algorithms under the influence of Cartesian integral error feedback is shown[14].

Stable interaction of a UAV with the environment can be achieved through different control principles. The most common and widely used UAV control principle is based on variation of rotor speed. The first multirotor UAV model, presented in 2002. in [18], was a quadrotor vehicle, and various modifications have since been proposed, resulting in many different UAV models. Most commonly, such vehicles are PID controlled. In addition to the classical actuation, the literature proposes different advances in actuation principles. One such proposal is based on the rotor tilt actuation, which enables both vertical and horizontal flight [19]. Another

approach is attitude control by variation of the vehicle center of mass [20]. Such approach enables us to use the payload to help stabilize the UAV body. As the rotorcraft design increases payload-to-weight ratio, the center of mass becomes ever more dominant dynamic component of the system. The ability to utilize it as a control mechanism, rather than a control disturbance, could help improve overall UAV performance. To that end, we aim to develop a generalized unmanned aerial manipulator model that unifies actuation concepts based on the centroid variation, thrust direction and thrust magnitude control. Within this research, a generalized control method based on the derived unmanned aerial manipulator model will be designed and validated for different control concepts.

1.1State of the Art

1.1.1Multirotor UAV types, modeling and control

The deployment of UAVs has expanded from the initial basic, simple and limited tasks, in large thanks to recent advancements in modeling and control. The past decade has seen a continuous increase in the number of developed control algorithms, varying from linear robust controllers to much more complex intelligent controllers. Such new controllers enable stable flight of the UAV even in difficult and challenging tasks. In addition to the recent improvements in control algorithms, there have also been significant contributions regarding UAV configuration and actuation. For example, the issues of the classical underactuated UAV system have for some complex tasks been addressed by developing additional actuation in the UAV configuration, namely by introduction of tilting propellers.

Using standard UAV configurations with rotors thrust variation actuation, in order to achieve motion the vehicle body needs to be tilted by changing the speed of the rotors. In other words, this standard configuration does not allow vehicle to be controlled in all 6 degrees of freedom. However, using an alternative propulsion system in the form of tilting rotors could be used to overcome this underactuation problem. Authors in [21] presented a mathematical model of the tiltable-rotor type quadrotor, along with proposed control algorithms. Similar results are found in [22], where the authors conclude that tilting rotors provide the vehicle with more agility and mobility, especially in narrow indoor and outdoor infrastructures. In [23] and [24], a quadrotor UAV with tilting propellers is presented, with controlled orientation of the 4 propellers, thus making it possible to overcome the aforementioned underactuation and behave as a fully-actuated flying vehicle. Another approach can be found in [25], where the authors propose a concept of a UAV capable of horizontally moving without tilting the vehicle body based on the moving mass control. Using the the shift in the center of gravity, which in turn produces roll and pitch moments, they can control the attitude of the UAV. The concept of a moving mass

control can be found in [20].

(a) (b)

Figure 1.3: The figure shows tilt configuration UAVs. In a) the quadrotor prototype with ability to control the orientation of its 4 propellers is presented [24], in b) a dual-axis tilting propeller is shown [22]. In paper one can found more about design, modeling, simulation and prototyping of such quadrotor.

Regardless of the UAV type, there are various control strategies developed for these vehicles. In the early research, linear controllers were sufficient to obtain stable flight. One of the most common linear controllers is proportional integral derivative controller (PID). This controller is one of the most popular controllers due to its simplicity, since it presents a classical approach that can be easily implemented and tuned. One of the first usage of the PID controller for a fully autonomous UAV can be found in [26]. A more complex aplication can be found in [27], where authors developed a multi-sensory control architecture for autonomous hovering over specified markers. They used two on-board sensors; a camera and an inertial measurement unit; with a closed-loop system using PID pose-controllers. Another interesting control framework with a PD controller is used in [28], where a UAV attitude controller is proposed capable of active disturbance rejection. The dynamic disturbances considered there are wind gusts, estimated using an extended state observer. An example of a more advanced linear controller that found a use-case in UAV control is a linear quadratic controller (LQR). Some of the more prominent examples of implementations of LQR are presented in [29, 30].

An alternative approach in UAV control are the nonlinear controllers. A large number of publications deploying nonlinear control strategies for the UAVs can be found, including examples with feedback linearization, backstepping control techniques, sliding mode control, etc. Among these, one of the most common approaches is the feedback linearization technique. Using this method, the inherently nonlinear system is transformed into an equivalent linear system, where standard linear control theory can be applied. Examples of this approach can be found in [31, 32]. Various examples of UAVs with nonlinear controllers such as backstepping can be found in the literature [33, 34, 35], as well as deployment of sliding mode control [36].

Another type of control relevant for this thesis is Model predictive control (MPC). Although this method requires a precise predictive model of the system, and a full-state estimation, it has an important advantage in the ability to enforce constraints on inputs and outputs. The MPC

control is in the focus of many papers. For example, in [37], the authors suggested a switching model predictive controller for environments where absolute localization data is inadequate. They successfully tested their control strategy in indoor position flight using an IMU, a sonar and an optical flow sensor. Furthermore, learning-based model predictive controllers (LBMPC) were presented in [38, 39, 40]. The results of these studies show that LBMPC can fit physically based updates to an initial model, demonstrating it on a quadrotor ball catching experiment, with ball thrown with an a priori unknown trajectory. Along with the MPC, other strategies should be mentioned such as fuzzy logic control methods [41, 42] and neural network based controllers [43].

1.1.2Aerial manipulators interacting with environment

With the development of UAV hardware and control algorithms, they are constantly being introduced into new deployment areas, meeting ever increasing task requirements. Since wide variety of autonomous operations could be resolved with robotic manipulation, an entire new research domain emerged, in the field of aerial manipulation. The scale of systems developed here ranges from simple grippers mounted on the UAV body for operations such as grasping and perching, to actual multi-degree of freedom robotic arms capable of complex task execution, such as as pick-and-place, peg-in-hole, or contact inspections, to name a few.

Various solutions and applications of such systems have already been presented in the existing state of the art work. One proposed division of the emerging results in this field is into the following two major categories [44]: free-flight operation, and motion-restricted operation. The first group, free-flight operations, are those operations in which the aerial manipulator conducts tasks during free-flight mode. This means that the contact force appears for a very small time period, and the contact force values are usually of negligible amplitudes during the interaction process. The second group, motion-restricted operations, represents those operations in which the aerial manipulator is required to physically interact with the environment or object with a fixed desired force, for a sustained time period. Since during this interaction time the UAV motion is usually restricted, these motion restrictions lead to the loss of some degrees of freedom.

When considering free-flight operations, most of the existing work is related to grasping and transporting. Among the exciting early examples was an experiment in which a moving target was grasped using an aerial manipulator [45]. Over the years, more research of similar grasping problems was further conducted by other research groups as well [46, 47, 48, 49]. The problem of transport is another important and interesting topic with various use-cases already developed and described, such as aerial manipulator for transporting barrels in [50], or an aerial manipulator for transporting a block in [51]. Recently, a flying modular platform capable of both grasping and transporting objects was presented [52]. The transporting use-case is especially

interesting in terms of exploring possibilities of autonomous delivery of goods [53]. However, with unknown shape, location and configuration of the manipulated objects, this research problem is particularly challenging. Other examples of free-flight operations include assembling [54], pick-and-place [49, 55], and so on.

One example of the motion-restricted operations, where aerial manipulator interacts with the environment or objects for a continuous time period with a desired force, is valve turning task, successfully performed and described in [56]. Furthermore, inspection of structures often requires physical contact and application of controlled force. Examples of such operations where stable physical interaction is achieved can be found in [57] and [58]. Another interesting result in contact-based missions has been disseminated in [59], where the system is able to perform complex operations that require the physical interaction with the surrounding environment while remaining airborne. A more detailed research about structure inspection can be found in [60], where a bridge inspection is described as a use case. More results on similar inspection and interaction tasks can be found in [23, 61, 62]. Other examples of motion-restricted operations include peg-in-hole operations [63], drawer opening [16], etc.

Despite the addition of a robotic manipulator, some tasks require even more complex setups due to other limitations of aerial manipulators, such as payload limits. One example is cooperative aerial manipulation, such as in transportation tasks, when a cooperative aerial manipulator system is used to carry a heavier or bulkier object, thanks to its greater capacity when compared to a single aerial manipulator. In [64], authors investigate pose manipulation of a rod-shaped object transported using two aerial manipulators in cooperation. Another interesting work is presented in [65], where a framework based on Parametric Dynamic Movement Primitives (PDMPs) is described, for coordination of multiple aerial robots and their manipulators quickly in an environment cluttered with obstacles.

In performing contact-based tasks, non-negligible contact force will be exerted during aerial manipulator interaction with environment. This reflects on the stability of the aerial manipulator. In the literature, a variety of the aerial manipulation tasks are described, and control strategies developed, where the force information is not taken into account [59, 66, 67]. However, it has been shown that using the force information can improve the performance of the task. One of the force control techniques often used in aerial manipulation tasks is hybrid pose/wrench control. For example, in [68], in order to maintain a steady contact with the environment, contact force control and position control are performed separately in two orthogonal subspaces. Another example is found in [69], where modeling and control solutions for a class of aerial manipulators is described. The design of hybrid force and position control laws is discussed in detail for these vehicles, capable of interacting with the environment and accomplishing robotic operations midair.

Another classic approach in the field of force control, in addition to the hybrid force/position

control, is the impedance control, deployed in the field of aerial manipulation as well. The idea behind impedance control is that to transform the force control into the position control problem, using desired, user-defined impedance relation. The resulting system, the aerial manipulator in a closed-loop control, behaves as a spring-mass-damper system, and can be described with equivalent stiffness and damping parameters. A wide variety of aerial manipulator interaction use-case based on impedance control can be found in literature [63, 70, 71].

1.1.3Beyond the current State of the Art

The research presented in this thesis goes beyond the State of the Art in aerial manipulator design, modeling, and control by developing a generalized unmanned aerial manipulator model that incorporates three different actuation principles. This allowed development of advanced control schemes based on all three actuation principles, enabling full 6 DoF control of the vehicle. Finally, an adaptive impedance controller was developed that enables stable interaction with the environment with precise force reference tracking.

This thesis is organised in 8 chapters. The first chapter gave an overview of the state of the art and the motivation for the presented work. The second chapter describes the considered actuation principles, while the third chapter develops the generalized unmanned aerial manipulator model on top of these principles, including both non linear and linear versions of the model. The following chapter describes the design procedure for assembly of such a vehicle on the example of an unmanned aerial manipulator with centroid variations and variable thrust direction (TRMMC-UAV) experimental vehicle, based on analyses of the influence of various model parameters to the system behavior. The fifth chapter develops a unified control method applicable to the generalized model. The sixth chapter deals with development of an adaptive impedance control for stable interaction of a robot with an unknown environment. Experimental results are given in the seventh chapter, and the conclusions are given in the last chapter.

CHAPTER 2

Unmanned aerial manipulator actuation principles

In this chapter we present the actuation principles for the unmanned aerial manipulator, with their dynamics unified in a generalized unmanned aerial manipulator model in Chapter 3. The first analyzed actuation principle is the most common way to control the unmanned aerial manipulator, i.e. the actuation principle based on rotor thrust magnitude. The second one is the concept based on control of the rotor thrust direction. In this concept the rotors are mounted on actuators that enables independent tilting of their rotation planes, and thus controlling the vehicle's attitude. The last concept analyzed within this thesis is the concept based on centroid variation. This concept is based on the work done by authors in paper [72], where they present a novel concept of attitude control for a multi-rotor unmanned aerial vehicle by actively controlling its center of gravity. Using stepper motors, which act as moving masses on the vehicle body, the work presents the framework for attitude control of a heavy lift multi-rotor two-stroke propulsion vehicle. In general, the moving masses can be replaced with other components, such as for example a robotic arm carrying a payload. The control of the vehicle CoG with such a payload was demonstrated in [73].

By combining the presented actuation principles, a fully actuated vehicle can be obtained. Similar results are presented in [74], where it was shown that all of the 6 DoFs of the vehicle can be controlled using tilted rotors and rotor thrust magnitude control. The discussed aerial manipulator actuation principles are shown in Figure 2.1. Please note that, for the simplicity of explanations, the actuation principles are presented for a four rotors vehicle, and in the *plus* configuration of the vehicle only.

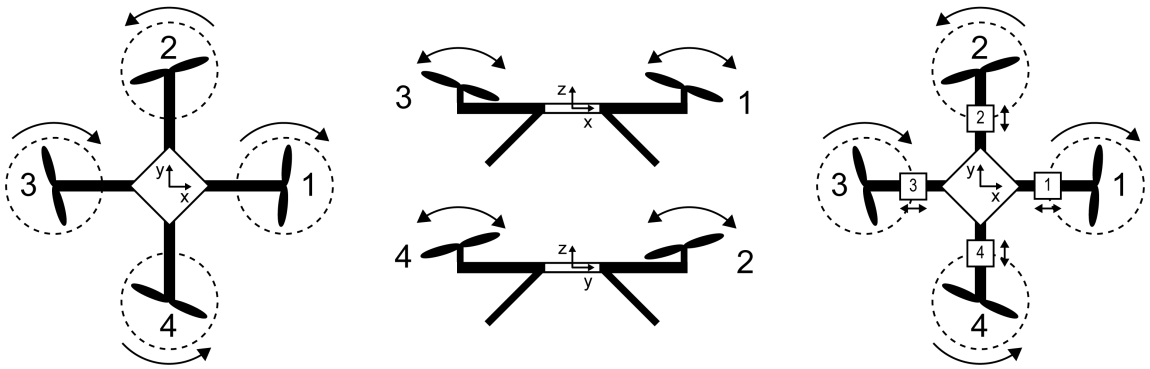

(a) (b) (c)

Figure 2.1: The figure shows illustration of each actuation principles presented in this thesis. In a) a concept based on rotor thrust magnitude is illustrated. Next, in b) a vehicle with tilting rotors is presented. And finally in c) a concept based on centroid variation is shown.

2.1Concept based on rotor thrust magnitude

This concept is the most common way to control the unmanned aerial manipulator. The vehicle can be composed of an arbitrary number of rotor pairs, where rotor pair consists of an counter-clockwise rotor and clockwise rotor. In this configuration the rotors are not tilted with respect to (w.r.t.) the vehicle frame, so they produce thrust in the direction perpendicular to the horizontal plane of the vehicle frame. To control the horizontal movement, the vehicle's roll and pitch angle are controlled to produce desired forces. This concept is constrained in a way that vehicle can not move horizontally without changing its body orientation in roll or pitch axis.

To control the vehicle's roll and pitch angle, the rotors thrust magnitude has to be changed. To change rotors thrust magnitude we control the speed of the rotors. The general control policy for controlling vehicle's roll and pitch angle for a simplified vehicle with four rotors in *plus* configuration are shown on Figure 2.2c and Figure 2.2d, respectively. A little bit different control policy is for the vehicle's yaw angle. This control policy is illustrated on Figure 2.2b. Here by increasing the speed of rotors that are rotating counterclockwise or clockwise, the vehicle can be rotated around its z axis in negative or positive direction, respectively. To control the vehicle's height, the speed of all rotors has to be changed by the same amount. For example, if the vehicle should ascend, the speed of all rotors should be increased. In the other case, if vehicle should descend, the speed of all rotors should be decreased. Such control policy is shown on Figure 2.2a.

Important factor in this control concept is rotor dynamics. The rotor dynamics has to be fast in order to ensure stability of the vehicle. This primary affects to the stability of the vehicle's roll and pitch angles. It is clear that the size and the mass of the vehicle, ie., the vehicle's moment of inertia is in general proportional to the required rotor dynamics. For the small vehicles, the

time constant of the rotors should be in range of 15-50ms [75].

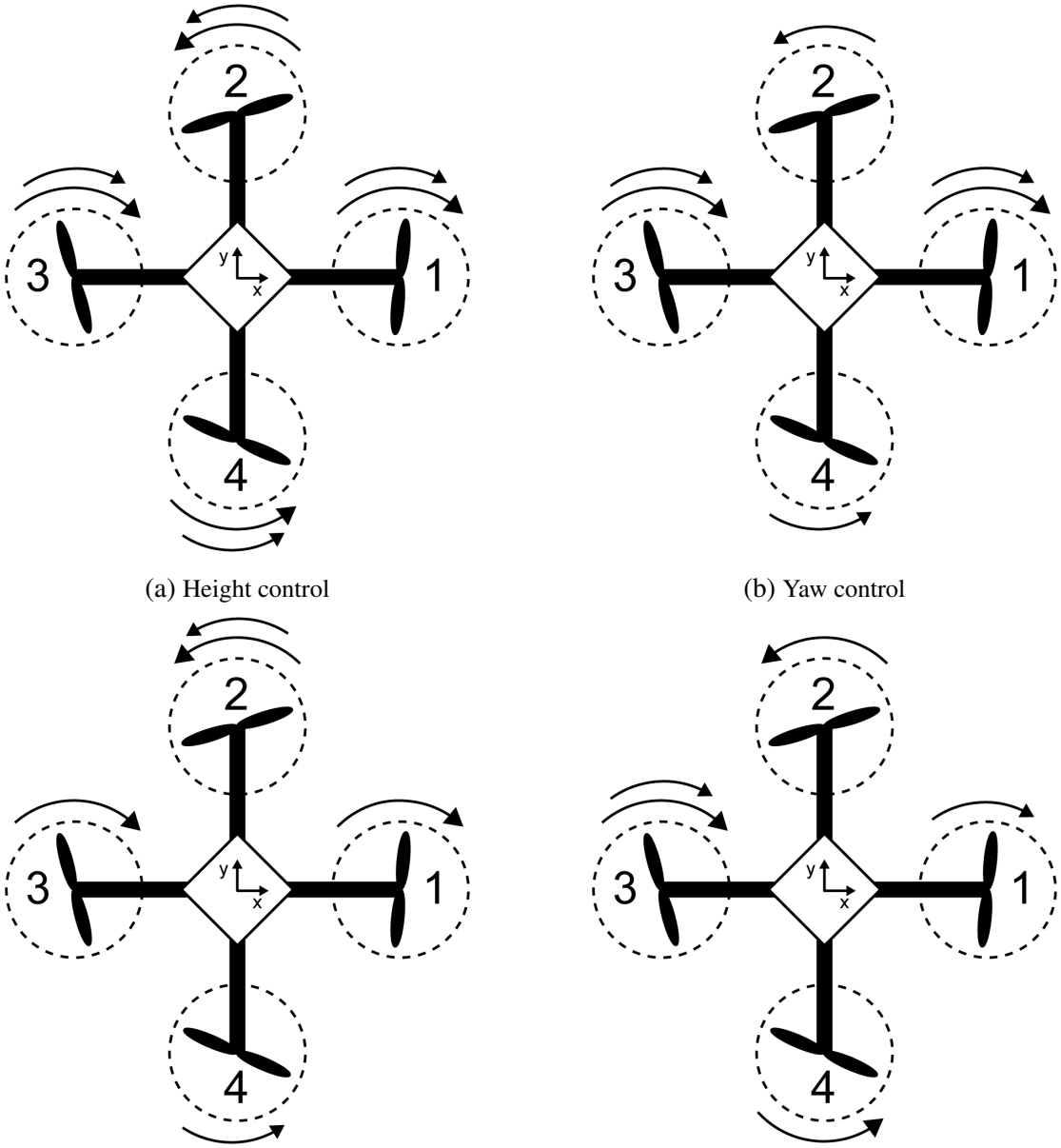

(a) Height control

(b) Yaw control

(c) Roll angle control

(d) Pitch angle control

Figure 2.2: The control policy for a four rotor vehicle in a *plus* configuration controlled with rotor thrust magnitude variations. Illustration in a) shows control policy for height control. To ascend, one must increase the speed of all rotors. Which is opposite from descending where speed of all rotors has to be decreased. To turn vehicle in positive yaw angle, the speed of 1-th and 3-th must be increased, which is shown in b). To turn vehicle in other direction, the speed of 2-th and 4-th rotor must be increased while speed of rotors 1 and 3 stays unchanged. In c) and d) the roll and pitch angle control policy is illustrated, respectively. To change roll angle of the vehicle in positive direction, the speed of 2-th rotor must be increased while for the positive pitch angle, we have to increase the speed of 3-th rotor. Changing the roll and pitch angle in negative direction will be the result of increasing the speed of 4-th and 1-th rotor, respectively.

2.2Concept based on rotor thrust direction

The rotor thrust direction concept is a concept where each rotor is mounted on a tilting actuator, which allows variations in rotor thrust direction. As in concept based on rotor thrust magnitude, the vehicle can be composed of an arbitrary number of rotor pairs, where rotor pair consists of an counterclockwise rotor and clockwise rotor. Difference is that rotors can be tilted with respect to the vehicle frame, so they can produce thrust in direction parallel to the horizontal plane of the vehicle frame. To control the horizontal movement, rotors are tilted which produce desired force and also changes the vehicle's roll and pitch angle. Using such concept in combination with rotor thrust magnitude concept we could achieve full 6 degree of freedom control of the vehicle. Such control could be useful for example carrying sensitive payload where tilting the vehicle's frame is not suitable.

In Figure 2.3 we depict the control policy for setting rotor speed and tilt reference in order to control height and yaw, pitch and roll angle. The control policy for the height and yaw angle is the same as for the rotor thrust magnitude. This control policies are shown on Figure 2.3a for height and on Figure 2.3b for yaw angle. Figure 2.3c shows illustration for changing roll angle of the vehicle. By tilting the 2-th and 4-th rotor vehicle rotates around x axis of body frame. On the other hand, to rotate vehicle around y axis of body frame, pitch angle, the 1-th and 3-th rotor has to be tilted. This is shown on Figure 2.3d. Illustrated control policies are shown on a simplified vehicle with four rotors in *plus* configuration.

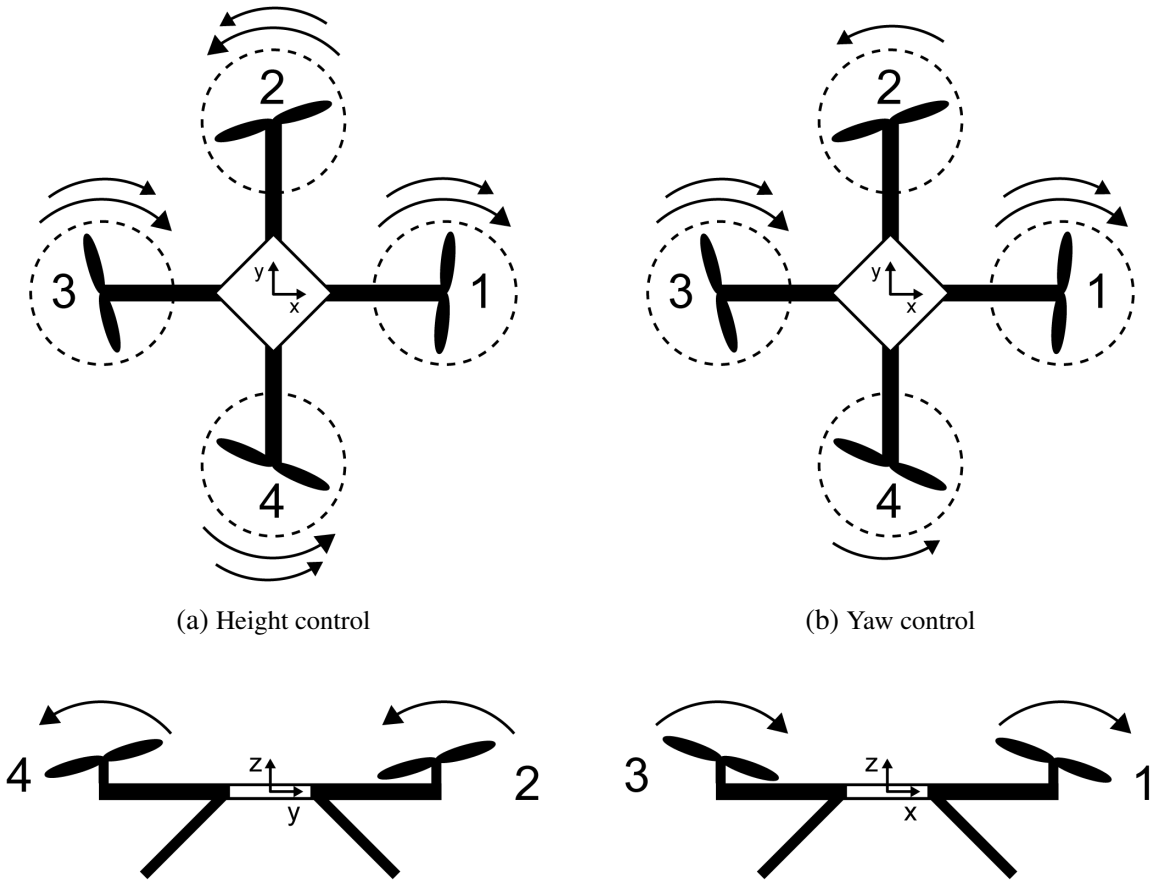

(a) Height control

(b) Yaw control

(c) Roll angle control

(d) Pitch angle control

Figure 2.3: The control policy for a four rotor vehicle in a *plus* configuration controlled using rotor thrust direction variation. Illustration in a) shows control policy for height control. To ascend, one must increase the speed of all rotors. Which is opposite from descending where speed of all rotors has to be decreased. To turn vehicle in positive yaw angle, the speed of 1-th and 3-th must be increased, which is shown in b). To turn vehicle in other direction, the speed of 2-th and 4-th rotor must be increased while speed of rotors 1 and 3 stays unchanged. In c) vehicle rotates in positive roll angle direction. To achieve negative roll angle direction rotor 2 and rotor 4 has to be tilted in opposite direction. Pitch angle is controlled by rotor 1 and rotor 3, which is shown in d). Illustration shows rotation in positive direction, to rotate vehicle in negative direction, the rotor 1 and rotor 3 has to be tilted in opposite direction.

2.3Concept based on centroid variation

The last concept that is part of this thesis is concept based on centroid variation. This concept relies on the change of the CoG of the vehicle in order to distribute the torque around the body to control its attitude. Using the shift in vehicle CoG, two degrees of freedom of the vehicle can be controlled, roll and pitch angles. Because of inability to control other vehicle's degrees of freedom, the traditional, rotor thrust magnitude, concept is applied to control vehicle's yaw angle and height. This, traditional, control concept is the same as described in Section 2.1. The moving mass dynamics is crucial for this control concept. The complete analysis of the influence of the moving mass to the system stability and performance can be found in [72]

The complete control policy illustration is shown in Figure 2.4. The height control and yaw control, shown in Figure 2.4a and Figure 2.4b, respectively, are the same as control policy for the concept based on rotor thrust magnitude. The two remaining degrees of freedom of the vehicle, roll and pitch angle, are controlled using shift in centre of mass by displacing external payload on the vehicle. This payload could be specially designed moving masses or for example a robotic arm carrying a payload. We illustrated control policy for the vehicle's roll and pitch angle on a simplified vehicle with four rotors and four moving masses, each one on one vehicle's arm, in a *plus* configuration. This control policies are shown on Figure 2.4c for roll axis and on Figure 2.4d for pitch axis. By vertical displacement of moving masses, in x and y direction, the vehicle's angles are controlled.

Another way to use changes in the vehicle's CoG to control the vehicle is in combination with the concept based on rotor thrust direction and magnitude. By using all three principles, it is possible to achieve full 6 degrees of freedom control of the vehicle. The concept based on rotor thrust is used for controlling the vehicle's roll, pitch, and yaw angles, as well as for height control. The other two concepts, thrust direction, and centroid variation can be used to control the vehicle's horizontal movement. A detailed description of such a concept is explained in Chapter 5.

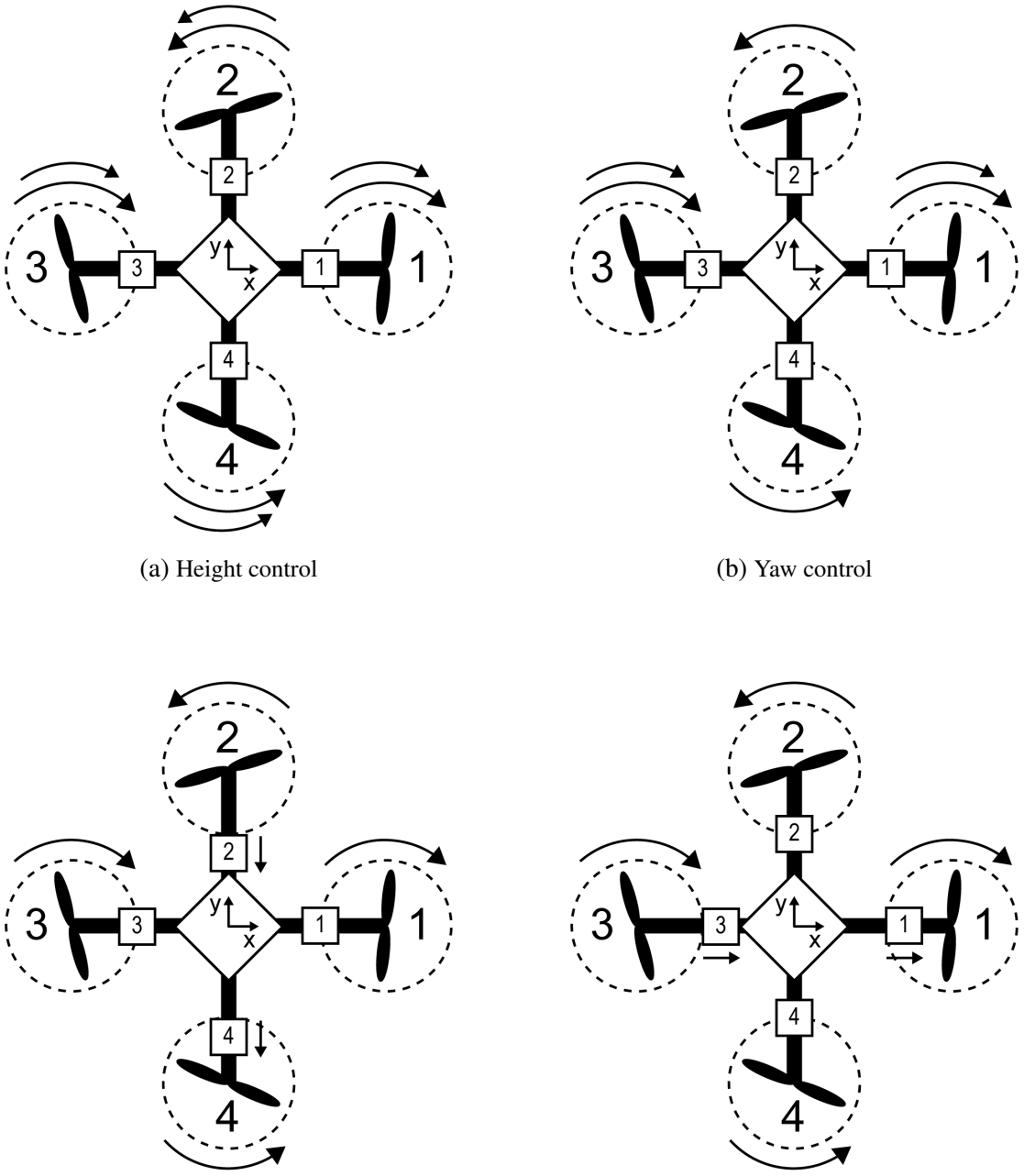

(a) Height control

(b) Yaw control

(c) Roll angle control

(d) Pitch angle control

Figure 2.4: The control policy for a four rotor vehicle in a *plus* configuration controlled with centroid variation. Illustration in a) shows control policy for height control. To ascend, one must increase the speed of all rotors. Which is opposite from descending where speed of all rotors has to be decreased. To turn vehicle in positive yaw angle, the speed of 1-th and 3-th must be increased, which is shown in b). To turn vehicle in other direction, the speed of 2-th and 4-th rotor must be increased while speed of rotors 1 and 3 stays unchanged. In c) the vehicle roll angle control policy is presented. For a positive roll angle, the moving masses should move in negative y direction, where for the negative roll angle, the moving masses should move in positive y direction. It is similar concept for pitch angle d). To turn vehicle by positive pitch angle, moving masses should move in positive x direction, and for negative pitch angle, moving masses should move in negative x direction.

CHAPTER 3

Generalized unmanned aerial manipulator model

In this chapter we derive generalized unmanned aerial manipulator model that unifies actuation concepts based on the centroid variation, thrust direction and thrust magnitude control, which are presented in Chapter 2. The developed model is restricted in a way that rotors can be tilted in only one direction. For modeling we used basic theory of rigid body dynamics. We model the unmanned aerial manipulator vehicle as a mechanical system comprised of $N_m + 1$ coupled rigid bodies, where N_m is number of moving masses on the vehicle (this masses can be manipulator links, payload and etc.). Additional rigid body is vehicle frame, which includes battery, central body, vehicle's arms and rotors. The model accounts for the ability to tilt the rotors through the arbitrary angle β. The developed model can be used for any configuration type of the unmanned aerial manipulator, with an arbitrary number of rotors and moving masses. In the remained of this chapter, we derive the complete generalized nonlinear dynamic model (Section 3.1), as well as the linear form suitable for control design. (Section 3.2).

3.1Nonlinear dynamical model

The nonlinear dynamic model of the unmanned aerial vehicle describes its rotation and translation dynamics. These are derived based on the vehicle kinematic model, and the dynamic models of vehicle components. In particular, the dynamics takes into account the actuator dynamics and the influence of external and inertial moments. Within the actuator dynamics, we analyze the effect of three internal sources, namely the rotor speed variation, rotor tilt, and centroid variation. The remaining moments acting on the vehicle body are the result of gravitational

forces and rotor drag. In order for the model to be generalized with respect to number of rotors or the actuator controlling the centroid variation, the model derivation starts from kinematic model derivation.

3.1.1Kinematic model

To obtain kinematic model of a unmanned aerial manipulator the Denavit–Hartenberg method is used. Using this method we can get a generalized kinematic model which can be easily used for any type and configuration of the unmanned aerial manipulator. The development of the kinematic model is driven with assumption that rotors can be tilted only in one direction. According to this representation, we chose L_0 as a base coordinate frame, L_j and $L_{j\beta}$ as a coordinate frames of the joints, where $j \in \{1,\ldots,N_r\}$ and N_r denotes number of rotors on the vehicle. First joint, joint j, is a fixed joint which allows us to rotate unmanned aerial manipulator arm by fixed angle θ_j around axis z_0. That way we can place as many arms as we want in any configuration type. Second joint, joint $j\beta$, is a joint which allows rotor to be tilted. This is a actuated joint with tilting angle denoted as β_j. Remaining Denavit–Hartenberg parameters can be found in Table 3.1 where a_j is length of a vehicle's arm and d_j is a distance between propeller and a vehicle's origin measured along z_0 axis. The Figure 3.1 shows an example of coordinate frames and Denavit-Hartenberg parameters for one unmanned aerial manipulator's arm.

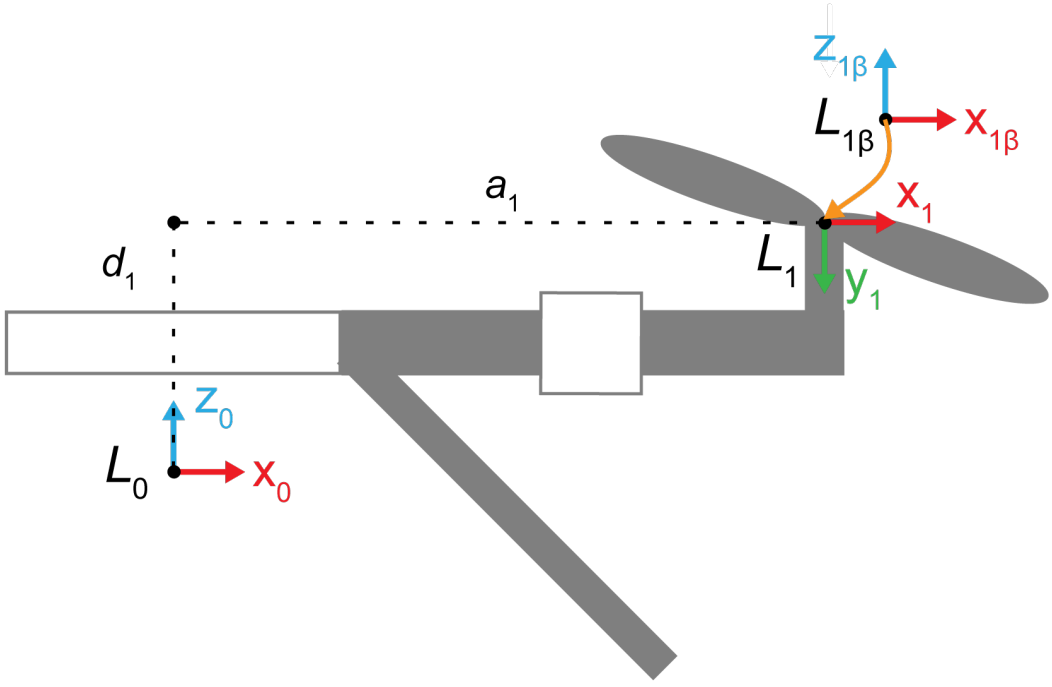

Figure 3.1: This figure shows coordinate frames and Denavit–Hartenberg parameters for one arm of the unmanned aerial manipulator. Note that origins of L_1 and $L_{1\beta}$ coincide. Using such representation we can derive kinematic model of a complex unmanned aerial manipulator with multiple arms.

Table 3.1: Denavit-Hartenberg parameters of the unmanned aerial manipulator

joint	θ	d	a	α
j	θ_j	d_j	a_j	$\frac{3}{2}\pi$
$j\beta$	β_j	0	0	$\frac{1}{2}\pi$

Using Denavit-Hartenberg parameters from Table 3.1 we can derive homogeneous transformation matrix between base coordinate frame L_0 and frame L_j as:

$$\mathbf{T}_0^j = \begin{bmatrix} C(\Theta_j) & 0 & -S(\Theta_j) & a_j C(\Theta_j) \\ S(\Theta_j) & 0 & C(\Theta_j) & a_j S(\Theta_j) \\ 0 & -1 & 0 & d_j \\ 0 & 0 & 0 & 1 \end{bmatrix}, \; j \in \{1,\ldots,N_r\}, \tag{3.1}$$

and second homogeneous transformation matrix between frame L_j and $L_{j\beta}$:

$$\mathbf{T}_j^{j\beta} = \begin{bmatrix} C(\beta_j) & 0 & S(\beta_j) & 0 \\ S(\beta_j) & 0 & -C(\beta_j) & 0 \\ 0 & 1 & 0 & 0 \\ 0 & 0 & 0 & 1 \end{bmatrix}, \; j \in \{1,\ldots,N_r\}. \tag{3.2}$$

where $S(x)$ and $C(x)$ represent $sin(x)$ and $cos(x)$ functions, respectively. Matrix $\mathbf{T}_0^j$ transforms moving coordinate system L_j in fixed base coordinate system L_0. Second matrix $\mathbf{T}_j^{j\beta}$ transforms moving coordinate system $L_{j\beta}$ in moving coordinate system L_j. Multiplying this two matrices we obtain homogeneous transformation matrix $\mathbf{T}_0^{j\beta}$ that transforms $L_{j\beta}$ in base coordinate system L_0. Such matrix is given with:

$$\mathbf{T}_0^{j\beta} = \mathbf{T}_0^j \cdot \mathbf{T}_j^{j\beta} = \begin{bmatrix} C(\beta_j)C(\Theta_j) & -S(\Theta_j) & S(\beta_j)C(\Theta_j) & a_j C(\Theta_j) \\ C(\beta_j)S(\Theta_j) & C(\Theta_j) & S(\beta_j)S(\Theta_j) & a_j S(\Theta_j) \\ -S(\beta_j) & 0 & C(\beta_j) & d_j \\ 0 & 0 & 0 & 1 \end{bmatrix}, \; j \in \{1,\ldots,N_r\}, \tag{3.3}$$

This matrix can be written in following form:

$$\mathbf{T}_0^{j\beta} = \begin{bmatrix} \mathbf{R}_0^{j\beta} & \mathbf{p}_0^{j\beta} \\ \mathbf{v}_1^{\mathsf{T}} & 1 \end{bmatrix}, \; j \in \{1,\ldots,N_r\}, \tag{3.4}$$

where vector $\mathbf{v}_1^{\mathsf{T}}$ is a zero vector, vector $\mathbf{p}_0^{j\beta} \in \mathbb{R}^{3x1}$ defines position of the j-th rotor in L_0 frame and matrix $\mathbf{R}_0^{j\beta} \in \mathbb{R}^{3x3}$ defines j-th rotor orientation in L_0 frame. This vectors can be written as:

$$\mathbf{v}_1^{\mathsf{T}} = \begin{bmatrix} 0 & 0 & 0 \end{bmatrix}, \tag{3.5}$$

$$\mathbf{p}_0^{j\beta} = \begin{bmatrix} a_j C(\Theta_j) & a_j S(\Theta_j) & d_j \end{bmatrix}^{\mathsf{T}}, \; j \in \{1,\ldots,N_r\}, \tag{3.6}$$

$$\mathbf{R}_0^{j\beta} = \begin{bmatrix} C(\beta_j)C(\Theta_j) & -S(\Theta_j) & S(\beta_j)C(\Theta_j) \\ C(\beta_j)S(\Theta_j) & C(\Theta_j) & S(\beta_j)S(\Theta_j) \\ -S(\beta_j) & 0 & C(\beta_j) \end{bmatrix}, \; j \in \{1,\ldots,N_r\}. \tag{3.7}$$

In Figure 3.2 we show relevant vectors for one unmanned aerial manipulator's arm. All vectors are expressed in the unmanned aerial manipulator body frame L_0. Vector $\mathbf{r}_{0,c}$ denotes position vector from the L_0 frame to the L_{CoG}. Vector $\mathbf{r}_{0,i}$ denotes position vector from the L_0 frame to the i-th moving mass. Next, position vector from the L_0 frame to the j-th rotor is denoted with $\mathbf{r}_{0,r_j}$ and vector $\mathbf{r}_{c,i}$ denotes position vector from the L_{CoG} frame to the i-th moving mass. The inertial frame is labeled as L_I.

The definition of position of the moving masses referenced in the L_0 frame is:

$$\mathbf{r}_{0,i} = \begin{bmatrix} x_i & y_i & z_i \end{bmatrix}^{\mathsf{T}}, \; i \in \{1,\ldots,N_m\} \tag{3.8}$$

where N_m is a number of moving masses. Variables x_i, y_i and z_i are displacement of the i-th moving mass in body x, y, and z axis, respectively.

The CoG of the vehicle observed in the body frame, denoted as $r_{0.c}$ is given by:

$$\mathbf{r}_{0,c} = \frac{m_b \mathbf{r}_{0,b} + \sum_{i=1}^{N_m} m_i \mathbf{r}_{0,i}}{m_b + \sum_{i=1}^{N_m} m_i} = \frac{\sum_{i=1}^{N_m} m_i \mathbf{r}_{0,i}}{M} = \mu \sum_{i=1}^{N_m} m_i \mathbf{r}_{0,i}, \tag{3.9}$$

with m_b as the mass of the aerial manipulator rigid body (without moving masses), m_i denotes the mass of the i-th moving mass, $\mathbf{r}_{0,i}$ and $\mathbf{r}_{0,b}$ represent the position of the i-th moving mass and aerial manipulator body, respectively, expressed in the body frame. M represents the total

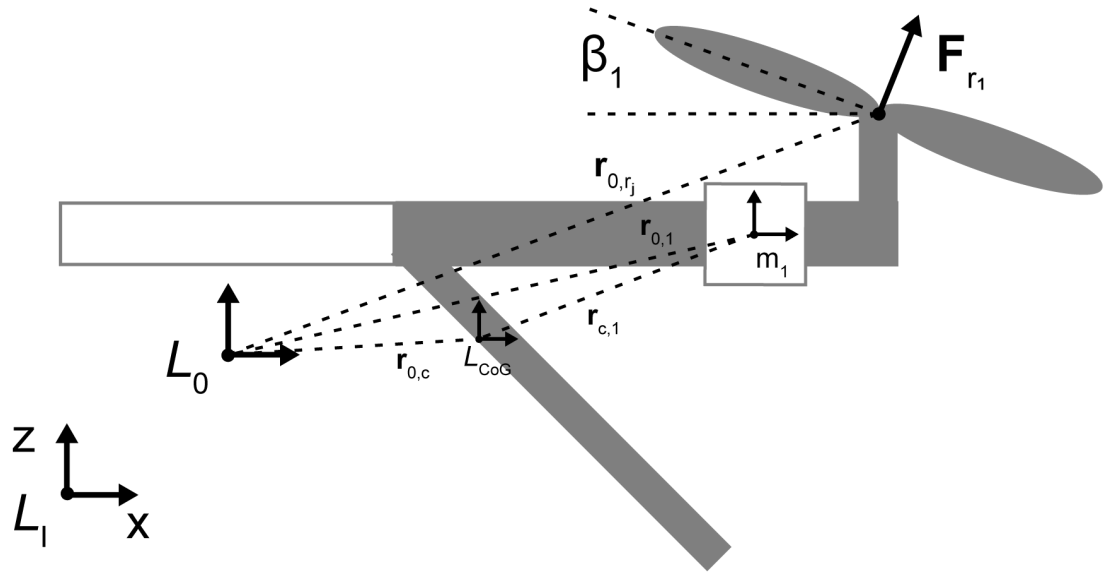

Figure 3.2: Figure shows vehicles body coordinate frame L_0, inertial frame L_I and the centre of gravity L_{CoG} with relevant vectors for first unmanned aerial manipulator's arm.

mass of the vehicle. Here, we introduce substitution $\mu = \frac{1}{M}$ for simplicity in remainder of this model derivation procedure. We use the assumption that the origin of the body frame coincides with the CoG of the aerial manipulator rigid body, which yields $\mathbf{r}_{0,b} = 0$. The complete equation for the CoG expressed in the body frame can be obtained by substituting the Equation (3.8) into Equation (3.9):

$$\mathbf{r}_{0,c} = \mu \sum_{i=1}^{N_m} m_i \begin{bmatrix} x_i & y_i & z_i \end{bmatrix}^{\mathsf{T}}. \tag{3.10}$$

The position of the rotors in the body frame L_0 are already expressed with Equation (3.6) and can be written as:

$$\mathbf{r}_{0,r_j} = \mathbf{p}_0^{j\beta},\ j \in \{1,\ldots,N_r\} \tag{3.11}$$

To get from inertial frame to body frame we use representation where vehicle is rotated around z, y and x axis, respectively. The rotation matrix from L_{CoG} to L_I frame and L_{CoG} to L_I frame is given with:

$$\mathbf{R}_c^I = \mathbf{R}_0^I = \begin{bmatrix} C(\theta)C(\psi) & S(\phi)S(\theta)C(\psi) - C(\theta)S(\psi) & C(\phi)S(\theta)C(\psi) + S(\phi)S(\psi) \\ C(\theta)S(\psi) & S(\phi)S(\theta)S(\psi) + C(\phi)C(\psi) & C(\phi)S(\theta)S(\psi) - S(\phi)C(\psi) \\ -S(\theta) & S(\phi)C(\theta) & C(\phi)C(\theta) \end{bmatrix}. \tag{3.12}$$

The rotation matrix $\mathbf{R}_c^I = \mathbf{R}_0^I$ since the L_{CoG} is aligned with L_0. The roll rate ($\dot{\phi}$), pitch rate ($\dot{\theta}$)

and yaw rate ($\dot{\psi}$) can be calculated from angular velocity ω with following transformation:

$$\begin{bmatrix} \dot{\phi} \\ \dot{\theta} \\ \dot{\psi} \end{bmatrix} = \begin{bmatrix} 1 & S(\phi)T(\theta) & C(\phi)T(\theta) \\ 0 & C(\phi) & -S(\phi) \\ 0 & \frac{S(\phi)}{C(\theta)} & \frac{C(\phi)}{C(\theta)} \end{bmatrix} \begin{bmatrix} \omega_x \\ \omega_y \\ \omega_z \end{bmatrix} \tag{3.13}$$

where ω_x, ω_y and ω_z are angular velocities in x, y, z axes, respectively, and $T(x)$ is $tan(x)$.

3.1.2Actuator dynamics

First, we will give the equations for the unmanned aerial manipulator propulsion system. The propulsion system of the vehicle consists of a motor with a rotor. In almost all cases the electrical motor with a rotor is used because of its small time constant. There are also examples of usage of a internal combustion engine with rotor as a propulsion system [76]. The expressions in this section are valid for any kind of propulsion system with rotor. The rotor thrust force can be written as a function of the rotor speed:

$$\mathbf{F}_{r_j} = b_f \Omega_j^2 \hat{\mathbf{z}}_0^{j\beta},\ j \in \{1,\ldots,N_r\}, \tag{3.14}$$

where b_f is the rotor thrust constant, which is equal for all rotors, Ω_j denotes the speed of the j-th rotor, $z_0^{j\beta}$ represent the unit vector perpendicular to the j-th rotor plane. This vector is obtained from Equation (3.7) as the last row in the matrix and can be expressed as:

$$\hat{\mathbf{z}}_0^{j\beta} = S(\beta_j)C(\Theta_j)\hat{\mathbf{i}} + S(\beta_j)S(\Theta_j)\hat{\mathbf{j}} + C(\beta_j)\hat{\mathbf{k}},\ j \in \{1,\ldots,N_r\}, \tag{3.15}$$

where $\hat{\mathbf{i}}$, $\hat{\mathbf{j}}$ and $\hat{\mathbf{k}}$ are the unit vectors of the aerial manipulator body frame. Next, we have to derive expression for the moment of force of a rotor. This moment is a result of a induced drag and can be written as:

$$\mathbf{M}_{r_j} = \zeta_j b_m b_f \Omega_j^2 \hat{\mathbf{z}}_0^{j\beta},\ j \in \{1,\ldots,N_r\}, \tag{3.16}$$

where $\zeta_j = 1$ if the j-th propeller is rotating clockwise or $\zeta_j = -1$ if the propeller is rotating counter-clockwise. Parameter b_m is the rotor moment constant.

Here we introduce another assumption, that the rotor speed is controlled and it's dynamics can be expressed as:

$$G_{\Omega_j} = \frac{\Omega_j(s)}{\Omega_{j,ref}(s)} = \frac{1}{\frac{1}{\omega_r^2}s^2 + \frac{2\zeta_r}{\omega_r}s + 1},\ j \in \{1,\ldots,N_r\}, \tag{3.17}$$

where ω_r and ζ_r are natural frequency and damping factor, respectively. The j-th rotor speed

reference is denoted with $\Omega_{j,ref}$ and rotor speed is denoted with Ω_j.

Another actuator that we need to take into account is a servo motor that is used for tilting the rotors. By observing the response of the servo motor we assumed that this system can be represent with PT_2S dynamics:

$$G_{tr_i} = \frac{\beta_j(s)}{\beta_{j,ref}(s)} = \frac{1}{\frac{1}{\omega_{tr}^2}s^2 + \frac{2\zeta_{tr}}{\omega_{tr}}s + 1},\ j \in \{1,\ldots,N_r\}, \tag{3.18}$$

where $\beta_{j,ref}$ is a tilting angle reference, ω_{tr} and ζ_{tr} are natural frequency and damping factor, respectively.

The last actuation system that has to be described is a moving mass actuation. This actuation is responsible for controlling the vehicle's CoG. As we already noted, this actuation can be manipulator links, payload, etc. We assume that this actuator type can be also represent with PT_2S dynamics. The transfer function of such actuation system is as follows:

$$G_{mm_i} = \frac{x_i(s)}{x_{i,ref}(s)} = \frac{y_i(s)}{y_{i,ref}(s)} = \frac{z_i(s)}{z_{i,ref}(s)} = \frac{1}{\frac{1}{\omega_{mm}^2}s^2 + \frac{2\zeta_{mm}}{\omega_{mm}}s + 1},\ i \in \{1,\ldots,N_m\}, \tag{3.19}$$

where x_i, y_i, z_i denotes position of the i-th moving mass in the body frame x, y and z axis, respectively, $x_{i,ref}$, $y_{i,ref}$ and $z_{i,ref}$ represents the reference of the i-th mass position in x, y and z axis, respectively. Moving mass natural frequency is denoted with ω_{mm} and damping factor with ζ_{mm}.

3.1.3Attitude dynamics

We shall now derive equations for the angular momentum of a unmanned aerial manipulator. As we observe unmanned aerial manipulator as a mechanical system comprised of $N_m + 1$ coupled rigid bodies, the total angular momentum of the vehicle can be written as the sum of the angular momentum of the vehicle's constituents:

$$\mathbf{L}_s = \mathbf{L}_b + \sum_{i=1}^{N_m} \mathbf{L}_i, \tag{3.20}$$

where $\mathbf{L}_s$ is the angular momentum of the overall system, $\mathbf{L}_b$ is the angular momentum of the aerial manipulator rigid body and $\mathbf{L}_i$ is the angular momentum of the i-th mass. Angular momentum is the quantity of rotation of a body, which is the product of its moment of inertia and its angular velocity. This also can be expressed as a cross product of the position vector $\mathbf{r}$ and the linear momentum $\mathbf{p} = m\mathbf{v}$ of the particle. For a system of particles the angular momentum about the point S is:

$$\mathbf{L} = \int_k \mathbf{r}_{S,k} \times \mathbf{v}_k dm_k. \tag{3.21}$$

where $\mathbf{r}_{S,k}$ is the vector from point S to the k-th part of the body, dm_k is the infinitesimal part of the body and $\mathbf{v}_k$ is its velocity. Using this definition we can derive angular momentum of the unmanned aerial vehicle expressed in the L_{CoG} frame w.r.t. the inertial frame:

$$\begin{aligned}\mathbf{L}_b &= \int_k \mathbf{r}_{c,k} \times \mathbf{v}_k dm_k, \\ \mathbf{L}_i &= \int_l \mathbf{r}_{c,l} \times \mathbf{v}_l dm_l,\end{aligned} \tag{3.22}$$

where $\mathbf{r}_{c,k}$ is a position vector from L_{CoG} to the k-th part of the vehicle body and $\mathbf{r}_{c,l}$ is the position vector from L_{CoG} to the l-th part of the moving mass. By substituting velocities, $\mathbf{v}_k$ and $\mathbf{v}_l$, expressed in the L_{CoG} frame w.r.t. inertial frame:

$$\begin{aligned}\mathbf{v}_k &= \mathbf{v}_c + \mathbf{v}_{c,k} + \boldsymbol{\omega} \times \mathbf{r}_{c,k}, \\ \mathbf{v}_l &= \mathbf{v}_c + \mathbf{v}_{c,l} + \boldsymbol{\omega} \times \mathbf{r}_{c,l},\end{aligned} \tag{3.23}$$

into Equation (3.22) we obtain angular momentum equation for each part of a system as:

$$\begin{aligned}\mathbf{L}_b &= m_b \mathbf{r}_{c,0} \times \mathbf{v}_c + m_b \mathbf{r}_{c,0} \times \mathbf{v}_{c,0} + \mathbf{I}_b^c \boldsymbol{\omega}, \\ \mathbf{L}_i &= m_i \mathbf{r}_{c,i} \times \mathbf{v}_c + m_i \mathbf{r}_{c,i} \times \mathbf{v}_{c,0} + m_i \mathbf{r}_{c,i} \times \mathbf{v}_{0,i} + \mathbf{I}_i^c \boldsymbol{\omega},\end{aligned} \tag{3.24}$$

where $\mathbf{v}_c$ is the velocity of the L_{CoG} frame w.r.t. inertial frame. Finally, using the Equation (3.20) and Equation (3.24) we can give overall angular momentum equation with:

$$\mathbf{L}_s = \mathbf{I}_b^c \boldsymbol{\omega} + \sum_{i=1}^{N_m} \mathbf{I}_i^c \boldsymbol{\omega} + \sum_{i=1}^{N_m} m_i \mathbf{r}_{c,i} \times \mathbf{v}_{0,i}, \tag{3.25}$$

or in more compact form:

$$\mathbf{L}_s = \mathbf{I}_s^c \boldsymbol{\omega} + \sum_{i=1}^{N_m} \mathbf{r}_{c,i} \times \mathbf{p}_{0,i}, \tag{3.26}$$

where $\mathbf{I}_s^c$ is the moment of inertia of the unmanned aerial manipulator w.r.t the vehicle CoG. Vector $\mathbf{r}_{c,i}$ denotes position vector from the L_{CoG} to the i-th moving mass frame and $\mathbf{p}_{0,i}$ is a linear momentum of the i-th moving mass w.r.t. the vehicles rigid body:

$$\mathbf{p}_{0,i} = m_i \mathbf{v}_{0,i}, \tag{3.27}$$

where $\mathbf{v}_{0,i}$ is the velocity of the i-th moving mass expressed in L_0 frame. We can calculate overall moment of inertia by summing inertial contributions of each part of the unmanned aerial manipulator:

$$\mathbf{I}_s^c = \mathbf{I}_b^c + \sum_{i=1}^{N_m} \mathbf{I}_i^c, \tag{3.28}$$

where $\mathbf{I}_i^c$ is a moment of inertia of the i-th moving mass w.r.t. the vehicle CoG, and $\mathbf{I}_b^c$ is the moment of inertia of the unmanned aerial manipulator rigid body w.r.t. the vehicle CoG. In order to compute moments of inertia of the vehicle rigid body and moving masses we use the parallel axis theorem, also known as Huygens–Steiner theorem. The moment of inertia of the unmanned aerial manipulator's rigid body can be calculated from:

$$\mathbf{I}_b^c = \mathbf{I}_b + m_b(\mathbf{r}_{0,c}^\mathsf{T} \cdot \mathbf{r}_{0,c}\mathbf{E}_3 - \mathbf{r}_{0,c} \cdot \mathbf{r}_{0,c}^\mathsf{T}), \tag{3.29}$$

where $\mathbf{I}_b$ is the moment of inertia of the unamnned aerial manipulator's rigid body w.r.t. its own CoG, and $\mathbf{E}_3$ is the $3x3$ identity matrix. We assume that products of inertia of $\mathbf{I}_b$ are zero, then matrix $\mathbf{I}_b$ can be written as:

$$\mathbf{I}_b = \begin{bmatrix} I_{b,xx} & 0 & 0 \\ 0 & I_{b,yy} & 0 \\ 0 & 0 & I_{b,zz} \end{bmatrix}, \tag{3.30}$$

where $I_{b,xx}$, $I_{b,yy}$ and $I_{b,zz}$ represent the vehicle rigid body moments of inertia in x, y and z axes, respectively. By substituting Equation (3.10) into Equation (3.29) we get full tensor of inertia of a unmanned aerial manipulator's rigid body:

$$\mathbf{I}_b^c = \begin{bmatrix} I_{b,xx}^c & I_{b,xy}^c & I_{b,xz}^c \\ I_{b,yx}^c & I_{b,yy}^c & I_{b,yz}^c \\ I_{b,zx}^c & I_{b,zy}^c & I_{b,zz}^c \end{bmatrix}, \tag{3.31}$$

$$I^c_{b,xx} = I_{b,xx} + m_b\mu^2 \left[\left(\sum_{i=1}^{N_m} m_i y_i \right)^2 + \left(\sum_{i=1}^{N_m} m_i z_i \right)^2 \right], \tag{3.32}$$

$$I^c_{b,yy} = I_{b,yy} + m_b\mu^2 \left[\left(\sum_{i=1}^{N_m} m_i x_i \right)^2 + \left(\sum_{i=1}^{N_m} m_i z_i \right)^2 \right], \tag{3.33}$$

$$I^c_{b,zz} = I_{b,zz} + m_b\mu^2 \left[\left(\sum_{i=1}^{N_m} m_i y_i \right)^2 + \left(\sum_{i=1}^{N_m} m_i x_i \right)^2 \right], \tag{3.34}$$

$$I^c_{b,xy} = I^c_{b,yx} = -m_b\mu^2 \left[\left(\sum_{i=1}^{N_m} m_i x_i \right) \left(\sum_{i=1}^{N_m} m_i y_i \right) \right], \tag{3.35}$$

$$I^c_{b,xz} = I^c_{b,zx} = -m_b\mu^2 \left[\left(\sum_{i=1}^{N_m} m_i z_i \right) \left(\sum_{i=1}^{N_m} m_i x_i \right) \right], \tag{3.36}$$

$$I^c_{b,yz} = I^c_{b,zy} = -m_b\mu^2 \left[\left(\sum_{i=1}^{N_m} m_i z_i \right) \left(\sum_{i=1}^{N_m} m_i y_i \right) \right]. \tag{3.37}$$

The expression for the moment of the inertia of the i-th moving masses is given with:

$$\mathbf{I}^c_i = \mathbf{I}_i + m_i(\mathbf{r}^\mathsf{T}_{c,i} \cdot \mathbf{r}_{c,i}\mathbf{E}_3 - \mathbf{r}_{c,i} \cdot \mathbf{r}^\mathsf{T}_{c,i}), \tag{3.38}$$

where $\mathbf{I}_i$ is moment of inertia of the i-th moving mass w.r.t. its own CoG. We assumed that a moving mass can be considered as a point mass, therefore $\mathbf{I}_i = \mathbf{0}$. Expression for the position vector $\mathbf{r}_{c,i}$ can be derived from position vectors $\mathbf{r}_{0,i}$ (Equation (3.8)) and $\mathbf{r}_{0,c}$ (Equation (3.10)):

$$\mathbf{r}_{c,i} = \begin{bmatrix} x_i - \mu \sum_{j=1}^{N_m} m_j x_j & y_i - \mu \sum_{j=1}^{N_m} m_j y_j & z_i - \mu \sum_{j=1}^{N_m} m_j z_j \end{bmatrix}^\mathsf{T}, \; i \in \{1, \ldots, N_m\}. \tag{3.39}$$

Substituting Equation (3.39) in Equation (3.38) we derive complete tensor matrix for the i-th moving mass:

$$\mathbf{I}^c_i = \begin{bmatrix} I^c_{i,xx} & I^c_{i,xy} & I^c_{i,xz} \\ I^c_{i,yx} & I^c_{i,yy} & I^c_{i,yz} \\ I^c_{i,zx} & I^c_{i,zy} & I^c_{i,zz} \end{bmatrix}, \tag{3.40}$$

$$I^c_{i,xx} = \left(y_i - \mu \sum_{j=1}^{N_m} m_j y_j \right)^2 + \left(z_i - \mu \sum_{j=1}^{N_m} m_j z_j \right)^2, \tag{3.41}$$

$$I^c_{i,yy} = \left(x_i - \mu \sum_{j=1}^{N_m} m_j x_j \right)^2 + \left(z_i - \mu \sum_{j=1}^{N_m} m_j z_j \right)^2, \tag{3.42}$$

$$I^c_{i,zz} = \left(x_i - \mu \sum_{j=1}^{N_m} m_j x_j \right)^2 + \left(y_i - \mu \sum_{j=1}^{N_m} m_j y_j \right)^2, \tag{3.43}$$

$$I^c_{i,xy} = I^c_{i,yx} = - \left(x_i - \mu \sum_{j=1}^{N_m} m_j x_j \right) \left(y_i - \mu \sum_{j=1}^{N_m} m_j y_j \right), \tag{3.44}$$

$$I^c_{i,xz} = I^c_{i,zx} = - \left(x_i - \mu \sum_{j=1}^{N_m} m_j x_j \right) \left(z_i - \mu \sum_{j=1}^{N_m} m_j z_j \right), \tag{3.45}$$

$$I^c_{i,yz} = I^c_{i,zy} = - \left(y_i - \mu \sum_{j=1}^{N_m} m_j y_j \right) \left(z_i - \mu \sum_{j=1}^{N_m} m_j z_j \right). \tag{3.46}$$

The whole system tensor matrix can be calculated from Equation (3.31), Equation (3.40) and Equation (3.28).

The torque is defined as the rate of change of angular momentum. From this definition we can derive expression for angular velocity rate $\dot{\omega}$ of the unmanned aerial manipulator:

$$\frac{d^{\omega}}{dt} \left(\mathbf{I}^c_s \omega + \sum_{i=1}^{N_m} \mathbf{r}_{c,i} \times \mathbf{p}_{0,i} \right) = \mathbf{M}_e. \tag{3.47}$$

With $\mathbf{M}_e$ we denoted sum of the external torques that affects the vehicle. We model three types of external torques:

- $\mathbf{M}_{f_j}$ moments of the rotor forces acting on some radius from CoG,
- $\mathbf{M}_{r_j}$ rotor torques due to the induced drag,
- $\mathbf{M}_g$ moment due to the gravity forces,

which can be summarize in equation:

$$\mathbf{M}_e = \sum_{j=1}^{N_r} \left(\mathbf{M}_{f_j} + \mathbf{M}_{r_j} \right) + \mathbf{M}_g. \tag{3.48}$$

Lets write equations for this external torques. The torque $\mathbf{M}_{f_j}$ can be written as:

$$\mathbf{M}_{f_j} = \mathbf{r}_{c,r_j} \times \mathbf{F}_{r_j} = \left(\mathbf{r}_{c,0} + \mathbf{r}_{0,r_j} \right) \times \mathbf{F}_{r_j}, \tag{3.49}$$

with $\mathbf{r}_{c,0} = -\mathbf{r}_{0,c}$ given with Equation (3.10) and $\mathbf{r}_{0,r_j}$ given with Equation (3.11). Vector $\mathbf{r}_{c,r_j}$ is a position vector from L_{CoG} to the j-th rotor. The rotor torque $\mathbf{M}_{r_j}$ is modeled with Equation

(3.16) and the gravity torque $\mathbf{M}_g$ is given with:

$$\mathbf{M}_g = \mathbf{r}_{c,0} \times (-m_b g \hat{\mathbf{K}}) + \sum_{i=1}^{N_m} \mathbf{r}_{c,i} \times (-m_i g \hat{\mathbf{K}}), \tag{3.50}$$

where g is gravitational acceleration and $\hat{\mathbf{K}}$ represents the unit vector of the L_I frame in z axis. We can easily show that $\mathbf{M}_g = \mathbf{0}$ as we are expressing angular momentum w.r.t. the system CoG. The position vector $\mathbf{r}_{c,i}$ can be written as a linear combination of position vectors $\mathbf{r}_{0,i}$ and $\mathbf{r}_{0,c}$:

$$\mathbf{r}_{c,i} = \mathbf{r}_{0,i} - \mathbf{r}_{0,c} \tag{3.51}$$

Substituting Equation (3.51) into Equation (3.50) we get:

$$\mathbf{M}_g = -\mathbf{r}_{c,0} \times (m_b g \hat{\mathbf{K}}) - g \sum_{i=1}^{N_m} m_i \mathbf{r}_{0,i} \times \hat{\mathbf{K}} + g \sum_{i=1}^{N_m} m_i \mathbf{r}_{0,c} \times \hat{\mathbf{K}}. \tag{3.52}$$

We can write position vector $\mathbf{r}_{c,0}$ as $\mathbf{r}_{c,0} = -\mathbf{r}_{0,c}$ and from Equation (3.9) we can express $\sum_{i=1}^{N_m} m_i \mathbf{r}_{0,i} = M\mathbf{r}_{0,c} = (m_b + \sum_{i=1}^{N_m} m_i)\mathbf{r}_{0,c}$. Including that into Equation (3.52) shows that $\mathbf{M}_g = \mathbf{0}$:

$$\mathbf{M}_g = g m_b \mathbf{r}_{0,c} \times \hat{\mathbf{K}} - g(m_b + \sum_{i=1}^{N_m} m_i)\mathbf{r}_{0,c} \times \hat{\mathbf{K}} + g \sum_{i=1}^{N_m} m_i \mathbf{r}_{0,c} \times \hat{\mathbf{K}} = \mathbf{0}. \tag{3.53}$$

To expand Equation (3.49) first we have to express position vector $\mathbf{r}_{c,r_j}$:

$$\mathbf{r}_{c,r_j} = \left(\mathbf{r}_{0,r_j} - \mathbf{r}_{0,c}\right) = \begin{bmatrix} a_j C(\Theta_j) - \mu \sum_{i=1}^{N_m} m_i x_i \\ a_j S(\Theta_j) - \mu \sum_{i=1}^{N_m} m_i y_i \\ d_j - \mu \sum_{i=1}^{N_m} m_i z_i. \end{bmatrix} \tag{3.54}$$

Next, substituting Equation (3.14) and Equation (3.54) into Equation (3.49) we get full expression for the moments produced by the rotor forces:

$$\begin{aligned} \mathbf{M}_{f_j} &= \mathbf{r}_{c,r_j} \times \mathbf{F}_{r_j} \\ &= b_f \Omega_j^2 \begin{bmatrix} \left[a_j S(\Theta_j) - \mu \sum_{i=1}^{N_m} m_i y_i\right] C(\beta_j) - \left[d_j - \mu \sum_{i=1}^{N_m} m_i z_i\right] S(\beta_j) S(\Theta_j) \\ \left[d_j - \mu \sum_{i=1}^{N_m} m_i z_i\right] S(\beta_j) C(\Theta_j) - \left[a_j C(\Theta_j) - \mu \sum_{i=1}^{N_m} m_i x_i\right] C(\beta_j) \\ \left[a_j C(\Theta_j) - \mu \sum_{i=1}^{N_m} m_i x_i\right] S(\beta_j) S(\Theta_j) - \left[a_j S(\Theta_j) - \mu \sum_{i=1}^{N_m} m_i y_i\right] S(\beta_j) C(\Theta_j) \end{bmatrix} \end{aligned} \tag{3.55}$$

Next, drag torque $\mathbf{M}_{r_j}$ is already given with Equation (3.16). The complete external torque

expression is given with:

$$\mathbf{M}_e = \sum_{j=1}^{N_r} \left(\mathbf{M}_{f_j} + \mathbf{M}_{r_j}\right) + \mathbf{M}_g = \\ b_f \sum_{j=1}^{N_r} \Omega_j^2 \begin{bmatrix} \left[a_j S(\Theta_j) - \mu \sum_{i=1}^{N_m} m_i y_i\right] C(\beta_j) - \left[d_j - \mu \sum_{i=1}^{N_m} m_i z_i\right] S(\beta_j) S(\Theta_j) + \zeta_j b_m S(\beta_j) C(\Theta_j) \\ \left[d_j - \mu \sum_{i=1}^{N_m} m_i z_i\right] S(\beta_j) C(\Theta_j) - \left[a_j C(\Theta_j) - \mu \sum_{i=1}^{N_m} m_i x_i\right] C(\beta_j) + \zeta_j b_m S(\beta_j) S(\Theta_j) \\ -\mu \sum_{i=1}^{N_m} m_i x_i S(\beta_j) S(\Theta_j) + \mu \sum_{i=1}^{N_m} m_i y_i S(\beta_j) C(\Theta_j) + \zeta_j b_m C(\beta_j) \end{bmatrix}. \tag{3.56}$$

Now we have to expand left-hand side term of the Equation (3.47) and extract the expression for angular velocity rate:

$$\dot{\mathbf{I}}_s^c \omega + \mathbf{I}_s^c \dot{\omega} + \omega \times \mathbf{I}_s^c \omega + \sum_{i=1}^{N_m} \dot{\mathbf{r}}_{c,i} \times \mathbf{p}_{0,i} + \sum_{i=1}^{N_m} \mathbf{r}_{c,i} \times \dot{\mathbf{p}}_{0,i} + \omega \times \sum_{i=1}^{N_m} \mathbf{r}_{c,i} \times \mathbf{p}_{0,i} + \sum_{i=1}^{N_m} \mathbf{r}_{c,i} \times \omega \times \mathbf{p}_{0,i} = \mathbf{M}_e. \tag{3.57}$$

It can be shown that fourth term $\sum_{i=1}^{N_m} \dot{\mathbf{r}}_{c,i} \times \mathbf{p}_{0,i} = \mathbf{0}$, and therefore is no contribution of that term to the attitude dynamics:

$$\mathbf{I}_s^c \dot{\omega} = \mathbf{M}_e - \omega \times \mathbf{I}_s^c \omega - \dot{\mathbf{I}}_s^c \omega - \sum_{i=1}^{N_m} \mathbf{r}_{c,i} \times \dot{\mathbf{p}}_{0,i} - \omega \times \sum_{i=1}^{N_m} \mathbf{r}_{c,i} \times \mathbf{p}_{0,i} - \sum_{i=1}^{N_m} \mathbf{r}_{c,i} \times \omega \times \mathbf{p}_{0,i}, \tag{3.58}$$

where

$$\begin{aligned} \dot{\mathbf{I}}_s^c &= \dot{\mathbf{I}}_b^c + \sum_{i=1}^{N_m} \dot{\mathbf{I}}_i^c, \\ \dot{\mathbf{I}}_b^c &= m_b(\dot{\mathbf{r}}_{0,c}^\top \cdot \mathbf{r}_{0,c} \mathbf{E}_3 + \mathbf{r}_{0,c}^\top \cdot \dot{\mathbf{r}}_{0,c} \mathbf{E}_3 - \dot{\mathbf{r}}_{0,c} \cdot \mathbf{r}_{0,c}^\top - \mathbf{r}_{0,c} \cdot \dot{\mathbf{r}}_{0,c}^\top), \\ \dot{\mathbf{I}}_i^c &= m_i(\dot{\mathbf{r}}_{c,i}^\top \cdot \mathbf{r}_{c,i} \mathbf{E}_3 + \mathbf{r}_{c,i}^\top \cdot \dot{\mathbf{r}}_{c,i} \mathbf{E}_3 - \dot{\mathbf{r}}_{c,i} \cdot \mathbf{r}_{c,i}^\top - \mathbf{r}_{c,i} \cdot \dot{\mathbf{r}}_{c,i}^\top). \end{aligned} \tag{3.59}$$

3.1.4Translation dynamics

Our final stage in deriving a nonlinear model of a unmanned aerial manipulator is to model the linear momentum. Linear momentum is the product of the mass and velocity of an object. As we model our system as a mechanical system comprised of several rigid bodies, total linear momentum of our system is a sum of the linear momentum of the vehicle's constituents:

$$\mathbf{p}_s = \mathbf{p}_b + \sum_{i=1}^{N_m} \mathbf{p}_i, \tag{3.60}$$

where $\mathbf{p}_b$ is a linear momentum of the unmanned aerial manipulator's body and $\mathbf{p}_i$ is the linear momentum of the i-th moving mass. Note that linear momentum of the vehicle is observed

w.r.t. inertial frame. We can write linear momentum of each rigid body as:

$$\mathbf{p}_b = m_b \mathbf{v}_b, \tag{3.61}$$

$$\mathbf{p}_i = m_i \mathbf{v}_i, \tag{3.62}$$

where $\mathbf{v}_b$ is velocity of the vehicle rigid body w.r.t. inertial frame and $\mathbf{v}_i$ is velocity of i-th moving mass w.r.t. inertial frame. We can expand equations for velocities in following way:

$$\mathbf{v}_i = \mathbf{v}_0 + \mathbf{v}_{0,i} + \boldsymbol{\omega} \times \mathbf{r}_{0,i}, \tag{3.63}$$

$$\mathbf{v}_b = \mathbf{v}_0 + \mathbf{v}_{0,b} + \boldsymbol{\omega} \times \mathbf{r}_{0,b}. \tag{3.64}$$

Note that we assume that origin of the body frame L_0 coincides with body frame L_b which implies $\mathbf{r}_{0,b} = \mathbf{0}$. Combining Equations (3.60) - (3.63) we get the overall linear momentum equation for the unmanned aerial manipulator:

$$\mathbf{p}_s = M(\mathbf{v}_0 + \boldsymbol{\omega} \times \mathbf{r}_{0,c}) + \sum_{i=1}^{N_m} m_i \mathbf{v}_{0,i}. \tag{3.65}$$

To obtain the expression for the unmanned aerial manipulator acceleration we have to use the definition of the rate of change of linear momentum which is given with:

$$\frac{d}{dt}\mathbf{p}_s = \mathbf{F}_s, \tag{3.66}$$

where $\mathbf{F}_s$ is total force acting on the vehicle. We modeled total force as two external forces acting on the vehicles, rotor's thrust, defined by Equation (3.14), and gravity force defined by:

$$\mathbf{F}_g = -Mg\hat{K}. \tag{3.67}$$

Then the total force can be expressed as:

$$\mathbf{F}_s = (\mathbf{R}_c^I)^\top \mathbf{F}_g + \sum_{j=1}^{N_r} \mathbf{F}_{r_j}, \tag{3.68}$$

Finally, using the definition of the rate of change of linear momentum, Equation (3.66), we get the expression for the unmanned aerial manipulator acceleration:

$$\frac{d^\omega}{dt}\mathbf{v}_0 = \frac{1}{M}\left((\mathbf{R}_c^I)^\top \mathbf{F}_g + \sum_{j=1}^{N_r} \mathbf{F}_{r_j} - \frac{d^\omega}{dt}\sum_{i=1}^{N_m} m_i \mathbf{v}_{0,i}\right) - \frac{d^\omega}{dt}(\boldsymbol{\omega} \times \mathbf{r}_{0,c}), \tag{3.69}$$

where

$$\frac{d^{\omega}}{dt}\mathbf{v}_0 = \dot{\mathbf{v}}_0 + \boldsymbol{\omega} \times \mathbf{v}_0, \tag{3.70}$$

$$\frac{d^{\omega}}{dt}\sum_{i=1}^{N_m} m_i \mathbf{v}_{0,i} = \sum_{i=1}^{N_m} m_i (\ddot{\mathbf{r}}_{0,i} + \boldsymbol{\omega} \times \dot{\mathbf{r}}_{0,i}), \tag{3.71}$$

$$\frac{d^{\omega}}{dt}(\boldsymbol{\omega} \times \mathbf{r}_{0,c}) = \dot{\boldsymbol{\omega}} \times \mathbf{r}_{0,c} + \boldsymbol{\omega} \times \dot{\mathbf{r}}_{0,c} + \boldsymbol{\omega} \times (\boldsymbol{\omega} \times \mathbf{r}_{0,c}) \tag{3.72}$$

Now we expand Equation (3.69) to get full expression suitable for linearization:

$$\begin{aligned}
\dot{\mathbf{v}}_0 = \mu \sum_{j=1}^{N_r} b_f \Omega_j^2 \begin{bmatrix} S(\beta_j)C(\Theta_j) \\ S(\beta_j)S(\Theta_j) \\ C(\beta_j) \end{bmatrix} - g \begin{bmatrix} -S(\theta) \\ S(\phi)C(\theta) \\ C(\phi)C(\theta) \end{bmatrix} - \mu \sum_{i=1}^{N_m} m_i \begin{bmatrix} \ddot{x}_i + \omega_y \dot{z}_i - \omega_z \dot{y}_i \\ \ddot{y}_i + \omega_z \dot{x}_i - \omega_x \dot{z}_i \\ \ddot{z}_i + \omega_x \dot{y}_i - \omega_y \dot{x}_i \end{bmatrix} \\
- \mu \sum_{i=1}^{N_m} m_i \begin{bmatrix} \omega_y \dot{z}_i - \omega_z \dot{y}_i + z_i(\dot{\omega}_y + \omega_z \omega_x) + y_i(\omega_y \omega_x - \dot{\omega}_z) - x_i(\omega_y^2 + \omega_z^2) \\ \omega_z \dot{x}_i - \omega_x \dot{z}_i + x_i(\dot{\omega}_z + \omega_x \omega_y) + z_i(\omega_z \omega_y - \dot{\omega}_x) - y_i(\omega_x^2 + \omega_z^2) \\ \omega_x \dot{y}_i - \omega_y \dot{x}_i + y_i(\dot{\omega}_x + \omega_y \omega_z) + x_i(\omega_x \omega_z - \dot{\omega}_y) - z_i(\omega_x^2 + \omega_y^2) \end{bmatrix} \\
- \begin{bmatrix} \omega_y \mathbf{v}_{0,z} - \omega_z \mathbf{v}_{0,y} \\ \omega_z \mathbf{v}_{0,x} - \omega_x \mathbf{v}_{0,z} \\ \omega_x \mathbf{v}_{0,y} - \omega_y \mathbf{v}_{0,x} \end{bmatrix}
\end{aligned} \tag{3.73}$$

To compute the velocity rate of the vehicle in the inertial coordinate frame (${}^I\mathbf{v}_0$), we transform body based velocity ($\mathbf{v}_0$) using transformation matrix $\mathbf{R}_0^I$:

$${}^I\mathbf{v}_0 = \mathbf{R}_0^I \mathbf{v}_0. \tag{3.74}$$

3.2Linearized dynamical model of the aerial manipulator

The derived model describes the translation and rotation dynamics of the aerial vehicle. This highly non-linear model is precise, but not adequate for analysis or controller tuning, since the most commonly used analysis and classical control methods are developed for the linear models. Considering equations 3.73 and 3.58, the linearization procedure derives first order approximations for the translation velocity and attitude dynamics, respectfully. The derived linearized models are later used for stability analysis around various operating points, as well as for tuning of controller parameters to achieve the desired behavior in closed control loop.

3.2.1Linearized attitude dynamics

As the first step in derivation of the linear model of the unmanned aerial manipulator we linearize attitude dynamics given with Equation (3.58). To that end, we give a generalized form of a linearized attitude dynamics for an arbitrary operating point:

$$\begin{aligned}\mathbf{I}_s^c\Delta\dot{\boldsymbol{\omega}} = \Delta\mathbf{M}_e - \mathscr{L}(\boldsymbol{\omega}\times\mathbf{I}_s^c\boldsymbol{\omega}) - \mathscr{L}(\dot{\mathbf{I}}_s^c\boldsymbol{\omega}) - \mathscr{L}(\sum_{i=1}^{N_m}\mathbf{r}_{c,i}\times\dot{\mathbf{p}}_{0,i})\\ - \mathscr{L}(\boldsymbol{\omega}\times\sum_{i=1}^{N_m}\mathbf{r}_{c,i}\times\mathbf{p}_{0,i}) - \mathscr{L}(\sum_{i=1}^{N_m}\mathbf{r}_{c,i}\times\boldsymbol{\omega}\times\mathbf{p}_{0,i})\end{aligned} \tag{3.75}$$

where $\mathscr{L}(x)$ is the linearization of x. Linearizing the first term in Equation (3.75), which is the sum of the external moments, we obtain:

$$\begin{aligned}\Delta\mathbf{M}_e = b_f\sum_{j=1}^{N_r}2\Omega_{0,j}&\begin{bmatrix}\left[a_jS(\Theta_j)-\mu\sum_{i=1}^{N_m}m_iy_{0,i}\right]C(\beta_{0,j}) - \left[\left(d_j-\mu\sum_{i=1}^{N_m}m_iz_{0,i}\right)S(\Theta_j)+\zeta_jb_mC(\Theta_j)\right]S(\beta_{0,j})\\ \left[\left(d_j-\mu\sum_{i=1}^{N_m}m_iz_{0,i}\right)C(\Theta_j)+\zeta_jb_mS(\Theta_j)\right]S(\beta_{0,j}) - \left[a_jC(\Theta_j)-\mu\sum_{i=1}^{N_m}m_ix_{0,i}\right]C(\beta_{0,j})\\ -\mu\sum_{i=1}^{N_m}m_ix_{0,i}S(\beta_{0,j})S(\Theta_j)+\mu\sum_{i=1}^{N_m}m_iy_{0,i}S(\beta_{0,j})C(\Theta_j)+\zeta_jb_mC(\beta_{0,j})\end{bmatrix}\Delta\Omega_j\\ +\Omega_{0,j}^2&\begin{bmatrix}-\left[a_jS(\Theta_j)-\mu\sum_{i=1}^{N_m}m_iy_{0,i}\right]S(\beta_{0,j}) - \left[d_j-\mu\sum_{i=1}^{N_m}m_iz_{0,i}\right]C(\beta_{0,j})S(\Theta_j)+\zeta_jb_mC(\beta_{0,j})C(\Theta_j)\\ \left[d_j-\mu\sum_{i=1}^{N_m}m_iz_{0,i}\right]C(\beta_{0,j})C(\Theta_j)+\left[a_jC(\Theta_j)-\mu\sum_{i=1}^{N_m}m_ix_{0,i}\right]S(\beta_{0,j})+\zeta_jb_mC(\beta_{0,j})S(\Theta_j)\\ -\mu\sum_{i=1}^{N_m}m_ix_{0,i}C(\beta_{0,j})S(\Theta_j)+\mu\sum_{i=1}^{N_m}m_iy_{0,i}C(\beta_{0,j})C(\Theta_j)-\zeta_jb_mS(\beta_{0,j})\end{bmatrix}\Delta\beta_j\\ +\Omega_{0,j}^2&\begin{bmatrix}-\mu C(\beta_{0,j})\sum_{i=1}^{N_m}m_i\Delta y_i+\mu S(\beta_{0,j})\sum_{i=1}^{N_m}m_i\Delta z_i\\ \mu C(\beta_{0,j})\sum_{i=1}^{N_m}m_i\Delta x_i-\mu S(\beta_{0,j})\sum_{i=1}^{N_m}m_i\Delta z_i\\ -\mu S(\beta_{0,j})\sum_{i=1}^{N_m}m_i\Delta x_i+\mu S(\beta_{0,j})\sum_{i=1}^{N_m}m_i\Delta y_i\end{bmatrix},\end{aligned} \tag{3.76}$$

where $\beta_{0,j}$ is a tilt angle of j-th rotor at operating point, $\Omega_{0,j}$ is a speed of j-th rotor at operating point and $x_{0,i}$, $y_{0,i}$ and $z_{0,i}$ are positions of i-th mass at operating point in x, y and z axis, respectively. Using a standard first order approximation for linearization, only linear terms

are taken into account, while any other term containing nonlinearities, such as product of two dynamics variables, is neglected. The first order approximation yields that the second and third term of Equation (3.75) are equal to zero, i.e. $\mathscr{L}(\boldsymbol{\omega} \times \mathbf{I}_s^c \boldsymbol{\omega}) = \mathbf{0}$ and $\mathscr{L}(\dot{\mathbf{I}}_s^c \boldsymbol{\omega}) = \mathbf{0}$. The fourth term can be written as:

$$\mathscr{L}(\sum_{i=1}^{N_m} \mathbf{r}_{c,i} \times \dot{\mathbf{p}}_{0,i}) = \sum_{i=1}^{N_m} m_i \begin{bmatrix} (y_{0,i} - \mu \sum_{j=1}^{N_m} m_j y_{0,j})\Delta\ddot{z}_i - (z_{0,i} - \mu \sum_{j=1}^{N_m} m_j z_{0,j})\Delta\ddot{y}_i \\ (z_{0,i} - \mu \sum_{j=1}^{N_m} m_j z_{0,j})\Delta\ddot{x}_i - (x_{0,i} - \mu \sum_{j=1}^{N_m} m_j x_{0,j})\Delta\ddot{z}_i \\ (x_{0,i} - \mu \sum_{j=1}^{N_m} m_j x_{0,j})\Delta\ddot{y}_i - (y_{0,i} - \mu \sum_{j=1}^{N_m} m_j y_{0,j})\Delta\ddot{x}_i \end{bmatrix}. \quad (3.77)$$

The remaining terms, fifth and sixth term, are products of multiple dynamics variables, and are hence neglected in the first order approximation procedure, $\mathscr{L}(\boldsymbol{\omega} \times \sum_{i=1}^{N_m} \mathbf{r}_{c,i} \times \mathbf{p}_{0,i}) = \mathbf{0}$ and $\mathscr{L}(\sum_{i=1}^{N_m} \mathbf{r}_{c,i} \times \boldsymbol{\omega} \times \mathbf{p}_{0,i}) = \mathbf{0}$.

3.2.2Linearized translation dynamics

Here we derive the linearized translation dynamics of the vehicle acceleration expressed by Equation (3.73). Linearization is computed in generalized form, for an arbitrary operating point. With the derived generalized expressions, linearized translation dynamics equation can be obtained for any particular operating point by simple substitution. Again, as in derivation of linearized attitude dynamics, the first order approximation is used for linearization. Finally, the generalized linearized translation dynamics equation is given with:

$$\begin{aligned} \Delta\dot{\mathbf{v}}_0 =& \mu \sum_{j=1}^{N_r} \left(2b_f\Omega_0 \begin{bmatrix} S(\beta_{0,j})C(\Theta_j) \\ S(\beta_{0,j})S(\Theta_j) \\ C(\beta_{0,j}) \end{bmatrix} \Delta\Omega_j + b_f\Omega_0^2 \begin{bmatrix} C(\beta_{0,j})C(\Theta_j) \\ C(\beta_{0,j})S(\Theta_j) \\ -S(\beta_{0,j}) \end{bmatrix} \Delta\beta_j \right) \\ & - g \begin{bmatrix} -C(\theta_0)\Delta\theta \\ -S(\phi_0)S(\theta_0)\Delta\theta + C(\phi_0)C(\theta_0)\Delta\phi \\ -C(\phi_0)S(\theta_0)\Delta\theta - S(\phi_0)C(\theta_0)\Delta\phi \end{bmatrix} \\ & - \mu \sum_{i=1}^{N_m} m_i \begin{bmatrix} \Delta\ddot{x}_i \\ \Delta\ddot{y}_i \\ \Delta\ddot{z}_i \end{bmatrix} - \mu \sum_{i=1}^{N_m} m_i \begin{bmatrix} z_{0,i}\Delta\dot{\omega}_y - y_{0,i}\Delta\dot{\omega}_z \\ x_{0,i}\Delta\dot{\omega}_z - z_{0,i}\Delta\dot{\omega}_x \\ y_{0,i}\Delta\dot{\omega}_x - x_{0,i}\Delta\dot{\omega}_y \end{bmatrix}, \end{aligned} \quad (3.78)$$

where θ_0 and ϕ_0 are roll angle and pitch angle in the operating point, respectively.

CHAPTER 4

Design of the unmanned aerial manipulator with centroid variations and variable thrust direction

In this chapter we present the mathematical and mechanical design of an unmanned aerial manipulator with centroid variations and variable thrust direction (TRMMC-UAV). The mathematical model is based on the generalized unmanned aerial manipulator model presented in Chapter 3. The vehicle design is driven by requirements to enable control based on all of the considered concepts: rotor speed variation, rotor thrust direction, and centroid variation. The particular system components are chosen based on the conducted dynamics analyses. The analyses results yield the requirements on actuator capabilities for stable system behavior.

In the final design, the vehicle is chosen as a multirotor vehicle with four rotors. Throughout the derivation, we rely on the *plus* configuration, since this way the shift of the Center of Gravity (CoG) and the rotor tilting motion in roll and pitch axes can be decoupled. The vehicle is designed with moving masses, enabling centroid variation through independent control of positions of the four moving masses mounted on the four arms of the vehicle. It should be noted that the centroid variation can in general be realized in a number of ways. For example, an aerial manipulator is a vehicle with such properties. Such a vehicle can be considered as a classical UAV, with a robot manipulator mounted on the body. Depending on the dynamics and joint configuration of the mounted manipulator arm, the centroid of the entire aerial manipulator vehicle can be changed, and therefore also controlled. However, in this work the proposed control strategy is shown on the moving mass example as a proof of concept. Other than the CoG shift, the second additional actuation control considered here, namely thrust direction control,

is enabled through the tilting mechanism for the rotors.

In addition to the mathematical model derivation and description of the mechanical design of the developed vehicle, this chapter provides stability analysis based on Hurwitz stability criterion and the root locus method. The analysis considers the influence of several mechanical parameters on the system dynamics, such as length of the vehicle arm, or vertical displacement of propellers and masses with respect to the vehicle CoG. The analysis yields stability limits, i.e. the allowed range for these parameters that can still ensure stable UAV control under the proposed control concept.

4.1Mathematical model of a TRMMC-UAV

Based on the generalized mathematical model derived in the previous chapter, this section derives a model for a TRMMC-UAV, the unmanned aerial manipulator with centroid variations and variable thrust direction. The derivation of these transfer functions is essential for control algorithm synthesis (Chapter 5) and for system stability analysis that additionally provides valuable insights for mechanical design, namely limits for important mechanical parameter.

We designed the vehicle as a quad-rotor. The rotors are placed in a *plus* configuration, which enables decoupling of the shift of the CoG from the rotor tilting motion in roll and pitch axes. Each rotor is equipped with an actuator that enables tilting up to $\beta_{max} = 18.3°$. The small moving masses mounted on each vehicle's arm are used for variation of the vehicle's center of mass. This vehicle configuration, shown in Figure 4.1, enables testing various control concepts.

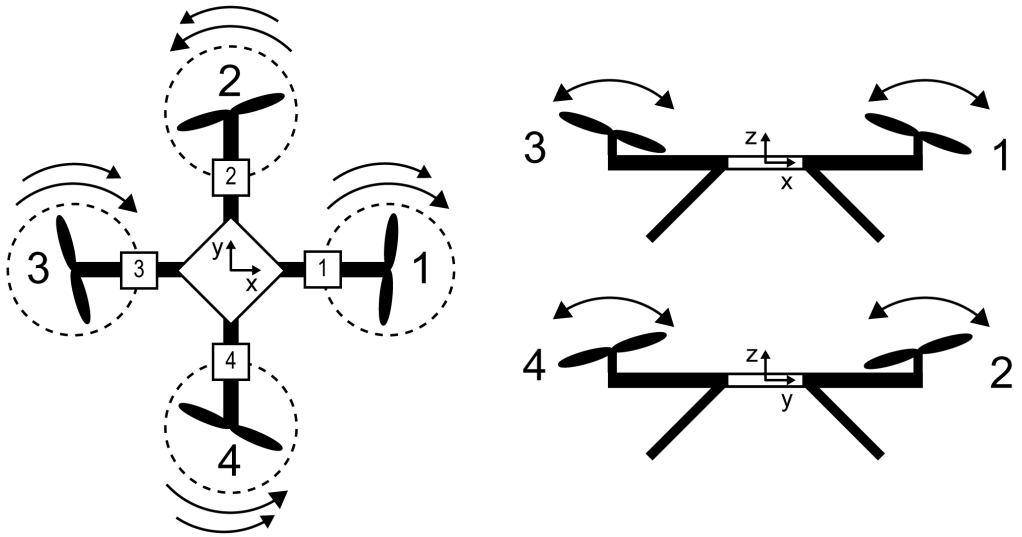

Figure 4.1: TRMMC-UAV concept.

In the previous chapter (Chapter 3), we have derived the linearized attitude and translation dynamics for a generalized unmanned aerial manipulator model. A linearized mathematical model for TRMMC-UAV can be obtained from this generalized model, by substituting model

mechanical parameters and kinematic constraints into equations (3.75) and (3.78) from Chapter 3. As already mentioned in the same chapter, the particular parameters that need to be set in order to model the vehicle as TRMMC-UAV, are defined with a set of equations (4.1). These parameters include: the number of rotors and moving masses N_r and N_m, the vehicle *plus*-configuration, rotation direction (ζ_i), uniform arm length L, propeller vertical displacement Z_r and moving mass vertical displacement Z_m for all 4 vehicle arms.

$$\begin{aligned} N_r = N_m = 4, \\ \Theta_1 = 0,\ \Theta_2 = \frac{\pi}{2},\ \Theta_3 = \pi,\ \Theta_4 = \frac{3\pi}{2}, \\ \zeta_1 = \zeta_3 = 1,\ \zeta_2 = \zeta_4 = -1, \\ a_1 = a_2 = a_3 = a_4 = L, \\ d_1 = d_2 = d_3 = d_4 = Z_r, \\ m_1 = m_2 = m_3 = m_4 = m, \\ z_{0,1} = z_{0,2} = z_{0,3} = z_{0,4} = Z_m. \end{aligned} \tag{4.1}$$

Other model assumptions, as stated in equations 4.2, define the following vehicle properties: the moving masses motion is constrained in z axis motion, and is only possible in the $x-y$ plane. The initial conditions place the moving masses into the middle position on the arms.

$$\begin{aligned} \Omega_{0,1} = \Omega_{0,2} = \Omega_{0,3} = \Omega_{0,4} = \Omega_0, \\ \Delta\ddot{z}_1 = \Delta\ddot{z}_2 = \Delta\ddot{z}_3 = \Delta\ddot{z}_4 = 0, \\ \Delta x_2 = \Delta x_4 = 0,\ \Delta y_1 = \Delta y_3 = 0, \\ \Delta z_1 = \Delta z_2 = \Delta z_3 = \Delta z_4 = 0, \\ x_{0,2} = x_{0,4} = y_{0,1} = y_{0,3} = 0, \\ x_{0,1} = y_{0,2} = \frac{L}{2}, \\ x_{0,3} = y_{0,4} = -\frac{L}{2}. \end{aligned} \tag{4.2}$$

With these substitutions, the resulting linearized attitude dynamics for the TRMMC-UAV

are given with:

$$
\begin{aligned}
\Delta\dot{\omega} = &
\begin{bmatrix}
-\frac{2b_f b_m \Omega_0}{I^c_{s,xx}}(S(\beta_{0,1})\Delta\Omega_1 - S(\beta_{0,3})\Delta\Omega_3) \\
-\frac{2b_f b_m \Omega_0}{I^c_{s,yy}}(S(\beta_{0,2})\Delta\Omega_2 - S(\beta_{0,4})\Delta\Omega_4) \\
\frac{2b_f b_m \Omega_0}{I^c_{s,zz}}(C(\beta_{0,1})\Delta\Omega_1 - C(\beta_{0,2})\Delta\Omega_2 + C(\beta_{0,3})\Delta\Omega_3 - C(\beta_{0,4})\Delta\Omega_4)
\end{bmatrix} \\
&+ \begin{bmatrix}
\frac{2b_f \Omega_0(\mu 4 m z_m - z_r)}{I^c_{s,xx}}(S(\beta_{0,2})\Delta\Omega_2 - S(\beta_{0,4})\Delta\Omega_4) \\
\frac{2b_f \Omega_0(z_r - \mu 4 m z_m)}{I^c_{s,yy}}(S(\beta_{0,1})\Delta\Omega_1 - S(\beta_{0,3})\Delta\Omega_3) \\
0
\end{bmatrix} \\
&+ \begin{bmatrix}
\frac{2Lb_f \Omega_0}{I^c_{s,xx}}(C(\beta_{0,2})\Delta\Omega_2 - C(\beta_{0,4})\Delta\Omega_4) \\
-\frac{2Lb_f \Omega_0}{I^c_{s,yy}}(C(\beta_{0,1})\Delta\Omega_1 - C(\beta_{0,3})\Delta\Omega_3) \\
0
\end{bmatrix} + \begin{bmatrix}
-\frac{Lb_f \Omega_0^2}{I^c_{s,xx}}(S(\beta_{0,2})\Delta\beta_2 - S(\beta_{0,4})\Delta\beta_4) \\
\frac{Lb_f \Omega_0^2}{I^c_{s,yy}}(S(\beta_{0,1})\Delta\beta_1 - S(\beta_{0,3})\Delta\beta_3) \\
0
\end{bmatrix} \\
&+ \begin{bmatrix}
\frac{b_f \Omega_0^2(\mu 4 m z_m - z_r)}{I^c_{s,xx}}(C(\beta_{0,2})\Delta\beta_2 - C(\beta_{0,4})\Delta\beta_4) + \frac{b_m b_f \Omega_0^2}{I^c_{s,xx}}(C(\beta_{0,1})\Delta\beta_1 - C(\beta_{0,3})\Delta\beta_3) \\
\frac{b_f \Omega_0^2(z_r - \mu 4 m z_m)}{I^c_{s,yy}}(C(\beta_{0,1})\Delta\beta_1 - C(\beta_{0,3})\Delta\beta_3) - \frac{b_m b_f \Omega_0^2}{I^c_{s,yy}}(C(\beta_{0,2})\Delta\beta_2 - C(\beta_{0,4})\Delta\beta_4) \\
\frac{b_m b_f \Omega_0^2}{I^c_{s,zz}}(S(\beta_{0,2})\Delta\beta_2 + S(\beta_{0,4})\Delta\beta_4 - S(\beta_{0,1})\Delta\beta_1 - S(\beta_{0,3})\Delta\beta_3)
\end{bmatrix} \\
&+ \begin{bmatrix}
-\frac{\mu b_f m \Omega_0^2 C_{\beta 0}}{I^c_{s,xx}}(\Delta y_2 + \Delta y_4) \\
\frac{\mu b_f m \Omega_0^2 C_{\beta 0}}{I^c_{s,yy}}(\Delta x_1 + \Delta x_3) \\
\frac{\mu b_f m \Omega_0^2 S_{\beta 0}}{I^c_{s,zz}}(\Delta y_2 + \Delta y_4 - \Delta x_1 - \Delta x_3)
\end{bmatrix} + \begin{bmatrix}
\frac{m z_m (1 - \mu 4 m)}{I^c_{s,xx}}(\Delta\ddot{y}_2 + \Delta\ddot{y}_4) \\
-\frac{m z_m (1 - \mu 4 m)}{I^c_{s,yy}}(\Delta\ddot{x}_1 + \Delta\ddot{x}_3) \\
0
\end{bmatrix},
\end{aligned}
\tag{4.3}
$$

where

$$C_{\beta 0} = C(\beta_{0,1}) + C(\beta_{0,2}) + C(\beta_{0,3}) + C(\beta_{0,4}), \tag{4.4}$$

$$S_{\beta 0} = S(\beta_{0,1}) + S(\beta_{0,2}) + S(\beta_{0,3}) + S(\beta_{0,4}). \tag{4.5}$$

$$\tag{4.6}$$

The linearized translation dynamics are given with:

$$\begin{aligned}\Delta\dot{\mathbf{v}}_0 =& \mu 2 b_f \Omega_0 \begin{bmatrix} S(\beta_{0,1})\Delta\Omega_1 - S(\beta_{0,3})\Delta\Omega_3 \\ S(\beta_{0,2})\Delta\Omega_2 - S(\beta_{0,4})\Delta\Omega_4 \\ C(\beta_{0,1})\Delta\Omega_1 + C(\beta_{0,2})\Delta\Omega_2 + C(\beta_{0,3})\Delta\Omega_3 + C(\beta_{0,4})\Delta\Omega_4 \end{bmatrix} \\ &+ \mu b_f \Omega_0^2 \begin{bmatrix} C(\beta_{0,1})\Delta\beta_1 - C(\beta_{0,3})\Delta\beta_3 \\ C(\beta_{0,2})\Delta\beta_2 - C(\beta_{0,4})\Delta\beta_4 \\ -S(\beta_{0,1})\Delta\beta_1 - S(\beta_{0,2})\Delta\beta_2 - S(\beta_{0,3})\Delta\beta_3 - S(\beta_{0,4})\Delta\beta_4 \end{bmatrix} \\ &- g \begin{bmatrix} -\Delta\theta \\ \Delta\phi \\ 0 \end{bmatrix} - \mu m \begin{bmatrix} \Delta\ddot{x}_1 + \Delta\ddot{x}_3 \\ \Delta\ddot{y}_2 + \Delta\ddot{y}_4 \\ 0 \end{bmatrix},\end{aligned} \tag{4.7}$$

where Ω_0 is defined as:

$$\Omega_0 = \sqrt{\frac{Mg}{4b_f}}. \tag{4.8}$$

Given equations are linearized around arbitrary tilting angle $\beta_{0,i}$ where $i \in \{1,...,N_r\}$. This gives ability to analyze system behavior in different initial conditions of tilting angle in order to deploy suitable control method for TRMMC-UAV.

4.2Mechanical design

The mechanical design of the TRMMC-UAV was developed starting with 3D model development. In modeling of the vehicle, solid modeling computer-aided design (CAD) program Solidworks was used as one of the standard software packages for such tasks. The first design step considered the tilting mechanism, consisting of two basic components: carbon fiber plates and tilting actuator. A digital servo motor is used as the tilting actuator, and it is attached to the vehicle arm using the carbon fiber plates. The other functionality of the plates is to attach the propulsion system to the tilting servo motors' shafts. This choice of components results in a mechanism with high angle accuracy, fast response, and minimized effect of the vibration forces caused by the propulsion system, which otherwise introduce error in angle tracking. The working range of the tilting mechanism is mechanically limited, so that there is no collision of the propeller and vehicle body at maximum tilting angle, even in case of failure of the tilting servo motor. The final design of the tilting mechanism with the tilting servo drive and propulsion brushless DC motor mounted on the tilting shaft is shown on Figure 4.2.

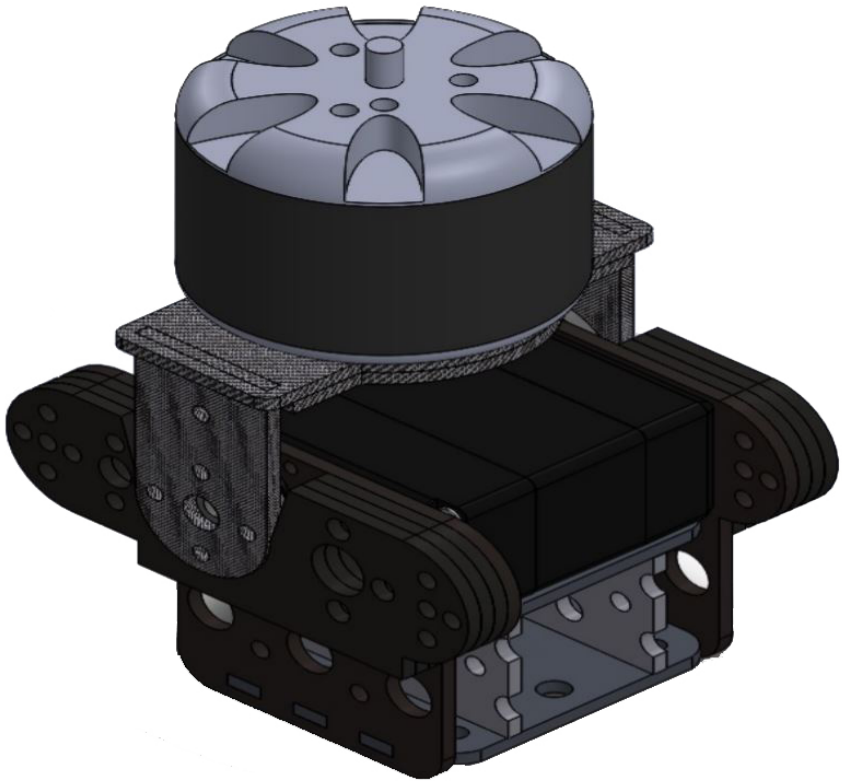

Figure 4.2: Tilting mechanism with servo motor and brushless DC motor

The following design step considered the actuator system for centroid variation. In this work, the moving mass concept was chosen for testing of the centroid variation control concepts, similar to [72]. In order not to overload the propulsion system for reliable control, it was

decided that the overall weight of the moving masses does not exceed 15% of the total thrust generated by the propulsion system. The moving mass mechanism is mounted on each arm of the vehicle. It consists of a square carbon tube with a linear guideway with bearing, a stepper motor, a carbon fiber mount for the stepper motor, a gear and a toothed rack. The gear and the toothed rack are used to transform the circular motion of the stepper motor into linear motion. The linear bearing for the stepper is mounted on the linear guideway of the square carbon tube, and is used to hold the stepper motor in a way that allows its linear motion. The toothed rack is designed with a length of 200*mm*, in effect limiting the motion of the moving masses to this range. For the linear bearing, we have chosen Hiwin MGN09H, and Hiwin MGNR09R for the guideway, making the design suitable for moving masses up to 1kg. The complete vehicle arm with moving mass mechanism and the rotor tilt mechanism is shown on Figure 4.3.

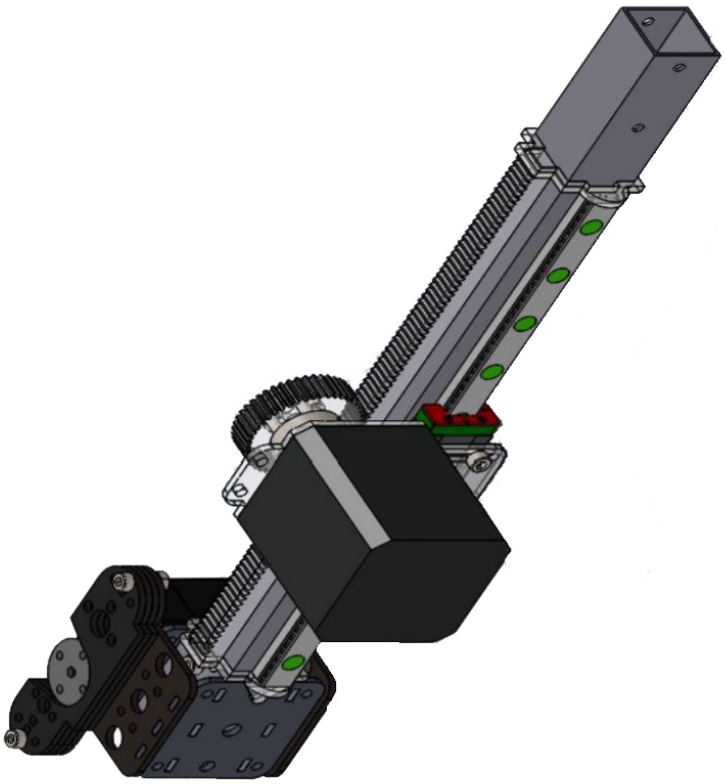

Figure 4.3: Vehicle's arm with moving mass and rotor tilt mechanism

The vehicle's body is simple and consists of two custom made carbon fiber plates, holding the four vehicle arms. The battery and all other necessary electronics are mounted on top plate for easy access. The design of the body plates follows the design of the previously described components, since it has to accommodate and fit their exact shapes and sizes. The complete mechanical design of the vehicle with four arms mounted between the carbon plates of the body is shown on Figure 4.4.

The vehicle mechanical parameters, i.e. masses and moments of inertia of the various com-

Figure 4.4: Complete mechanical design of the vehicle

ponents, are calculated using the Solidworks tools. The tool can also calculate the overall moment of inertia for the entire vehicle. All of the relevant mechanical parameters are given in Table 4.1.

4.3Actuator dynamics analysis

The choice of mechanical components is crucial for the behavior of the system. As such, the influence of actuator dynamics, such as moving mass, rotor tilt, and rotor speed, on the system's stability and robustness is analyzed as a part of the mechanical design process. To this end, we linearize the vehicle dynamics around the operating point for the tilting angle in the middle of working range, with a $\beta_{0,i}$ value of:

$$\beta_{0,1} = \beta_{0,2} = \beta_{0,3} = \beta_{0,4} = 0. \tag{4.9}$$

Using this initial conditions we obtain following dynamics equations for attitude:

$$\begin{aligned}\Delta\dot{\omega} = &\begin{bmatrix} \frac{2b_f L\Omega_0}{I^c_{s,xx}}(\Delta\Omega_2 - \Delta\Omega_4) \\ -\frac{2b_f L\Omega_0}{I^c_{s,yy}}(\Delta\Omega_1 - \Delta\Omega_3) \\ \frac{2b_f b_m\Omega_0}{I^c_{s,zz}}(\Delta\Omega_1 - \Delta\Omega_2 + \Delta\Omega_3 - \Delta\Omega_4) \end{bmatrix} + \begin{bmatrix} \frac{b_f\Omega_0^2(\mu 4mz_m - z_r)}{I^c_{s,xx}}(\Delta\beta_2 - \Delta\beta_4) + \frac{b_m b_f\Omega_0^2}{I^c_{s,xx}}(\Delta\beta_1 - \Delta\beta_3) \\ \frac{b_f\Omega_0^2(z_r - \mu 4mz_m)}{I^c_{s,yy}}(\Delta\beta_1 - \Delta\beta_3) - \frac{b_m b_f\Omega_0^2}{I^c_{s,yy}}(\Delta\beta_2 - \Delta\beta_4) \\ 0 \end{bmatrix} \\ &+ \begin{bmatrix} -\frac{4\mu b_f m\Omega_0^2}{I^c_{s,xx}}(\Delta y_2 + \Delta y_4) \\ \frac{4\mu b_f m\Omega_0^2}{I^c_{s,yy}}(\Delta x_1 + \Delta x_3) \\ 0 \end{bmatrix} + \begin{bmatrix} \frac{mz_m(1-\mu 4m)}{I^c_{s,xx}}(\Delta\ddot{y}_2 + \Delta\ddot{y}_4) \\ -\frac{mz_m(1-\mu 4m)}{I^c_{s,yy}}(\Delta\ddot{x}_1 + \Delta\ddot{x}_3) \\ 0 \end{bmatrix}, \end{aligned} \tag{4.10}$$

and translation:

$$\begin{aligned}\Delta\dot{\mathbf{v}}_0 = &\mu \left(2b_f\Omega_0 \begin{bmatrix} 0 \\ 0 \\ 1 \end{bmatrix} (\Delta\Omega_1 + \Delta\Omega_2 + \Delta\Omega_3 + \Delta\Omega_4) + b_f\Omega_0^2 \begin{bmatrix} \Delta\beta_1 - \Delta\beta_3 \\ \Delta\beta_2 - \Delta\beta_4 \\ 0 \end{bmatrix} \right) \\ &- g \begin{bmatrix} -\Delta\theta \\ \Delta\phi \\ 0 \end{bmatrix} - \mu m \begin{bmatrix} \Delta\ddot{x}_1 + \Delta\ddot{x}_3 \\ \Delta\ddot{y}_2 + \Delta\ddot{y}_4 \\ 0 \end{bmatrix}, \end{aligned} \tag{4.11}$$

The control variables for this kind of vehicle are given with following equations:

$$\Delta\Omega_{1,ref} = \Delta\Omega_z - \Delta\Omega_\theta + \Delta\Omega_\psi \tag{4.12}$$

$$\Delta\Omega_{2,ref} = \Delta\Omega_z + \Delta\Omega_\phi - \Delta\Omega_\psi \tag{4.13}$$

$$\Delta\Omega_{3,ref} = \Delta\Omega_z + \Delta\Omega_\theta + \Delta\Omega_\psi \tag{4.14}$$

$$\Delta\Omega_{4,ref} = \Delta\Omega_z - \Delta\Omega_\phi - \Delta\Omega_\psi \tag{4.15}$$

$$u_{mm,x} = \Delta x_{1,ref} = \Delta x_{3,ref} \tag{4.16}$$

$$u_{mm,y} = -\Delta y_{2,ref} = -\Delta y_{4,ref} \tag{4.17}$$

$$u_{\beta,x} = \Delta\beta_{1,ref} = -\Delta\beta_{3,ref} \tag{4.18}$$

$$u_{\beta,y} = -\Delta\beta_{2,ref} = \Delta\beta_{4,ref} \tag{4.19}$$

$$u_{r,\phi} = \Delta\Omega_\phi \tag{4.20}$$

$$u_{r,\theta} = \Delta\Omega_\theta \tag{4.21}$$

$$u_{r,\psi} = \Delta\Omega_\psi \tag{4.22}$$

$$u_z = \Delta\Omega_z \tag{4.23}$$

Combining Equations (4.10) - (4.23) with actuator dynamics given with Equations (3.17), (3.18) and (3.19) we obtain the attitude transfer functions of the TRMMC-UAV:

$$s\boldsymbol{\omega}(s) = \begin{bmatrix} \frac{4b_f L\Omega_0}{I^c_{s,xx}(\frac{1}{\omega_r^2}s^2+\frac{2\zeta_r}{\omega_r}s+1)}u_{r,\phi}(s) \\ \frac{4b_f L\Omega_0}{I^c_{s,yy}(\frac{1}{\omega_r^2}s^2+\frac{2\zeta_r}{\omega_r}s+1)}u_{r,\theta}(s) \\ \frac{8b_f b_m\Omega_0}{I^c_{s,zz}(\frac{1}{\omega_r^2}s^2+\frac{2\zeta_r}{\omega_r}s+1)}u_{r,\psi}(s) \end{bmatrix} + \begin{bmatrix} \frac{2b_f\Omega_0^2(z_r-\mu 4mz_m)}{I^c_{s,xx}(\frac{1}{\omega_{tr}^2}s^2+\frac{2\zeta_{tr}}{\omega_{tr}}s+1)}u_{\beta,y}(s) + \frac{2b_m b_f\Omega_0^2}{I^c_{s,xx}(\frac{1}{\omega_{tr}^2}s^2+\frac{2\zeta_{tr}}{\omega_{tr}}s+1)}u_{\beta,x}(s) \\ \frac{2b_f\Omega_0^2(z_r-\mu 4mz_m)}{I^c_{s,yy}(\frac{1}{\omega_{tr}^2}s^2+\frac{2\zeta_{tr}}{\omega_{tr}}s+1)}u_{\beta,x}(s) + \frac{2b_m b_f\Omega_0^2}{I^c_{s,yy}(\frac{1}{\omega_{tr}^2}s^2+\frac{2\zeta_{tr}}{\omega_{tr}}s+1)}u_{\beta,y}(s) \\ 0 \end{bmatrix}$$

$$+ \begin{bmatrix} \frac{8\mu b_f m\Omega_0^2-2mz_m(1-\mu 4m)s^2}{I^c_{s,xx}(\frac{1}{\omega_{mm}^2}s^2+\frac{2\zeta_{mm}}{\omega_{mm}}s+1)}u_{mm,y}(s) \\ \frac{8\mu b_f m\Omega_0^2-2mz_m(1-\mu 4m)s^2}{I^c_{s,yy}(\frac{1}{\omega_{mm}^2}s^2+\frac{2\zeta_{mm}}{\omega_{mm}}s+1)}u_{mm,x}(s) \\ 0 \end{bmatrix}, \tag{4.24}$$

and the translation dynamics transfer functions:

$$s\mathbf{v}_0(s) = \begin{bmatrix} \frac{2\mu b_f \Omega_0^2}{\frac{1}{\omega_{tr}^2}s^2+\frac{2\zeta_{tr}}{\omega_{tr}}s+1}u_{\beta,x}(s) + g\theta(s) - \frac{2\mu m s^2}{\frac{1}{\omega_{mm}^2}s^2+\frac{2\zeta_{mm}}{\omega_{mm}}s+1}u_{mm,x}(s) \\ -\frac{2\mu b_f \Omega_0^2}{\frac{1}{\omega_{tr}^2}s^2+\frac{2\zeta_{tr}}{\omega_{tr}}s+1}u_{\beta,y}(s) - g\phi(s) + \frac{2\mu m s^2}{\frac{1}{\omega_{mm}^2}s^2+\frac{2\zeta_{mm}}{\omega_{mm}}s+1}u_{mm,y}(s) \\ \frac{8\mu b_f \Omega_0}{\frac{1}{\omega_r^2}s^2+\frac{2\zeta_r}{\omega_r}s+1}u_z(s) \end{bmatrix}. \tag{4.25}$$

Using derived linearized equations, we compute the gain margin, phase margin and crossover frequency of the vehicle roll angular velocity transfer function, as a function of actuator natural frequency ω_n. According to the technical optimum, we chose the damping factor with a value of 0.7. Since there was no significant difference in the analyzed frequency characteristics for damping factors greater than 0.6, this chosen value was used throughout the analysis. Furthermore, the natural frequency is varied in the range [1,100] rad/s. The obtained responses are shown in Figure 4.5, where $G_{\omega_\phi,mm}(s)$ is a transfer function of vehicle's roll angular velocity using the actuation based on centroid variation, $G_{\omega_\phi,r}(s)$ is a transfer function of vehicle's roll angular velocity with actuation based on rotor thrust magnitude (rotor speed), and finally, $G_{\omega_\phi,tr}(s)$ is a transfer function of vehicle's roll angular velocity using actuation based on rotor thrust direction (tilting rotors). These transfer functions can be derived from Equation (4.24) as:

$$G_{\omega_\phi,r}(s) = \frac{4b_f L\Omega_0}{I^c_{s,xx}(\frac{1}{\omega_r^2}s^2 + \frac{2\zeta_r}{\omega_r}s+1)s}, \tag{4.26}$$

$$G_{\omega_\phi,mm}(s) = \frac{8\mu b_f m\Omega_0^2 - 2mz_m(1-\mu 4m)s^2}{I^c_{s,xx}(\frac{1}{\omega_{mm}^2}s^2 + \frac{2\zeta_{mm}}{\omega_{mm}}s+1)s}, \tag{4.27}$$

$$G_{\omega_\phi,tr}(s) = \frac{2b_f\Omega_0^2(z_r - \mu 4mz_m)}{I^c_{s,xx}(\frac{1}{\omega_{tr}^2}s^2 + \frac{2\zeta_{tr}}{\omega_{tr}}s+1)s}, \tag{4.28}$$

where ω_r, ω_{mm} and ω_{tr} are varied in the range [1,100] rad/s, and ζ_r, ζ_{mm} and ζ_{tr} are chosen as 0.7 rad/s. Remaining parameters are given in Table 4.1.

According to figure 4.5, both gain and phase margin increase with the natural frequency of actuators. This implies that faster actuator dynamics results in a system with a greater area of stability. Figure 4.5a shows that for the chosen natural frequency range, the gain margin is positive and increases with the frequency. Interesting results are shown in Figure 4.5b, where for the chosen natural frequency, the system with rotor thrust magnitude based actuation has the largest phase margin. The actuation based on centroid variation follows, and finally the system with actuation based on rotor thrust direction has the smallest phase margin.

The system crossover frequency increases with the actuator's natural frequency up to a limit

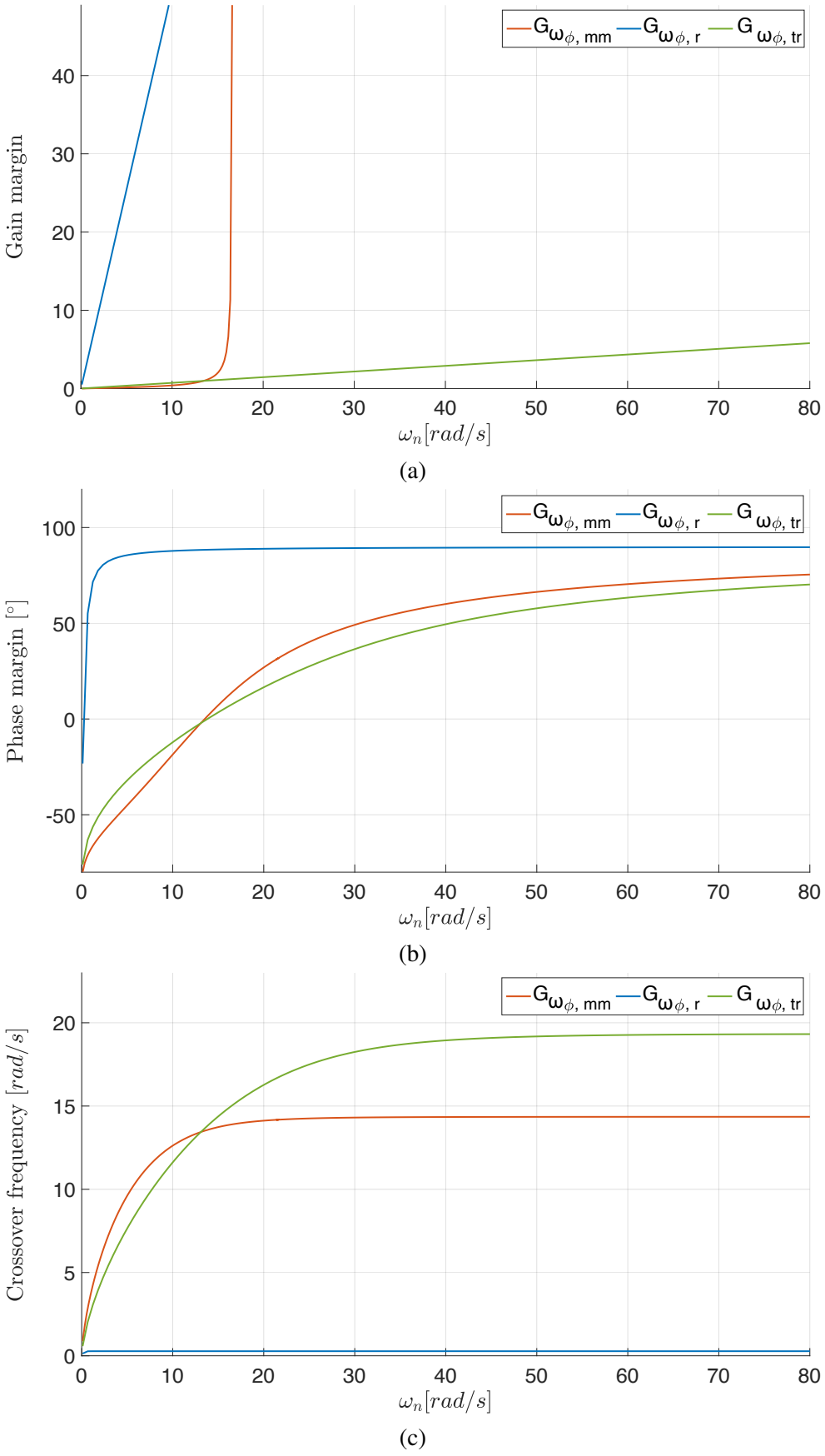

Figure 4.5: Frequency analysis of the roll rate dynamics as a function of the actuators natural frequency

value, as seen in Figure 4.5c. From the phase margin characteristics, one can notice that for the actuation based on rotor thrust magnitude, the phase margin is positive for natural frequency greater than 0.266 rad/s. For the actuation based on rotor thrust direction the phase margin is positive for natural frequency greater than 13.8 rad/s, and for the actuation based on centroid variation the phase margin is positive for natural frequency greater than 13.48 rad/s. This implies that rotor speed variation provides a system with greater area of stability whereas the centroid variation dynamics have to be very fast in order to provide a stable system.

Taking into account results obtained from the conducted analysis we chose the most appropriate actuators for our TRMMC-UAV. For the propulsion system, we chose a brushless DC motor, namely T-motor MN4014 400KV, and propellers with 16" diameter and 5.4" pitch. We can easily calculate motor natural frequency and damping factor, using provided documentation by the manufacturer. The transfer function of rotor speed is given with Equation 3.17 and the calculated parameters are in Table 4.1. According to the conducted stability analysis of the vehicle's roll rate, we conclude that the natural frequency of the rotors should be at least 0.266 rad/s. The chosen motor natural frequency satisfies this criterion, as can be seen in the step response shown in Figure 4.6.

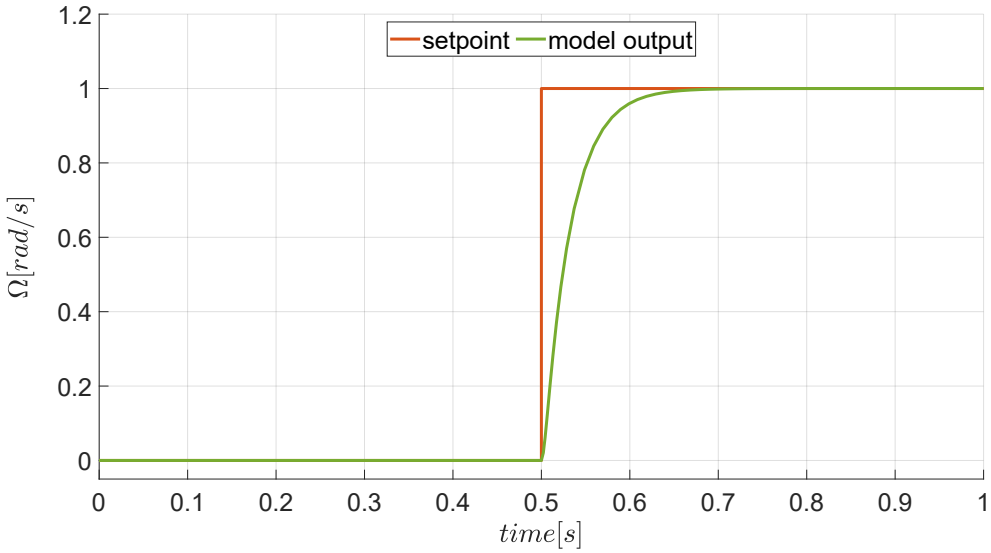

Figure 4.6: Step response of a rotor speed transfer function

The next design step is choosing the correct servo motor model for the tilting mechanism actuation. According to the payload requirements, the digital servo model RDS3115 was chosen thanks to its design with metal gears and high torque. The dynamics of this actuator are identified in a set of experiments, using Optitrack system for angle measurements and System Identification Toolbox in Matlab. The identification procedure was conducted for a second order transfer function as defined with Equation 3.18. The accuracy of the identified model is shown in Figure 4.7a, where the model response is plotted along with the recorded setpoint and response of the real actuator. The dynamic response of the identified dynamics, with identified

parameters given in Table 4.1 are shown in fig. 4.7b. The natural frequency of the chosen motors again satisfies the limits determined by the stability analysis.

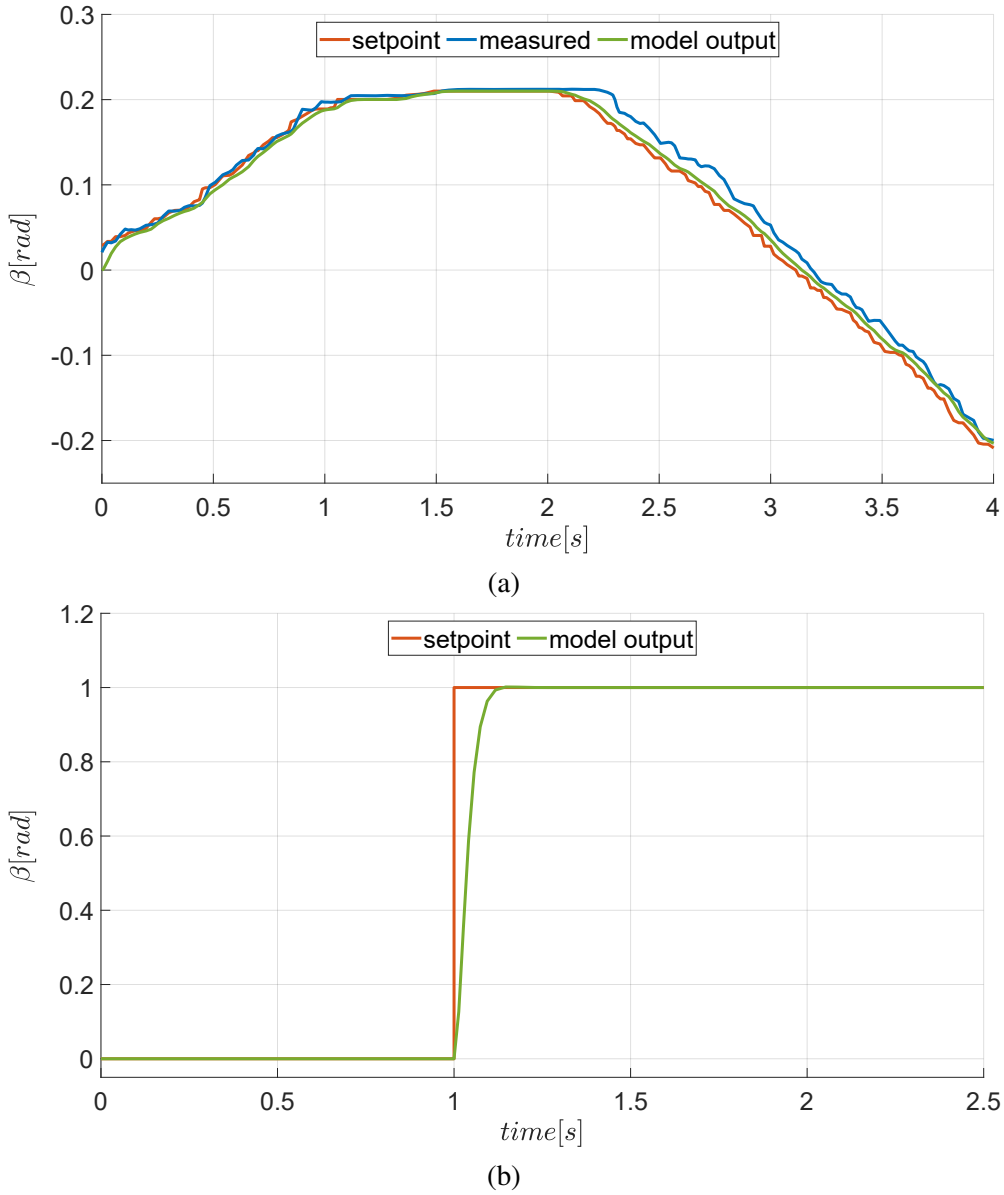

Figure 4.7: Figure shows recorded data used for the system identification alongside with the identified model step response.

For the moving mass we chose NEMA 13 stepper motor. Such motors are used in 3D printers and CNC machines, where high torque and precision is required. We conducted similar identification procedure as we did for the tilting mechanism. Using Optitrack system, we measured response of the moving mass on a given setpoint. Using System Identification Toolbox in Matlab we identified the moving mass system as a second order system with a natural frequency of 13.24 rad/s and damping factor of 0.81 rad/s. Parameters are given in Table 4.1, while the transfer function of the moving mass system is given with Equation 3.19. The accuracy of the identified model is shown in Figure 4.8a, where the measured value is shown alongside the set-

point and identified model output. Figure 4.8b shows the step response of the identified model. The obtained natural frequency of the moving mass system is on the edge of the limits determined by the stability analysis. This problem will be overcome by appropriate control design which is a topic in next section.

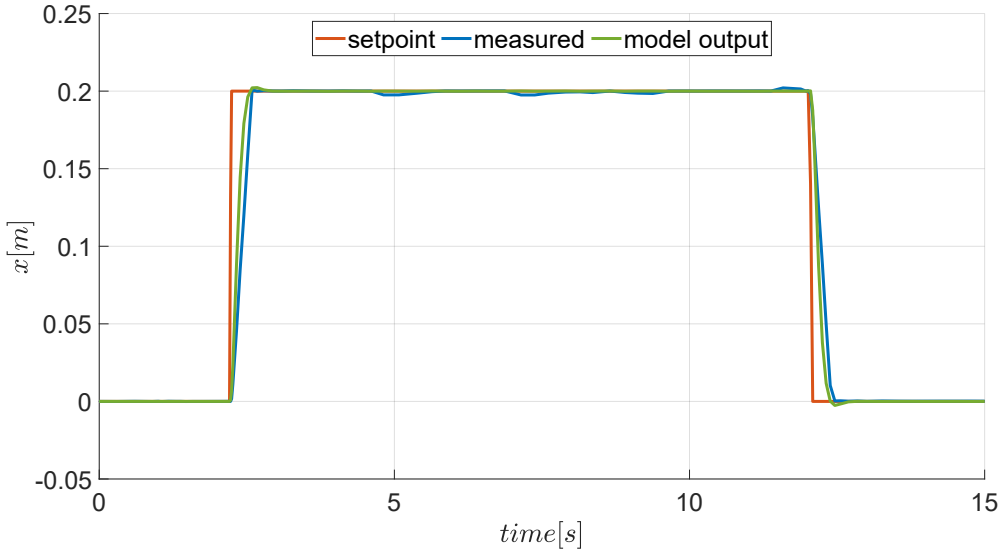

(a)

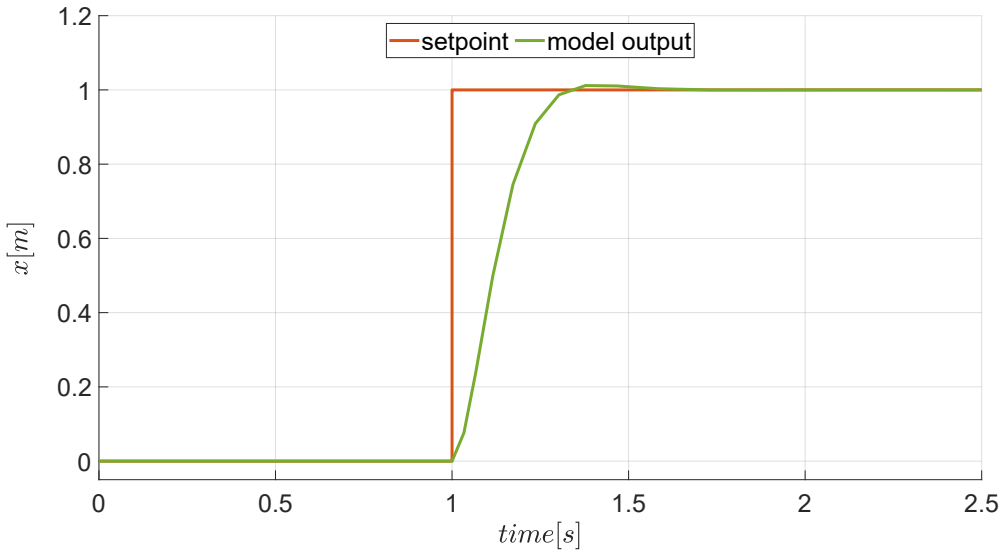

(b)

Figure 4.8: On a) the measured moving mass displacement measured with Optitrack system is shown alongside with the setpoint and identified model output. in b) we show the identified model step response.

All vehicle's dynamics and mechanical parameters are given in Table 4.1.

Table 4.1: Model parameters of the TRMMC-UAV

Symbol	Value	Unit	Description
$I^c_{s,xx}$	0.149	kgm^2	Vehicle's moment of inertia in x axis
$I^c_{s,yy}$	0.149	kgm^2	Vehicle's moment of inertia in y axis
$I^c_{s,zz}$	0.206	kgm^2	Vehicle's moment of inertia in z axis
m	0.416	kg	Mass of the moving mass
M	5.6	kg	Vehicle overall mass
b_f	$6.9146e-05$	kgm	Rotor thrust constant
b_m	0.016	-	Moment constant of a brushless DC motor
g	9.81	m/s^2	Gravitational acceleration
z_m	-0.05	m	Displacement of the moving masses in z axis
z_r	0.09	m	Distance between propeller and a vehicle's origin in z axis
L	0.333	m	Length of a vehicle's arm
ω_r	105.41	rad/s	Natural frequency of the rotor
ζ_r	1.74	rad/s	Damping factor of the rotor
ω_{tr}	44.91	rad/s	Natural frequency of the tilting servo motor
ζ_{tr}	0.89	rad/s	Damping factor of the tilting servo motor
ω_{mm}	13.24	rad/s	Natural frequency of the moving masses
ζ_{mm}	0.81	rad/s	Damping factor of the moving masses
β_{max}	0.32	rad	Maximum value of the β angle

4.4Influence of mechanical parameters on system dynamics

In this section, we analyze the influence of various vehicle parameters on the system dynamics. In particular, we consider variation in the vehicle arm length, and in vertical displacement of the propeller and the moving masses planes w.r.t. the vehicle CoG, and analyze the effect of these variations on the system dynamics. The analysis is based on the Hurwitz stability criterion and the root locus method.

4.4.1Vehicle's arm length

First, we analyze the effect vehicle's arm length variation on the system stability using Hurwitz stability criterion on Equation (4.26). The following conditions are obtained:

$$I^c_{s,xx} > 0, \tag{4.29}$$

$$\frac{2\zeta_r I^c_{s,xx}}{\omega_r} > 0, \tag{4.30}$$

$$\frac{L}{I^c_{s,xx}} < \frac{\omega_r \zeta_r}{2 b_f \Omega_0}, \tag{4.31}$$

$$4 L b_f \Omega_0 > 0. \tag{4.32}$$

The first two conditions are not related to the length of the arm, but only provide limits for the vehicle moment of inertia (condition 4.29), and the dynamics of the rotor actuators (condition 4.30). The influence of the rotor dynamics on the system stability is already discussed in the previous section. With the last condition 4.32 trivial, condition 4.31 remains to be discussed.

As can also be seen in the bode plot and the root locus analysis in Figure 4.9, the Hurwitz criterium 4.31 states that the system stability depends on the ratio of the arm length and the vehicle moment of inertia, in such a way that a larger ratio moves the system towards the stability limits, moving the zeros towards and into the right half-plane. The system becomes unstable above a certain threshold, which can be realized either by increasing the arm length, or by decreasing the vehicles overall moment of inertia. The latter can, for example, be realized by concentrating most of the vehicles body weight close to the body center. In this case, the length of the arm influences the vehicle dynamics through a higher gain, increasing the system sensitivity. If the overall mass is on the contrary distributed along the arms, the influence of the arm length is not as prominent, and the system sensitivity is reduced.

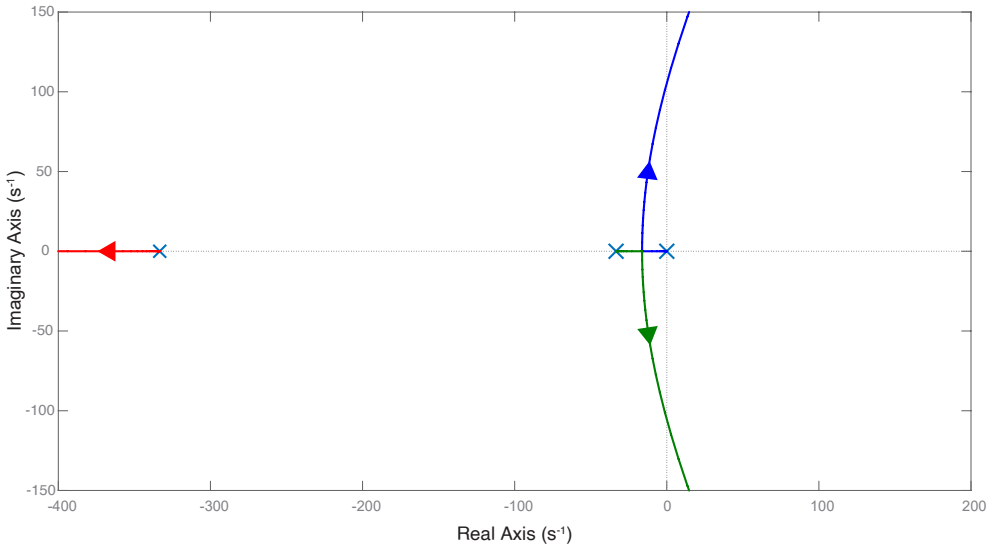

Figure 4.9: Root locus curve for vehicle's roll rate transfer function using rotor's magnitude variation control.

4.4.2The propeller vertical displacement

The influence of the propeller vertical displacement on the system stability is analysed with respect to the rotor tilt the transfer function as given in Equation 4.28.

Taking into account equations obtained from Hurwitz stability criterion (Equations (4.33) - (4.36)) we can conclude that in order to ensure the vehicle stability this displacement depend on the vehicles centre of mass displacement, ie. moving mass displacement. If there is no moving masses on the vehicle, the propeller vertical displacement should be positive regardless of other vehicle parameters. Furthermore, increasing the displacement also increases the system gain, as can also be seen in the root locus plot given in Fig. 4.10. The root locus analysis shows that the right-most zero, shown in blue in Fig. 4.10, moves towards the left half-plane into the stable region. However, above a certain level the vertical displacement of the propellers increases the system gain by too much, which leads to instability as is visible with the two system zeros moving into the right half-plane.

$$I^c_{s,xx} > 0, \tag{4.33}$$

$$\frac{2\zeta_{tr} I^c_{s,xx}}{\omega_{tr}} > 0, \tag{4.34}$$

$$z_r - 4\mu m z_m < \frac{\zeta_{tr} I^c_{s,xx} \omega_{tr}}{b_f \Omega_0^2}, \tag{4.35}$$

$$2b_f \Omega_0^2 (z_r - 4\mu m z_m) > 0. \tag{4.36}$$

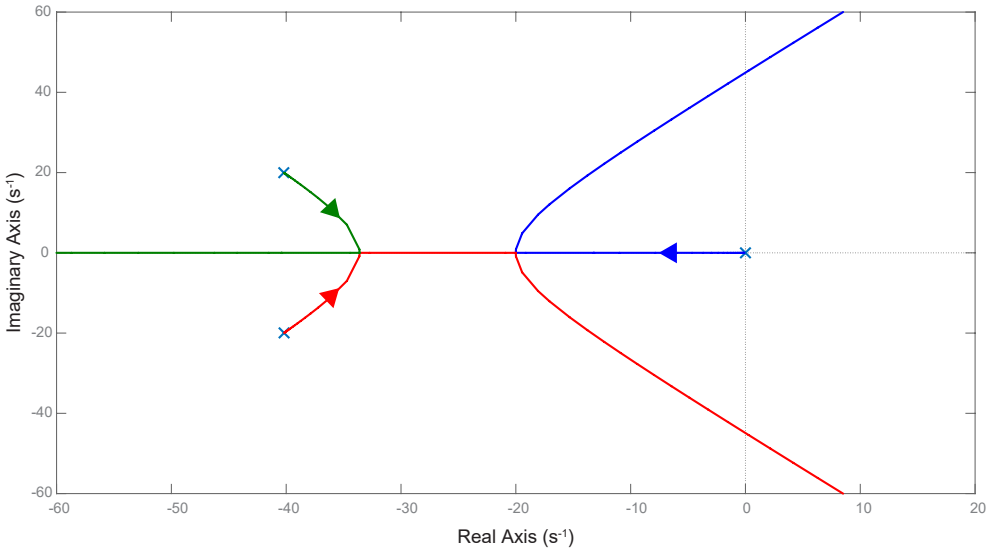

Figure 4.10: Root locus curve for vehicle's roll rate transfer function using rotor's thrust direction control.

4.4.3The moving mass vertical displacement

Analysis of influence of the moving masses' vertical displacement on the system stability has already been discussed in detail in [77]. In addition to this thorough analysis, we provide a discussion of influence of vertical displacement of the moving masses or of a carried load on stability of transfer function 4.27. Formally, stability limits can be defined for z_m using Hurwitz stability criterion, depending on other system parameters. The parameter relations that ensure stable system behavior are given with inequalities in 4.37-4.40.

$$I^c_{s,xx} > 0, \tag{4.37}$$

$$z_m < \frac{2\zeta_{mm} I^c_{s,xx}}{2m(1-4m\mu)\omega_{mm}}, \tag{4.38}$$

$$z_m < \frac{2\zeta_{mm} I^c_{s,xx}\omega_{mm} - 8\mu b_f \Omega_0^2 m}{2m(1-4m\mu)\omega^2_{mm}}, \tag{4.39}$$

$$8\mu b_f \Omega_0^2 m > 0. \tag{4.40}$$

Another tool used in the analysis, the root locus method, is conducted for three separate cases, depending on the range of displacement values along the local z axis. The results are shown over three graphs given in Figures 4.11-4.13, as root locus graphs for cases where $z_m = 0$, $z_m > 0$, and $z_m < 0$, respectively. Fig. 4.11 shows root locus analysis for the roll rate transfer function, 4.26 for a system actuated using the moving masses. As can be seen from this graph, generated for the case where $z_m = 0$, this system does not have zeros.

Next, the positive range of z_m is examined. From root locus graph in fig. 4.12 for $z_m \in [0.01, 0.1]$, it can be seen that a gain margin guarantees system stability within the defined range. It also shows that the transfer function has a non-minimum phase zero as well. Similar

analysis for negative z_m from $[-0.1, -0.01]$ in Fig. 4.13 shows there are no non-minimum phase zeros in this kind of system.

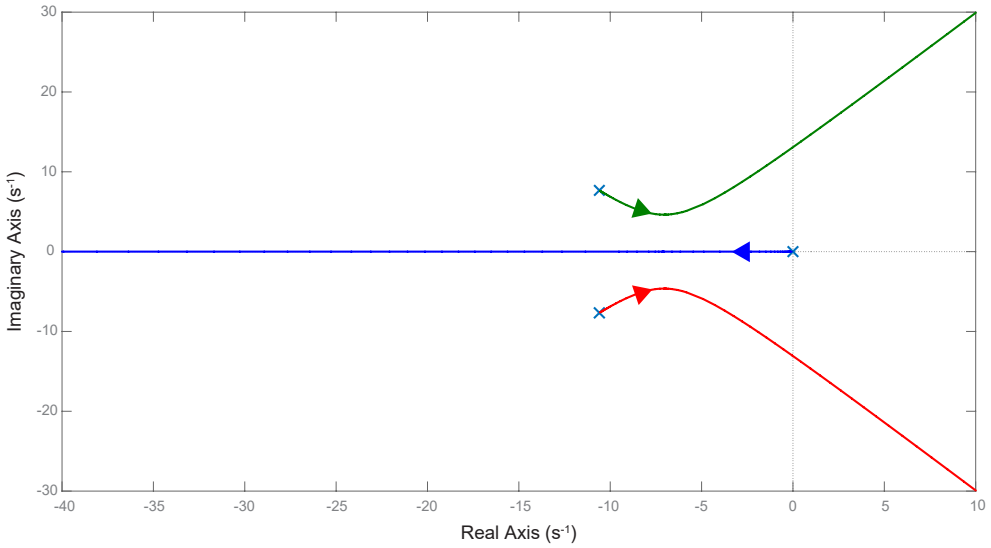

Figure 4.11: Root locus curve for vehicle's roll rate transfer function using moving mass control with $z_m = 0$.

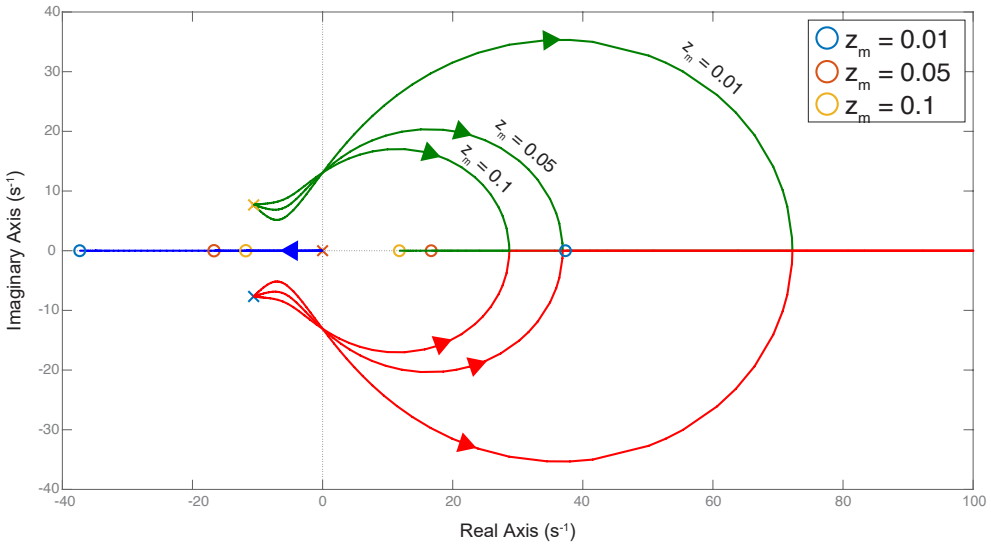

Figure 4.12: Root locus curve for vehicle's roll rate transfer function using moving mass control with $z_m > 0$.

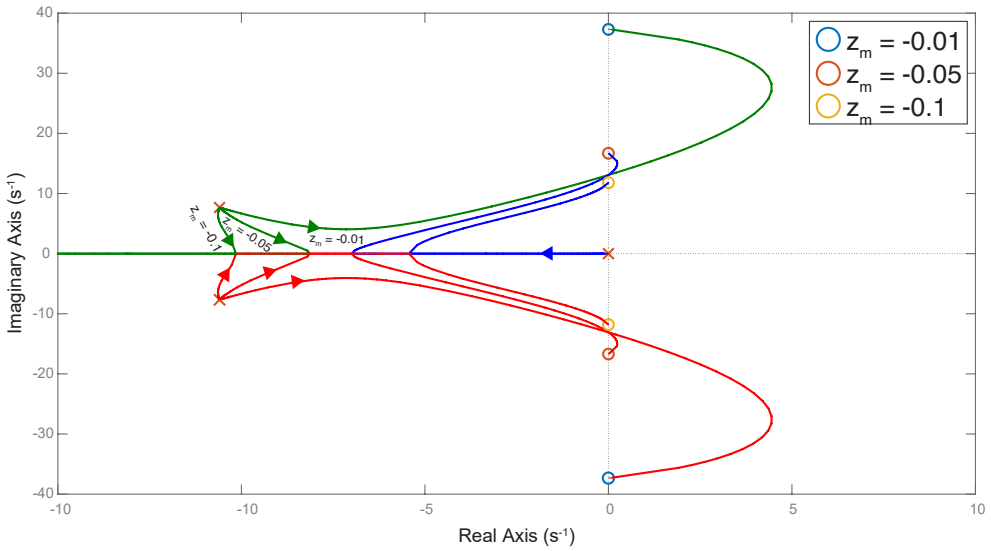

Figure 4.13: Root locus curve for vehicle's roll rate transfer function using moving mass control with $z_m < 0$.

4.5Generalized model - relation to the State of the Art

This section proves that the model can generalize to other UAV types, such as the one in [78]. In that work, a UAV with 4 moving masses is considered without rotor thrust direction control. The generalized model developed in this thesis can be reduced to the model developed in [78] by fixing the rotor thrust direction, i.e. by using

$$\beta_{0,i} = 0 \tag{4.41}$$

in Equations (4.3) and (4.7). With the moving mass (centroid variation) concept corresponding to the one presented in [78], we obtain the following equations for attitude:

$$\begin{aligned}\Delta\dot{\omega} = &\begin{bmatrix} \frac{2b_f L\Omega_0}{I^c_{s,xx}}(\Delta\Omega_2 - \Delta\Omega_4) \\ -\frac{2b_f L\Omega_0}{I^c_{s,yy}}(\Delta\Omega_1 - \Delta\Omega_3) \\ \frac{2b_f b_m\Omega_0}{I^c_{s,zz}}(\Delta\Omega_1 - \Delta\Omega_2 + \Delta\Omega_3 - \Delta\Omega_4) \end{bmatrix} + \begin{bmatrix} -\frac{4\mu b_f m\Omega_0^2}{I^c_{s,xx}}(\Delta y_2 + \Delta y_4) \\ \frac{4\mu b_f m\Omega_0^2}{I^c_{s,yy}}(\Delta x_1 + \Delta x_3) \\ 0 \end{bmatrix} \\ &+ \begin{bmatrix} \frac{mz_m(1-\mu 4m)}{I^c_{s,xx}}(\Delta\ddot{y}_2 + \Delta\ddot{y}_4) \\ -\frac{mz_m(1-\mu 4m)}{I^c_{s,yy}}(\Delta\ddot{x}_1 + \Delta\ddot{x}_3) \\ 0 \end{bmatrix},\end{aligned} \tag{4.42}$$

and translation:

$$\begin{aligned}\Delta\dot{\mathbf{v}}_0 = &\mu \left(2b_f\Omega_0 \begin{bmatrix} 0 \\ 0 \\ 1 \end{bmatrix} (\Delta\Omega_1 + \Delta\Omega_2 + \Delta\Omega_3 + \Delta\Omega_4) \right) \\ &- g \begin{bmatrix} -\Delta\theta \\ \Delta\phi \\ 0 \end{bmatrix} - \mu m \begin{bmatrix} \Delta\ddot{x}_1 + \Delta\ddot{x}_3 \\ \Delta\ddot{y}_2 + \Delta\ddot{y}_4 \\ 0 \end{bmatrix},\end{aligned} \tag{4.43}$$

which correspond to the results given by [78].

CHAPTER 5

Unmanned aerial manipulator control method

In this chapter, we present several control algorithms for an unmanned aerial manipulator. All proposed algorithms are implemented in MATLAB and verified in a simulation setup. First, we introduce the developed attitude and height control based on the standard rotor variation method. This control method proved to be the best choice for attitude and height control and, when combined with position control, can keep the vehicle in a neutral attitude while performing a translational movement, thereby improving the precision and accuracy of task execution. For future work, this method can be extended to take into account the influence of centroid variation and rotor thrust direction variation to improve vehicle stability and attitude tracking capability.

Furthermore, we present two different position control algorithms. By combining centroid variation and rotor thrust direction variation, the vehicle can be controlled in a free flight regime, enabling better response to disturbances and providing control of all six degrees of freedom of the vehicle. For contact-based tasks, we present a position control method based only on rotor thrust direction variations. In such tasks, the vehicle's CoG moves to the point of contact, and using a centroid variation control method has no effect on the vehicle.

5.1Attitude and height control

Based on the frequency analysis presented in Chapter 4, it is evident that the standard rotor variation method control principle remains the best choice for controlling the attitude of unmanned aerial vehicles. This control principle ensures fast reference tracking, robust performance, and provides stability to the vehicle. Additionally, the rotor variation method in combination with

thrust direction variation and centroid variation method in position control is particularly beneficial in contact-based aerial manipulation tasks or when transporting sensitive loads. This combination can keep the vehicle in a neutral attitude, thereby improving the precision and accuracy of the task execution. Therefore, rotor thrust variation is the most appropriate actuation method for vehicle attitude control for further experimental analysis.

The main goal of attitude control is to achieve precise stabilization of an unmanned aerial manipulator around the desired angle of 0. To derive attitude control of the vehicle we will use linearized vehicle dynamics around the operating point for the tilting angle in the middle of working range, as given by Equations (4.24) and (4.25). Although our primary focus is on designing a controller for the roll axis, we use the same controller for the pitch axis due to the symmetry of the vehicle. The transfer functions for the roll angle dynamics are given by Equations (4.26) -(4.28). Since we are using the standard rotor variation method to control the attitude of the vehicle, we use the transfer function given by Equation (4.26) for controller analysis and design. The influence of rotor tilt and centroid variation on vehicle attitude dynamics is considered as a disturbance. The design goal is to develop a controller that is robust and optimal in terms of minimizing the effects of these disturbances on the attitude of the vehicle. By incorporating appropriate control algorithms and tuning parameters, we can ensure that the UAV responds rapidly to external disturbances and quickly recovers to the desired attitude, thus improving its overall stability and reliability.

The controller design follows a standard cascade control design for a VTOL vehicle. The inner loop of the cascade control is a standard PI angular velocity controller, followed by a standard PI angle control outer loop, as shown in Figure 5.1. Since the goal of the controller design is to achieve optimal control in terms of minimizing effects of tilting rotors and centroid variation, which are considered as a disturbance, we choose to tune both loops according to symmetrical optimum condition for optimizing system behavior with respect to disturbance signals.

It is possible to use a more advanced control method that could utilize the system model to achieve better performance with respect to disturbance signals, namely tilting rotors and centroid variation. For example, the control could use information about manipulator motion in order to reduce the impact of centroid variation on attitude dynamics, or information about the tilting angle in a similar manner. These two actuators are used in higher level control of the vehicle, and have significant influence on the attitude tracking performance. Using these in attitude control could improve the overall performance of the system. This could be achieved using model predictive control, but this is outside of the scope of this thesis and should be analyzed in future work.

The design of the attitude controller is based on the linearized attitude model given with

Equation (4.10), with following control variables:

$$\Delta\Omega_{1,ref} = \Delta\Omega_z - \Delta\Omega_\theta + \Delta\Omega_\psi \tag{5.1}$$

$$\Delta\Omega_{2,ref} = \Delta\Omega_z + \Delta\Omega_\phi - \Delta\Omega_\psi \tag{5.2}$$

$$\Delta\Omega_{3,ref} = \Delta\Omega_z + \Delta\Omega_\theta + \Delta\Omega_\psi \tag{5.3}$$

$$\Delta\Omega_{4,ref} = \Delta\Omega_z - \Delta\Omega_\phi - \Delta\Omega_\psi \tag{5.4}$$

$$u_{r,\phi} = \Delta\Omega_\phi \tag{5.5}$$

$$u_{r,\theta} = \Delta\Omega_\theta \tag{5.6}$$

$$u_{r,\psi} = \Delta\Omega_\psi \tag{5.7}$$

$$u_z = \Delta\Omega_z. \tag{5.8}$$

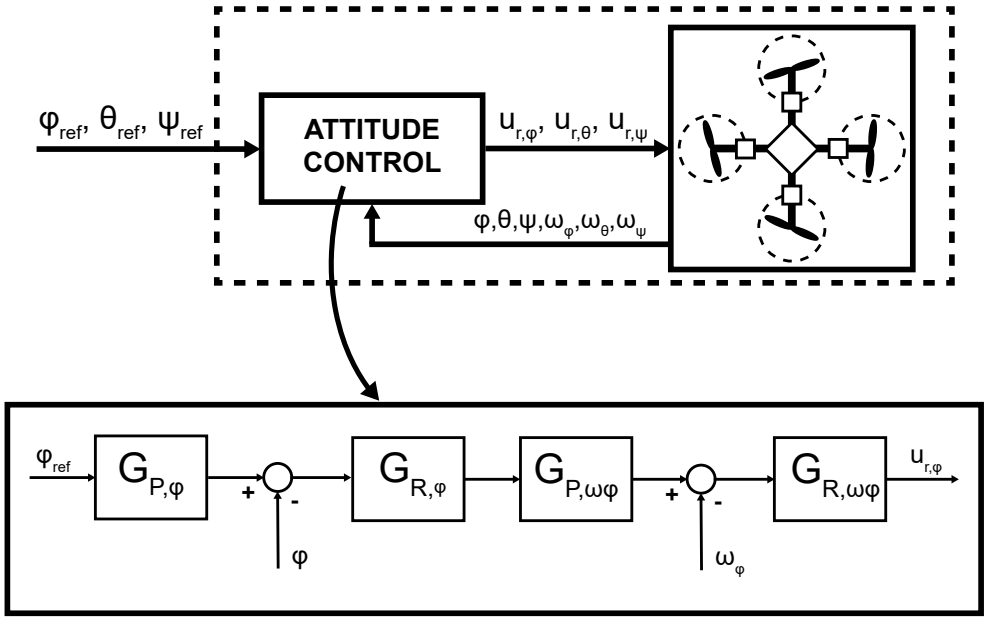

Figure 5.1: This figure shows the attitude control scheme. The attitude commands are achieved by varying rotor velocities.

5.1.1Inner control loop

The roll angular velocity time constants, T_{1,ω_ϕ} and T_{2,ω_ϕ}, can be calculated using transfer function given with Equation (4.26). The system has a first-order steady-state error, with one pole located at the origin. This characteristic makes it well-suited for tuning the control loop using symmetrical optimum. The system transfer function can be rewritten as:

$$G_{\omega_\phi}(s) = \frac{4b_f L\Omega_0}{I^c_{s,xx}(\frac{1}{\omega_r^2}s^2 + \frac{2\zeta_r}{\omega_r}s + 1)s} = \frac{K_{\omega_\phi}}{T_{i,\omega_\phi}s(T_{1,\omega_\phi}s+1)(T_{2,\omega_\phi}s+1)}, \tag{5.9}$$

where

$$K_{\omega_\phi} = 4b_f L\Omega_0, \tag{5.10}$$

$$T_{1,\omega_\phi} = \frac{1}{\omega_r(\zeta_r - \sqrt{\zeta_r^2 - 1})}, \tag{5.11}$$

$$T_{2,\omega_\phi} = \frac{1}{\omega_r(\zeta_r + \sqrt{\zeta_r^2 - 1})}, \tag{5.12}$$

$$T_{i,\omega_\phi} = I^c_{s,xx}. \tag{5.13}$$

The two time constants of the system, T_{1,ω_ϕ} and T_{2,ω_ϕ}, can be approximated as $T_{\Sigma,\omega_\phi} = T_{1,\omega_\phi} + T_{2,\omega_\phi}$, as they have a minor influence on the system dynamics. This gives us the following system approximation:

$$G_{\omega_\phi}(s) = \frac{K_{\omega_\phi}}{T_{i,\omega_\phi} s(T_{\Sigma,\omega_\phi} s + 1)}. \tag{5.14}$$

Introducing the standard PI controller:

$$G_{R,\omega_\phi}(s) = K_{R,\omega_\phi} \frac{1 + T_{I,\omega_\phi} s}{T_{I,\omega_\phi} s}, \tag{5.15}$$

the open loop transfer function can be written as:

$$G_{O,\omega_\phi}(s) = G_{R,\omega_\phi}(s) G_{\omega_\phi}(s) = \frac{K_{R,\omega_\phi} K_{\omega_\phi}}{T_{I,\omega_\phi} T_{i,\omega_\phi} s^2} \frac{1 + T_{I,\omega_\phi} s}{1 + T_{\Sigma,\omega_\phi} s}. \tag{5.16}$$

The symmetrical optimum tuning criteria for this system gives the PI controller parameters as

$$K_{R,\omega_\phi} = \frac{T_{i,\omega_\phi}}{a K_{\omega_\phi} T_{\Sigma,\omega_\phi}}, \tag{5.17}$$

$$T_{I,\omega_\phi} = a^2 T_{\Sigma,\omega_\phi}, \tag{5.18}$$

$$a = 2. \tag{5.19}$$

Using these parameters, the resulting open loop frequency characteristic will have a maximum phase at crossover frequency ω_c and the amplitude-frequency characteristic becomes symmetrical with respect to axis 0 dB, as can be seen in Figure 5.2. Most of the literature use $a = 2$ for the optimization according to conventional symmetrical optimum tuning [79]. The resulting performance gives an overshoot of around 43% and a phase margin of about 37°. The phase margin value is low and the system has a high overshoot, but still the system response is fast.

The overshoot is compensated by employing the following filter in the reference signal:

$$G_{P,\omega_\phi} = \frac{1}{1 + a^2 T_{\sum,\omega_\phi} s}, \tag{5.20}$$

which decreases the overshoot to 8%.

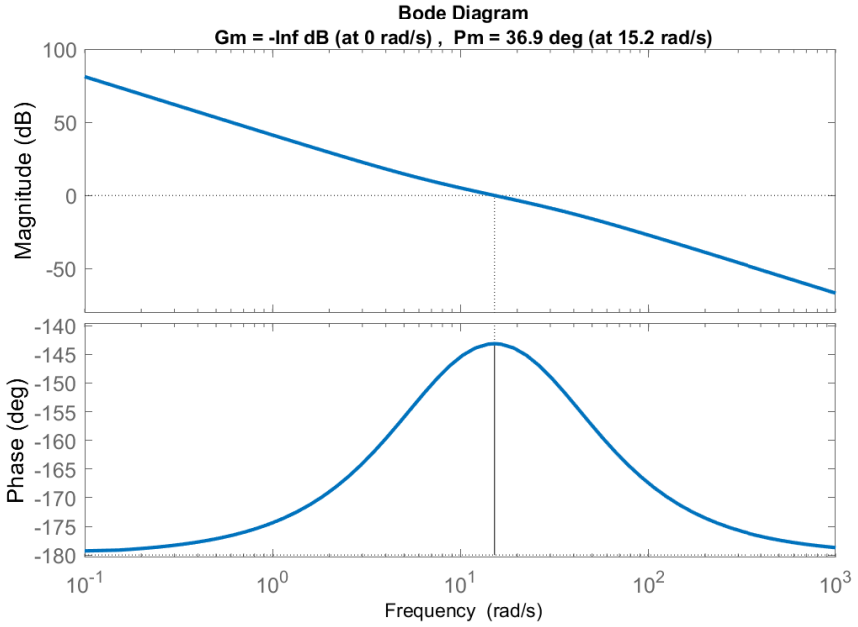

Figure 5.2: Bode diagram of the inner control loop (angular velocity).

This same inner loop control method design and tuning is applied to the pitch rate, yaw rate and z axis velocity. The transfer functions used for inner control loop design for these axes are given in Equation (4.24) and Equation (4.25) as:

$$G_{\omega_\theta}(s) = \frac{4 b_f L \Omega_0}{I^c_{s,yy}(\frac{1}{\omega_r^2}s^2 + \frac{2\zeta_r}{\omega_r}s + 1)s}, \tag{5.21}$$

$$G_{\omega_\psi}(s) = \frac{8 b_f b_m \Omega_0}{I^c_{s,zz}(\frac{1}{\omega_r^2}s^2 + \frac{2\zeta_r}{\omega_r}s + 1)s}, \tag{5.22}$$

$$G_{\dot{z}}(s) = \frac{8 \mu b_f \Omega_0}{(\frac{1}{\omega_r^2}s^2 + \frac{2\zeta_r}{\omega_r}s + 1)s}, \tag{5.23}$$

where $G_{\omega_\theta}(s)$ represents the transfer function for the vehicle's pitch angular velocity with actuation based on rotor thrust magnitude, $G_{\omega_\psi}(s)$ represents the transfer function for the vehicle's yaw angular velocity with actuation based on rotor thrust magnitude and $G_{\dot{z}}(s)$ represents the transfer function of the vehicle z translational velocity with actuation based on rotor thrust magnitude variation. Since the closed-loop dynamics are the same for all axes, we only show the responses of the system with respect to the roll rate dynamics. The presented structure has been validated in Matlab Simulink environment. The closed system step response is given with Fig-

ure 5.3 with controller outputs (motors velocities) shown in Figure 5.4. The system response is fast, with a small overshoot of 8%. Due to the vehicle's configuration, only motors 2 and 4 are responsible for controlling the roll axis, which also can be seen from Equations (5.1) - (5.8).

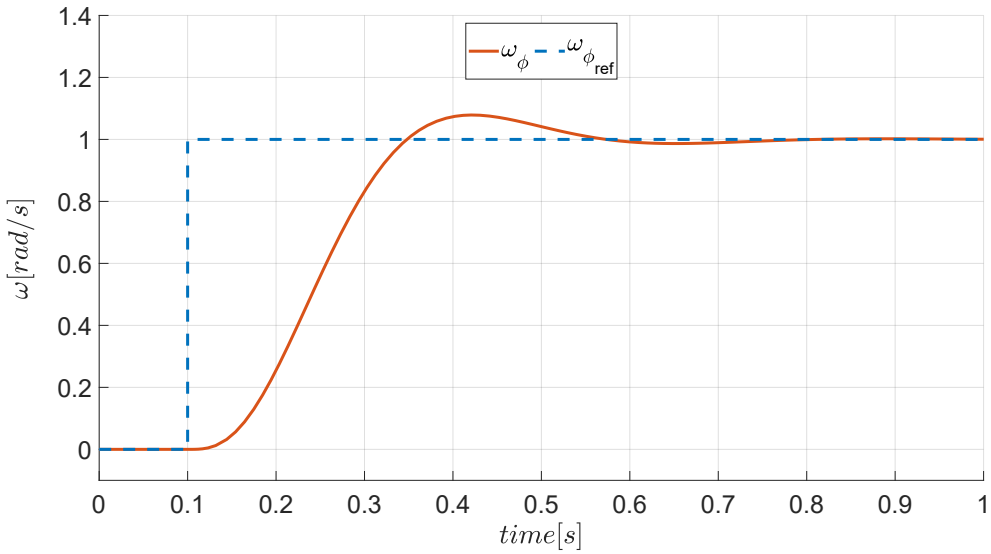

Figure 5.3: This figure shows the measured and reference angular velocity of the roll angle. The loop has been tuned according to the symmetrical optimum with filter in reference signal, resulting in an overshoot of 8%.

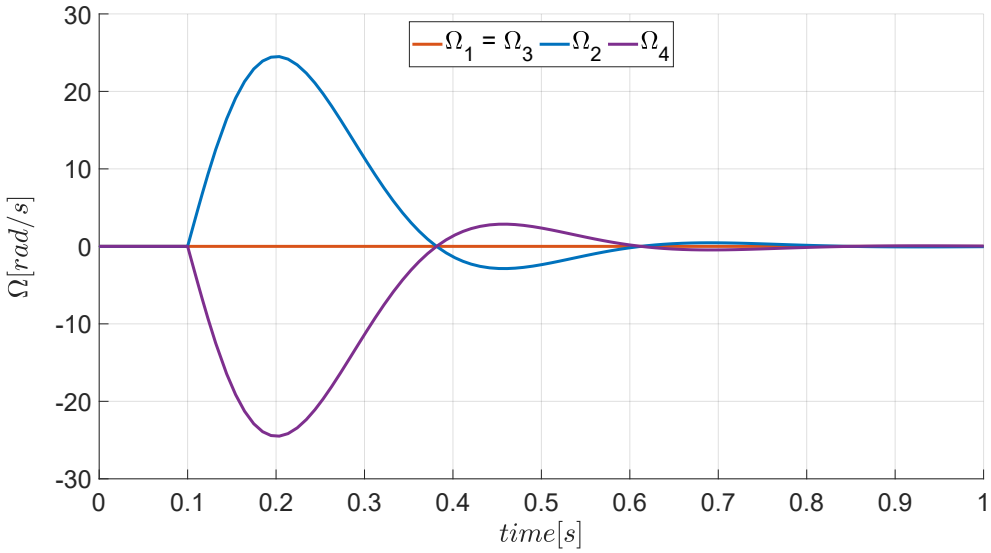

Figure 5.4: Figure shows the rotor velocities which are commanded by the PI controller.

5.1.2Outer control loop

The outer control loop, angle control, is designed in a same way as inner control loop using symmetrical optimum optimization method. For that purpose, the transfer function of inner control loop is calculated:

$$G_{CL,\omega_\phi}(s) = \frac{1}{1 + a^2 T_{\Sigma,\omega_\phi} s + a^3 T^2_{\Sigma,\omega_\phi} s^2 + a^3 T^3_{\Sigma,\omega_\phi} s^3}. \tag{5.24}$$

According to the symmetrical optimum, such transfer function can roughly be approximated with:

$$G_{CL,\omega_\phi}(s) = \frac{1}{1 + 3.7 T_{\Sigma,\omega_\phi} s}, \tag{5.25}$$

which give us suitable transfer function form for calculating outer loop control parameters. By adding a integrator to the obtained inner closed loop transfer function we get vehicle angle dynamics. This can be written as:

$$G_\phi(s) = G_{CL,\omega_\phi}(s)\frac{1}{s} = \frac{1}{s(1 + 3.7 T_{\Sigma,\omega_\phi} s)} = \frac{K_\phi}{T_{i,\phi} s (T_{\Sigma,\phi} s + 1)}, \tag{5.26}$$

where

$$K_\phi = 1, \tag{5.27}$$

$$T_{\Sigma,\phi} = 3.7 T_{\Sigma,\omega_\phi}, \tag{5.28}$$

$$T_{i,\phi} = 1. \tag{5.29}$$

The same type of PI controller is used as in inner loop control design, which is given with equation:

$$G_{R,\phi}(s) = K_{R,\phi}\frac{1 + T_{I,\phi} s}{T_{I,\phi} s}. \tag{5.30}$$

The symmetrical optimum tuning criteria for this system gives following PI controller parameters:

$$K_{R,\phi} = \frac{T_{i,\phi}}{a K_\phi T_{\Sigma,\phi}}, \tag{5.31}$$

$$T_{I,\phi} = a^2 T_{\Sigma,\phi}, \tag{5.32}$$

$$a = 2, \tag{5.33}$$

with angle reference signal filter as

$$G_{P,\phi} = \frac{1}{1 + a^2 T_{\sum,\phi} s}. \tag{5.34}$$

The controller performance was tested within Matlab Simulink environment. We analyzed system behavior on step reference which response is given with Figure 5.5. The system shows fast response with small overshoot of 8%. The commanded angular velocity is well tracked which indicates that inner control loop is finely tuned. We have only presented responses of the roll angle control loop, as the pitch angle, yaw angle and height control has similar results.

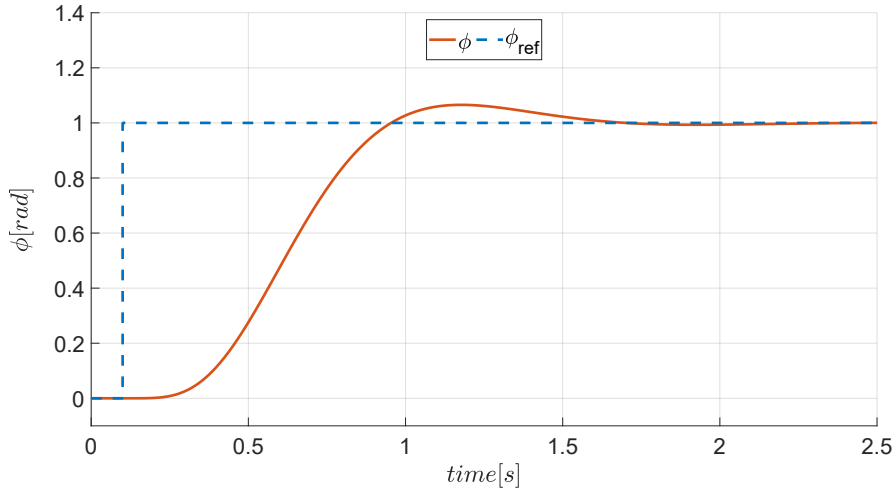

(a)

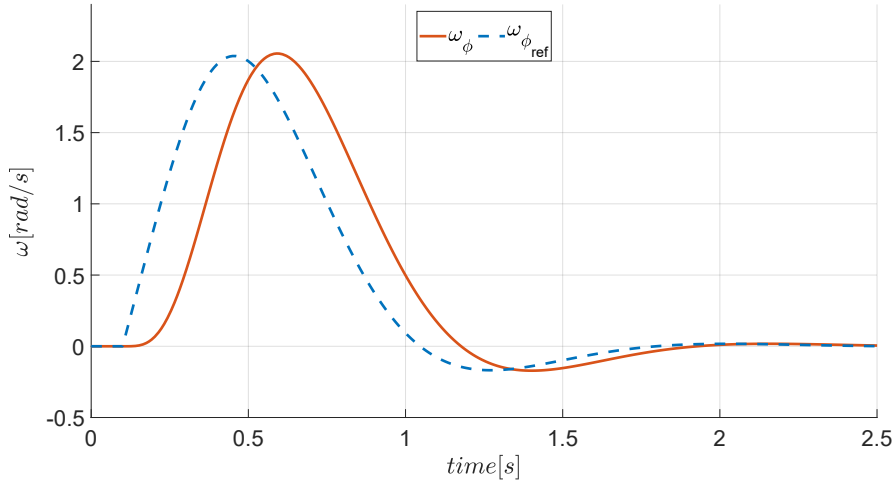

(b)

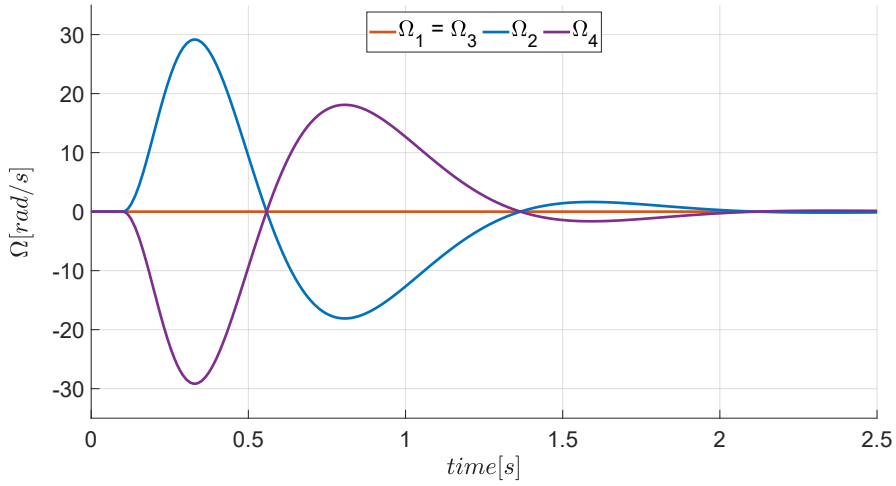

(c)

Figure 5.5: These figures show the system's response to a roll step reference. In a), the step reference with measured angle is presented. We can notice a small overshoot and no steady-state error. In b), the roll controller output is shown, which serves as a reference to the inner control loop, the roll angular velocity controller. This figure shows good tracking, which is crucial for good overall system performance. The references for the motor velocities are also shown in b).

5.2Horizontal position control

Previous sections of this thesis dealt with attitude and height control. To achieve a fully actuated system, we need to develop a position controller for the remaining 2 degrees of freedom. As the rotor thrust magnitude variation method is used for attitude and height reference tracking, here we rely on rotor thrust direction variation and centroid variation. With rotor tilt, thrust forces can be distributed to achieve reference acceleration along desired axes. The centroid variation control concept is more complex, since the thrust distribution is only indirectly linked with the CoG control. Another challenge with this control concept occurs when the UAV is in contact with the environment. In these scenarios, the CoG is displaced into the contact point of the UAV and the environment, and the centroid variation control concept used for free flight is not applicable any longer.

By observing the linearized attitude dynamics of an unmanned aerial manipulator, shown in Equation (4.3), and it's linearized translation dynamics, shown in Equation (4.7), it becomes apparent that the vehicle can operate in two different working regimes depending on the angle β. To aid in understanding, we will split the working ranges of rotor tilt angles into two zones: Zone A, where the rotor tilting angle $\beta_{0,j} \geq 0$, and Zone B, where the rotor tilting angle $\beta_{0,j} < 0$, with $j \in 1,...,N_r$. Visual representation of Zone A and Zone B for one axis is shown in Figure 5.6. Having in mind that attitude controller is designed based on control variables given with Equations (5.1) - (5.8), we can observe that if rotor 2 and rotor 4 are in Zone A or Zone B, centroid variation, for example as a result of moving a payload with robotic arm, will cause the vehicle's horizontal acceleration along the x axis. The same is valid for rotor 1 and rotor 3 for acceleration along y axis. Contrary, if one of the rotors, for example rotor 2 or rotor 4, is in Zone A and other one in Zone B, centroid variation does not have a significant influence on the vehicle acceleration along x axis. The same is valid for the y axis and rotor 1 and rotor 3.

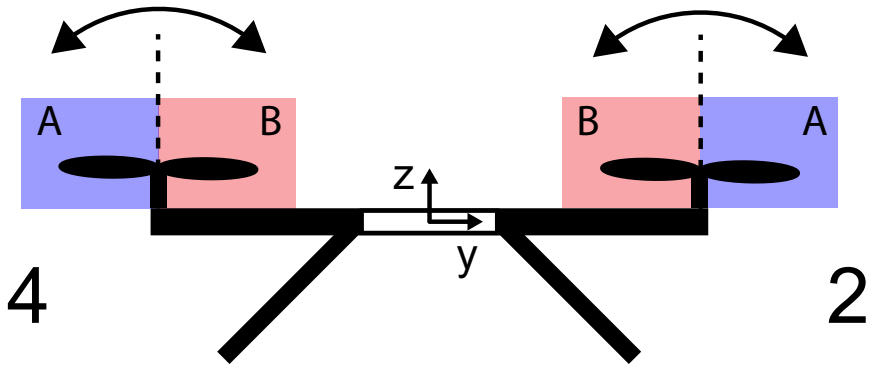

Figure 5.6: Illustrative representation of rotor tilting zones. If both rotors, rotor 2 and rotor 4, are in zone A or zone B, the vehicle's horizontal acceleration along the x axis can be controlled using centroid variation. However, if one of the rotors is in zone A and the other one is in zone B, the vehicle's horizontal movement in the x-axis cannot be controlled using centroid variation. The same applies to rotor 1 and rotor 3 for controlling the vehicle's acceleration along the y-axis.

Let's first analyze the regime in which both rotor pairs are either in Zone A or in Zone B. In order to explain this working regime more easily, we will linearize the vehicle dynamics around the operating point for the tilting angle in the middle of Zone B, with a $\beta_{0,j}$ value of:

$$\beta_{0,1} = \beta_{0,2} = \beta_{0,3} = \beta_{0,4} = -\frac{\beta_{max}}{2} = -0.16rad. \tag{5.35}$$

Applying a small angle approximation theorem, we obtain:

$$S(\beta_{0,1}) = S(\beta_{0,2}) = S(\beta_{0,3}) = S(\beta_{0,4}) = -0.16, \tag{5.36}$$

$$C(\beta_{0,1}) = C(\beta_{0,2}) = C(\beta_{0,3}) = C(\beta_{0,4}) = 1. \tag{5.37}$$

Taking into account the operating point from Equations (5.36) and (5.37) in Equation for linearized attitude dynamics for TRMMC-UAV (4.3) we can derive the following expression for attitude dynamics:

$$\begin{aligned}
\Delta\dot{\omega} = &\begin{bmatrix} 0.16\frac{2b_f b_m\Omega_0}{I^c_{s,xx}}(\Delta\Omega_1 - \Delta\Omega_3) \\ 0.16\frac{2b_f b_m\Omega_0}{I^c_{s,yy}}(\Delta\Omega_2 - \Delta\Omega_4) \\ \frac{2b_f b_m\Omega_0}{I^c_{s,zz}}(\Delta\Omega_1 - \Delta\Omega_2 + \Delta\Omega_3 - \Delta\Omega_4) \end{bmatrix} + \begin{bmatrix} 0.16\frac{2b_f\Omega_0(z_r - \mu 4mz_m)}{I^c_{s,xx}}(\Delta\Omega_2 - \Delta\Omega_4) \\ 0.16\frac{2b_f\Omega_0(\mu 4mz_m - z_r)}{I^c_{s,yy}}(\Delta\Omega_1 - \Delta\Omega_3) \\ 0 \end{bmatrix} \\
&+ \begin{bmatrix} \frac{2Lb_f\Omega_0}{I^c_{s,xx}}(\Delta\Omega_2 - \Delta\Omega_4) \\ -\frac{2Lb_f\Omega_0}{I^c_{s,yy}}(\Delta\Omega_1 - \Delta\Omega_3) \\ 0 \end{bmatrix} + \begin{bmatrix} 0.16\frac{Lb_f\Omega_0^2}{I^c_{s,xx}}(\Delta\beta_2 - \Delta\beta_4) \\ -0.16\frac{Lb_f\Omega_0^2}{I^c_{s,yy}}(\Delta\beta_1 - \Delta\beta_3) \\ 0 \end{bmatrix} \\
&+ \begin{bmatrix} \frac{b_f\Omega_0^2(\mu 4mz_m - z_r)}{I^c_{s,xx}}(\Delta\beta_2 - \Delta\beta_4) + \frac{b_m b_f\Omega_0^2}{I^c_{s,xx}}(\Delta\beta_1 - \Delta\beta_3) \\ \frac{b_f\Omega_0^2(z_r - \mu 4mz_m)}{I^c_{s,yy}}(\Delta\beta_1 - \Delta\beta_3) - \frac{b_m b_f\Omega_0^2}{I^c_{s,yy}}(\Delta\beta_2 - \Delta\beta_4) \\ -0.16\frac{b_m b_f\Omega_0^2}{I^c_{s,zz}}(\Delta\beta_2 + \Delta\beta_4 - \Delta\beta_1 - \Delta\beta_3) \end{bmatrix} \\
&+ \begin{bmatrix} -\frac{4\mu b_f m\Omega_0^2}{I^c_{s,xx}}(\Delta y_2 + \Delta y_4) \\ \frac{4\mu b_f m\Omega_0^2}{I^c_{s,yy}}(\Delta x_1 + \Delta x_3) \\ -0.64\frac{\mu b_f m\Omega_0^2}{I^c_{s,zz}}(\Delta y_2 + \Delta y_4 - \Delta x_1 - \Delta x_3) \end{bmatrix} + \begin{bmatrix} \frac{mz_m(1-\mu 4m)}{I^c_{s,xx}}(\Delta\ddot{y}_2 + \Delta\ddot{y}_4) \\ -\frac{mz_m(1-\mu 4m)}{I^c_{s,yy}}(\Delta\ddot{x}_1 + \Delta\ddot{x}_3) \\ 0 \end{bmatrix},
\end{aligned} \tag{5.38}$$

and similarly, using operating point Equations (5.36) and (5.37) in Equation (4.7) we can obtain

the expression for linearized translation dynamics as:

$$\Delta\dot{\mathbf{v}}_0 = \mu 2 b_f \Omega_0 \begin{bmatrix} -0.16\,(\Delta\Omega_1 - \Delta\Omega_3) \\ -0.16\,(\Delta\Omega_2 - \Delta\Omega_4) \\ \Delta\Omega_1 + \Delta\Omega_2 + \Delta\Omega_3 + \Delta\Omega_4 \end{bmatrix} + \mu b_f \Omega_0^2 \begin{bmatrix} \Delta\beta_1 - \Delta\beta_3 \\ \Delta\beta_2 - \Delta\beta_4 \\ 0.16\,(\Delta\beta_1 + \Delta\beta_2 + \Delta\beta_3 + \Delta\beta_4) \end{bmatrix}$$
$$- g \begin{bmatrix} -\Delta\theta \\ \Delta\phi \\ 0 \end{bmatrix} - \mu m \begin{bmatrix} \Delta\ddot{x}_1 + \Delta\ddot{x}_3 \\ \Delta\ddot{y}_2 + \Delta\ddot{y}_4 \\ 0 \end{bmatrix}. \tag{5.39}$$

Having in mind that the attitude controller is designed based on control variables given with Equations (5.1) - (5.8), we choose the following control variables for centroid variation and rotor tilt:

$$u_{mm,x} = \Delta x_{1,ref} = \Delta x_{3,ref}, \tag{5.40}$$
$$u_{mm,y} = -\Delta y_{2,ref} = -\Delta y_{4,ref}, \tag{5.41}$$
$$u_{\beta,x} = \Delta\beta_{1,ref} = -\Delta\beta_{3,ref}, \tag{5.42}$$
$$u_{\beta,y} = -\Delta\beta_{2,ref} = \Delta\beta_{4,ref}. \tag{5.43}$$

Combining Equations (5.38) - (5.43) with actuator dynamics given with Equations (3.17), (3.18) and (3.19) we obtain the translation dynamics transfer functions:

$$s\mathbf{v}_0(s) = \begin{bmatrix} \frac{0.64\mu b_f \Omega_0}{\frac{1}{\omega_r^2}s^2 + \frac{2\zeta_r}{\omega_r}s + 1} u_\theta(s) \\ -\frac{0.64\mu b_f \Omega_0}{\frac{1}{\omega_r^2}s^2 + \frac{2\zeta_r}{\omega_r}s + 1} u_\phi(s) \\ \frac{8\mu b_f \Omega_0}{\frac{1}{\omega_r^2}s^2 + \frac{2\zeta_r}{\omega_r}s + 1} u_z(s) \end{bmatrix}. + \begin{bmatrix} \frac{2\mu b_f \Omega_0^2}{\frac{1}{\omega_{tr}^2}s^2 + \frac{2\zeta_{tr}}{\omega_{tr}}s + 1} u_{\beta,x}(s) \\ -\frac{2\mu b_f \Omega_0^2}{\frac{1}{\omega_{tr}^2}s^2 + \frac{2\zeta_{tr}}{\omega_{tr}}s + 1} u_{\beta,y}(s) \\ 0 \end{bmatrix}$$
$$+ \begin{bmatrix} g\theta(s) \\ -g\phi(s) \\ 0 \end{bmatrix} + \begin{bmatrix} -\frac{2\mu m s^2}{\frac{1}{\omega_{mm}^2}s^2 + \frac{2\zeta_{mm}}{\omega_{mm}}s + 1} u_{mm,x}(s) \\ \frac{2\mu m s^2}{\frac{1}{\omega_{mm}^2}s^2 + \frac{2\zeta_{mm}}{\omega_{mm}}s + 1} u_{mm,y}(s) \\ 0 \end{bmatrix} \tag{5.44}$$

and the attitude transfer functions:

$$
\begin{aligned}
s\boldsymbol{\omega}(s) = &
\begin{bmatrix}
\frac{4b_f\Omega_0(L+0.16(z_r-\mu 4mz_m))}{I^c_{s,xx}(\frac{1}{\omega_r^2}s^2+\frac{2\zeta_r}{\omega_r}s+1)}u_{r,\phi}(s) - \frac{0.64b_fb_m\Omega_0}{I^c_{s,xx}(\frac{1}{\omega_r^2}s^2+\frac{2\zeta_r}{\omega_r}s+1)}u_{r,\theta}(s) \\
\frac{4b_f\Omega_0(L+0.16(z_r-\mu 4mz_m))}{I^c_{s,yy}(\frac{1}{\omega_r^2}s^2+\frac{2\zeta_r}{\omega_r}s+1)}u_{r,\theta}(s) + \frac{0.64b_fb_m\Omega_0}{I^c_{s,yy}(\frac{1}{\omega_r^2}s^2+\frac{2\zeta_r}{\omega_r}s+1)}u_{r,\phi}(s) \\
\frac{8b_fb_m\Omega_0}{I^c_{s,zz}(\frac{1}{\omega_r^2}s^2+\frac{2\zeta_r}{\omega_r}s+1)}u_{r,\psi}(s)
\end{bmatrix} \\
&+ \begin{bmatrix}
\frac{2b_f\Omega_0^2((z_r-\mu 4mz_m)-0.16L)}{I^c_{s,xx}(\frac{1}{\omega_{tr}^2}s^2+\frac{2\zeta_{tr}}{\omega_{tr}}s+1)}u_{\beta,y}(s) + \frac{2b_mb_f\Omega_0^2}{I^c_{s,xx}(\frac{1}{\omega_{tr}^2}s^2+\frac{2\zeta_{tr}}{\omega_{tr}}s+1)}u_{\beta,x}(s) \\
\frac{2b_f\Omega_0^2((z_r-\mu 4mz_m)-0.16L)}{I^c_{s,yy}(\frac{1}{\omega_{tr}^2}s^2+\frac{2\zeta_{tr}}{\omega_{tr}}s+1)}u_{\beta,x}(s) + \frac{2b_mb_f\Omega_0^2}{I^c_{s,yy}(\frac{1}{\omega_{tr}^2}s^2+\frac{2\zeta_{tr}}{\omega_{tr}}s+1)}u_{\beta,y}(s) \\
0
\end{bmatrix} \\
&+ \begin{bmatrix}
\frac{8\mu b_fm\Omega_0^2-2mz_m(1-\mu 4m)s^2}{I^c_{s,xx}(\frac{1}{\omega_{mm}^2}s^2+\frac{2\zeta_{mm}}{\omega_{mm}}s+1)}u_{mm,y}(s) \\
\frac{8\mu b_fm\Omega_0^2-2mz_m(1-\mu 4m)s^2}{I^c_{s,yy}(\frac{1}{\omega_{mm}^2}s^2+\frac{2\zeta_{mm}}{\omega_{mm}}s+1)}u_{mm,x}(s) \\
\frac{1.28\mu b_fm\Omega_0^2}{I^c_{s,zz}(\frac{1}{\omega_{mm}^2}s^2+\frac{2\zeta_{mm}}{\omega_{mm}}s+1)}u_{mm,x}(s) + \frac{1.28\mu b_fm\Omega_0^2}{I^c_{s,zz}(\frac{1}{\omega_{mm}^2}s^2+\frac{2\zeta_{mm}}{\omega_{mm}}s+1)}u_{mm,y}(s)
\end{bmatrix},
\end{aligned}
\tag{5.45}
$$

From Equation (5.45), it is apparent that altering the rotor angle or shifting the vehicle's center of gravity will impact the vehicle's attitude dynamics. As outlined in Section 5.1, altitude control is achieved by varying the rotors' thrust magnitude through control variables $u_{r,\phi}$, $u_{r,\theta}$, and $u_{r,\psi}$, while any influence from centroid variation or rotor thrust direction variation is considered a disturbance.

Adjusting the rotor angle control variables $u_{\beta,y}$ and $u_{\beta,x}$ will slightly affect the vehicle's roll and pitch angles, respectively, as we optimize the angle control loop for effective disturbance rejection. However, changes in $u_{\beta,y}$ and $u_{\beta,x}$ have a significant impact on the vehicle's translation dynamics in the y-axis direction and x-axis direction, respectively, as demonstrated in Equation (5.44). An increase in $u_{\beta,y}$ results in a negative acceleration of the vehicle, while the roll control loop maintains the desired roll angle. Figure 5.7 depicts the behavior of the system in the y-axis, i.e. roll angle, which is equivalent to the behavior in the x-axis, pitch angle. Due to the selected control variables for rotor thrust direction variation, changes in the reference angle $\beta_{j,ref}$ do not affect the vehicle's yaw angle dynamics, as shown in Equation (5.45).

Let's examine how changes of the CoG affect the dynamics of the overall system. According to Equation (5.45), any shift in the vehicle's center of gravity, such as moving the manipulator on the aerial vehicle, can impact the vehicle's attitude dynamics. If the CoG of the vehicle moves in the negative y direction, i.e., when $u_{mm,y} > 0$, there will be a positive disturbance in the roll

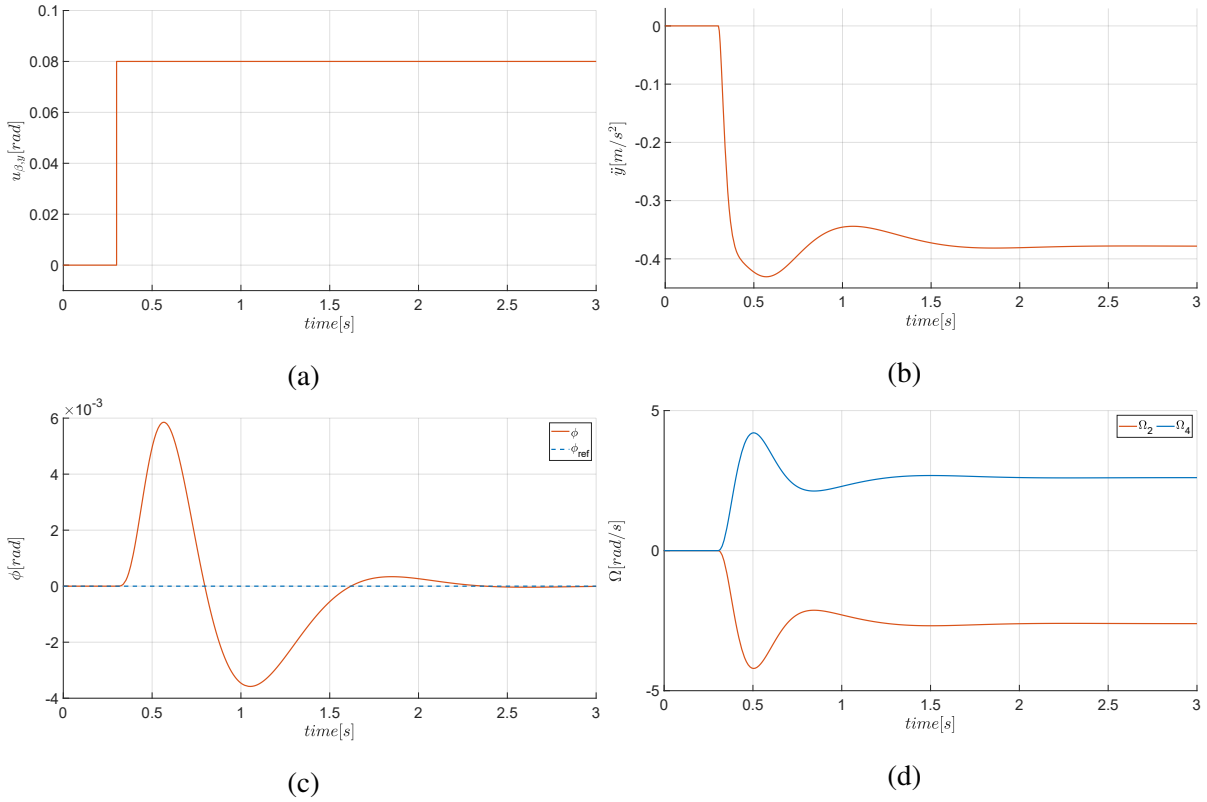

Figure 5.7: The figures demonstrate the system's response to a step change in the control variable $u_{\beta,y}$. a) shows the control variable step reference, while b) displays the vehicle's translational acceleration in the y-axis direction. When the rotors tilt, they introduce a disturbance to the vehicle's roll angle, which can be seen in c). However, the attitude controller quickly overcomes this disturbance by varying the rotor speeds, as shown in d).

angle dynamics. Conversely, if the CoG moves in the positive x direction, i.e., when $u_{mm,x} > 0$, there will be a positive disturbance in the pitch angle dynamics. However, this disturbance can be easily addressed by the attitude control loop, which is presented in Section 5.1.

Interestingly, if the rotors are located in Zone A or Zone B, a shift in the CoG can produce a unique effect, as shown in Figure 5.8. By moving the CoG of the vehicle in the negative y axis direction, $u_{mm,y} > 0$, due to the disturbance in roll control loop, the controller needs to adjust rotors speed to ensure that vehicle stays in the given reference point. Accordingly, the speed of the rotor 4 is increased and speed of the rotor 2 is decreased by the same amount, $u_{r,\phi}$. This results in larger thrust generated by rotor 4 than by rotor 2. As the rotors are tilted so that the angle lies in the Zone B, the sum of the forces generated by rotors has a horizontal component in positive y axis. This behaviour of the system is evident from Equation (5.44) and Equation (5.45). The same principle is valid for the x-axis direction. Using this effect, the vehicle's linear acceleration can be controlled just by moving the vehicle's CoG.

In addition to the described effect of the centroid variation on aerial manipulator dynamics, Equation (5.45) also indicates that the centroid variation has a slight influence on the yaw angle dynamics. However, this influence is minor and can be easily overcome by proper yaw con-

trol design. The same situation applies to translation dynamics, where the acceleration of the centroid variation influences the vehicle acceleration in the x and y axes. This influence will be considered as a disturbance in the position controller design. Figure 5.9 shows the system's response to a step input of the control variable $u_{mm,y}$, illustrating the described effect of the centroid variation on system dynamics.

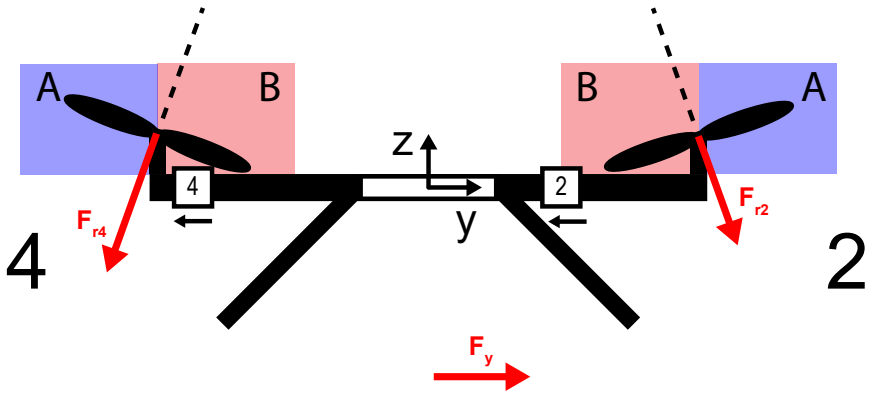

Figure 5.8: The figure presented depicts a scenario in which both rotors are situated in Zone B, enabling control of the vehicle's linear acceleration through centroid variation. When the vehicle's CoG shifts in the negative y-axis direction, as illustrated by masses 2 and 4 in the figure, the vehicle's attitude controller must increase the velocity of rotor 4 and decrease the velocity of rotor 2 to maintain the desired roll reference. This results in rotor 4 generating more thrust than rotor 2. Since the rotors are tilted at an arbitrary angle $\beta_{j,ref}$, the combined force produced by motors 2 and 4 generates acceleration in the y-axis direction.

The second working regime of the vehicle we consider here is the one in which one rotor of the pair, either rotor 2 or rotor 4, is in Zone A, and the other one is in the opposite zone, Zone B. The same applies to the other axis, rotor 1 and rotor 3. To explain this working regime, we will use linearized vehicle dynamics around the operating point for the tilting angle in the middle of the working range, with a $\beta_{0,i}$ value of:

$$\beta_{0,1} = \beta_{0,2} = \beta_{0,3} = \beta_{0,4} = 0, \tag{5.46}$$

which is given with Equations (4.24) and (4.25). It can be noticed that centroid variation, i.e. control variables $u_{mm,x}$ and $u_{mm,y}$, and rotor thrust direction variation, i.e. control variables $u_{\beta,x}$ and $u_{\beta,y}$, act as disturbance on the vehicle angle control loop. This influence is analyzed in Section 5.1. As the angle control loop aims to overcome this disturbance, it has to adapt the control variables $u_{r,\phi}$ or $u_{r,\theta}$. Unlike the first explained vehicle working regime, these two control variables do not affect the vehicle's translation dynamics in this working regime, as can be seen from Equation (4.25). Therefore, using centroid variation to control vehicle translation has no significant influence. Figure 5.10 illustrates the influence of the centroid variation on the system dynamics. It can be observed that changing the vehicle's CoG in the y-axis causes a disturbance in the vehicle's roll angle. However, this disturbance is quickly rejected by the

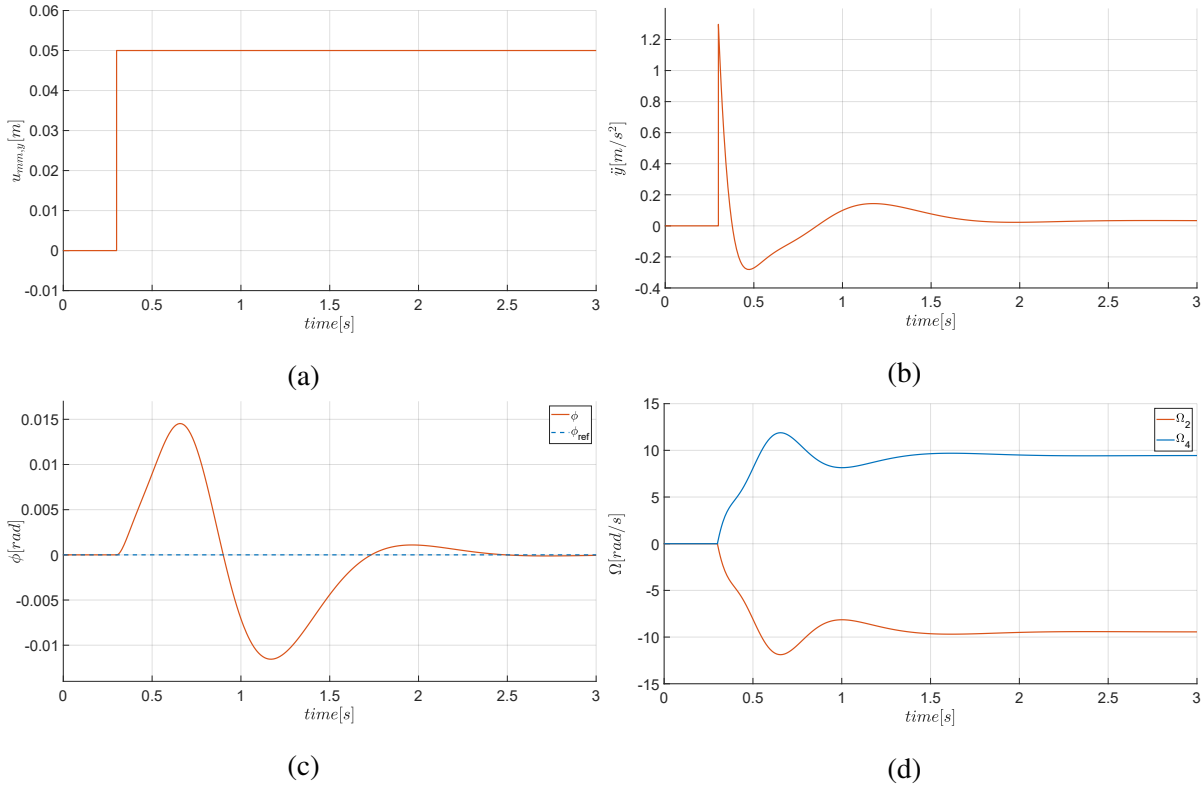

Figure 5.9: The figures depict the response of the system to a step change in the control variable $u_{mm,y}$. a) shows the control variable step reference, while b) displays the vehicle's translational acceleration in the y-axis direction. It's worth noting that altering the vehicle's center of gravity results in a small acceleration in steady state. Additionally, changes in the centroid of the vehicle introduce a disturbance to the roll angle, which is visible in c). Nevertheless, the attitude controller quickly compensates for this disturbance by adjusting the rotor speeds, as demonstrated in d).

roll angle control loop. Additionally, the centroid variation has a small impact on the vehicle's linear acceleration in the y-axis, which disturbs the system but returns to steady state quickly. The steady state of the y-axis linear acceleration is zero, indicating that the centroid variation has no significant impact on the translation dynamics. The same conclusions can be applied to x-axis.

Influence of the control variables $u_{\beta,y}$ on system dynamics can be seen in Figure 5.11. The graphs show that tilting rotors introduce disturbance to angle control loop, as discussed earlier. This disturbance can quickly be compensated for by the angle controller. Furthermore, with the vehicle reference angle set to zero, the vehicle has linear acceleration thanks to the tilting rotors. This enables control of all 6 vehicle's DOFs by using rotors thrust magnitude variation for attitude control, and rotors thrust direction variation for position control. In this working regime, neither the centroid variation nor the rotors thrust direction variation affect the yaw angle dynamics.

The influence of the control variables $u_{\beta,y}$ on system dynamics can be observed in Figure 5.11. As previously stated, tilting rotors introduce disturbances to the angle control loop. However, these disturbances are quickly overcome by the angle controller. Despite the vehicle's

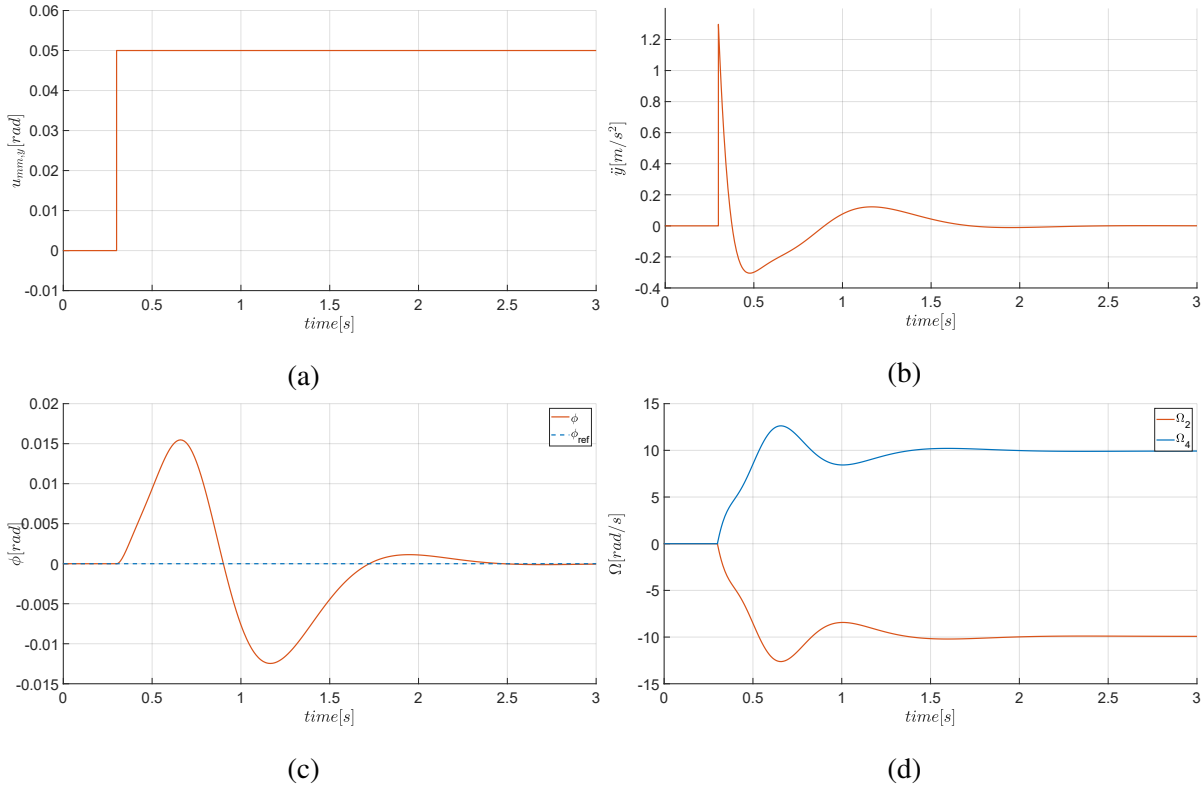

Figure 5.10: The figure demonstrates the effect of centroid variation on system dynamics when the vehicle is in the second working regime. a) displays the control variable $u_{mm,y}$, which introduces a small disturbance in the vehicle's translational acceleration, shown in b), that quickly returns to steady state. The steady state is zero, indicating that the centroid variation has no significant impact on the translational acceleration, and the vehicle's translational movement cannot be controlled by centroid variation. Changes in the vehicle's centroid also introduce a disturbance to the roll angle, visible in c). However, the attitude controller rapidly compensates for this disturbance by adjusting the rotor speeds, as shown in d).

referenced angle being set to zero, the tilting rotors enable linear acceleration of the vehicle, allowing for all six degrees of freedom control using variations in rotor thrust magnitude for attitude control and rotor thrust direction for position control. The same conclusions can be applied to x-axis and control variable $u_{\beta,x}$. In this operating regime, neither the centroid variation nor the rotors' thrust direction variation affects the yaw angle dynamics.

Based on the given analysis, the first regime considered here is suitable for free flight scenarios, but is not the optimal approach for vehicle control during contact. As already discussed, the CoG of the system during contact moves into the contact point and changes the dynamics parameters [80], most importantly attenuating the effect of centroid variation on the vehicle dynamics. Therefore, a controller based on centroid and rotor thrust direction variation will be designed for free flight using this regime, as it can ensure full 6 DoF control. Such control is essential in use-cases involving carrying payloads, where tilting the vehicle's frame is not advisable, and weight of the load can be used for vehicle's linear acceleration control.

The second considered regime will on the other hand be considered for vehicle control when

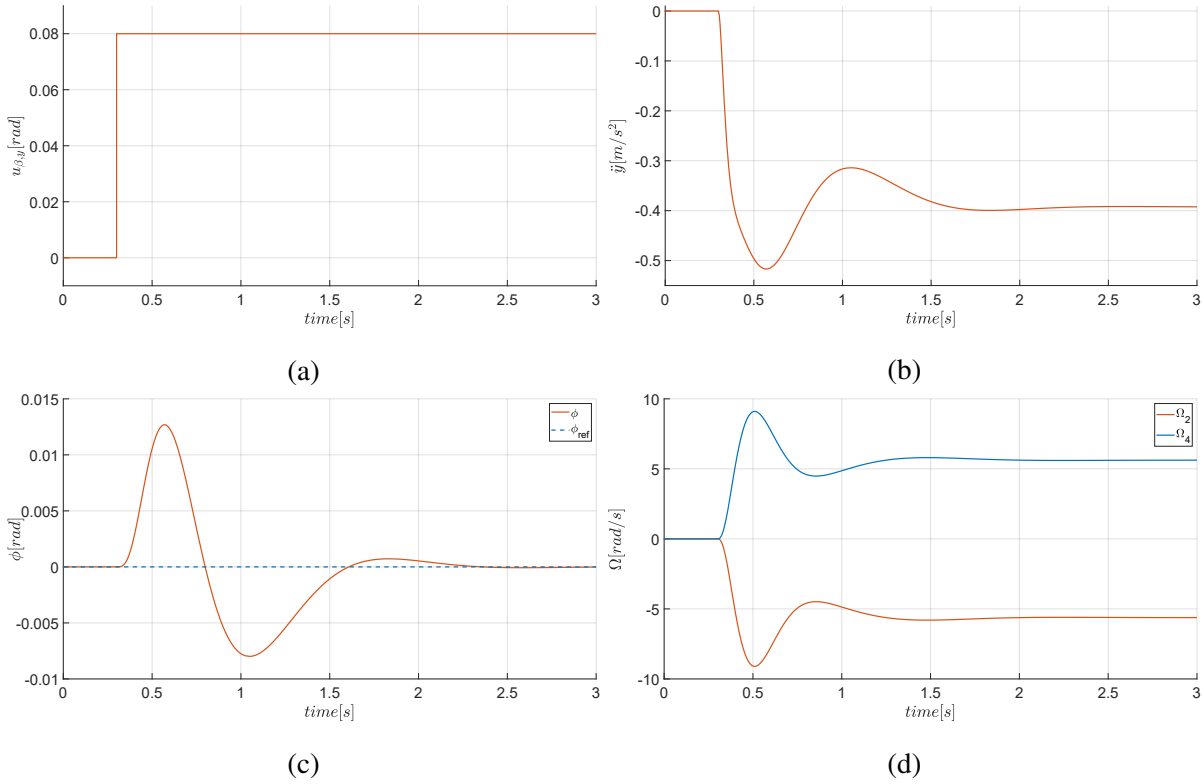

Figure 5.11: The figures show how the system responds to a step change in the control variable $u_{\beta,y}$. a) displays the control variable step reference, while b) shows the vehicle's translational acceleration in the y-axis direction. When the rotors tilt, they cause a disturbance in the vehicle's roll angle, as visible in c). However, the attitude controller effectively compensates for this disturbance by adjusting the rotor speeds, as demonstrated in d).

performing contact based tasks. As the analysis shows, the centroid variation does not have such a significant impact on the vehicle translation dynamics in this regime, allowing 6 DoF control based on rotor trust direction variation only. The design of both of these controllers will be considered in the following subsections. The switching between these two working regimes is beyond the scope of this thesis and remains an open question for future research.

5.2.1Position control based on rotor thrust direction variation

A position controller that follows a standard cascade control design is deployed for vehicle control in contact based tasks. In this regime, we use the rotor's thrust direction variation method with the control variable $u_{\beta,x}$ for x-axis position control and control variable $u_{\beta,y}$ for y-axis position control. The inner loop of the cascade control is a standard PI translation velocity controller, followed by a standard PI position control outer loop, as shown in Figure 5.12. To optimize the system behavior with respect to disturbance signals, we tune both loops according to symmetrical optimum conditions, the same tuning method that was used for attitude and height control. The analysis in this subsection considers y-axis control, and the same principles apply to x-axis. To tune the inner velocity control loop, we can derive the transfer function for

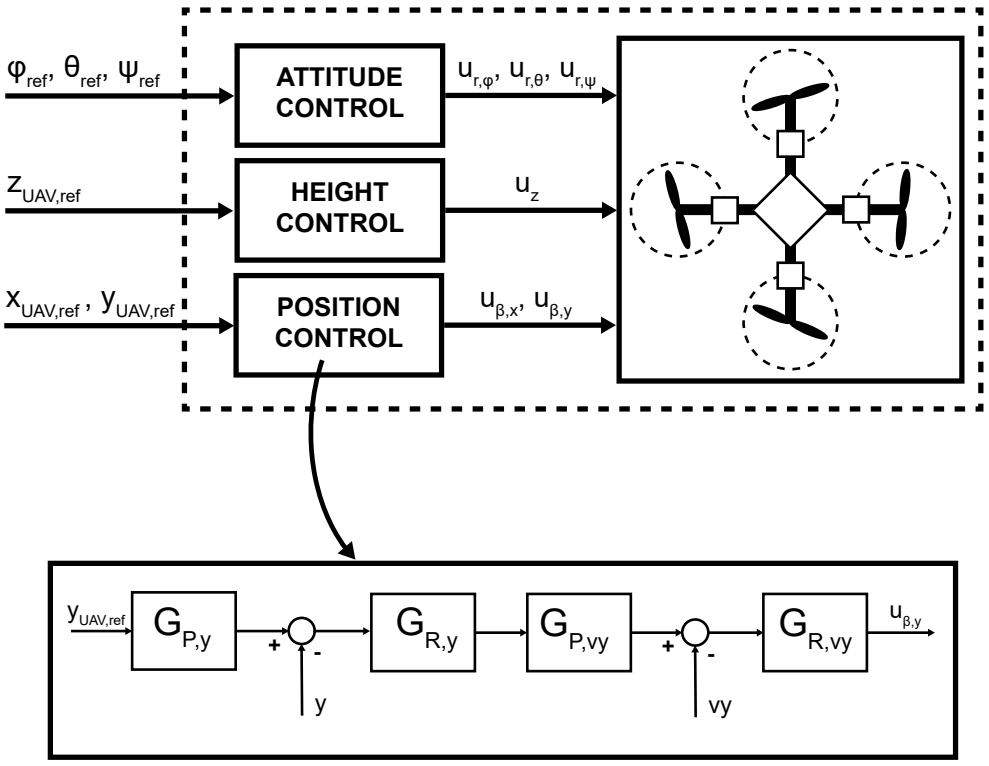

Figure 5.12: The figure shows a position control scheme for contact based tasks based on rotor thrust direction variation.

the vehicle's translation velocity in the y-axis from Equation (4.25) as follows:

$$G_{v_y,tr}(s) = \frac{2\mu b_f \Omega_0^2}{(\frac{1}{\omega_{tr}^2}s^2 + \frac{2\zeta_{tr}}{\omega_{tr}}s + 1)s}. \tag{5.47}$$

Let's rewrite this transfer function into a form more suitable for deriving parameters for controllers using symmetrical optimum:

$$G_{v_y,tr}(s) = \frac{K_{v_y}}{T_{i,v_y}s(T_{1,v_y}s+1)(T_{2,v_y}s+1)}, \tag{5.48}$$

where

$$K_{v_y} = 2\mu b_f \Omega_0^2, \tag{5.49}$$

$$T_{1,v_y} = \frac{1}{\omega_{tr}(\zeta_{tr} - \sqrt{\zeta_{tr}^2 - 1})}, \tag{5.50}$$

$$T_{2,v_y} = \frac{1}{\omega_{tr}(\zeta_{tr} + \sqrt{\zeta_{tr}^2 - 1})}, \tag{5.51}$$

$$T_{i,v_y} = 1. \tag{5.52}$$

Time constants of the system are approximated with a single time constant as $T_{\Sigma,v_y} = T_{1,v_y} + T_{2,v_y}$ which leads to the following system approximation:

$$G_{v_y,tr}(s) = \frac{K_{v_y}}{T_{i,v_y}s(T_{\Sigma,v_y}s+1)}. \tag{5.53}$$

Using a standard PI controller:

$$G_{R,v_y}(s) = K_{R,v_y}\frac{1+T_{I,v_y}s}{T_{I,v_y}s}, \tag{5.54}$$

the symmetrical optimum tuning criteria for this system give the PI controller parameters as

$$K_{R,v_y} = \frac{T_{i,v_y}}{aK_{v_y}T_{\Sigma,v_y}}, \tag{5.55}$$

$$T_{I,v_y} = a^2 T_{\Sigma,v_y}, \tag{5.56}$$

$$a = 2. \tag{5.57}$$

with translation velocity reference signal filter as

$$G_{P,v_y} = \frac{1}{1+a^2T_{\Sigma,v_y}s}. \tag{5.58}$$

The performance of the designed velocity controller was tested within Matlab Simulink environment. Step reference response is shown in Figure 5.13. The system response is fast, and a small overshoot can be observed. The nonlinearities on the response are due to the limitation of the tilting angle β_{max}. Reference tracking is achieved without steady state error, which indicates that inner control loop is finely tuned.

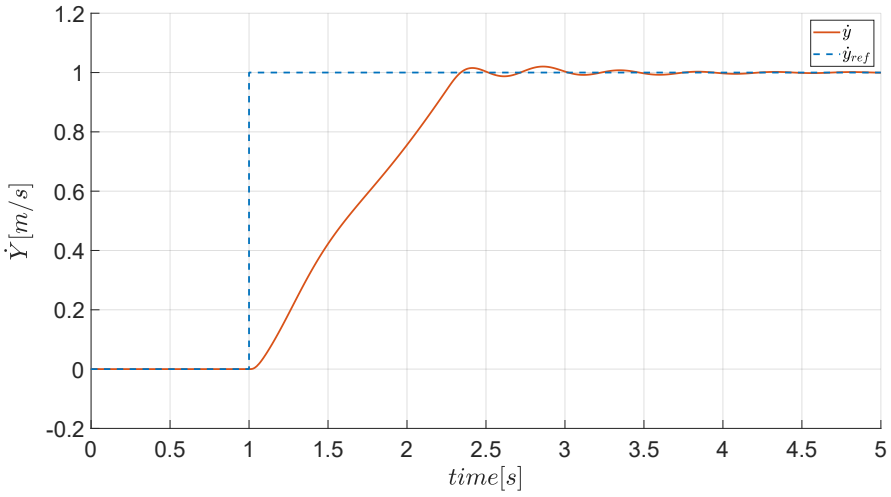

(a)

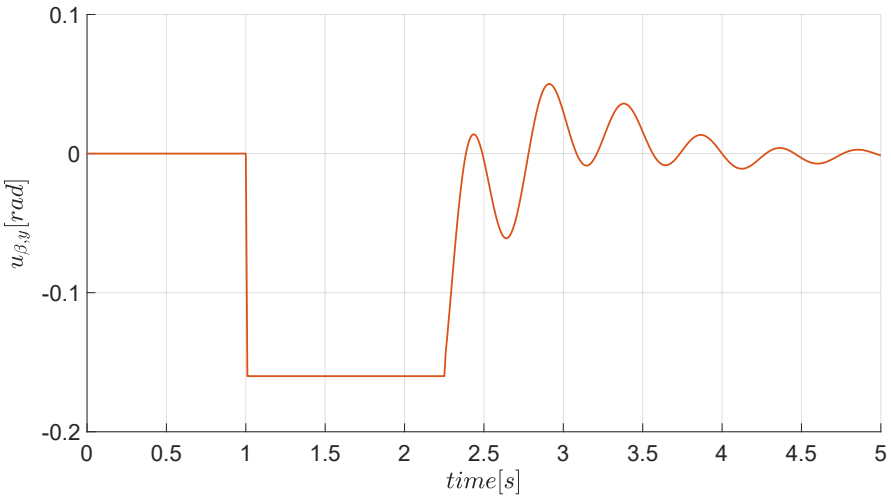

(b)

Figure 5.13: These figures show the system's response to a velocity step reference. In (a), the step reference with the measured system velocity is presented. We can observe a small overshoot and no steady-state error. Minor nonlinearities are present due to the limitation of the tilting angle. In (b), the velocity controller output, which is the tilting angle control variable, is shown.

The inner and outer control loops are tuned using the same approach. To derive parameters for the outer loop, we first approximate the inner control loop with the following transfer function:

$$G_{CL,v_y}(s) = \frac{1}{1+3.7T_{\Sigma,v_y}s}. \tag{5.59}$$

By adding an integrator to this transfer function, we obtain the dynamics of the vehicle's position, which can be expressed as:

$$G_y(s) = G_{CL,v_y}(s)\frac{1}{s} = \frac{1}{s(1+3.7T_{\Sigma,v_y}s)} = \frac{K_y}{T_{i,y}s(T_{\Sigma,y}s+1)}, \tag{5.60}$$

where

$$K_y = 1, \tag{5.61}$$

$$T_{\Sigma,y} = 3.7T_{\Sigma,v_y}, \tag{5.62}$$

$$T_{i,y} = 1. \tag{5.63}$$

The PI controller used in the inner loop is also used in the outer loop and can be represented as:

$$G_{R,y}(s) = K_{R,y}\frac{1+T_{I,y}s}{T_{I,y}s}. \tag{5.64}$$

The symmetrical optimum tuning criteria for the system yields the following PI controller parameters:

$$K_{R,y} = \frac{T_{i,y}}{aK_yT_{\Sigma,y}}, \tag{5.65}$$

$$T_{I,y} = a^2T_{\Sigma,y}, \tag{5.66}$$

$$a = 2, \tag{5.67}$$

with position reference signal filter as

$$G_{P,y} = \frac{1}{1+a^2T_{\Sigma,y}s}. \tag{5.68}$$

The system's response to a position step reference is shown in Figure 5.14, with the reference depicted as dashed lines and the measured signals as solid lines. The system exhibits a small overshoot and no steady-state error.

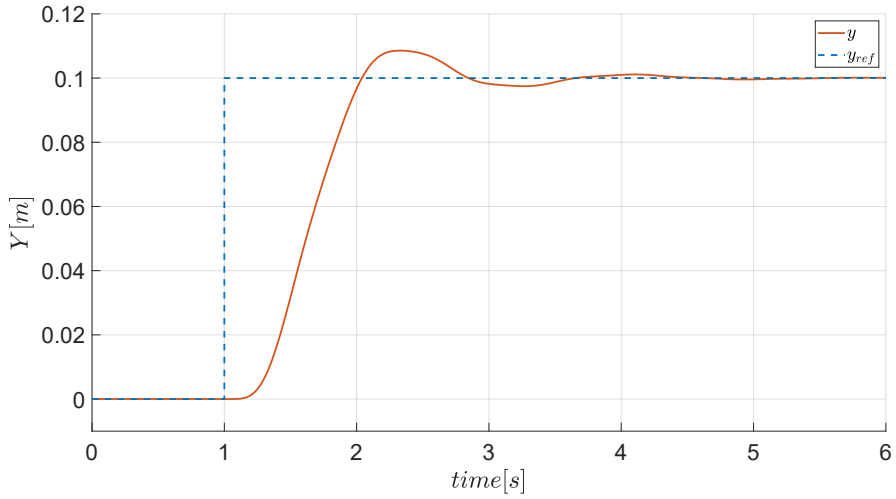

(a)

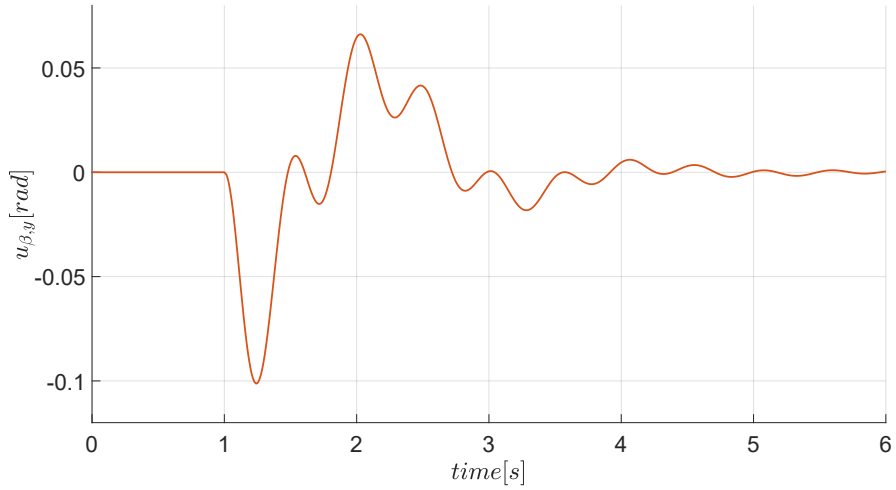

(b)

Figure 5.14: The provided figures depict how the system reacts to a position step reference. In (a), the measured system position is compared with the step reference, revealing a slight overshoot and zero steady-state error. In (b), the output of the velocity controller, which controls the tilting angle, is displayed.

5.2.2Position control based on centroid and rotor thrust direction variation

The position control for the vehicle in a free flight regime is based on two control concepts, namely centroid and rotor thrust direction variation. While the cascade control loops for the rotor thrust direction is the same as in the contact based control regime, it is additionally integrated with the centroid variation control through a control concept known as valve position control (VPC). Such control for unmanned aerial vehicles has been introduced by author in [20]. This control is used for multiple-input single-output systems (MISO). The idea behind this concept is to rely on two actuator systems of different capabilities. Usually, the characteristics of the actuators are complementary in terms of bandwidth, precision or operating range. Typical example is a liquid flow control with two valves of different size [81]. The slower response system is considered a as large, less precise valve, that enables the faster system, small valve, to always operate at the middle of its range and thus precisely track the reference. This way, the fast system can quickly compensate the disturbances. In this case, the rotor tilt can exhibit a fast response to any disturbance. Then, the vehicle can slowly redistribute the weight in order to shift it's CoG. This centroid variation enables returning the rotor thrust direction back to the middle position. This subsection analyses the sensitivity of the system to centroid variation as a function of rotor thrust direction, proving the VPC approach is justified.

First we will analyse and evaluate the impact of centroid variation on the system dynamics. We begin by analyzing the system's response at three different operating points of the rotor tilting angles $\beta_{0,i} = \beta_0$, where $i \in \{1,...,N_r\}$. Specifically, we linearize the system dynamics around the following three operating points:

1. $\beta_0 = -0.08rad$,
2. $\beta_0 = -0.16rad$,
3. $\beta_0 = -0.32rad$.

We analyse roll and yaw angles responses, as they are impacted by position control along y axis. Figure 5.15 shows the reference signals for the control variable $u_{mm,y}$ in three experiments, at three distinct step values. Several experimental results are shown in the following figures, all following the same convention: line style denotes the centroid displacement reference value, and line color denotes the operating point for the rotor thrust direction angle (the linearization point for the system).

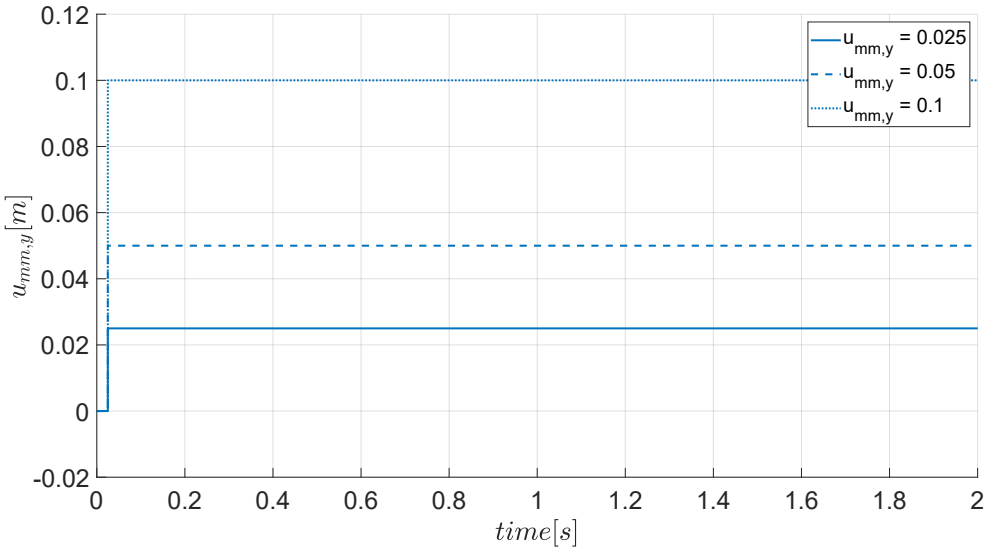

Figure 5.15: Figure show step reference for control variable $u_{mm,y}$ used in system sensitivity analysis to centroid variation as a function of rotor thrust direction.

Figure 5.16 shows the impact of displacement of the center of gravity on the roll angle dynamics. With a larger CoG displacement, the attitude disturbance is stronger. The tilting angle has an opposite effect, namely the disturbance of the attitude is smaller with a larger tilting angle. This behavior is in line with Equation (4.3), where centroid variation influences the roll and pitch dynamics with cosine of the tilting angle.

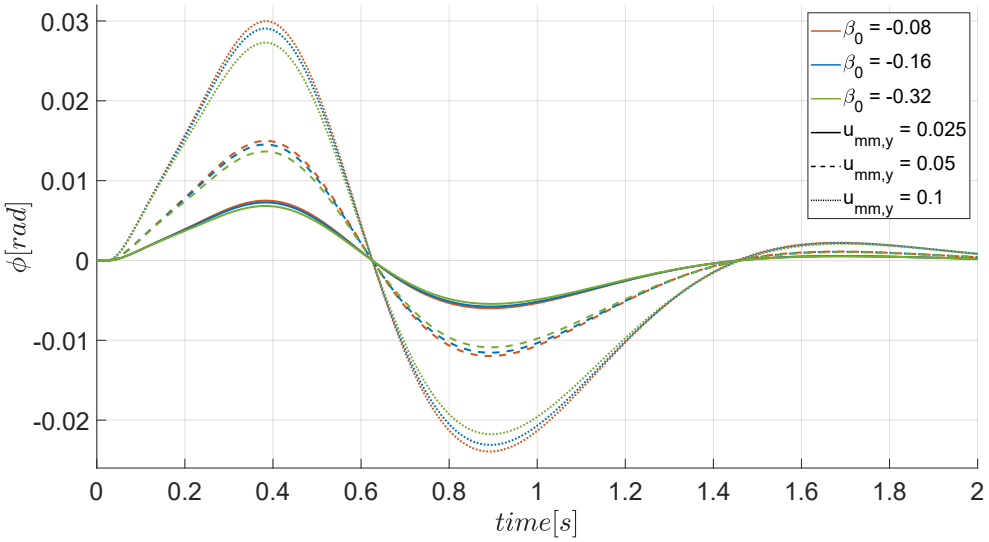

Figure 5.16: System roll response on different step reference of control variable $u_{mm,y}$.

Unlike roll dynamics, an increase in tilting angle results in a greater disturbance in yaw angle. This can be observed in Figure 5.17. The reason for this is that centroid variation affects yaw angle dynamics with the sine of the tilting angle. An increase in centroid displacement on the other hand has the same impact on yaw dynamics as it does on roll or pitch dynamics.

The response shown in the Figure 5.18 can be divided into two parts. The first part is where

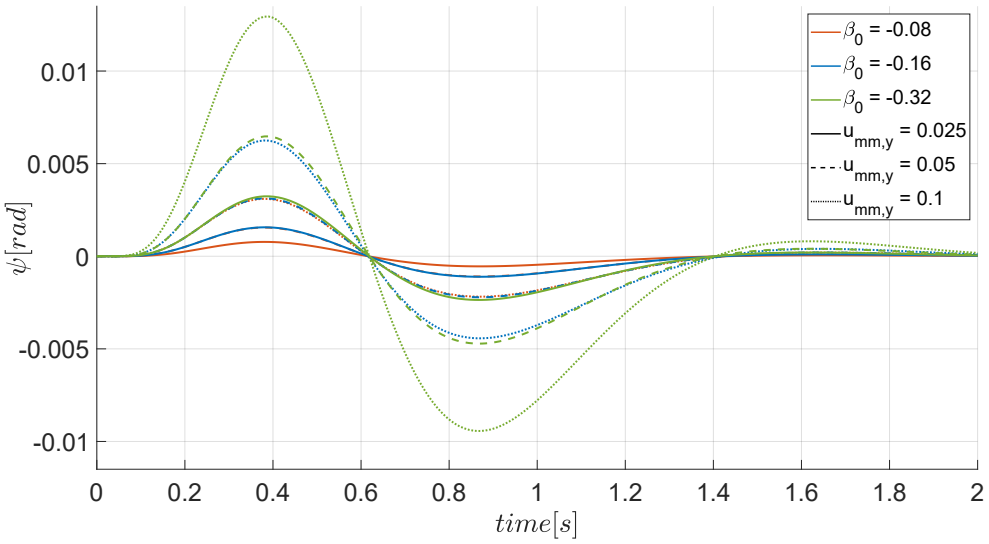

Figure 5.17: System yaw response on different step reference of control variable $u_{mm,y}$.

the CoG acceleration has the most significant impact on the vehicle dynamics. The rotor tilt has practically no effect during this phase, only the acceleration of the center of mass, as seen in Equation (4.7). The acceleration gain is so strong that it can only be considered as a short lasting disturbance.

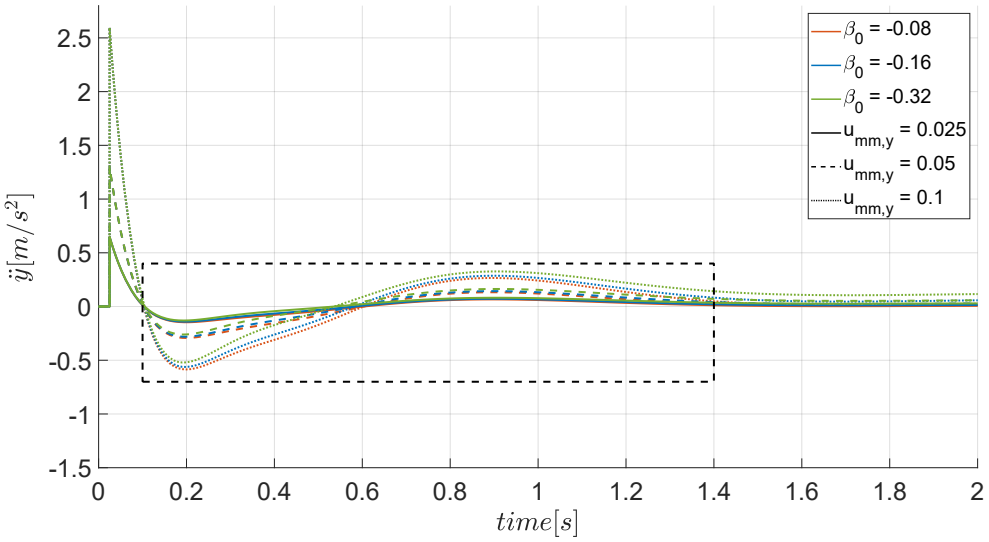

Figure 5.18: Figure shows influence of the centroid variation on vehicles translational acceleration.

The second part of the response is when the dominant effect is that of CoG position on attitude the vehicle, when the acceleration value is attenuated. The effect of CoG displacement on the vehicle translational motion is however indirect: as the center of mass displacement causes a disturbance in the attitude, the attitude control adapts control variables $u_{r,\phi}$ or $u_{r,\theta}$ (rotor speed). Then, these control variables affect the translational accelerations of the vehicle in the y or x axis, respectively. This effect can be seen in Equation (4.7). In Figure 5.19, this effect is shown more clearly, as this portion of the response graph is zoomed in.

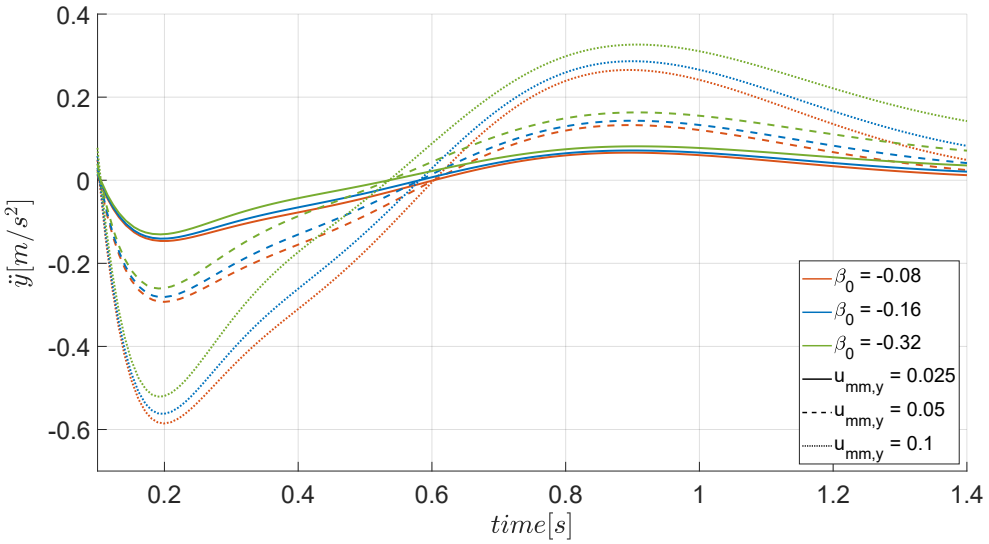

Figure 5.19: The figure shows the system's translational acceleration in response to centroid variation. The zoomed portion of the system's response shown in Figure 5.18.

The effect of the two control paradigms is shown in Figure 5.20 in responses of vehicle translational position (as a second integral of the accelerations shown in Figure 5.19). The same effect of increased tilting angle and displacement of the vehicle CoG can be observed in faster vehicle position change.

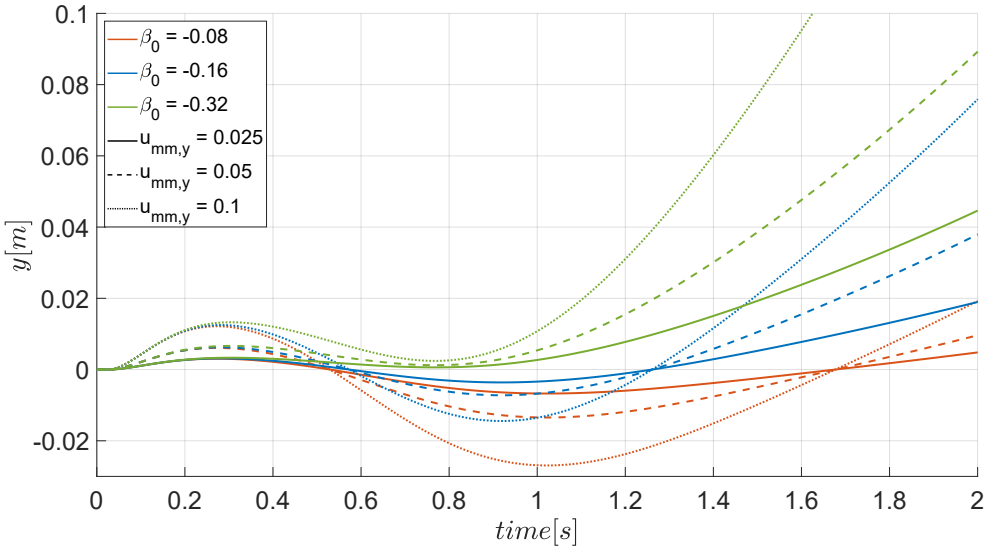

Figure 5.20: The figure shows the vehicle's position on the y-axis. It is evident that the greater the centroid variation, the larger the vehicle's movement in the y-axis. This effect is even more pronounced at larger tilting angles.

Figures 5.21 - 5.23 show the responses of the rotor velocities during the same experiment. As mentioned, the centroid variation effect on the vehicle attitude has to be compensated by adapting the rotor speed. In particular, rotors 1 and 3 shown in Figure 5.21 compensate the yaw angle disturbance. It is clear from these responses that a larger CoG shift results in a larger yaw angle disturbance, requiring stronger actuator response. Furthermore, the tilting angle

of the rotor additionally enhances this effect, namely the same CoG shift requires stronger compensation for yaw tracking with a larger tilt of the rotors.

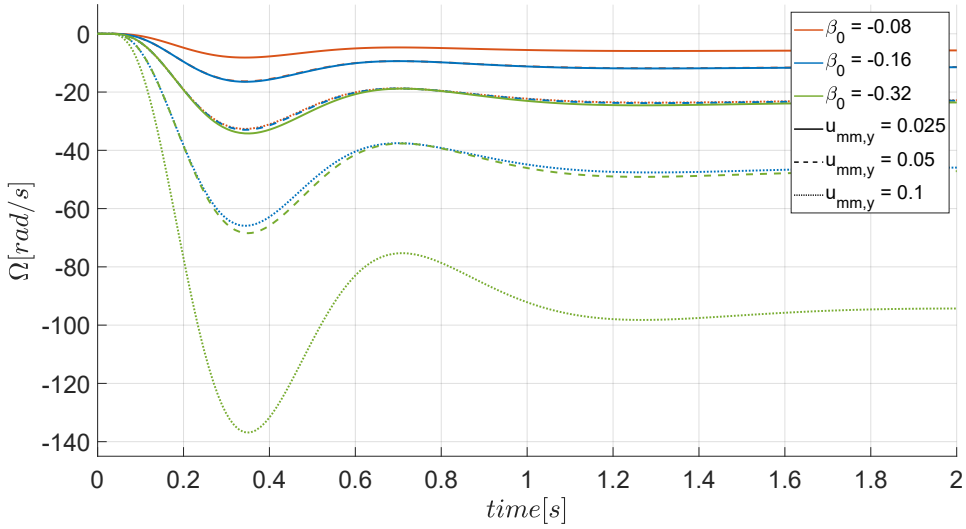

Figure 5.21: The figure shows the speed of rotor 1 and rotor 3. These two rotors have the same speed, as they are used to compensate for the disturbances caused by centroid variation in the yaw angle.

Figures 5.22 and 5.23 show the speed of rotors 2 and 4, which compensate the yaw and roll angle disturbances caused by centroid variation. The differences between the responses are due to different effect of CoG variation on the yaw and roll angles. In order to compensate for the roll disturbance, speeds of rotor 2 and rotor 4 must be adapted by the same amount in opposite directions assuming the vehicle is moving along the y axis.

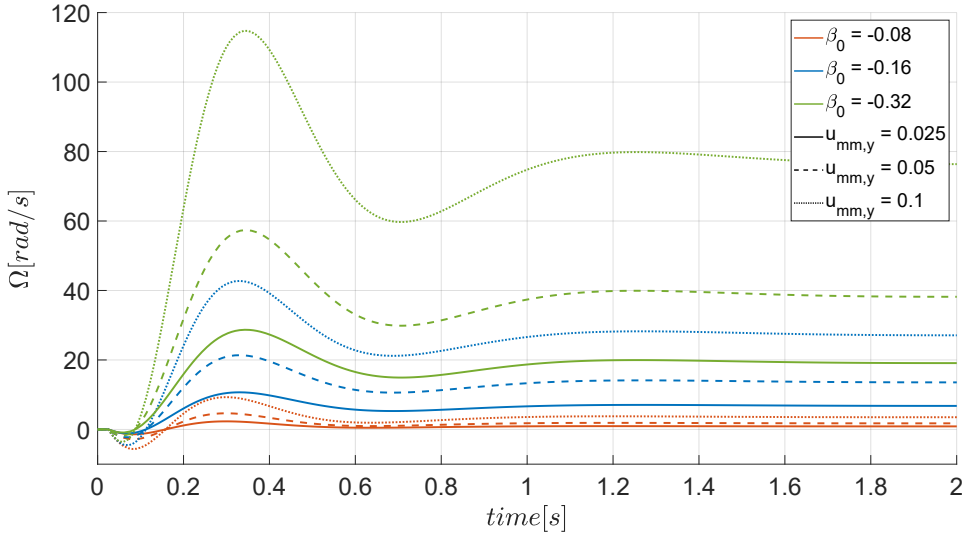

Figure 5.22: The figure shows the speed of rotor 2, which is varied to enable the vehicle to maintain the reference values of roll and yaw angles.

The analysis above shows that deploying VPC scheme is a reasonable design decision with the proposed system with three types of actuatrs. The centroid variation is chosen as the large valve due to it's slow response. A faster response of the CoG variation would involve large

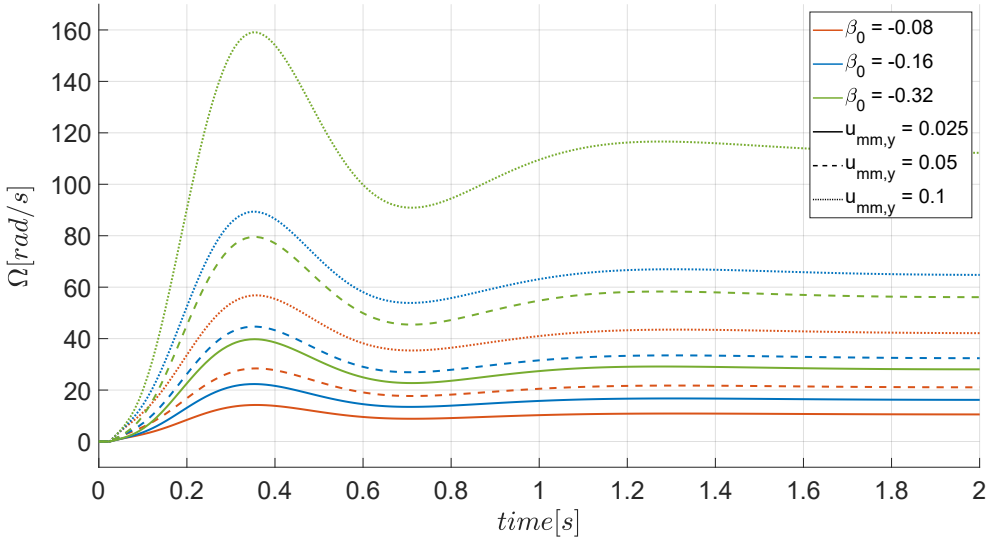

Figure 5.23: The figure shows the speed of rotor 4, which is varied to enable the vehicle to maintain the reference values of roll and yaw angles.

accelerations of the moving masses, which have been shown to introduce large disturbances into vehicle behavior. As the steady state response is desirable, this actuator system is tuned for slower control. The small valve, i.e. the faster actuator, for which it is desirable to always operate around the middle of its range, is the rotor thrust direction variation.

Finally, the VPC control is designed according to scheme shown in Figure 5.24. Building upon the rotor thrust direction variation control described in the previous chapter, we introduce the VPC framework by adding the centroid variation controller with a reference signal guiding the rotor thrust direction towards the operating point. We chose centroid variation controller as:

$$G_{R,mm,y} = -\frac{K_{mm,y}}{s}, \tag{5.69}$$

which is in fact an integration element, with a arbitrarily tuned gain. The vehicle behavior with this control scheme is shown in Figure 5.25, where two experiments are compared, one with rotor tilt position control (labeled TV), and the other with position control based on VPC (labeled TCV), justifying the control system design. In terms of position tracking, there appears to be no significant difference between these two methods. However, the difference becomes clear when considering the control variables. Especially for the rotor thrust direction variation, where the control variable $u_{\beta,y}$ returns to the middle of its range in the case of combined control using VPC method, while when using just the rotor thrust direction variation method, the rotors need to stay tilted away from the middle of their range to move the vehicle. The combined control has a larger impact on the roll angle, as seen in c). Lastly, the centroid variation control variable response is shown, the same for both control methods.

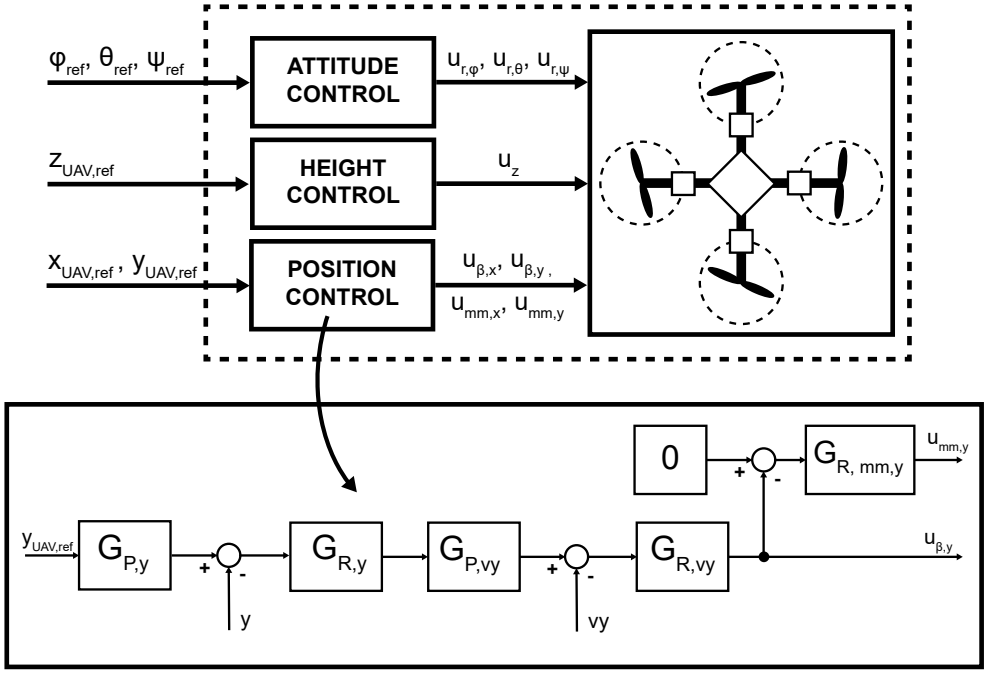

Figure 5.24: The figure shows a position control scheme for free flight tasks based on rotor thrust direction variation and centroid variation.

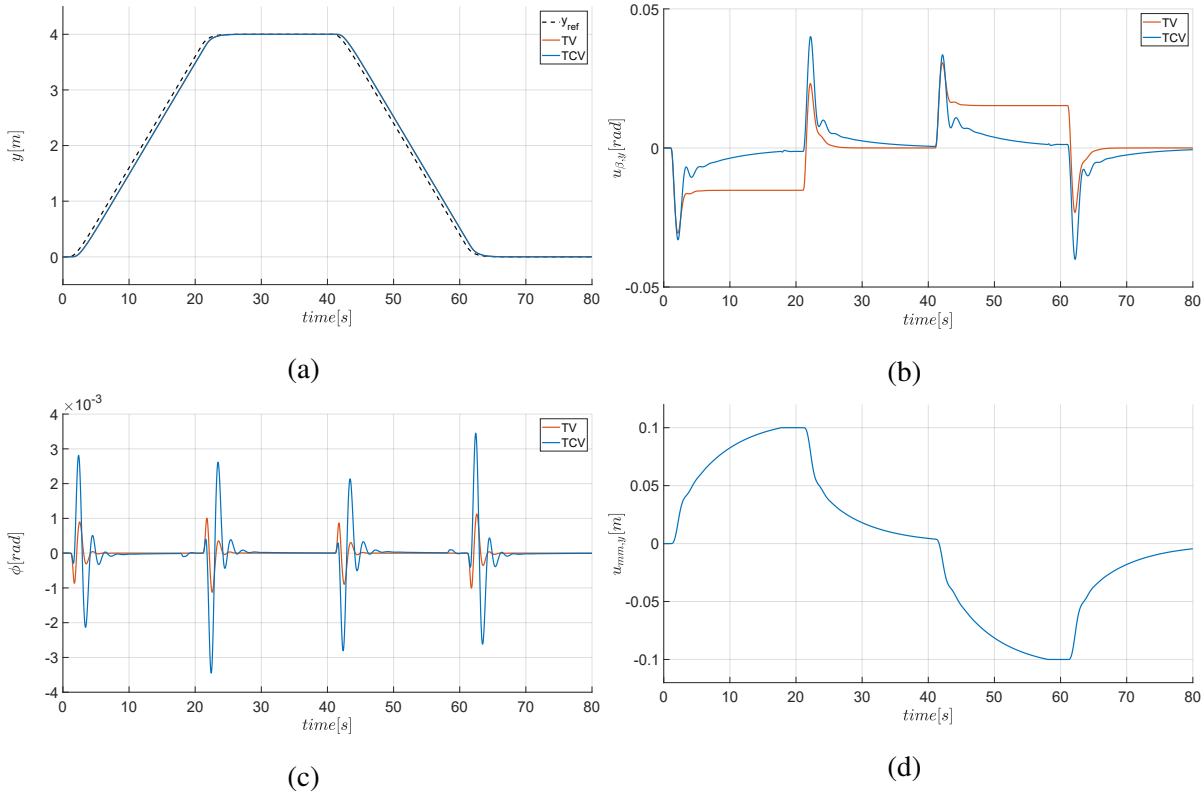

Figure 5.25: y-axis position control. The rotor thrust direction variation method is labeled TV, and VPC control is labeled TCV. a) position responses; b) rotor thrust direction control variable; c) roll response; d) centroid variation control variable.

CHAPTER 6

Adaptive impedance control system design

Traditionally, the industrial tasks considered as candidates for automation were those that required very precise positioning of the work tools, with fine repeatability. The force applied to the environment was not strictly considered, since the only requirement was to exert sufficient force to complete the task. One example are the drilling tasks, where the exact amount of force is irrelevant, as long as the hole is drilled precisely at the desired position. For this reason, the industrial robots, deployed instead of humans at such dull, difficult or dangerous industrial tasks, were designed primarily to repeat their task perfectly in terms of position control. With the development of technology and as a consequence of globalization, the robots are leaving the strictly industrial environments where they handled robust materials. Instead, they are deployed in more complex tasks in the unstructured everyday environments, where fragile object and sensitive materials are handled. In such tasks, the interaction with the environment has to be controlled both regarding robot position and contact force.

An opposite approach to the position control of robot manipulators is direct force control. While such robots can be programmed to follow the desired interaction force reference precisely, the problem arises during free space motion. Using the concepts of impedance control, the classical industrial manipulators, with a single low-level control interface, can be programmed to follow both position and force references, thus attaining compliant and safe behaviour. In this work, the focus is on one such control concept, namely adaptive position-based impedance control.

6.1Position-based impedance control

One common, widely recognized and practical method for compliant control of position based robots is the position-based impedance control. This concept allows simultaneous control of manipulator position and contact force, while only a single interface is available at low joint level control, such as joint position control. It should be noted that impedance control can be implemented in Cartesian space, when the aim is to control the end-effector interaction with the environment, but it can be implemented at joint level as well, when safety if the primary concern. The use case described in this work deals with the former application, namely Cartesian impedance.

The objective of the basic impedance controller is to establish a desired user-specified dynamic relationship between contact force and robot position, referred to as the *target impedance*. This work is built upon the structure of a basic position-based impedance control loop, shown in Fig. 6.1. The standard elements of the aerial manipulator control scheme, namely position and attitude controllers, are extended with an impedance filter. The impedance filter determines a position setpoint for the position controller, based on the desired contact force during the physical interaction. The inner loop represents the non-modified robot position controller. Since there is no direct force control interface for the robot, the outer loop uses force feedback signal by modifying the inputs to the position controller, at the same time satisfying the impedance filter dynamic equation. To model the robot-environment interaction, the environment is considered as an equivalent linear spring, with $n \times n$ constant diagonal stiffness K_e. This way, the measured contact force can be considered a result of a linear spring compression, or simply

$$\mathbf{F} = K_e(\mathbf{X} - \mathbf{X}_e), \tag{6.1}$$

where $\mathbf{F}$ is an $n \times 1$ vector that represents the measured force, $\mathbf{X}$ is an $n \times 1$ measured robot position vector, and $\mathbf{X}_e$ is the position vector of the environment, with dimensions $n \times 1$. The environment position $\mathbf{X}_e$ is considered constant in the unexcited state, namely in the state without contact. As the (measured) robot position $\mathbf{X}$ progresses into the environment, there is a displacement between the measured robot position and the unexcited environment position, i.e. the elasticity of the environment generates a force that acts on the robot.

The impedance filter defines the target impedance behaviour of the robot-environment interaction system. The filter is designed as a linear second-order system. This enables setting the dynamic relationship between the robot position and the force tracking error $\mathbf{E} = \mathbf{F}_r - \mathbf{F}$, so that it mimics a mass-spring-damper system. The $n \times 1$ force reference vector $\mathbf{F}_r$ can be freely chosen by the user. Throughout this work, the target impedance is defined as

$$\mathbf{E} = M(\ddot{\mathbf{X}}_c - \ddot{\mathbf{X}}_r) + B(\dot{\mathbf{X}}_c - \dot{\mathbf{X}}_r) + K(\mathbf{X}_c - \mathbf{X}_r), \tag{6.2}$$

where M, B and K are the $n \times n$ constant diagonal mass, damping and stiffness matrices of the target impedance, respectively. These matrices are arbitrarily specified by user, setting the system behaviour to the desired target impedance. Signals $\mathbf{X}_c$ and $\mathbf{X}_r$ are vectors in Cartesian space, and represent the commanded and reference position of the robot, respectively. The commanded position is the one used as input to the robot inner loop position controller, usually through an inverse kinematics or Jacobian in the form of joint position. The reference position, on the other hand, is the user defined desired cartesian position of the robot.

During free-space motion, while there is no force tracking error $\mathbf{E} = \mathbf{0}$, the commanded position $\mathbf{X}_c$ tracks the reference position $\mathbf{X}_r$ accurately, with the dynamics specified with Equation (6.2). As the end-effector comes into contact with the environment, the contact force $\mathbf{F}$ is measured by the force sensor. This results in a modified robot position command $\mathbf{X}_c$, since at that point, the dynamics of the target impedance cannot allow precise tracking of referenced position $\mathbf{X}_r$, without resulting in force tracking error signal $\mathbf{E}$. In other words, the impedance filter balances the position and force tracking error, depending on the filter parameters. A more detailed position-based impedance control analysis can be found in [82].

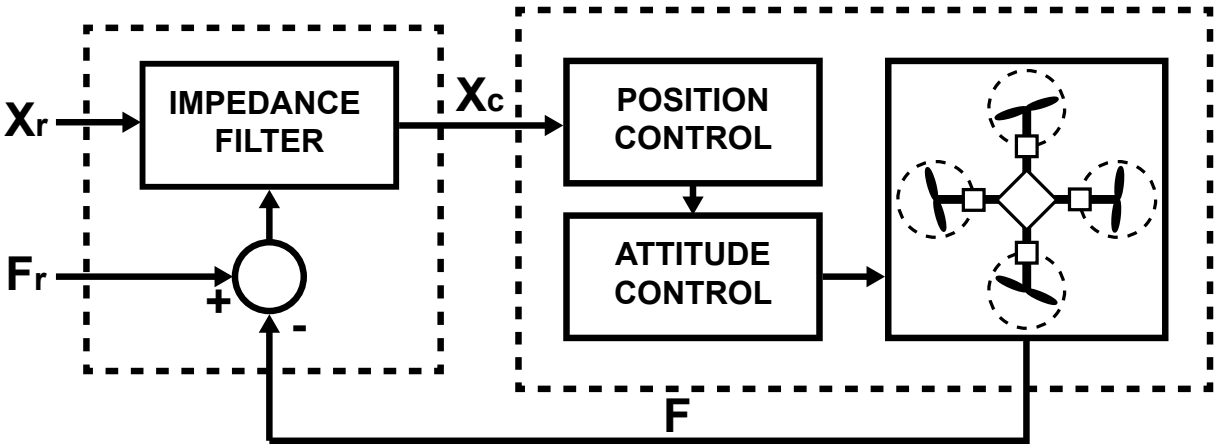

Figure 6.1: Position-based impedance control scheme. The impedance filter output is reference for the UAV position controller, hence position-based impedance control.

Consider the practical case, in which the environment stiffness K_e is unknown, and the exact position of the environment $\mathbf{X}_e$ is inaccurate. While in contact with the environment, these uncertainties can considerably degrade the performance of the system. To analyze this behavior, we start from the linear spring model of the environment, with stiffness K_e. For simplicity, we consider a case where force is applied along one axis only, with equivalent stiffness k_e. As already stated in Eq. (6.1), the measured force can be considered a result of spring compression, namely $f(t) = k_e(x(t) - x_e(t))$. Let us expand the force error $e(t)$ as

$$e(t) = f_r(t) - f(t) = f_r(t) - k_e(x(t) - x_e(t)). \tag{6.3}$$

From the force tracking error equation (6.3), the position of the aerial manipulator can be ex-

pressed as:

$$x(t) = \frac{f_r(t) - e(t)}{k_e} + x_e(t). \tag{6.4}$$

Assuming further that the force reference $f_r(t)$ is constant, $f_r(t) = F_r$, the time derivatives of Eq. (6.4) yield:

$$\dot{x}(t) = \frac{\dot{e}(t)}{k_e} + \dot{x}_e(t) \tag{6.5}$$

$$\ddot{x}(t) = \frac{\ddot{e}(t)}{k_e} + \ddot{x}_e(t) \tag{6.6}$$

Assuming that the aerial manipulator tracks the position reference with negligible dynamics, $x(t) \approx x_c(t)$, the force tracking error dynamics can be derived from the Equation (6.4), Equation (6.5), Equation (6.6) and the target impedance Equation (6.2):

$$\begin{aligned} m\ddot{e}(t) + b\dot{e}(t) + (k+k_e)e(t) =& m(\ddot{x}_e(t) - \ddot{x}_r(t)) \\ &+ b(\dot{x}_e(t) - \dot{x}_r(t)) \\ &+ k(F_r + k_e x_e(t) - k_e x_r(t)). \end{aligned} \tag{6.7}$$

Here, the target impedance behaviour is also defined along one axis only, with mass, damping and stiffness parameters m, b, and k respectively. The Equation 6.7 shows that it is possible to control the force error trajectory through the input signal x_r. The steady-state force error e_{ss} can then be obtained by applying the final value theorem to the Laplace transform of Equation (6.7):

$$e_{ss} = \frac{k}{k+k_e}[(F_r + k_e x_e) - k_e x_r]. \tag{6.8}$$

The steady-state force error will be zero, if the following condition on the reference position trajectory is satisfied:

$$x_r = \frac{F_r}{k_e} + x_e. \tag{6.9}$$

In other words, if the precise environment position x_e is known, as well as the value of the environment equivalent stiffness k_e, a reference position trajectory x_r can be generated, that will result in robot-environment interaction in which exactly the desired contact force is exerted. However, the environmental parameters are in practice never known precisely, and even small errors in the environment parameters k_e and x_e can result in large force errors. One possible solution to this issue is the estimation of these parameters. As we show in the following chapter, the estimation of these parameters can be used in adaptation of the impedance filter inputs, resulting in desired robot behaviour and precise position and contact force tracking, even with environment position and stiffness unknown a-priori.

6.2Adaptive impedance control

The method we propose here is developed for deployment in robot-environment interaction tasks in which the working environment is not completely known. In particular, we assume a robot manipulation setup in which the environment stiffness is unknown, but the position of the environment can be obtained through other remote sensing setup, such as visual or radar/lidar based sensing. Idea for this method starts with Equation (6.9). If the environment position is well known, the only parameter that needs to be adapted is environment stiffness in order to force steady-state force error to zero. This method can easily be implemented and deployed along with the existing position-based impedance control, as shown in Figure 6.2.

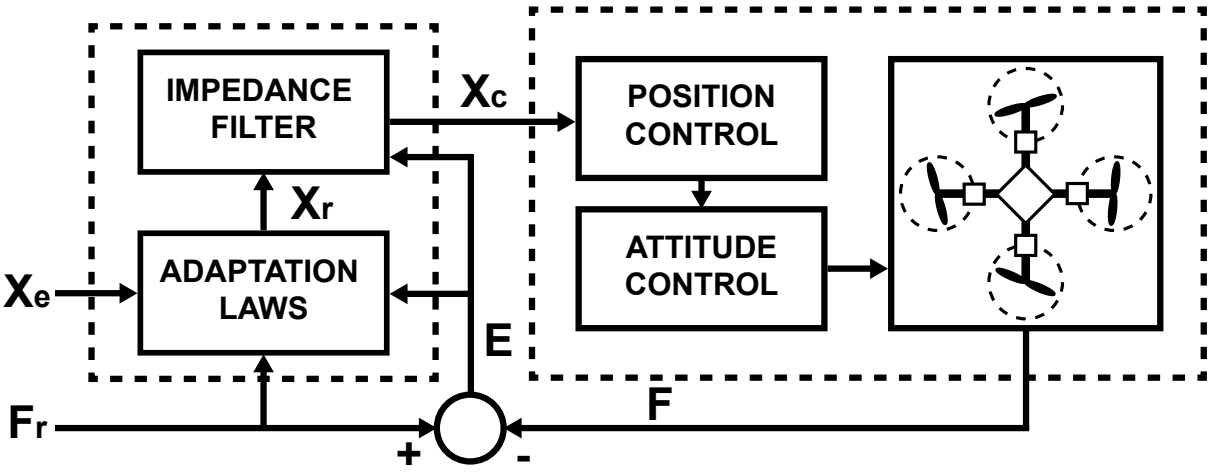

Figure 6.2: Adaptive impedance control scheme.

The adaptive impedance algorithm consist of two parts. First part is impedance filter which is described in Section 6.1. Second part is adaptation algorithm which takes into account environment position, interaction force and desired force and calculates reference position for the impedance filter. Reference position is calculated based on adaptation of the environment stiffness.

6.2.1Derivation of the Adaptation Laws

The derivation of the adaptation laws requires an assumption that the variation of the system parameters is slower than the speed of adaptation. If this assumption is not satisfied, the adaptive gains will not converge. Therefore, we use proportional-plus-integral adaptation laws derived using an improved Lyapunov-based adaptation method for decentralized systems. These laws,

in comparison to the conventional integral laws, have better transient response, improved convergence and increased flexibility [83].

The adaptation law is derived starting from Equation (6.9). An adaptive parameter $\kappa(t)$ is introduced, that can account for elastic properties of environment under external force, by adapting the position reference with respect to initial position of the environment and force reference:

$$x_r(t) = \kappa(t)F_r + x_e(t), \tag{6.10}$$

where $x_r(t)$ is reference position (input to the impedance filter) and $x_e(t)$ is a environment position. Assuming that force reference F_r is constant, the time derivatives of Equation (6.10) are:

$$\dot{x}_r(t) = \dot{\kappa}(t)F_r + \dot{x}_e(t), \tag{6.11}$$

$$\ddot{x}_r(t) = \ddot{\kappa}(t)F_r + \ddot{x}_e(t). \tag{6.12}$$

We first assume that the environment position $x_e(t)$ is precisely known and that only environment stiffness needs to be adapted. This can be ensured e.g. by an auxiliary sensory system based on visual or other non-contact technology. To derive the adaptation laws for $\kappa(t)$, we first substitute $x_r(t)$, $\dot{x}_r(t)$ and $\ddot{x}_r(t)$ in the equation of the force error dynamics (6.7) with (6.10), (6.11) and (6.12). From here, we derive the equation for the complete adjustable system:

$$\ddot{e}(t) + a_1(t)\dot{e}(t) + a_2(t)e(t) = \phi_1(t), \tag{6.13}$$

where

$$\begin{aligned} a_1(t) &= \frac{b}{m}, \\ a_2(t) &= \frac{k + k_e}{m}, \\ \phi_1(t) &= F_r \left[\frac{k(1 - k_e\kappa(t)) - bk_e\dot{\kappa}(t)}{m} - k_e\ddot{\kappa}(t) \right]. \end{aligned} \tag{6.14}$$

Writing $\mathbf{e} = [e(t), \dot{e}(t)]^\top$, the state-space representation of Equation (6.13) can be expressed as

$$\dot{\mathbf{e}} = \begin{bmatrix} 0 & 1 \\ -a_2(t) & -a_1(t) \end{bmatrix} \mathbf{e} + \begin{bmatrix} 0 \\ \phi_1(t) \end{bmatrix}. \tag{6.15}$$

To proceed with Lyapunov equation we have to ensure that system error is stable. to that end we use Routh–Hurwitz criterion. We can write characteristic equation of the system given with

Equation (6.15) as:

$$P(s) = s^2 + a_1 s + a_2. \tag{6.16}$$

The system force error is stable by Hurwitz if and only if both coefficients satisfy $a_i > 0$. By substituting Equation (6.14) into that condition we obtain:

$$\begin{aligned} \frac{b}{m} &> 0, \\ \frac{k + ke}{m} &> 0. \end{aligned} \tag{6.17}$$

If we choose such m, b and k that this conditions are satisfied, we can ensure stability of the system force error. To write system error dynamics, Equation (6.15), in more adequate form for the Lyapunov function candidate, we can rewrite Equation (6.15) as:

$$\dot{\mathbf{e}} = D\mathbf{e} + \mathbf{h}, \tag{6.18}$$

where

$$D = \begin{bmatrix} 0 & 1 \\ -a_2(t) & -a_1(t) \end{bmatrix}, \tag{6.19}$$

$$\mathbf{h}(t) = \begin{bmatrix} 0 \\ \phi_1(t) \end{bmatrix}. \tag{6.20}$$

Since error dynamic is stable, Equation (6.13), for all $Q = Q^\top \in \mathbb{R}^{2x2}$ there exists a unique positive-definite matrix $P = P^\top \in \mathbb{R}^{2x2}$ satisfying the Lyapunov equation

$$D^\top P + PD = -Q. \tag{6.21}$$

Choosing Q as

$$Q = \begin{bmatrix} 2q_1 & 0 \\ 0 & 2q_2 \end{bmatrix}, \tag{6.22}$$

where q_1 and q_2 are positive scalars. From Equation (6.21), we can derive the solution for P:

$$P = \begin{bmatrix} p_1 & p_2 \\ p_2 & p_3 \end{bmatrix} = \begin{bmatrix} \frac{1}{a_1}(q_1(1 + \frac{a_1^2}{a_2}) + a_2 q_2) & \frac{q_1}{a_2} \\ \frac{q_1}{a_2} & \frac{1}{a_1}(\frac{q_1}{a_2} + q_2) \end{bmatrix}. \tag{6.23}$$

Elements of matrix P must be chosen as $p_1, p_2, p_3 > 0$ and $p_2 < p_3 \frac{b}{m}$ for the matrices Q and P to be positive-definite.

The adaptation law determines the dynamics of the adaptation parameter $\kappa(t)$ and defines the dynamics of the contact force error. Formally, the adaptation law should enforce $\phi_1(t) \to \phi_1^*$ such that $e(t) \to 0$ and $\kappa(t) \to 1/k_e$. To derive the adaptation laws, we can define the following positive-definite scalar Lyapunov function candidate:

$$V(\mathbf{e}, \Phi) = \mathbf{e}^\top P \mathbf{e} + (\Phi - \Phi^*)^\top \Gamma^{-1} (\Phi - \Phi^*), \tag{6.24}$$

where $\Gamma = [\gamma_1]$, γ_1 is positive constants, $\Phi = [\phi_1(t)]$ is parameter vector, P is matrix that satisfies the Lyapunov equation (6.21) and $\Phi^* = [\phi_1^*(t)]$. The time derivative of (6.24) is given with

$$\begin{aligned} \dot{V}(\mathbf{e}, \Phi) = &- \mathbf{e}^\top Q \mathbf{e} + 2\mathbf{e}^\top P \mathbf{h}(t) \\ &+ (\dot{\Phi} - \dot{\Phi}^*)^\top \Gamma^{-1} (\Phi - \Phi^*) \\ &+ (\Phi - \Phi^*)^\top \Gamma^{-1} (\dot{\Phi} - \dot{\Phi}^*). \end{aligned} \tag{6.25}$$

Further simplifying the equations, the time derivative of V can be written as

$$\begin{aligned} \dot{V}(\mathbf{e}, \Phi) = &- \mathbf{e}^\top Q \mathbf{e} \\ &+ \frac{2}{\gamma_1} \phi_1(t)(\dot{\phi}_1(t) - \dot{\phi}_1^*(t)) + 2q(t)\phi_1(t) \\ &- \frac{2}{\gamma_1} \phi_1^*(t)(\dot{\phi}_1(t) - \dot{\phi}_1^*(t)), \end{aligned} \tag{6.26}$$

where $q(t) = p_2 e(t) + p_3 \dot{e}(t)$. To ensure asymptotic stability, the time derivative of V must be a negative-definite function. In that case, we set

$$\begin{aligned} \frac{2}{\gamma_1} \phi_1(t)(\dot{\phi}_1(t) - \dot{\phi}_1^*(t)) - 2q(t)\phi_1(t) = 0 \\ \Rightarrow \dot{\phi}_1(t) - \dot{\phi}_1^*(t) = -\gamma_1 q(t). \end{aligned} \tag{6.27}$$

The Equation (6.25) is reduced to

$$\dot{V}(\mathbf{e}, \Phi) = -\mathbf{e}^\top Q \mathbf{e} + 2\phi_1^*(t) q(t). \tag{6.28}$$

Now, let us choose $\phi_1^*(t)$ as follows:

$$\phi_1^*(t) = -\gamma_1^* q(t), \tag{6.29}$$

where γ_1^* is zero or positive constant. Hence, Equation (6.25) reduces to

$$\dot{V}(\mathbf{e},\Phi) = -\mathbf{e}^\top Q\mathbf{e} - 2\gamma_1^* q(t)^2, \tag{6.30}$$

which is a negative-definite function of $\mathbf{e}$. According to the Lyapunov stability theorem, the expression Equation (6.30) guarantees the global stability and the global tracking convergence of the system using the control law (6.10). From equalization of (6.27) and (6.29), the adaptation law for Φ can be obtained

$$\dot{\Phi} = \left[-\gamma_1 q(t) - \gamma_1^* \dot{q}(t) \right]. \tag{6.31}$$

The adaptive gains κ defined in the control law (6.10) can be derived from (6.31) and (6.14):

$$\dot{\Phi} = \left[\dot{\phi}_1 \right] = \left[-F_r\left(\frac{kk_e\dot{\kappa}(t) + bk_e\ddot{\kappa}(t)}{m} + k_e\dddot{\kappa}(t)\right) \right]. \tag{6.32}$$

The adaptation law is finally obtained by taking the Equation (6.31), and substituting $\dot{\phi}(t)$ with Equation (6.32):

$$\begin{aligned} k\dot{\kappa}(t) + b\ddot{\kappa}(t) + m\dddot{\kappa}(t) &= \gamma_1 q(t) + \gamma_1^* \dot{q}(t), \\ q(t) &= p_2 e(t) + p_3 \dot{e}(t). \end{aligned} \tag{6.33}$$

6.3Position reference distribution

Adaptive impedance controller outputs a position reference for the robotic manipulator, with which it should be better able to achieve the referenced contact force. As the global position of the end-effector can be controlled by two actuation systems: the UAV's global position control and the manipulator's joint position control, the position reference can be achieved controlling either of these, or both simultaneously. As there is an evident coupling between the motion of the body and the manipulator arm, we introduce a parameter, $\nu \in [0,1]$, to distribute the end-effector motion commands between the two systems. The following distribution relationship is defined:

$$\begin{aligned} \Delta\mathbf{P}_{UAV} &= \nu \cdot \Delta\mathbf{P}, \\ \Delta\mathbf{P}_{arm} &= (1-\nu) \cdot \Delta\mathbf{P}. \end{aligned} \tag{6.34}$$

Here, $\Delta\mathbf{P}_{UAV}$ denotes the displacement of the UAV and $\Delta\mathbf{P}_{arm}$ denotes the displacement of the manipulator arm, both expressed in the coordinate system L_0. The equation that presents the aerial manipulator displacement, $\Delta\mathbf{P}$, is as follows:

$$\begin{aligned} \Delta\mathbf{P} &= \Delta\mathbf{P}_{UAV} + \Delta\mathbf{P}_{arm} \\ &= \nu \cdot \Delta\mathbf{P} + (1-\nu) \cdot \Delta\mathbf{P}. \end{aligned} \tag{6.35}$$

With $\nu = 1$, the UAV's motion is used to control the position of the end-effector, while with $\nu = 0$, the manipulator's motion is used. For values of ν between 0 and 1, the end-effector's motion is a combination of both the UAV body and the manipulator arm motion.

CHAPTER 7

Experimental results

In this chapter, we analyse and evaluate the results of this thesis on experimental platforms. First, the developed generalized model of a UAV is evaluated on an experimental platform against a linearized simulation model. Then, the proposed adaptive impedance control scheme is tested on robotic testbeds. Finally, we present the experimental results of robotic interaction with the environment based on the developed adaptive impedance control scheme and the generalized UAV model.

7.1Experimental validation of generalized model

The practical relevance and precision of the developed generalized model was tested in a set of experiments by comparing the behavior of a real vehicle with a linearized simulation model, as described in the section below.

7.1.1 *Toucan* Description

The concept of a multirotor vehicle with tilting propellers provides numerous advantages, such as enabling slanted hovering and horizontal flight configurations. *Toucan*, initially developed as a plus configuration quadrotor, implements tilting propellers. Its design closely follows the method described in Section 4, only without moving masses. The vehicle is fitted with a Pixhawk 2.1 autopilot with Ardupilot firmware, which is utilized for low-level attitude and tilt servo control. Additionally, to enhance processing power, the Toucan is equipped with an Intel NUC i7-8650U onboard computer that runs Ubuntu Linux 16.04 with ROS Melodic. A fixed configuration robotic arm is attached to the bottom of the body frame, with a mounted force-sensor on the end-effector. Due to a 6-DOF nature of the vehicle with tilting propellers, it is

permissible for the manipulator to be in a fixed configuration.

The control scheme used for performing the experiments is presented in Figure 5.24. The presented controller accepts both orientation and position commands. Orientation control is performed using a low-level attitude controller in the *Arducopter* firmware. Position commands are achieved by issuing PPM commands to the servo motors that adjust the propeller tilt. This is done using a cascading PID controller implemented on the on-board computer. All the experiments are performed with the same controllers, tuned by the parameters obtained by simulating the generalised model of the *Toucan* vehicle. The linearized model for this vehicle is given with Equation (4.24) for attitude and linearized translational dynamics is given with Equation (4.25). Vehicle parameters for this model are given in Table 7.1.

Table 7.1: Model parameters of the *Toucan* aerial manipulator.

Symbol	Value	Unit	Description
$I^c_{s,xx}$	0.149	kgm^2	Vehicle's moment of inertia in x axis
$I^c_{s,yy}$	0.149	kgm^2	Vehicle's moment of inertia in y axis
$I^c_{s,zz}$	0.206	kgm^2	Vehicle's moment of inertia in z axis
m	0	kg	Mass of the moving mass
M	$3,95$	kg	Vehicle overall mass
b_f	$6.9146e-05$	kgm	Rotor thrust constant
b_m	0.016	-	Moment constant of a brushless DC motor
g	9.81	m/s^2	Gravitational acceleration
z_m	0	m	Displacement of the moving masses in z axis
z_r	0.09	m	Distance between propeller and a vehicle's origin in z axis
L	0.333	m	Length of a vehicle's arm
ω_r	105.41	rad/s	Natural frequency of the rotor
ζ_r	1.74	rad/s	Damping factor of the rotor
ω_{tr}	44.91	rad/s	Natural frequency of the tilting servo motor
ζ_{tr}	0.89	rad/s	Damping factor of the tilting servo motor
β_{max}	0.32	rad	Maximum value of the β angle

7.1.2Model Validation Results

The objective of this subsection is to evaluate and validate the linearized model given with Equation 4.24 and Equation 4.25, which is specifically developed for the *Toucan* aerial vehicle with tilting propellers. The addition of tilting propellers makes the vehicle fully actuated. The

validation is conducted in two stages: first, using only position reference values, and second, using both position and orientation reference values. The system is simulated using Matlab, while real-world experiments are conducted in a laboratory environment with the aid of the Optitrack motion capture system. We present comparative results in two sets, each with different reference values. The first set involves changes in position reference values along the y-axis, while keeping the orientation neutral. The second set involves changes in both position along the y-axis and the roll angle.

Figures 7.1 - 7.4 depict the comparative results between the simulation and laboratory experiment for the first experiment set. It can be seen that trends and dynamics of the system behavior are strongly correlated between the linearized generalized model simulated in Matlab and the experimental vehicle *Toucan*. Matching dynamics are detected on position and orientation responses for both of the result sets. Naturally, the measured rotor velocities, shown in Fig. 7.3 produce significantly more noise during the experimental validation, but the trends can clearly be observed regardless. Figure 7.5 shows the *Toucan* vehicle performing the first experiment set demonstrating horizontal flight while keeping the attitude neutral.

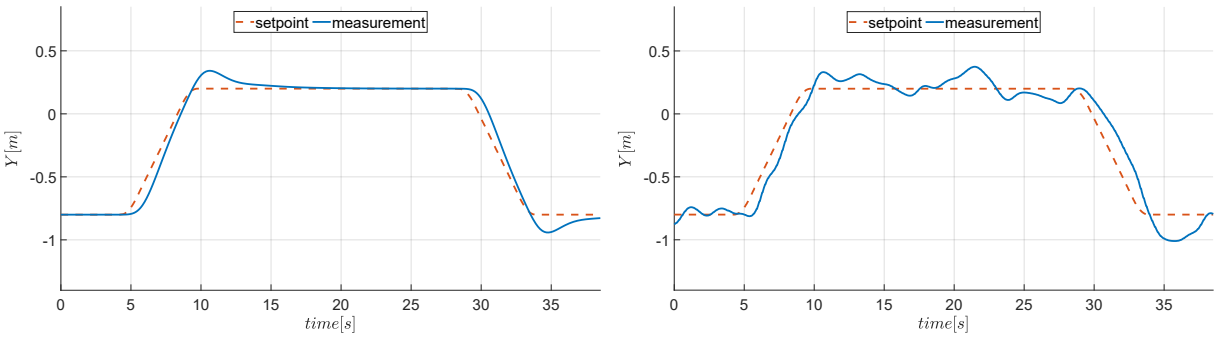

(a) (b)

Figure 7.1: These figures show the measured and referent position along the y-axis in the simulation (a) and in the real world experiment (b). The referent attitude is kept at the hover state.

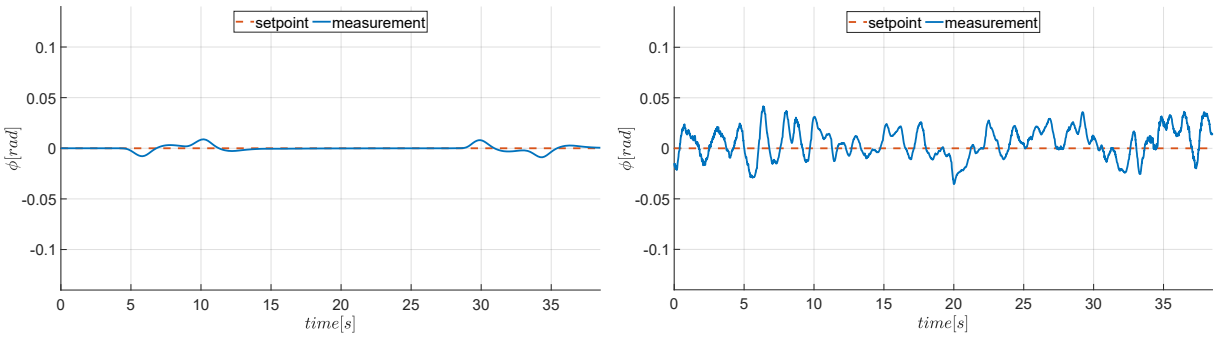

(a) (b)

Figure 7.2: These figures show the measured and referent roll angles in the simulation (a) and in the real world experiment (b). The referent roll value is kept neutral during horizontal flight.

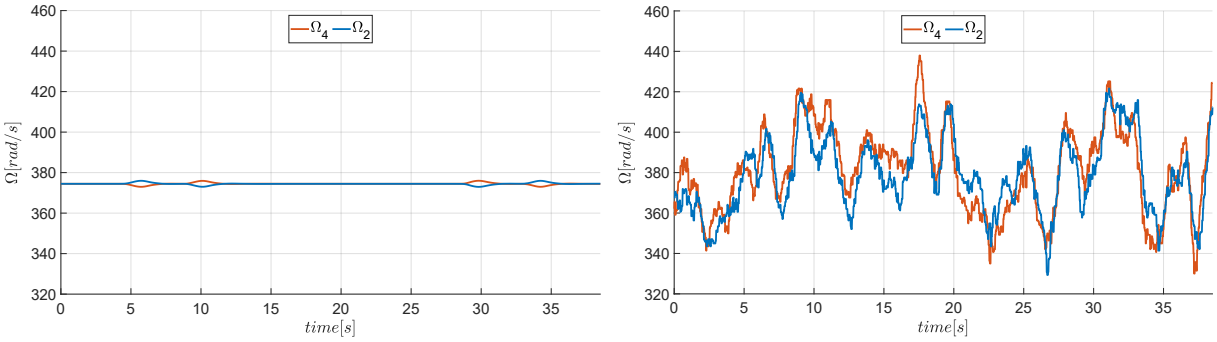

(a) (b)

Figure 7.3: These figures show the rotor velocities in the simulation (a) and in the real world experiment (b). Only the rotors that affect the roll angle are shown. The produced control inputs are the result of referent position value changes along the y-axis and neutral orientation.

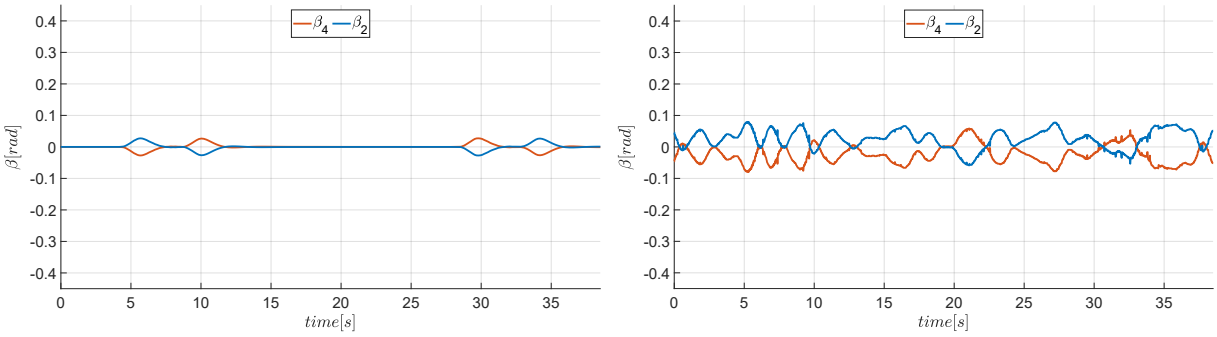

(a) (b)

Figure 7.4: These figures show propeller tilt angles in the simulation (a) and the real world experiment (b). The generated control inputs are the result of changes in the referent position along the y-axis and the neutral orientation.

Results from the second experiment set are shown on Figures 7.6 - 7.9. We show the comparative results between the simulation and laboratory experiment. The graphs clearly show a strong correlation between the simulated system and the experimental vehicle. The trends can again be clearly observed, especially when reference for roll value is increased. It can be seen that the rotor tilt angles work very hard to achieve continuous horizontal flight, while the rotor velocities are responsible for meeting the attitude demands.

The results show that the generalised modelling methodology is applicable to complex aerial systems such as the *Toucan* vehicle. In addition, the system successfully achieves slanted hover and neutral attitude horizontal flight configurations, which have useful applications when it comes to aerial manipulator operations.

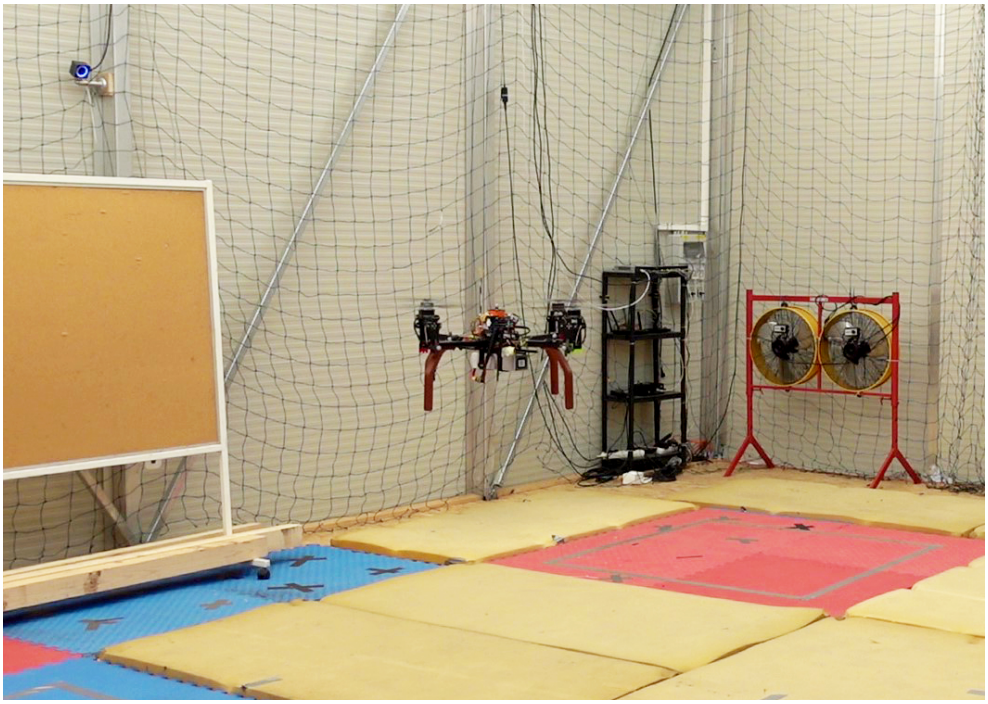

Figure 7.5: The figure shows the *Toucan* vehicle performing the first experiment set demonstrating horizontal flight while keeping the attitude neutral.

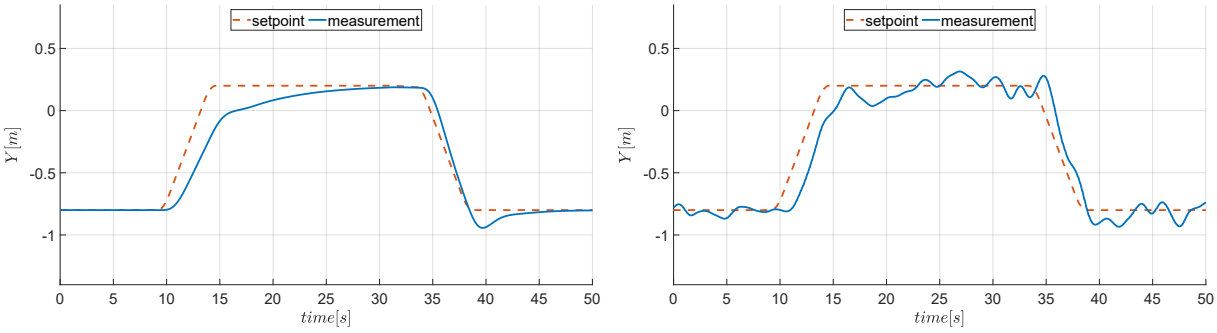

(a) (b)

Figure 7.6: These figures show the measured and referent position along the y-axis in the simulation (a) and in the real world experiment (b). The referent attitude is increased to 8 degrees of roll.

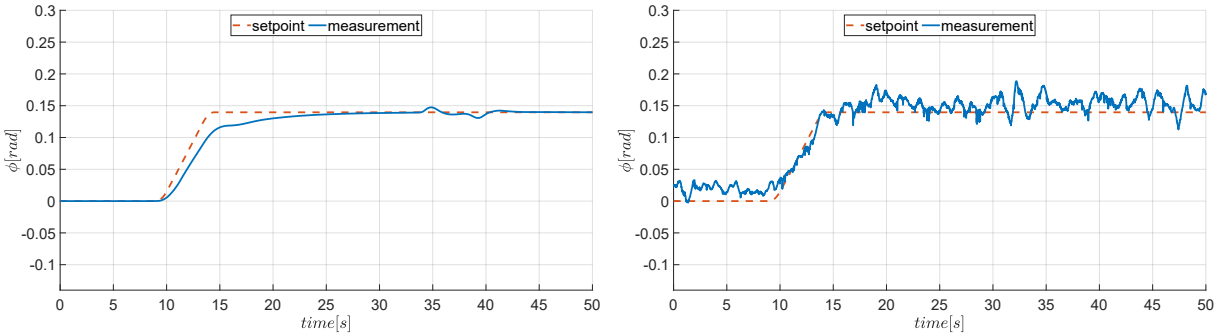

(a) (b)

Figure 7.7: These figures show the measured and referent roll angles in the simulation (a) and in the real world experiment (b). The referent value is steadily increased to 8 degrees simultaneously with the change in referent position.

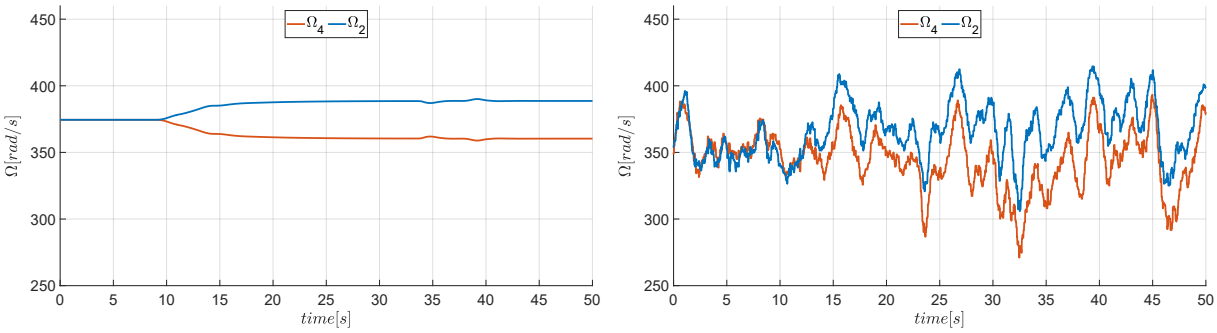

(a) (b)

Figure 7.8: These figures show the rotor velocities in the simulation (a) and in the real world experiment (b). Only the rotors that affect the roll angle are shown. The produced control inputs are the result of referent position value changes along the y-axis and an increase to 8 degrees of roll.

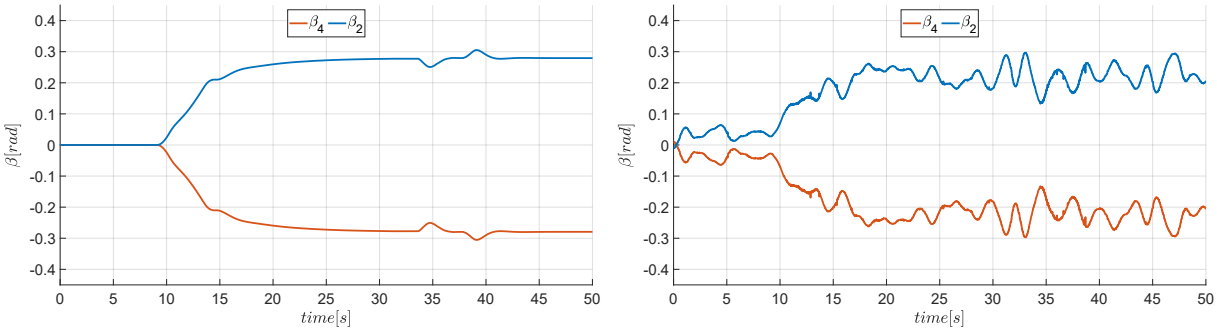

(a) (b)

Figure 7.9: These figures show propeller tilt angles in the simulation (a) and the real world experiment (b). The generated control inputs are the result of changes in the referent position along the y-axis and an increase in referent roll value of 8 degrees.

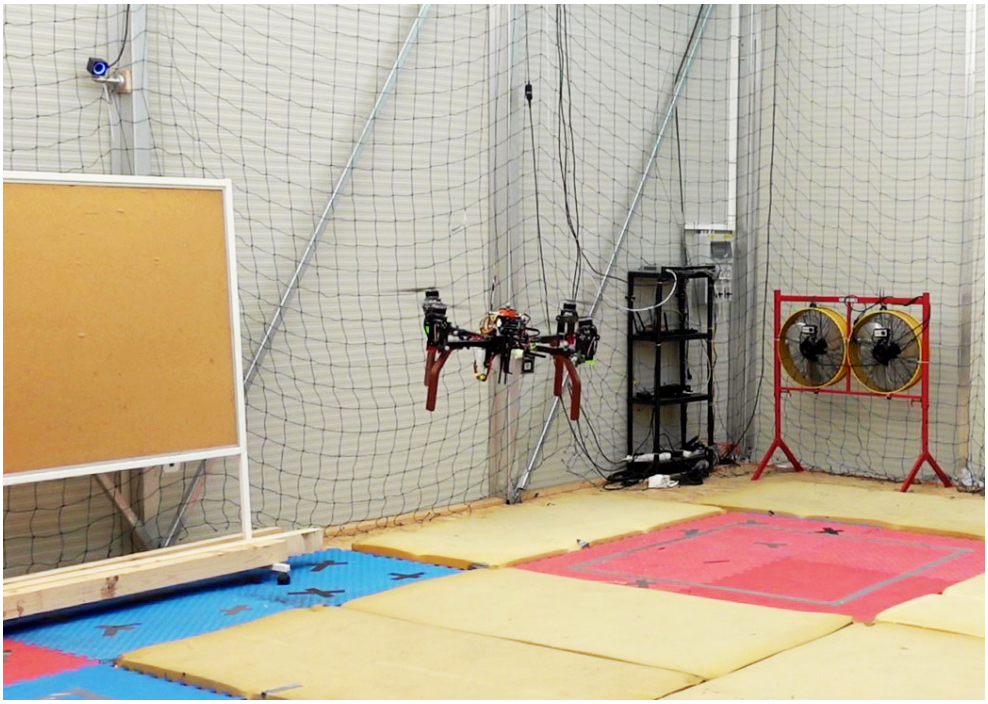

Figure 7.10: The figure shows the *Toucan* vehicle performing the second experiment set demonstrating horizontal flight while keeping the attitude tilted by 8 degrees of roll.

7.2Robotic interaction with the environment

To demonstrate the proposed control algorithm for stable interaction with environment, presented in Chapter 6, we conducted several experiments on the simulated and the real physical platforms utilizing the Robot Operating System (ROS) environment. In this section, the simulation results using the realistic Gazebo simulator, and the results of the real-world experiments using different robotic platforms are presented. We conducted two set of experiments for two approach types, namely vertical and horizontal approach.

7.2.1Vertical approach

In vertical approach experiments, the robots are referenced with position and force references along the global z axis, aligned with gravity. Three kinds of experiments were conducted, first in simulation using classical impedance control. Then, using an experimental UAV in a fastening a bolt task, again using classical impedance control. Finally, the adaptive impedance approach developed within this thesis is tested on a robot manipulator platform in soil moisture measurement task using IoT capacitive sensor as the robot tool.

Simulation results of classical impedance control

Here we show results on classic position based impedance control approach utilized in simulated peg-in-hole task. We created a realistic simulation environment in Gazebo simulator within ROS. We model the UAV as a single rigid body with rotating joints attached to ends of its arms. We put propellers on rotating joints and use open source plugin from *rotors_simulator* [84] package to simulate rotor dynamics. We equip the UAV with realistic sensors from *hector_gazebo* [85] to measure and control vehicle's attitude and pose. The UAV interacts with the environment with a dual arm manipulator attached on the UAV model. Each arm is attached to a landing gear, so that both arms oppose each other. Both arms consist of three links and joints, where each joint position is controlled using standard PID controller. During the experiments, the end effector of the dual arm manipulator is set to a fixed position holding a screw.

Linearized mathematical model of this aerial manipulator can be described using Equations (4.24) and (4.25). As the attached manipulator does not move during the experiments, we can say that there is no influence of the CoG shift on the vehicle, and the control variables for centroid variations can therefore be written as $u_{mm,x}(s) = u_{mm,y}(s) = 0$. As there are no tilting rotors on the vehicle, the control variables for rotor tilt can be written as $u_{\beta,x}(s) = u_{\beta,y}(s) = 0$. Vehicle translational movement is controlled using standard rotor thrust magnitude variation, by tilting the vehicle's body.

A stand with a force sensor is placed in the Gazebo environment alongside with the UAV, as

shown in Figure 7.11. The force sensor measures the force that the screw applies to the stand surface plate. All control algorithms, namely impedance control, position, and attitude control are implemented within ROS environment. Position and attitude control are implemented in the standard cascade control form with PID controller.

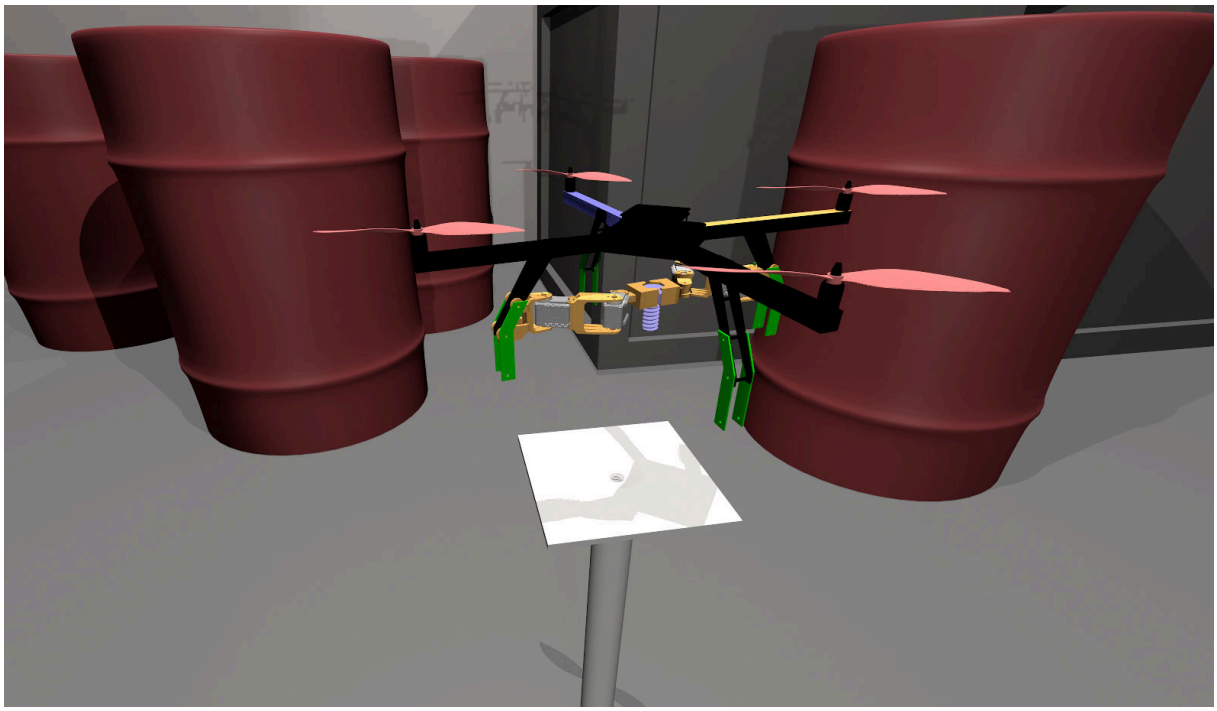

Figure 7.11: Image shows a mockup environment where a UAV equipped with a multi degree of freedom dual arm manipulator inserts a peg (screw) in hole (stand with the designated insertion hole). The proposed system can be applied to various scenarios including, but not limited to maintenance, inspection or repair missions.

We conducted an experiment where the UAV's end effector is set to apply a force to the surface plane on the stand along the z-axis of the Cartesian coordinate system only. The UAV hold the screw with the dual arm manipulator and pushes the screw toward the stand. First, the end effector position is set to the position close to the $\mathbf{X}_e$, and then, the force reference of $2N$ is given. In the second experiment, we give sequence of force reference. The environment parameters are constant but unknown.

The first experiment consisted of first bringing the UAV to the position in which the end effector is close to the environment position z_e, then, applying force reference of $2N$ along z-axis. Parameters used for the target impedance model are set as: $m = 1$, $b = 2\sqrt{10}$ and $k = 10$. The experiment results are shown on Figure 7.12. Measured force data shows slow force tracking performance with RMS error of $0.2895N$, settling time $t_{1\%} = 26.03s$ and no overshoot. In second experiment, the force reference was changed every 6 seconds as shown on Figure 7.13. One can notice that using classic impedance control approach results with steady-state error. This is due to the inaccurate environmental parameters, stiffness k_e and location z_e, which can not be compensated without adaptive control. Complete simulation experimental

results on this peg-in-hole task can be found in [86].

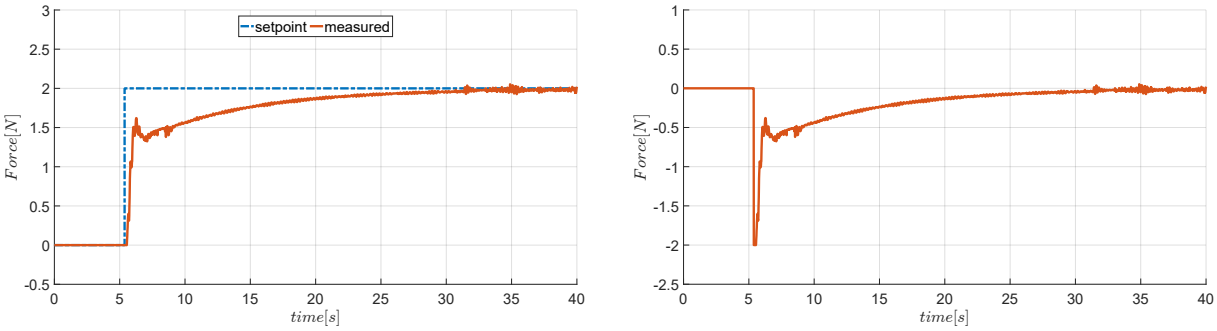

(a) (b)

Figure 7.12: The results of impedance control. a) shows the force step response and b) shows the force tracking error.

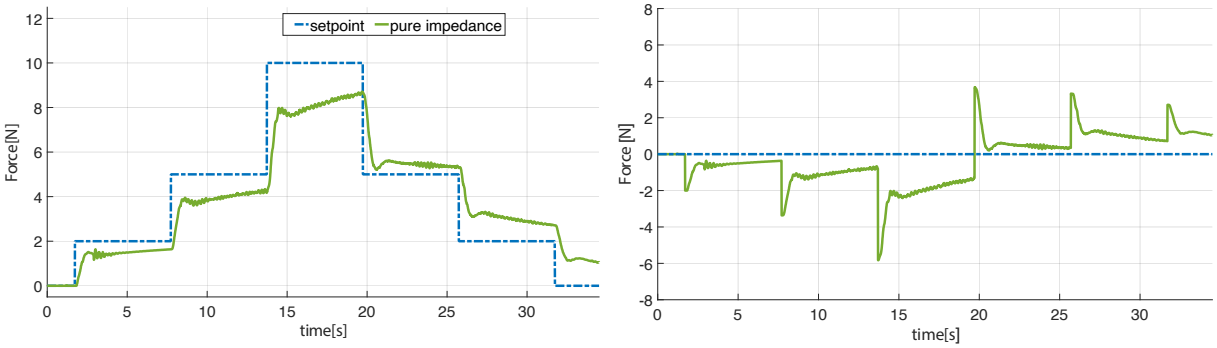

(a) (b)

Figure 7.13: Figures illustrate the simulation results for force tracking via impedance control. a) shows the force response, while b) presents the tracking error in force reference.

Fastening a bolt

The process of fastening a bolt is classified as a type of classical manipulation problem called peg-in-hole. This task involves interacting with the environment in a more complex manner than simply inserting the peg into the hole. To accomplish this task, the desired end-effector wrench f_d and twist τ_d are specified with respect to an additional orthogonal frame called the *task frame* L_T (as shown in Figure 7.14). To complete the procedure we impose the so called *artificial constraints*, which are in case of rigid environment equal to *natural constraints* imposed from the surroundings. The task frames can be represented as a finite state automaton that guides the system through each step of the process, including taking off with the bolt, locating the target, inserting and fastening the bolt, and releasing it. The state machine and the rest of the experiment design was conducted in [63].

The initial phase of the automaton illustrated in Figure 7.15 involves the aerial robot flying towards the predetermined insertion point, denoted by $\mathbf{X}_I$. This location is assumed to be al-

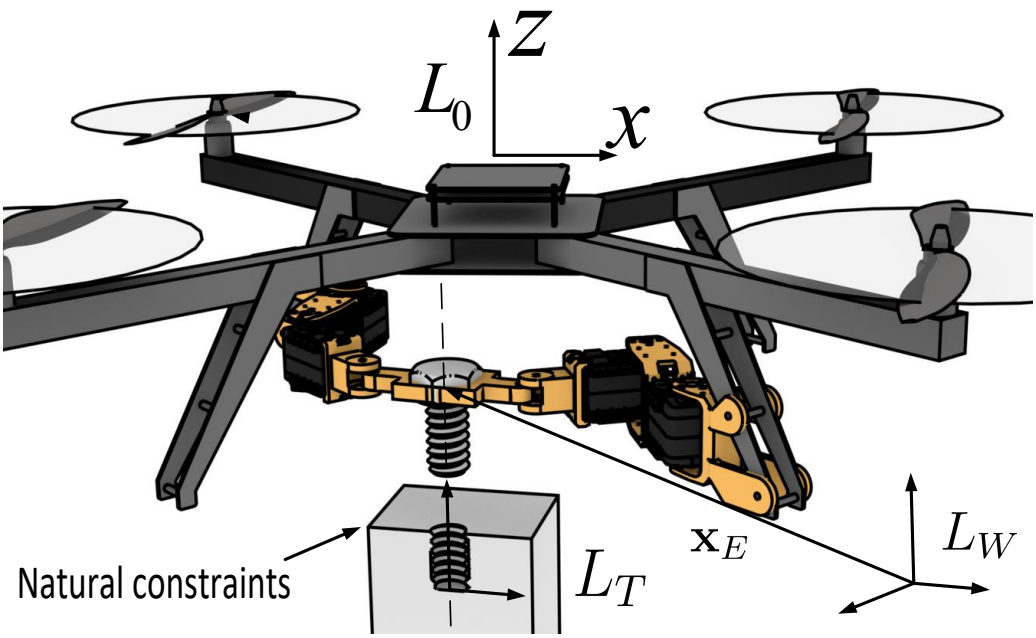

Figure 7.14: Image shows the proposed aerial manipulator w.r.t. the task frame, the insertion point for the bolt.

ready known and set as a reference point, $\mathbf{X}_r = \mathbf{X}_I$. However, when humans insert bolts into holes, we typically rely not just on vision but also on our sense of touch. Based on this experience, we define the second phase of the automaton as tactile perception. During this stage, we use the pure impedance control method outlined in Section 6.1 to regulate a constant pressure force f_d that is perpendicular to the flat surface surrounding the hole. We assume that this surface is flat (i.e., the proposed testbed) and by applying a constant force to this normal surface, the aerial manipulator can detect the insertion hole. Simultaneously, the aerial manipulator follows a planned trajectory, which is executed using a spiral movement to search for the hole while the distance between the robot and the hole is less than ε. The planned trajectory is given with:

$$X_r(t) = [x_I + t \cdot \sin(n \cdot t), y_I + t \cdot \cos(n \cdot t), z_I]^T. \tag{7.1}$$

The automaton detects the successful insertion of the bolt into the hole by monitoring two conditions. Firstly, it searches for a sudden change in position along the z-axis that is greater than ε_z. Secondly, it relies on a change in the force measurement that is greater than ε_f. When both of these conditions coincide, the automaton recognizes that the bolt has been inserted successfully and transitions to the third phase, which involves turning the bolt.

In the next state, the aerial robot applies a constant torque τ_d along the z-axis in addition to the constant pressure force f_d. The user defines τ_d, which can result in artificial constraints. During this state, the UAV twists the bolt while the manipulator controls lateral movement. In this state the end-effectors of each arm face each other. To detect successful bolt fastening, we check if the measured torque exceeds the threshold τ_r. Once the bolt is properly fastened, the

manipulator releases it, and the UAV is free to fly away after a short delay ΔT_{set}.

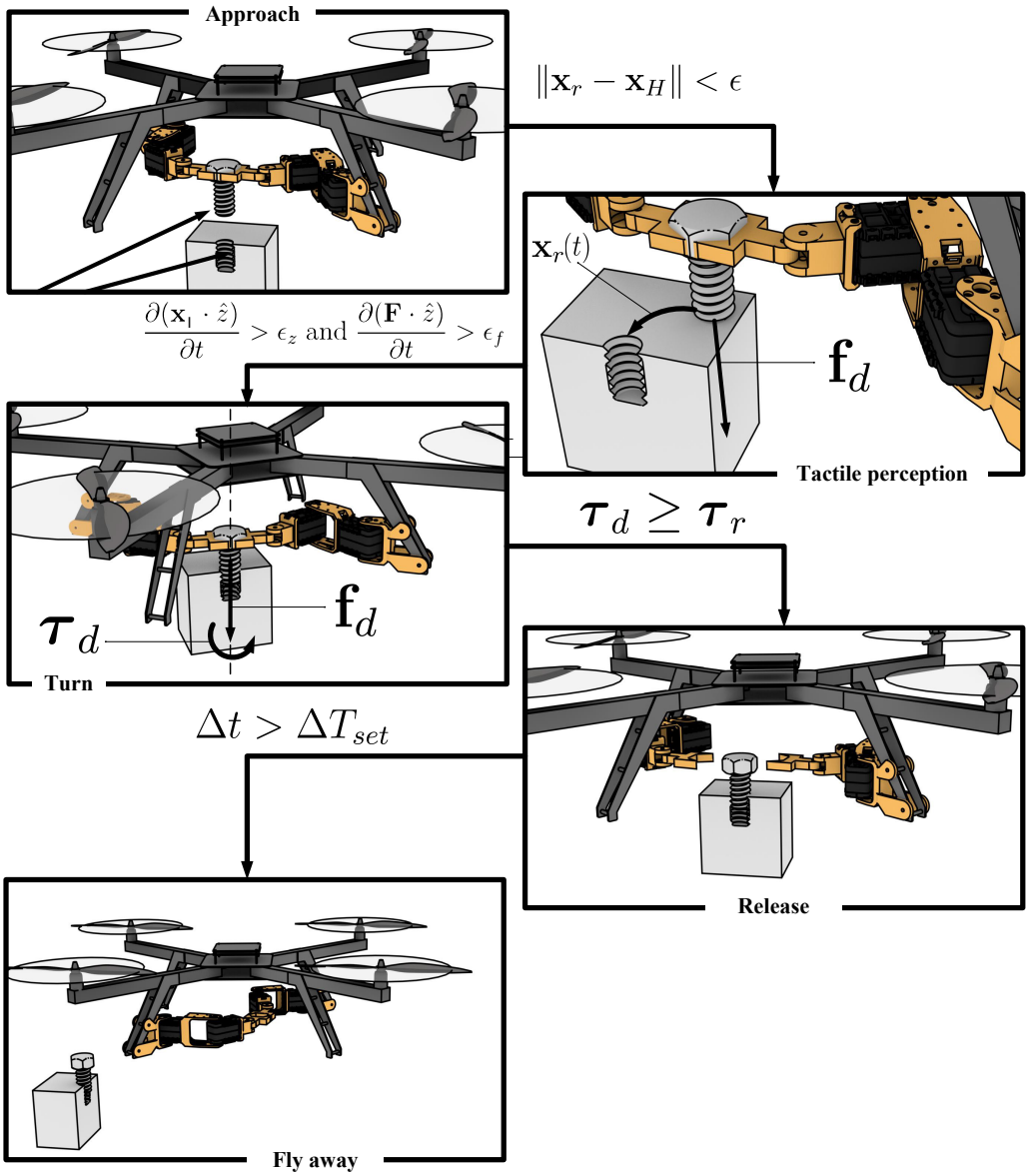

Figure 7.15: State automaton showing different stages of bolt insertion task. Each stage is shown with a notable image. Equations are shown as triggers that switch between the states of automaton.

In the proposed approach the aerial manipulator with a multi degree of freedom dual arm manipulator is used [63]. Each arm is attached to the body of the aerial manipulator, where both arms oppose each other as shown in Figure 7.16. Both arms consist of three carefully placed links and joints. Joints $q_{i,1}$ and $q_{i,2}$ are consider to be active, placed in the coordinate systems $L_{i,1}$ and $L_{i,2}$, where i denotes which arm we refer to. The joints are controlled using standard PID controllers, except the final joint, $q_{i,3}$, which is passive with rotational axis $z_{i,3}$ in $L_{i,3}$. This allows to take advantage of the null-space of the dual arm manipulator.

DH parameters of dual arm manipulator can be found in Table 7.2. Note that one virtual joint is placed in L_0. Parameters for both arms are the same, except for the virtual joint where d_0

and a_0 are system parameters depending on manipulator placement on landing gear. Asterisk symbol for $q_{i,3}$ denotes passive joints. It is worth mentioning that this manipulator operates only in $x-y$ plane and cannot move the tool along z axis. When both arms grab the payload (i.e. bolt), what were previously considered as two serial link manipulators, become one parallel manipulator attached through the payload. Inverse kinematic solution for four active joints must be found so that the two passive joints never lose grip on the bolt. More details can be found in [63].

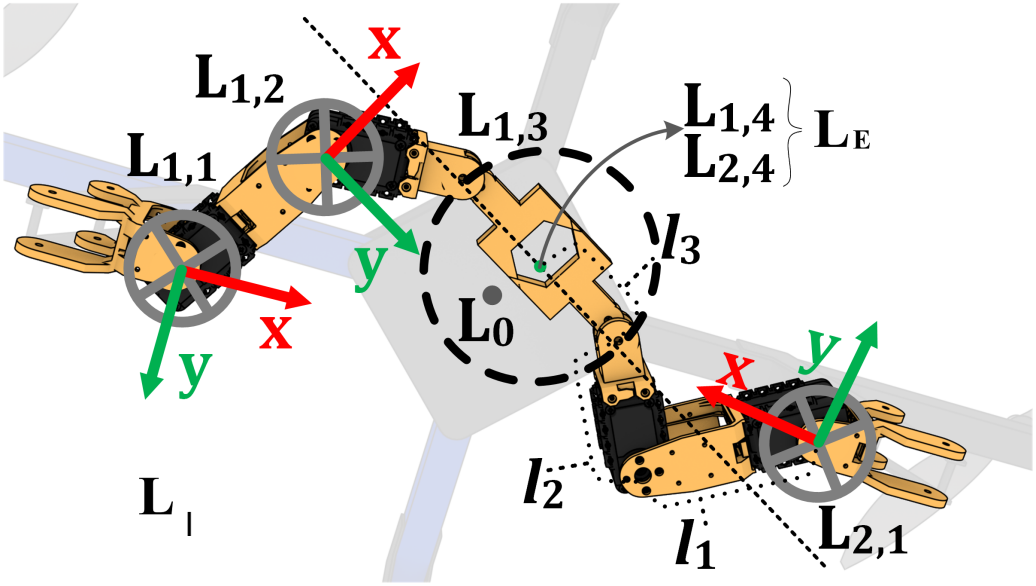

Figure 7.16: Dual arm aerial manipulator consisting of two 3 DoF manipulators. Both arms are joined together holding an object placed in end-effector coordinate system L_4. Note that L_4 is below L_0 and L_E is a end-effector reference frame.

Table 7.2: DH parameters of dual arm manipulator

	θ	d	α	a
$q_{i,0}$	$-\pi/2+i\cdot\pi$	d_0	0	$-a_o$
$q_{i,1}$	0	0	0	l_1
$q_{i,2}$	0	0	0	l_2
$q^*_{i,3}$	0	0	0	l_3

Bolt fastening task is preformed using AscTec NEO hexa-copter equipped with an Intel NUC onboard computer that operates on ROS framework. Position feedback is obtained through Optitrack motion capture system. Each arm of the manipulator is attached to the UAV with a 3D printed mechanical adaptation, and the active joints are actuated with the Dynamixel AX-12 servo motors. The obtained values for DH parameters from Table 7.2 are: $d_0 = 12.2cm$, $a_0 = 13.9cm$, $l_1 = 9.4cm$, $l_2 = 6.1cm$ and $l_3 = 4.6cm$.

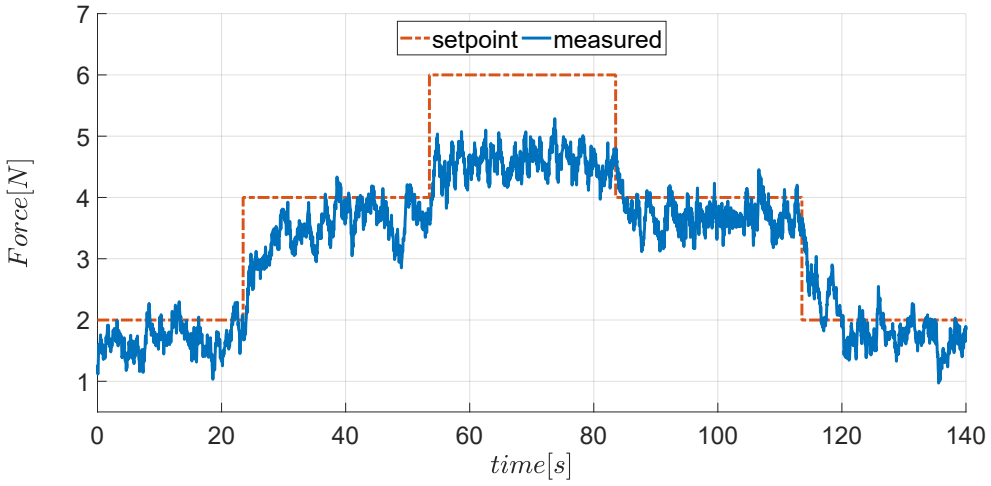

Figure 7.17: The results of impedance control, controlling the contact force of z-axis of the Cartesian coordinate system between the end-effector and the environment. Figure shows the force response on a series of step references. The steady state error is due to the inaccurate environmental parameters, stiffness k_e and location x_e, which can not be compensated without adaptive control.

Applied force is measured with Optoforce HEX-70-CE-2000N force-torque sensor, capable of measuring both force and torque in all three axes. The sensor is connected to a ground station and the data obtained from it is sent to the UAV over network. To minimize the effects of the ground effect, the sensor is mounted on a stand $1m$ above the ground. On top of the sensor, a square $15cm \times 15cm$ board with a threaded hole in the center is mounted. The end-effectors of the manipulator are specifically designed to fit the hexagonal head of the bolt in order to get a firm hold on the bolt.

Before fastening the bolt an experiment is conducted where the UAV's end-effector is set to apply a force to the surface plane along the z-axis of the Cartesian coordinate system. First, the end-effector reference position is set to the environment position $x_e = 1m$, and then, a set of force references are given. The results are shown in Figure 7.17. One can notice that a stable contact with adequate force tracking performance is achieved. The steady state error that escalates at 6N is due to inaccurate, unknown environmental parameters: stiffness k_e and the location of the environment boundaries x_e.

After a successful test of an impedance control algorithm, the proposed finite state machine is put into action. Figure 7.18 shows the transitions between phases and triggers that ultimately drive the robot to tighten the bolt. At the same time, in Figure 7.19 a steady rise in the torque applied from tightening the bolt can be observed. Fastening threshold is chosen as $\tau_r = -0.1Nm$, which is 30% of the maximum torque that can be produced by the AscTec NEO. This procedure is slowed down for safety reasons and to provide time to adjust to disturbance forces in lateral direction, visible in Figure 7.20. The constants ε, ε_z and ε_f, are chosen arbitrarily as $0.05m$, $0.1m/s$ and $20N/s$ respectively.

A set of 8 experiments was conducted, 7 out of which with successful outcomes (bolt fas-

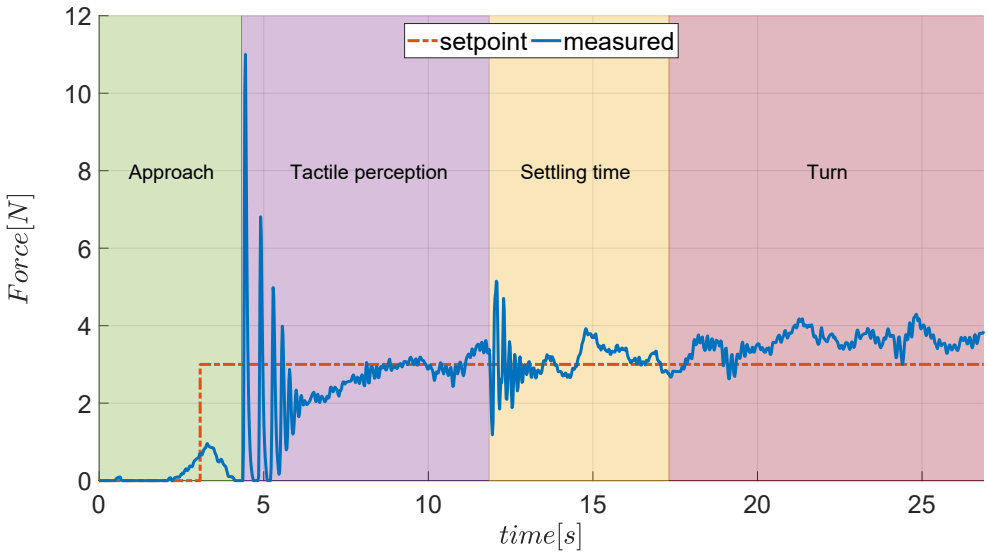

Figure 7.18: Shows z-axis force setpoint and response during each task frame. The oscillations in the forces are due to bouncing the multirotor during the contact.

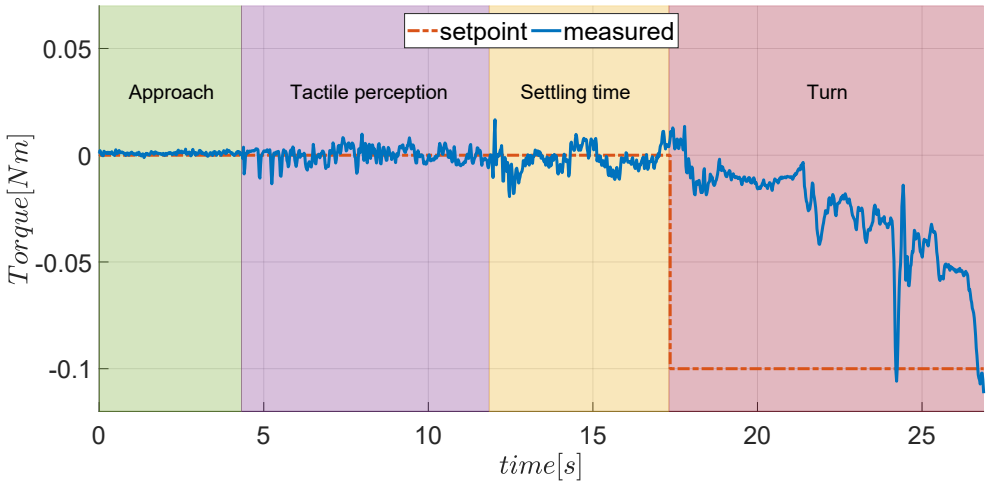

Figure 7.19: The end-effector z-axis twist response on fastening a bolt. The bolt is released in the moment when the measured torque is $t = 0.2s$ bellow $\tau_r = -0.1Nm$.

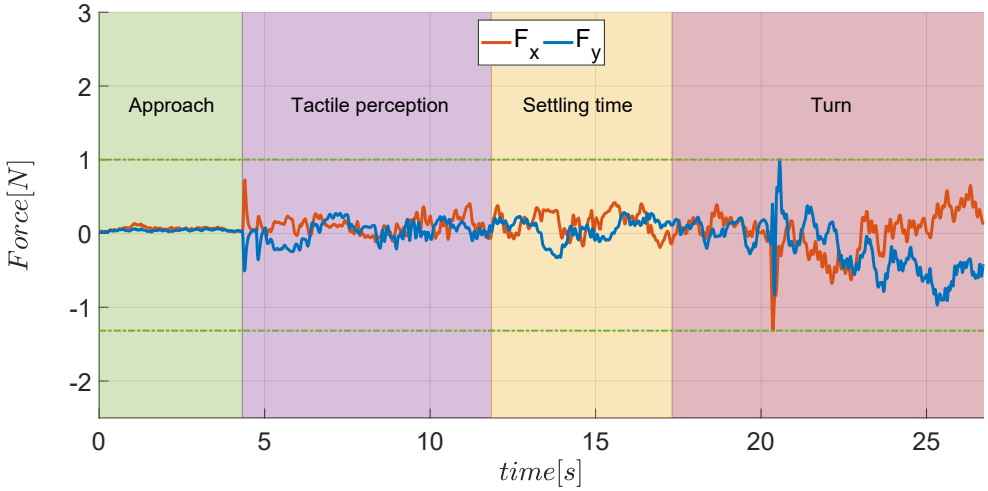

Figure 7.20: The responses of x-axis and y-axis forces during the experiment. The force setpoints are set to zero, and the impedance controller manage to keep them within $1.5N$.

tened). In the single unsuccessful attempt the bolt remained attached to the unmanned aerial vehicle's arm.

Soil moisture measurement task

The classical impedance control in practice fails in precise tracking of force reference due to the unknown parameters of the environment, most often environment position and stiffness. In development of an adaptive controller, we have conducted a series of experiments to verify how well a robotic system behaves with adaptive impedance controller, on a task of soil stiffness estimation [87].

These experiments were conducted using a Franka Panda collaborative robot arm. The adaptive impedance control method described in Section 6.2 was used during these experiments, which were carried out in three different scenarios to analyze the behavior of the framework under different soil conditions. The first scenario involved moist soil, which represents the softest scenario, while the second scenario involved dry soil, which represents a stiff scenario. The third scenario involved a collision with a rigid object, such as a stone in the soil. Three experimental repetitions were conducted for each scenario, and the results are presented in Figures 7.21-7.23.

Figures 7.21-7.23 show the force responses obtained with the same adaptive impedance filter and adaptation controller parameters. The results indicate that the framework is capable of reaching the desired contact force setpoint regardless of the stiffness of the manipulated object. However, it should be noted that the measurement is provided by the Franka Panda dynamics estimation model, which can be imprecise, particularly in the variable baseline offset in the measurements at the beginning and end of each experiment. The estimated forces are non-zero due to model imprecision and vary depending on the robot pose and velocity.

The adaptation framework implicitly models the stiffness of the manipulated object. The curves in Figures 7.21-7.23 show the dynamics of the inverse variable $1/K_e$, which could be considered compliance of the manipulated object (soil). For safety reasons, it is initially assumed that the manipulated object is infinitely stiff (zero compliance), and the adaptation of the estimated stiffness gradually reaches the actual value along with the desired contact forces. The results indicate that throughout the repetitions, the estimations converge to the same region of values, proving the stability of the adaptation method with respect to robot dynamics and detection imprecision. These results show the practical relevance of the method as a first step towards deployment on unmanned aerial manipulators.

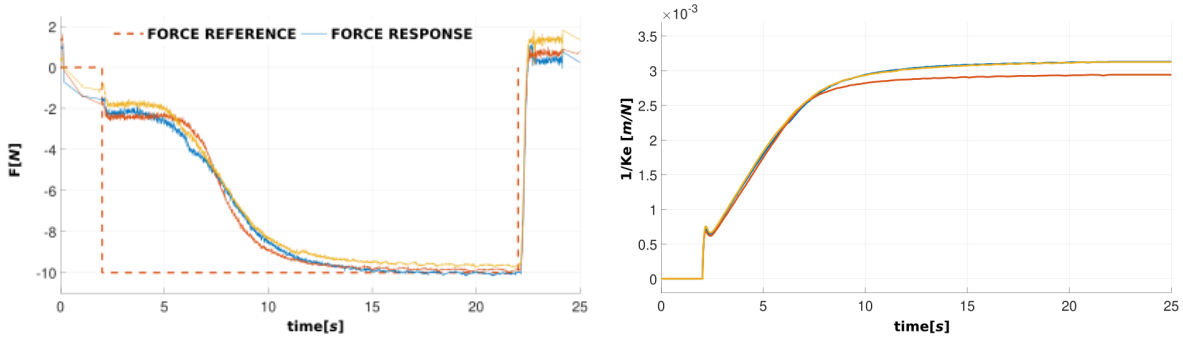

(a) (b)

Figure 7.21: a) Force tracking and b) the adaptation parameter $\kappa(t)$ during the experiment on the softest object, moist soil.

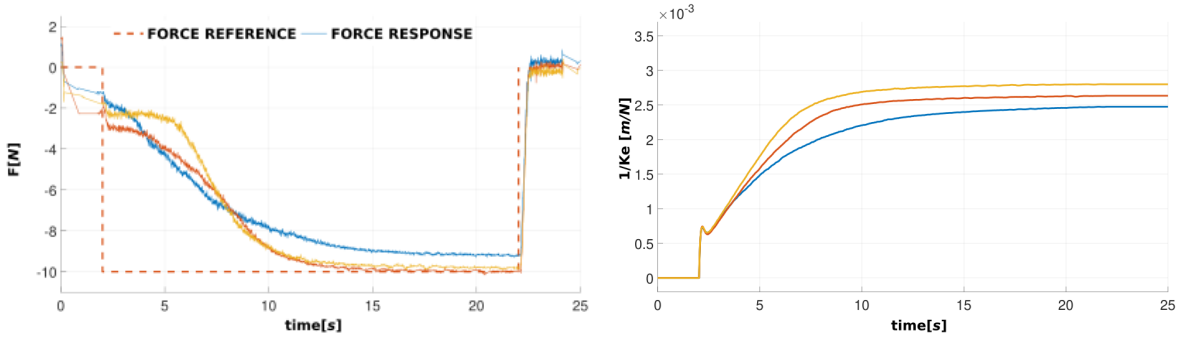

(a) (b)

Figure 7.22: a) Force tracking and b) the adaptation parameter $\kappa(t)$ during the experiment on the stiffer object, namely dry soil.

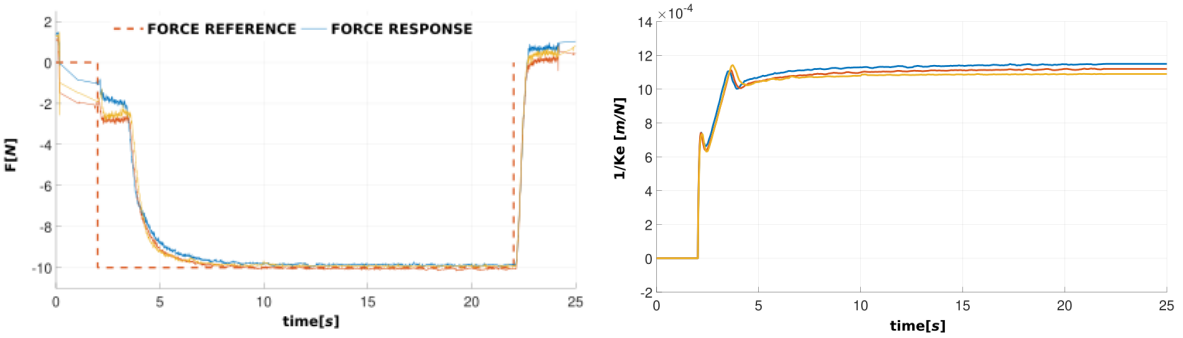

(a) (b)

Figure 7.23: a) Force tracking and b) Adaptation parameter $\kappa(t)$ during a collision experiment with a rigid object.

7.2.2Horizontal approach

After successfull tests of adaptive impedance on a robotic testbed in vertical axis, horizontal axes interaction with the environment was tested in two sets of experiments using UAVs. First, adaptive impedance control was used in a contact based wall inspection with an experimental UAV platform. Then, the performance was further improved by employing the generalized model based position control on the *Toucan* vehicle in a contact task.

Contact-based Inspection task with single actuator vehicle

To demonstrate the contact-based inspection task with a single actuator vehicle, we conducted experiments on a realistic Gazebo simulator, and real-world experiments using the *AscTec NEO* hexacopter equipped with a custom-built 3 DoF manipulator. In this experiment, the rotor tilt and centroid variation were not considered, and only rotor thrust was used as actuation. The mathematical model of the vehicle used in this experiment is therefore the same as the one described in Section 7.2.1.

The manipulator is attached to the UAV body above its center of gravity and is allowed to move in the X-Y plane of the UAV body-fixed frame, as shown in Figure 7.24. The inertial frame is denoted by L_I. The body-fixed frame of the aerial manipulator is denoted by L_0 and is attached to the aerial manipulator's center of mass.

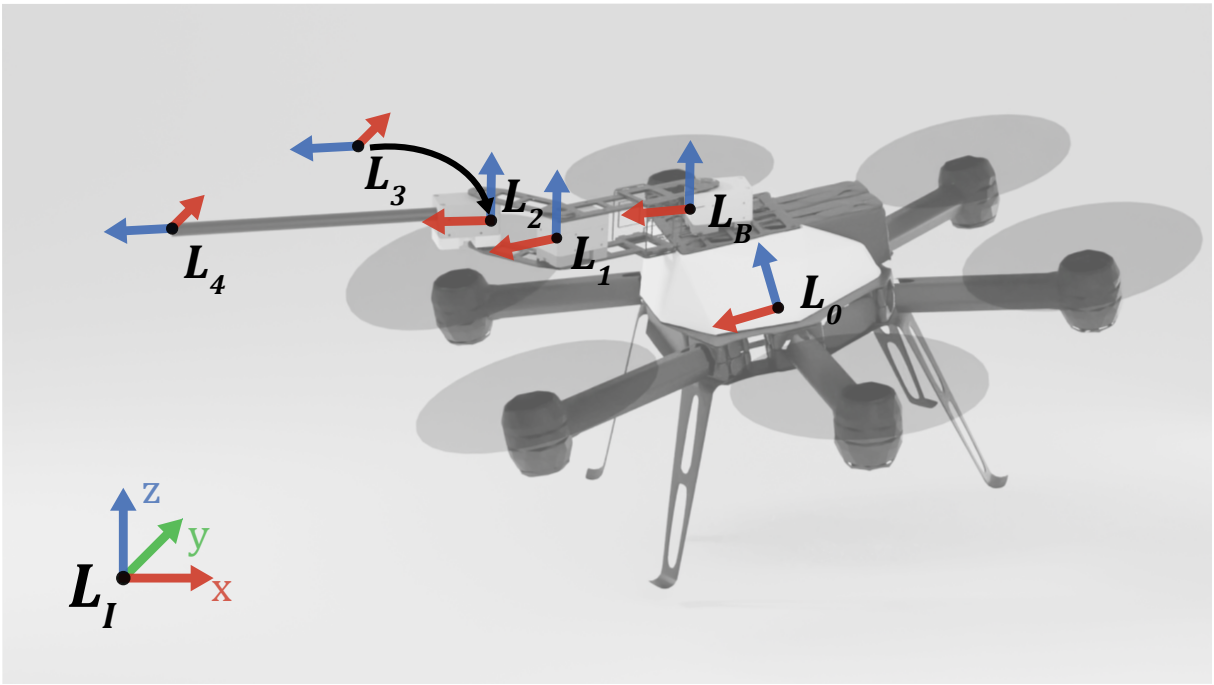

Figure 7.24: The figure expresses coordinate frames of the UAV and the 3 DOF manipulator. Note that origins of L_2 and L_4 coincide where L_3 represents a virtual joint required to obtain manipulator's DH parameters.

As the global position of the end-effector can be controlled by two actuation systems: the

UAV global position control and manipulator joint position control, we can choose which of these will be deployed using parameter ν, as a function of the current manipulator position, which can be written as follows:

$$\nu = \begin{cases} 0, & ||\mathbf{e}||_2 < \varepsilon \\ 1, & ||\mathbf{e}||_2 \geq \varepsilon \end{cases} \tag{7.2}$$

The joint error $||\mathbf{e}||_2$ is a Euclidean norm where $\mathbf{e} = \begin{bmatrix} q_1^* - q_1^{ref} & \dots & q_n^* - q_n^{ref} \end{bmatrix}^T$, where n is the number of manipulator joints, q_n^* is the optimal joint position and q_n^{ref} is the reference joint position calculated from the manipulator displacement $\Delta\mathbf{P}_{arm}$, using inverse kinematics of a single arm manipulator. Namely, since the manipulator has limited reach and maneuverability, an optimal position in the middle of the working range is predefined in the manipulator joint space. As shown in Equation (7.2), a threshold is applied to the manipulator deviation from the optimal joint position, where the deviation is defined as the norm of the joint position error vector. If the current manipulator position error is within the allowed range ε from the optimal joint positions, the desired end-effector displacement is referenced to the manipulator arm through setting $\nu = 0$ in Equation (6.35). Otherwise, if the arm is already in a joint configuration that is far from optimal, the position reference is forwarded to the UAV position control.

The conducted experiment follows the following procedure both in simulation and real-world experiments: after takes off, the high-level planner waits for a contact point detection. Once obtained, a path to the contact surface is generated and subsequently executed by the position control loop. When the estimated position of the contact area is reached, the force reference is set. The described procedure is performed using both pure impedance control and adaptive impedance control with environment stiffness estimation. In both cases the force measurements are obtained in the local coordinate frame of end-effector L_4. To use them in adaptive and pure impedance control we transform them into the world coordinate frame L_I.

The simulation is performed with a plus configuration unmanned aerial manipulator using a standard PID cascade position control method. The vehicle is controlled using rotors variation actuation principle and it is equipped with realistic sensors to measure its attitude and position. A 3-DOF manipulator is mounted on top of the vehicle with a force sensor on the end-effector. Each joint of the manipulator is controlled with a PID controller. In addition to the manipulator, the unmanned aerial manipulator frame is equipped with a stereo camera. Stereo camera is used to detect and estimate distance between the vehicle and the wall. A wall detection algorithm is out of scope of this work, but it's details can be found in [88]. A wall model, used as a contact surface, is placed within the line-of-sight of the stereo camera. The pure impedance and the adaptive impedance control are tested within this simulation experiments. The used parameters

are as follows: $m = 25$, $b = 100$, $k = 100$, $p_1 = 1.5$, $p_2 = 0.8$, $\gamma = 0.04$ and $\gamma_d = 0.1$. The simulated experiments included two scenarios: one in which the wall estimation is intentionally skewed (incorrect initial position reference for the manipulator), and another with a precise wall position as manipulator position reference.

The results of the first scenario experiment comparing pure and adaptive impedance control are shown in the following figures. Figure 7.25 shows stages of the contact inspection with corresponding position references. After approaching the (incorrectly) detected surface, the force reference of $-0.5N$ is applied. The results show the potential of the adaptive control scheme to outperform the pure impedance controller, thanks to its ability to overcome the error in the initial surface position estimate. In the process of adaptation, the parameter κ is tuned to achieve the contact force reference by position reference adaptation. The effect of the adaptation process is the environment stiffness estimate $\frac{1}{\kappa}$ at a value lower than the real one, since it takes into account both the actual stiffness of the surface, and the position error compensation through the free space. Figure 7.26 compares the contact forces obtained with the pure and the adaptive

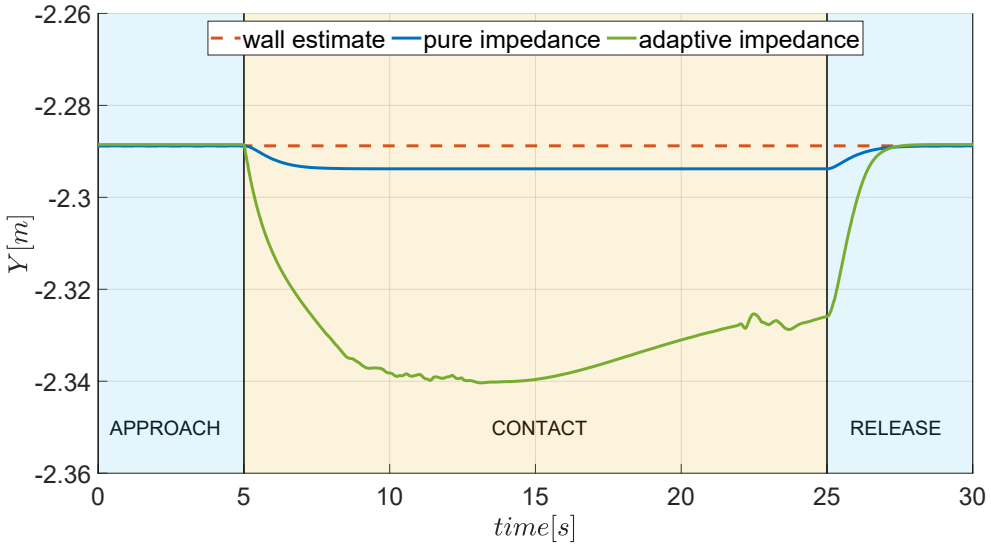

Figure 7.25: The y-axis position reference during the experiment with both pure impedance and adaptive impedance in the Gazebo simulation environment. Only one axis is shown because the applied force is parallel to it.

controllers. The adaptation algorithm was able to achieve the desired force reference, despite the inaccuracy in surface position estimate. The adaptation of the parameter κ is shown in Figure 7.27.

The behaviour of the adaptive impedance scheme was also compared with the pure impedance control with precisely know surface position. The experimental results shown in Figure 7.28 clearly show that the adaptive scheme again outperforms the pure impedance scheme. This is due to the unknown environment stiffness, to which the adaptive controller can adapt.

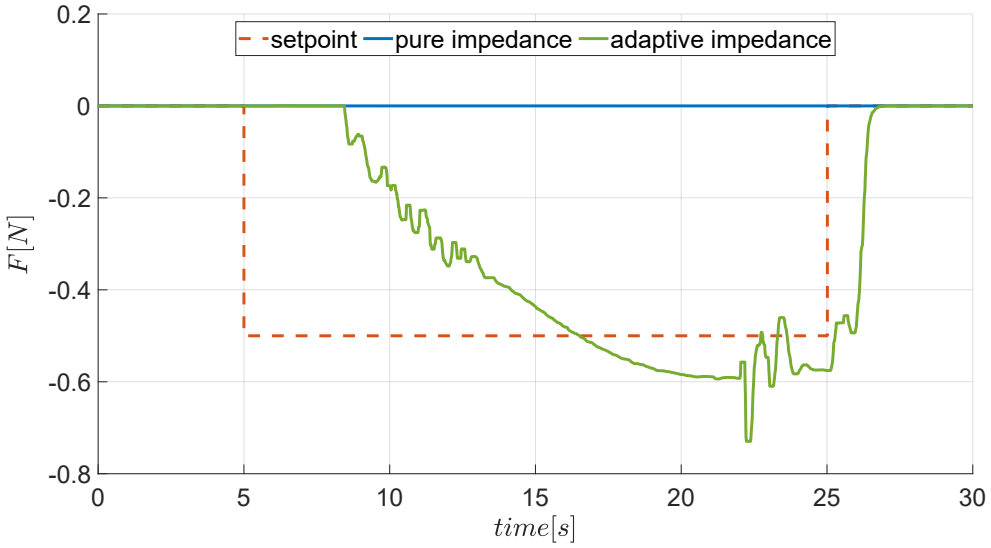

Figure 7.26: The forces during the simulation experiments. The impedance controller could not achieve the desired force due to inaccurate surface position and small stiffness parameter k, while the adaptive impedance controller manages to adapt to the inaccuracies and apply the desired force.

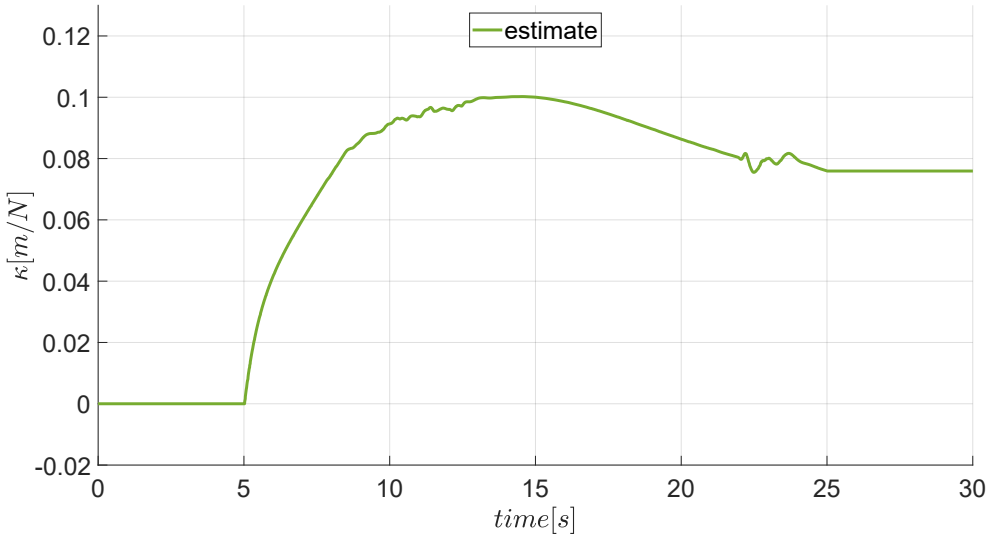

Figure 7.27: The adaptation parameter $\kappa(t)$ during the simulation experiment. It can be noticed that the parameter $\kappa(t)$ converges to the value $\kappa \approx 0.08 m/N$, which implies adaptation stability.

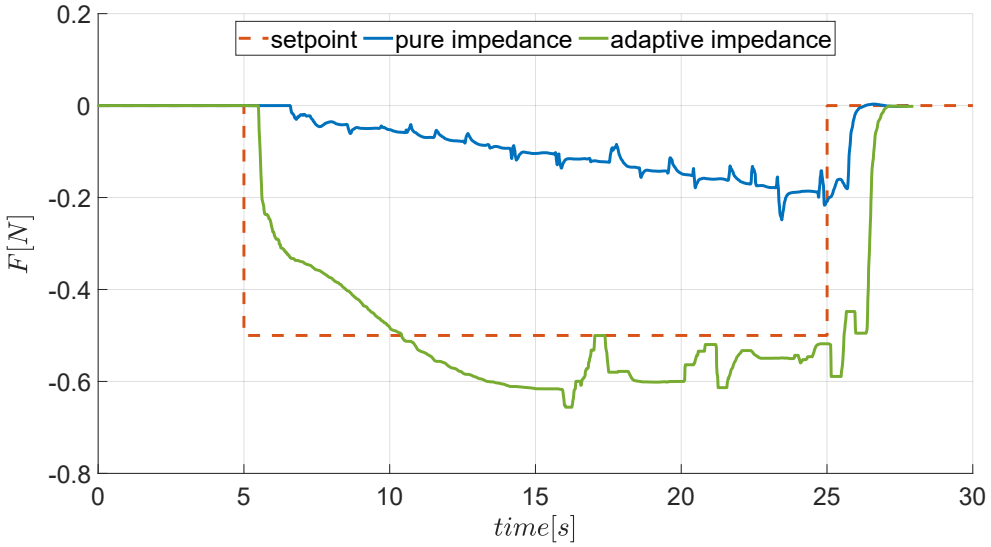

Figure 7.28: Here are the measured forces during the simulation experiment where the position of the contact surface is accurate. The adaptive impedance shows better force tracking performance.

Real-world experiments are conducted indoors and rely on the *Optitrack* motion capture system for feedback measurements. In addition to the 3-DOF manipulator, the *AscTec* NEO hexacopter is equipped with an *Intel Realsense* D435 camera to provide depth information, an *Intel NUC* on-board computer and the *AscTex Trinity* flight controller. A model predictive position control loop[89] runs on the on-board computer alongside low-level attitude control running on the flight controller. A mock-up wall, used as a contact surface, is placed within the line of sight of the UAV. The equipped 3-DOF manipulator is custom built from carbon fiber links and joints driven by the *Dynamixel XM430-W350R* servo motors. A 3-axis force sensor *OMD-20- SE -40N* is attached to the end effector. The sensor is connected to the on-board computer via the USB interface. The impedance and adaptive impedance control parameters are as follows: $m = 100$, $b = 200$, $k = 100$, $p_1 = 1.5$, $p_2 = 0.8$, $\gamma = 0.001$ and $\gamma_d = 0.018$.

Figure 7.29-7.32 shows real-world experimental results. Similar to the simulation results, different stages of contact inspection can be recognized. The real-world experiments are in accordance with the simulation results. The pure impedance controller failed to follow the contact force reference due to the error in the initial surface position estimate. The adaptive controller, on the other hand, was able to overcome the initial error, and to maintain stable contact. The force tracking response is oscillatory but stable, and could be improved by further tuning the adaptation parameter. The adaptation dynamics of the adaptation parameter κ is shown in Figure 7.31. As in the simulation experiments, here it also converges into a stable estimate, that compensates for errors in both the surface position estimate and the environment stiffness estimate. When examining Figure 7.32, it becomes apparent that the vehicle's roll angle is non-zero. This is a natural consequence of the vehicle's design, as it needs to tilt in order to apply force to the environment. However, to overcome this limitation, an additional actuator can be introduced to the vehicle, such as the one used in the *Toucan* vehicle.

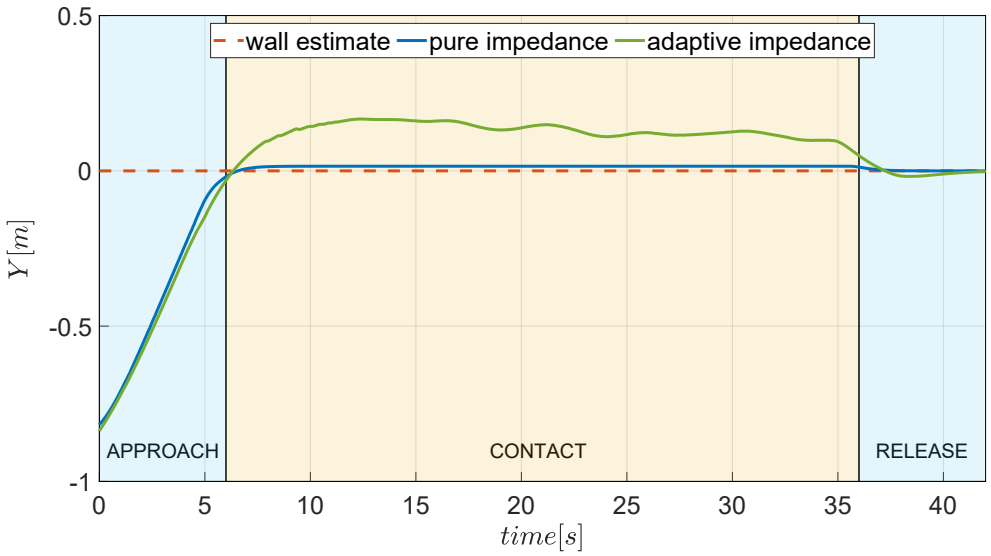

Figure 7.29: The aerial manipulator position reference during both experiments. The pure impedance output position could not sufficiently adapt to inaccurate surface estimates due to the small impedance filter stiffness k, while the adaptive impedance accounts for these inaccuracies with adaptation of the parameter κ.

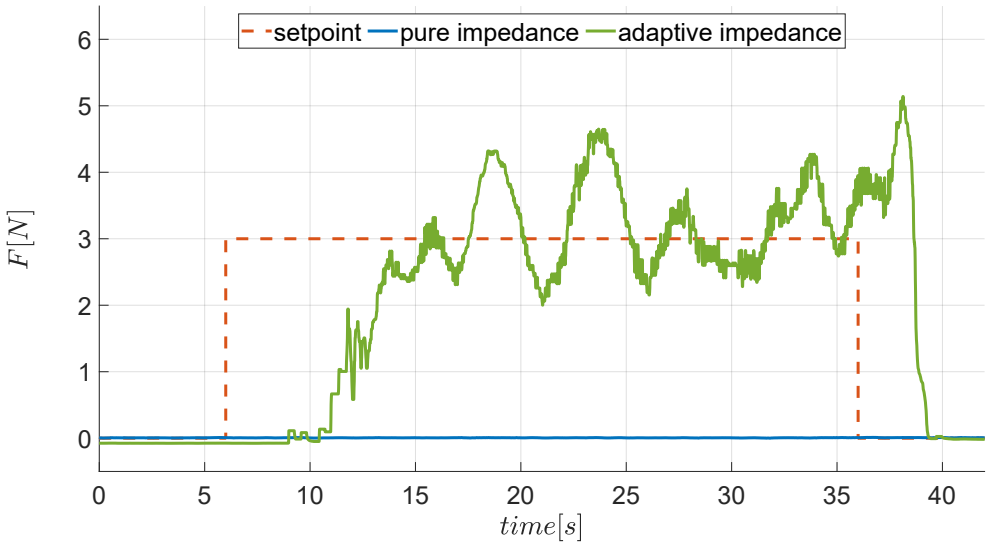

Figure 7.30: The results of the force tracking with adaptive impedance control and pure impedance control. With pure impedance control, the aerial manipulator was unable to apply force to the surface. The inaccurate sensor measurements prevent a correct surface estimation. In contrast, the adaptive scheme can overcome this limitation.

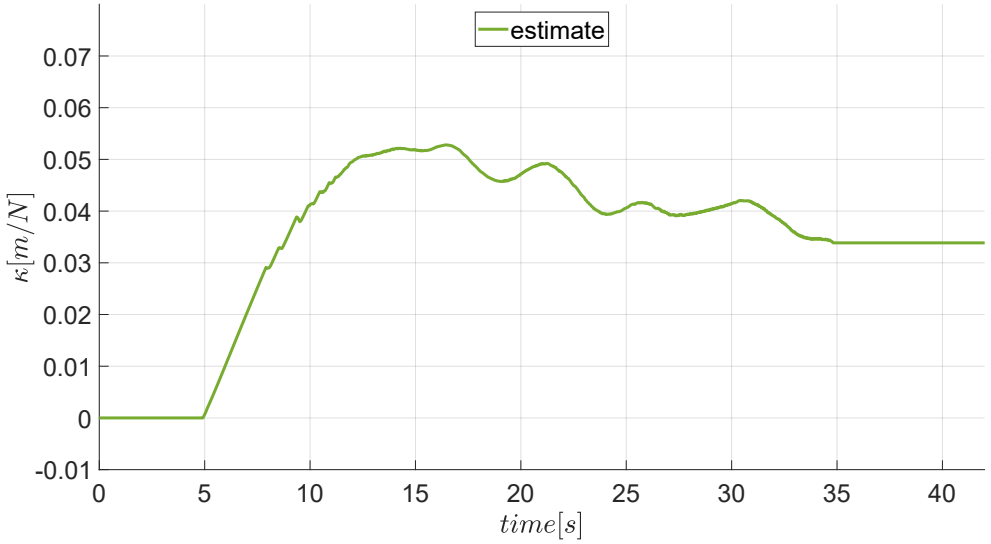

Figure 7.31: The adaptation parameter $\kappa(t)$ during a real-world inspection experiment. One can notice how the parameter $\kappa(t)$ converges towards the value $\kappa \approx 0.04 m/N$, implying stability of the adaptation algorithm.

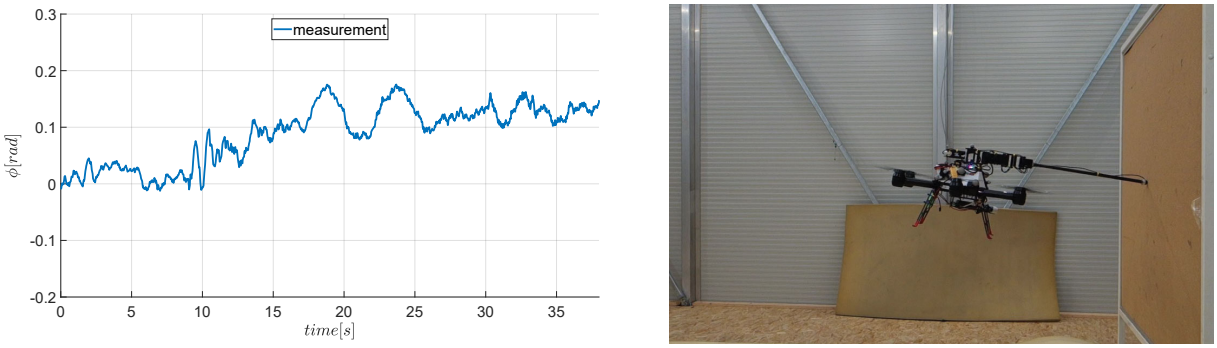

(a) (b)

Figure 7.32: The aerial manipulator in the figure is shown performing a contact-based inspection. a) displays the measured orientation of the vehicle, while b) shows the experimental setup with the vehicle. The proposed system is versatile and can be utilized in a variety of inspection, maintenance, or repair scenarios. It is worth noting that the vehicle must be tilted to apply force to the environment, which can be addressed by introducing an additional actuator to the vehicle.

Contact-based Inspection task with *Toucan* vehicle

In this subsection, a specific application is presented that exploits an interesting property of the *Toucan* system. Contact-based actions are among the most dangerous when it comes to performing them safely, especially when force tracking requirements are added. In previous section, force tracking was performed using a standard multirotor vehicle with a mounted manipulator arm. Force tracking was successfully performed with a vehicle pitch of 10 degrees. Here, the same experiment is performed, but instead of a standard aerial manipulator, the *Toucan* vehicle is used. Leveraging its ability of horizontal flight with neutral attitude, and the proposed adaptive impedance controller from Chapter 6, *Toucan* is able to achieve similar results without additional pitching towards the contact surface. It achieves this by using rotor thrust direction variation method to maintain stable contact and rotor thrust magnitude variation to achieve neutral attitude. This results in a safer and more stable interaction, than using a standard multirotor vehicle.

The contact experiment is performed in a laboratory environment using the Optitrack system. An *a priori* known contact-point is supplied to the adaptive impedance controller. The controller then starts generating referent position values towards the contact point, as shown in Figure 7.33a, while setting neutral target attitude, Figure 7.35. Once the contact point is reached, the impedance controller starts tracking the referent force value, demonstrated by Figure 7.33b and the adaptation law begins estimating the environment stiffness, shown by Figure 7.34.

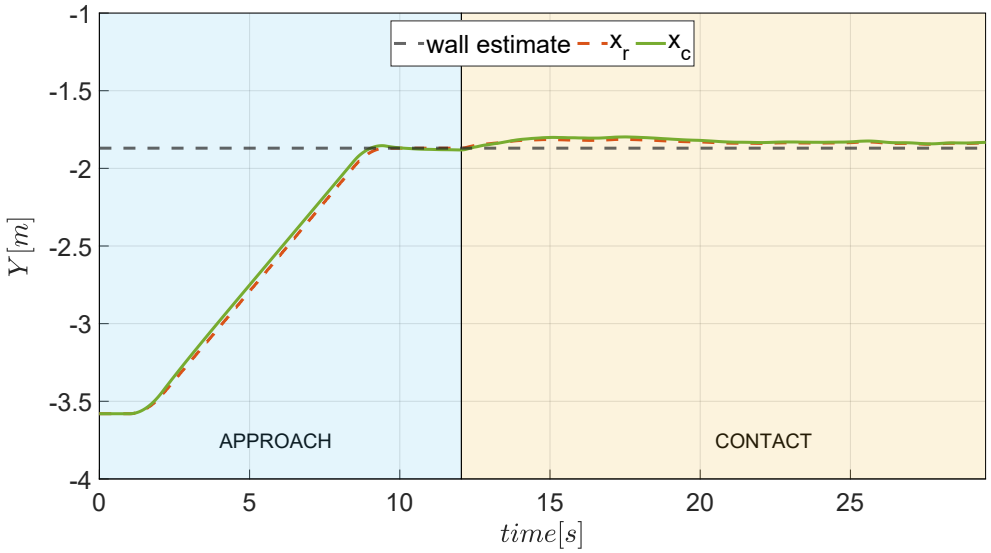

(a)

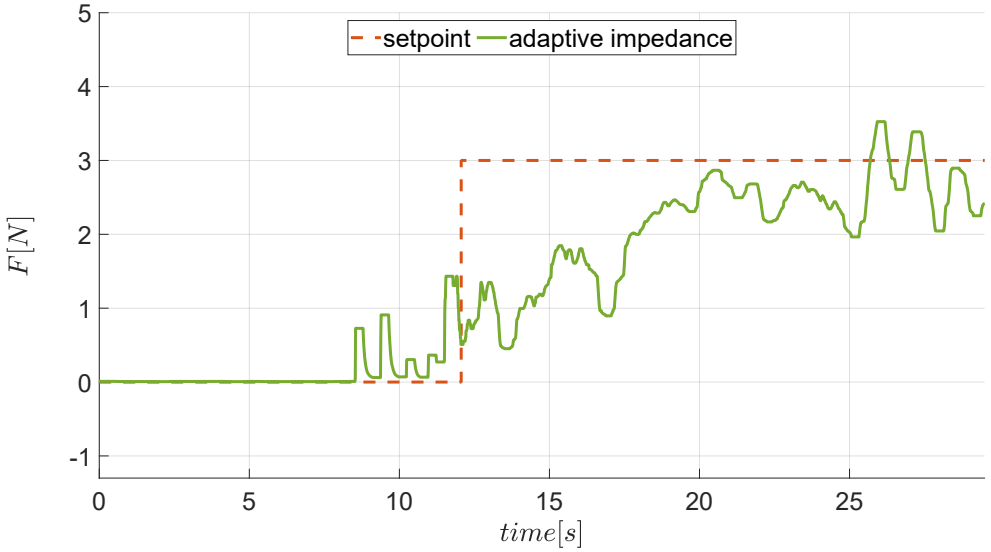

(b)

Figure 7.33: These figures show the referent and measured *Toucan* positions as well as the contact point estimate (a) and the referent and measured force of the end-effector (b). A clear distinction between the approach and the contact phase of the experiment is also shown at about the 12s mark. The force tracking starts after *Toucan* reaches the contact point with the end-effector.

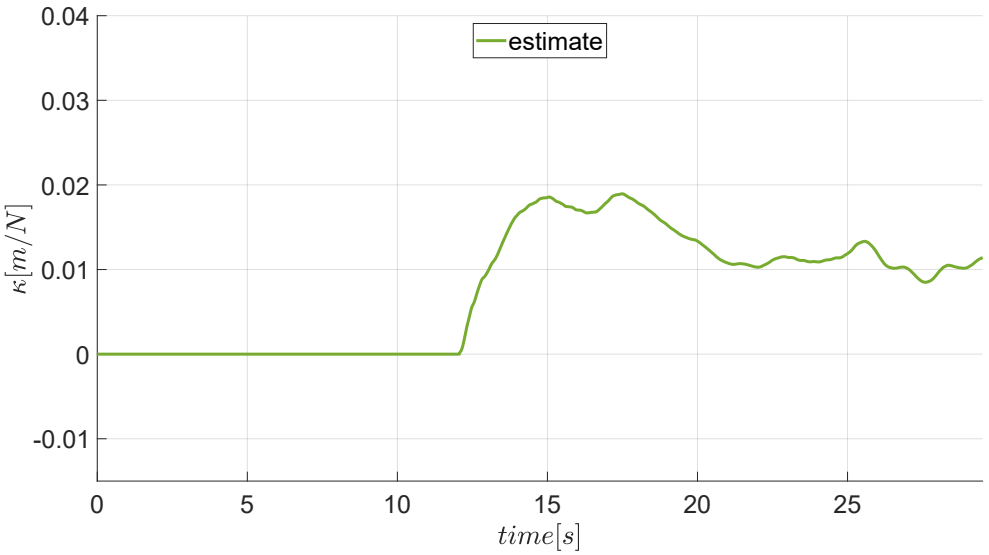

Figure 7.34: This figure shows the adaptation of the environment stiffness estimate κ during the contact-based inspection experiment. The value starts changing as soon as the force tracking begins at about the 12s mark. After 10 seconds it converges to a stable estimate.

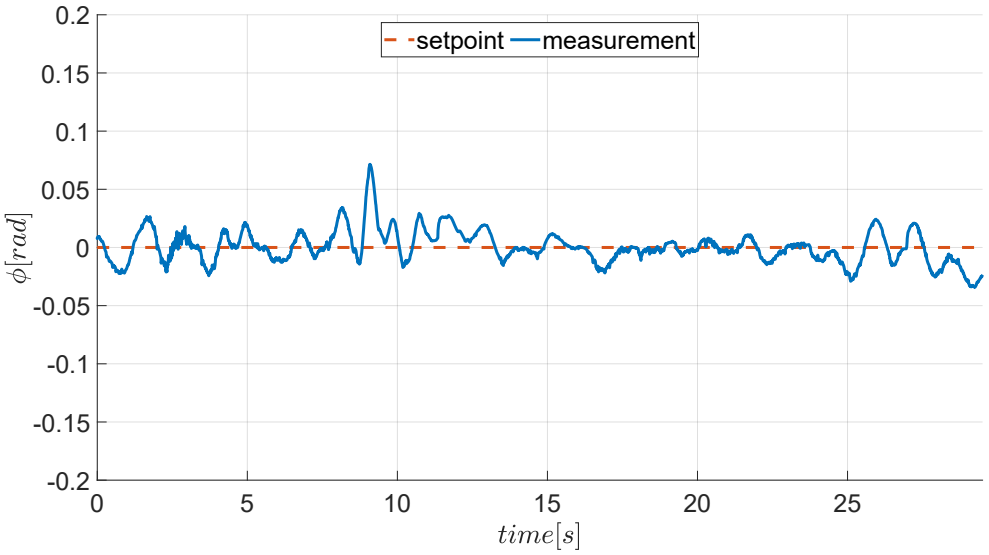

Figure 7.35: This figure shows the referent and measured pitch orientation during the contact-based inspection experiment. One of the ideas of the experiment is to maintain neutral attitude during the approach and contact phases. This graph shows that even though the aerial manipulator is applying the desired contact force on the surface, as presented in Fig. 7.33b, its orientation is kept neutral. This fact greatly increases the stability of the contact-based inspection tasks.

CHAPTER 8

Conclusion

This thesis presented several novel results in the field of unmanned aerial manipulation. The most important result is the developed generalized unmanned aerial manipulator model that incorporates three different actuation principles. Development of this theoretical model enables design of fully actuated 6 DoF control principles for aerial manipulators, depending on the available vehicles, as well as the production and deployment of these vehicles in real experiments and applications. Another important result of the thesis, used both together with the developed generalized aerial manipulator and with other robotic platforms is the adaptive impedance controller that enables stable interaction with the environment with precise force reference tracking. The main contributions of this thesis are formalized as follows.

A generalized unmanned aerial manipulator model unifying actuation concepts based on centre of mass variation, rotor thrust direction and amplitude.

This thesis proposes a generalized model of the unmanned aerial manipulator that unifies three different actuation concepts, namely the classical rotor thrust amplitude, the rotor thrust direction, and centre of mass variation. As an extension of the classical rotor thrust amplitude control, this approach enables development of fully actuated vehicles with 6 DoF control. This is especially important in complex involving vehicle cooperation, environment interaction, or transportation of dangerous or fragile loads. The generalization of the model is also suitable for other types of possibly under-actuated vehicles, by simply fixing or setting certain variable parameters to zero.

The generalized model was linearized, so that the classical linear control analysis tools could be applied to verify the stability and to choose the optimal parameters when designing the actual

vehicles using existing hardware. Furthermore, the controllers were tuned based on these linear approximation models. Several experimental runs have confirmed the precision and practical relevance of the developed model by comparing the theoretical expectations with experimental behavior of the real robotic platform.

Unmanned aerial manipulator control method based on the generalized model.

The developed generalized model enabled design of novel control strategies that incorporate multiple actuation systems in stable vehicle control. Several methods are presented in the thesis, relying on all or some of the possible actuation principles. A position controller was designed based on rotor thrust amplitude and direction actuation systems. This developed control principle was experimentally validated both in free flight, and in interaction with the environment.

A position controller incorporating all three actuation principles was also developed, based on the valve position control scheme. Here, one actuation system is considered as a faster response system, preferably maintained around the middle of the working range, and another is considered as a slower system, that responds after the fast system, but maintains the steady state response such that the fast system can return to middle position. This controller was tested in a simulation environment.

The attitude control is in both cases based on rotor thrust amplitude variation only. However, the developed generalized model, in theory, enables deploying control strategies such as model predictive control to improve attitude control by taking into account centroid variation and rotor thrust direction variation, as well. The latter two actuation principles are in this work only considered as disturbance, and this possibility remains open for future work.

Impedance control system for stable interaction of unmanned aerial manipulator with the environment based on the generalized model.

The final result of the thesis is the adaptive impedance control strategy that enables stable interaction of a robotic manipulator with the environment regardless of the uncertainties. In other words, even with the unknown precise position of the environment and the unknown environment stiffness, the robot is able to reach the desired referenced forces in a stable manner. The adaptation is based on environment stiffness online estimation based on the measured error signals. The adaptive impedance controller outputs position references for the robot, that will lead it towards reaching the referenced force setpoint.

In addition to the adaptive impedance controller, the generalized vehicle model and the stable position and attitude controllers, this thesis also proposes a strategy to handle the position references provided by the adaptive impedance controller, in order to efficiently distribute the

payload across the vehicle components. Namely, depending on the vehicle and manipulator configuration, one or the other is in a better position to reconfigure, change it's position or exert necessary force on the environment. This thesis proposes a solution for distribution of the position reference, resolving the question of over-actuated inverse kinematics problem as well.

The developed adaptive impedance approach is tested in several experimental testbeds, including a standalone robotic manipulator, as well as on an unmanned aerial manipulator, where the desired interaction with the environment was successfully realized with a vehicle under full 6 DoF control.

Bibliography

[1]Hoffmann, G., Huang, H., Waslander, S., Tomlin, C., “Quadrotor helicopter flight dynamics and control: Theory and experiment”, AIAA Guidance, Navigation and Control Conference and Exhibit, 08 2007.

[2]Lee, T., Leok, M., McClamroch, N. H., “Geometric tracking control of a quadrotor uav on se(3)”, in 49th IEEE Conference on Decision and Control (CDC), 2010, str. 5420-5425.

[3]LaValle, S. M., Planning Algorithms. Cambridge University Press, 2006.

[4]Schäfer, B. E., Picchi, D., Engelhardt, T., Abel, D., “Multicopter unmanned aerial vehicle for automated inspection of wind turbines”, in 2016 24th Mediterranean Conference on Control and Automation (MED), 2016, str. 244-249.

[5]Stokkeland, M., Klausen, K., Johansen, T. A., “Autonomous visual navigation of unmanned aerial vehicle for wind turbine inspection”, in 2015 International Conference on Unmanned Aircraft Systems (ICUAS), 2015, str. 998-1007.

[6]Car, M., Markovic, L., Ivanovic, A., Orsag, M., Bogdan, S., “Autonomous wind-turbine blade inspection using lidar-equipped unmanned aerial vehicle”, IEEE Access, Vol. 8, 2020, str. 131 380-131 387.

[7]Luque-Vega, L. F., Castillo-Toledo, B., Loukianov, A., Gonzalez-Jimenez, L. E., “Power line inspection via an unmanned aerial system based on the quadrotor helicopter”, in MELECON 2014 - 2014 17th IEEE Mediterranean Electrotechnical Conference, 2014, str. 393-397.

[8]Tognon, M., Chávez, H. A. T., Gasparin, E., Sablé, Q., Bicego, D., Mallet, A., Lany, M., Santi, G., Revaz, B., Cortés, J., Franchi, A., “A truly-redundant aerial manipulator system with application to push-and-slide inspection in industrial plants”, IEEE Robotics and Automation Letters, Vol. 4, No. 2, 2019, str. 1846-1851.

[9]Trujillo, M., Martinez-de Dios, J. R., Martín, C., Viguria, A., Ollero, A., "Novel aerial manipulator for accurate and robust industrial ndt contact inspection: A new tool for the oil and gas inspection industry", Sensors, Vol. 19, 03 2019, str. 1305.

[10]Ikeda, T., Yasui, S., Fujihara, M., Ohara, K., Ashizawa, S., Ichikawa, A., Okino, A., Oomichi, T., Fukuda, T., "Wall contact by octo-rotor uav with one dof manipulator for bridge inspection", in 2017 IEEE/RSJ International Conference on Intelligent Robots and Systems (IROS), 2017, str. 5122-5127.

[11]Dorafshan, S., Maguire, M., Hoffer, N. V., Coopmans, C., "Challenges in bridge inspection using small unmanned aerial systems: Results and lessons learned", in 2017 International Conference on Unmanned Aircraft Systems (ICUAS), 2017, str. 1722-1730.

[12]Ghadiok, V., Goldin, J., Ren, W., "Autonomous indoor aerial gripping using a quadrotor", in 2011 IEEE/RSJ International Conference on Intelligent Robots and Systems, 2011, str. 4645-4651.

[13]Mellinger, D., Lindsey, Q., Shomin, M., Kumar, V., "Design, modeling, estimation and control for aerial grasping and manipulation", in 2011 IEEE/RSJ International Conference on Intelligent Robots and Systems, 2011, str. 2668-2673.

[14]Sánchez, M. I., Acosta, J. A., Ollero, A., "Integral action in first-order closed-loop inverse kinematics. application to aerial manipulators", in 2015 IEEE International Conference on Robotics and Automation (ICRA), 2015, str. 5297-5302.

[15]Orsag, M., Korpela, C., Bogdan, S., Oh, P., "Valve turning using a dual-arm aerial manipulator", in 2014 International Conference on Unmanned Aircraft Systems (ICUAS), 2014, str. 836-841.

[16]Kim, S., Hoseong Seo, Kim, H. J., "Operating an unknown drawer using an aerial manipulator", in 2015 IEEE International Conference on Robotics and Automation (ICRA), 2015, str. 5503-5508.

[17]Kamel, M., Alexis, K., Siegwart, R., "Design and modeling of dexterous aerial manipulator", in 2016 IEEE/RSJ International Conference on Intelligent Robots and Systems (IROS), 2016, str. 4870-4876.

[18]Hamel, T., Mahony, R., Lozano, R., Ostrowski, J., "Dynamic modelling and configuration stabilization for an x4-flyer", IFAC Proceedings Volumes, Vol. 35, 07 2002.

[19]Ryll, M., Bülthoff, H. H., Giordano, P. R., "Modeling and control of a quadrotor uav with tilting propellers", in 2012 IEEE International Conference on Robotics and Automation, 2012, str. 4606-4613.

[20]Haus, T., Prkut, N., Borovina, K., Mari ć, B., Orsag, M., Bogdan, S., "A novel concept of attitude control for large multirotor-uavs based on moving mass control", in 2016 24th Mediterranean Conference on Control and Automation (MED), 2016, str. 832-839.

[21]Şenkul, F., Altu ğ, E., "Modeling and control of a novel tilt — roll rotor quadrotor uav", in 2013 International Conference on Unmanned Aircraft Systems (ICUAS), 2013, str. 1071-1076.

[22]Bin Junaid, A., Sanchez, A., Bosch, J., Vitzilaios, N., Zweiri, Y., "Design and implementation of a dual-axis tilting quadcopter", Robotics, Vol. 7, 10 2018, str. 65.

[23]Ryll, M., Muscio, G., Pierri, F., Cataldi, E., Antonelli, G., Caccavale, F., Franchi, A., "6d physical interaction with a fully actuated aerial robot", in 2017 IEEE International Conference on Robotics and Automation (ICRA), 2017, str. 5190-5195.

[24]Ryll, M., Bülthoff, H. H., Giordano, P. R., "First flight tests for a quadrotor uav with tilting propellers", in 2013 IEEE International Conference on Robotics and Automation, 2013, str. 295-302.

[25]Haus, T., Orsag, M., Bogdan, S., "A concept of a non-tilting multirotor-uav based on moving mass control", in 2017 International Conference on Unmanned Aircraft Systems (ICUAS), 2017, str. 1618-1624.

[26]Bouabdallah, S., Murrieri, P., Siegwart, R., "Towards autonomous indoor micro vtol", Auton. Robots, Vol. 18, 03 2005, str. 171-183.

[27]Zhang, T., Kang, Y., Achtelik, M., Kuhnlenz, K., Buss, M., "Autonomous hovering of a vision/imu guided quadrotor", in 2009 International Conference on Mechatronics and Automation, 2009, str. 2870-2875.

[28]Yang, H., Cheng, L., Xia, Y., Yuan, Y., "Active disturbance rejection attitude control for a dual closed-loop quadrotor under gust wind", IEEE Transactions on Control Systems Technology, Vol. 26, No. 4, 2018, str. 1400-1405.

[29]HOW, J. P., BEHIHKE, B., FRANK, A., DALE, D., VIAN, J., "Real-time indoor autonomous vehicle test environment", IEEE Control Systems Magazine, Vol. 28, No. 2, 2008, str. 51-64.

[30]Yu, B., Zhang, Y., Minchala, I., Qu, Y., "Fault-tolerant control with linear quadratic and model predictive control techniques against actuator faults in a quadrotor uav", in 2013 Conference on Control and Fault-Tolerant Systems (SysTol), 2013, str. 661-666.

[31]Lee, D., Sastry, S., "Feedback linearization vs. adaptive sliding mode control for a quadrotor helicopter. international journal of control, automation and systems, 7(3), 419-428", International Journal of Control, Automation and Systems, Vol. 7, 06 2009, str. 419-428.

[32]Voos, H., "Nonlinear control of a quadrotor micro-uav using feedback-linearization", in 2009 IEEE International Conference on Mechatronics, 2009, str. 1-6.

[33]Bouabdallah, S., Siegwart, R., "Full control of a quadrotor", in 2007 IEEE/RSJ International Conference on Intelligent Robots and Systems, 2007, str. 153-158.

[34]Colorado, J., Barrientos, A., Martinez, A., Lafaverges, B., Valente, J., "Mini-quadrotor attitude control based on hybrid backstepping amp; frenet-serret theory", in 2010 IEEE International Conference on Robotics and Automation, 2010, str. 1617-1622.

[35]Lippiello, V., Ruggiero, F., Serra, D., "Emergency landing for a quadrotor in case of a propeller failure: A backstepping approach", in 2014 IEEE/RSJ International Conference on Intelligent Robots and Systems, 2014, str. 4782-4788.

[36]Xu, R., Ozguner, U., "Sliding mode control of a quadrotor helicopter", in Proceedings of the 45th IEEE Conference on Decision and Control, 2006, str. 4957-4962.

[37]Alexis, K., Papachristos, C., Nikolakopoulos, G., Tzes, A., "Model predictive quadrotor indoor position control", in 2011 19th Mediterranean Conference on Control & Automation (MED), 2011, str. 1247-1252.

[38]Aswani, A., Gonzalez, H., Sastry, S., Tomlin, C., "Provably safe and robust learning-based model predictive control", Automatica, Vol. 49, 07 2011.

[39]Aswani, A., Bouffard, P., Tomlin, C., "Extensions of learning-based model predictive control for real-time application to a quadrotor helicopter", in 2012 American Control Conference (ACC), 2012, str. 4661-4666.

[40]Bouffard, P., Aswani, A., Tomlin, C., "Learning-based model predictive control on a quadrotor: Onboard implementation and experimental results", in 2012 IEEE International Conference on Robotics and Automation, 2012, str. 279-284.

[41]Coza, C., Macnab, C., "A new robust adaptive-fuzzy control method applied to quadrotor helicopter stabilization", in NAFIPS 2006 - 2006 Annual Meeting of the North American Fuzzy Information Processing Society, 2006, str. 454-458.

[42]Amoozgar, M., Chamseddine, A., Zhang, Y., "Fault-tolerant fuzzy gain-scheduled pid for a quadrotor helicopter testbed in the presence of actuator faults", IFAC Proceedings Volumes (IFAC-PapersOnline), Vol. 2, 12 2012.

[43]Dierks, T., Jagannathan, S., "Output feedback control of a quadrotor uav using neural networks", IEEE Transactions on Neural Networks, Vol. 21, No. 1, 2010, str. 50-66.

[44]Meng, X., He, Y., Han, J., "Survey on aerial manipulator: System, modeling, and control", Robotica, Vol. 38, No. 7, 2020, str. 1288–1317.

[45]Spica, R., Franchi, A., Oriolo, G., Bülthoff, H. H., Giordano, P. R., "Aerial grasping of a moving target with a quadrotor uav", in 2012 IEEE/RSJ International Conference on Intelligent Robots and Systems, 2012, str. 4985-4992.

[46]Pounds, P. E. I., Bersak, D. R., Dollar, A. M., "Practical aerial grasping of unstructured objects", in 2011 IEEE Conference on Technologies for Practical Robot Applications, 2011, str. 99-104.

[47]Seo, H., Kim, S., Kim, H. J., "Aerial grasping of cylindrical object using visual servoing based on stochastic model predictive control", in 2017 IEEE International Conference on Robotics and Automation (ICRA), 2017, str. 6362-6368.

[48]Zhang, G., He, Y., Dai, B., Gu, F., Yang, L., Han, J., Liu, G., Qi, J., "Grasp a moving target from the air: System control of an aerial manipulator", in 2018 IEEE International Conference on Robotics and Automation (ICRA), 2018, str. 1681-1687.

[49]Garimella, G., Kobilarov, M., "Towards model-predictive control for aerial pick-and-place", in 2015 IEEE International Conference on Robotics and Automation (ICRA), 2015, str. 4692-4697.

[50]Wu, C., Qi, J., Song, D., Qi, X., Lin, T., Han, J., "Development of an unmanned helicopter automatic barrels transportation system", in 2015 IEEE International Conference on Robotics and Automation (ICRA), 2015, str. 4686-4691.

[51]Orsag, M., Korpela, C., Pekala, M., Oh, P., "Stability control in aerial manipulation", in 2013 American Control Conference, 2013, str. 5581-5586.

[52]Gabrich, B., Saldaña, D., Kumar, V., Yim, M., "A flying gripper based on cuboid modular robots", in 2018 IEEE International Conference on Robotics and Automation (ICRA), 2018, str. 7024-7030.

[53]Gawel, A., Kamel, M., Novkovic, T., Widauer, J., Schindler, D., von Altishofen, B. P., Siegwart, R., Nieto, J., "Aerial picking and delivery of magnetic objects with mavs", in 2017 IEEE International Conference on Robotics and Automation (ICRA), 2017, str. 5746-5752.

[54]Jimenez-Cano, A., Martin, J., Heredia, G., Ollero, A., Cano, R., "Control of an aerial robot with multi-link arm for assembly tasks", in 2013 IEEE International Conference on Robotics and Automation, 2013, str. 4916-4921.

[55]Kim, S., Choi, S., Kim, H. J., "Aerial manipulation using a quadrotor with a two dof robotic arm", in 2013 IEEE/RSJ International Conference on Intelligent Robots and Systems, 2013, str. 4990-4995.

[56]Korpela, C., Orsag, M., Pekala, M., Oh, P., "Dynamic stability of a mobile manipulating unmanned aerial vehicle", in 2013 IEEE International Conference on Robotics and Automation, 2013, str. 4922-4927.

[57]Jimenez-Cano, A., Braga, J., Heredia, G., Ollero, A., "Aerial manipulator for structure inspection by contact from the underside", in 2015 IEEE/RSJ International Conference on Intelligent Robots and Systems (IROS), 2015, str. 1879-1884.

[58]Darivianakis, G., Alexis, K., Burri, M., Siegwart, R., "Hybrid predictive control for aerial robotic physical interaction towards inspection operations", in 2014 IEEE International Conference on Robotics and Automation (ICRA), 2014, str. 53-58.

[59]Forte, F., Naldi, R., Macchelli, A., Marconi, L., "On the control of an aerial manipulator interacting with the environment", in 2014 IEEE International Conference on Robotics and Automation (ICRA), 2014, str. 4487-4492.

[60]Jimenez-Cano, A., Heredia, G., Ollero, A., "Aerial manipulator with a compliant arm for bridge inspection", in 2017 International Conference on Unmanned Aircraft Systems (ICUAS), 2017, str. 1217-1222.

[61]Ollero, A., Heredia, G., Franchi, A., Antonelli, G., Kondak, K., Sanfeliu, A., Viguria, A., Martinez-de Dios, J. R., Pierri, F., Cortes, J., Santamaria-Navarro, A., Trujillo Soto, M. A., Balachandran, R., Andrade-Cetto, J., Rodriguez, A., "The aeroarms project: Aerial robots with advanced manipulation capabilities for inspection and maintenance", IEEE Robotics Automation Magazine, Vol. 25, No. 4, 2018, str. 12-23.

[62]Scholten, J. L., Fumagalli, M., Stramigioli, S., Carloni, R., "Interaction control of an uav endowed with a manipulator", in 2013 IEEE International Conference on Robotics and Automation, 2013, str. 4910-4915.

[63]Car, M., Ivanovic, A., Orsag, M., Bogdan, S., "Impedance based force control for aerial robot peg-in-hole insertion tasks", in 2018 IEEE/RSJ International Conference on Intelligent Robots and Systems (IROS), 2018, str. 6734-6739.

[64]Kim, S., Seo, H., Shin, J., Kim, H. J., "Cooperative aerial manipulation using multirotors with multi-dof robotic arms", IEEE/ASME Transactions on Mechatronics, Vol. 23, No. 2, 2018, str. 702-713.

[65]Kim, H., Lee, H., Choi, S., Noh, Y.-k., Kim, H. J., "Motion planning with movement primitives for cooperative aerial transportation in obstacle environment", in 2017 IEEE International Conference on Robotics and Automation (ICRA), 2017, str. 2328-2334.

[66]Orsag, M., Korpela, C., Bogdan, S., Oh, P., "Dexterous aerial robots—mobile manipulation using unmanned aerial systems", IEEE Transactions on Robotics, Vol. 33, No. 6, 2017, str. 1453-1466.

[67]Huber, F., Kondak, K., Krieger, K., Sommer, D., Schwarzbach, M., Laiacker, M., Kossyk, I., Parusel, S., Haddadin, S., Albu-Schäffer, A., "First analysis and experiments in aerial manipulation using fully actuated redundant robot arm", in 2013 IEEE/RSJ International Conference on Intelligent Robots and Systems, 2013, str. 3452-3457.

[68]Meng, X., He, Y., Han, J., "Hybrid force/motion control and implementation of an aerial manipulator towards sustained contact operations", in 2019 IEEE/RSJ International Conference on Intelligent Robots and Systems (IROS), 2019, str. 3678-3683.

[69]Marconi, L., Naldi, R., "Control of aerial robots: Hybrid force and position feedback for a ducted fan", IEEE Control Systems Magazine, Vol. 32, No. 4, 2012, str. 43-65.

[70]Cataldi, E., Muscio, G., Trujillo, M. A., Rodriguez, Y., Pierri, F., Antonelli, G., Caccavale, F., Viguria, A., Chiaverini, S., Ollero, A., "Impedance control of an aerial-manipulator: Preliminary results", in 2016 IEEE/RSJ International Conference on Intelligent Robots and Systems (IROS), 2016, str. 3848-3853.

[71]Caccavale, F., Giglio, G., Muscio, G., Pierri, F., "Cooperative impedance control for multiple uavs with a robotic arm", in 2015 IEEE/RSJ International Conference on Intelligent Robots and Systems (IROS), 2015, str. 2366-2371.

[72]Haus, T., Orsag, M., Bogdan, S., "Mathematical modelling and control of an unmanned aerial vehicle with moving mass control concept", Journal of Intelligent & Robotic Systems, Vol. 88, 12 2017, str. 1-28.

[73]Markovic, L., Ivanovic, A., Car, M., Orsag, M., Bogdan, S., "Geometric tracking control of aerial robots based on centroid vectoring", in 2019 18th European Control Conference (ECC), 2019, str. 2701-2706.

[74]Allenspach, M., Bodie, K., Brunner, M., Rinsoz, L., Taylor, Z., Kamel, M., Siegwart, R., Nieto, J., "Design and optimal control of a tiltrotor micro-aerial vehicle for efficient omnidirectional flight", The International Journal of Robotics Research, Vol. 39, No. 10-11, 2020, str. 1305-1325, available at: https://doi.org/10.1177/0278364920943654

[75]Pounds, P., Mahony, R., Corke, P., "Modelling and control of a large quadrotor robot", Control Engineering Practice, Vol. 18, No. 7, 2010, str. 691-699, special Issue on Aerial Robotics, available at: https://www.sciencedirect.com/science/article/pii/S0967066110000456

[76]Haus, T., Car, M., Orsag, M., Bogdan, S., "Identification results of an internal combustion engine as a quadrotor propulsion system", in 2017 25th Mediterranean Conference on Control and Automation (MED), 2017, str. 713-718.

[77]Haus, T., Orsag, M., Bogdan, S., "Design considerations for a large quadrotor with moving mass control", in 2016 International Conference on Unmanned Aircraft Systems (ICUAS), 2016, str. 1327-1334.

[78]Haus, T., "Control of multirotor unmanned aerial vehicle based on moving mass concept", PhD Thesis, University of Zagreb, 2017.

[79]Preitl, S., Precup, R.-E., "An extension of tuning relations after symmetrical optimum method for pi and pid controllers", Automatica, Vol. 35, No. 10, 1999, str. 1731-1736, available at: https://www.sciencedirect.com/science/article/pii/S0005109899000916

[80]Orsag, M., Korpela, C., Bogdan, S., Oh, P., "Dexterous aerial robots—mobile manipulation using unmanned aerial systems", IEEE Transactions on Robotics, Vol. 33, No. 6, 2017, str. 1453-1466.

[81]Allison, B. J., Isaksson, A. J., "Design and performance of mid-ranging controllers", Journal of Process Control, Vol. 8, No. 5, 1998, str. 469-474, aDCHEM '97 IFAC Symposium: Advanced Control of Chemical Processes, available at: https://www.sciencedirect.com/science/article/pii/S0959152498000122

[82]Seraji, H., Colbaugh, R., "Force tracking in impedance control", in [1993] Proceedings IEEE International Conference on Robotics and Automation. IEEE Comput. Soc. Press, 1993, str. 499–506, available at: http://ieeexplore.ieee.org/document/291908/

[83]Seraji, H., "Decentralized adaptive control of manipulators: theory, simulation, and experimentation", IEEE Transactions on Robotics and Automation, Vol. 5, No. 2, apr 1989, str. 183–201, available at: http://ieeexplore.ieee.org/document/88039/

[84]Furrer, F., Burri, M., Achtelik, M., Siegwart, R., Robot Operating System (ROS): The Complete Reference (Volume 1). Cham: Springer International Publishing, 2016, ch. RotorS—A Modular Gazebo MAV Simulator Framework, str. 595–625, available at: http://dx.doi.org/10.1007/978-3-319-26054-9_23

[85]Meyer, J., Sendobry, A., Kohlbrecher, S., Klingauf, U., von Stryk, O., "Comprehensive simulation of quadrotor uavs using ros and gazebo", in 3rd Int. Conf. on Simulation, Modeling and Programming for Autonomous Robots (SIMPAR), 2012, str. to appear.

[86]Car, M., Ivanovic, A., Orsag, M., Bogdan, S., "Position-based adaptive impedance control for a uav", in 2018 International Conference on Unmanned Aircraft Systems (ICUAS), 2018, str. 957-963.

[87]Polic, M., Car, M., Tabak, J., Orsag, M., "Robotic irrigation water management: Estimating soil moisture content by feel and appearance", in 2022 19th International Conference on Ubiquitous Robots (UR), 2022, str. 16-22.

[88]Markovi ć, L., Car, M., Orsag, M., Bogdan, S., "Adaptive stiffness estimation impedance control for achieving sustained contact in aerial manipulation", in 2021 IEEE International Conference on Robotics and Automation (ICRA), 2021, str. 117-123.

[89]Kamel, M., Stastny, T., Alexis, K., Siegwart, R., "Model predictive control for trajectory tracking of unmanned aerial vehicles using robot operating system", in Robot Operating System (ROS) The Complete Reference, Volume 2, Koubaa, A., (ur.). Springer, 2017.

Biography

Marko Car obtained his degree from the Faculty of Electrical Engineering and Computing (UNIZG-FER) at the University of Zagreb in 2015. Since then, he has been working as a research and teaching assistant at the Laboratory for Robotics and Intelligent Control Systems (LARICS) under the guidance of Prof. Stjepan Bogdan. During his undergraduate studies, he was awarded the Rector's Award for his project on "Augmented human machine interface for aerial manipulators." His research interests lie in the field of robotics, unmanned aerial vehicles, aerial manipulation, and compliant control. In 2018, he was a visiting researcher at the United States Military Academy, West Point, where he worked on a heterogeneous robot system (UAV-UGV) for collaborative payload transport. A year later, in 2019, he spent a few weeks as a visiting researcher at Imperial College London, where he worked on the development of an origami structure for UAV contact sensing and protection in collisions. As a researcher, he has contributed to various international, national, and industrial research projects. Furthermore, he was a member of the LARICS team that participated in the European Robotics Challenge (EuRoC), ERL Emergency Robots 2019, and MBZIRC 2020 robotics competitions. He has authored or co-authored 16 conference papers, 3 journal papers, and 2 book chapters.

List of publications

Book chapters

1.Arbanas, B., Petric, F., Batinovi ć, A., Polić, M., Vatavuk, I., Marković, L., Car, M., Hrabar, I., Ivanović, A., Bogdan, S., "From ERL to MBZIRC: Development of an aerial-ground robotic team for search and rescue", Automation and Control - Theories and Applications, 2022 May 25.

2.Toli ć, D., Palunko, I., Ivanović, A., Car, M. and Bogdan, S., "Decentralized cooperative control in degraded communication environments", Control of Complex Systems: Theory and Applications, pp. 373-395. 2016.

Journal papers

1.Ivanovi ć, A., Marković, L., Car, M., Duvnjak, I., Orsag, M., "Towards Autonomous Bridge Inspection: Sensor Mounting Using Aerial Manipulators", Applied Sciences, 2021, 11, 8279.

2.Car, M., Markovi ć, L., Ivanović, A., Orsag, M. and Bogdan, S., "Autonomous Wind-Turbine Blade Inspection Using LiDAR-Equipped Unmanned Aerial Vehicle," in IEEE Access, vol. 8, pp. 131380-131387, 2020.

3.Arbanas, B., Ivanovi ć, A., Car, M., Orsag, M., Petrović, T. and Bogdan, S., "Decentralized planning and control for UAV—UGV cooperative teams", Autonomous Robots, Vol. 42, Issue 8, February 2018, pp. 1601–1618.

Conference papers

1.Markovi ć, L., Kovač, M., Milijaš, R., Car, M. and Bogdan, S., "Error State Extended Kalman Filter Multi-Sensor Fusion for Unmanned Aerial Vehicle Localization in GPS and Magnetometer Denied Indoor Environments," 2022 International Conference on Unmanned Aircraft Systems (ICUAS), Dubrovnik, Croatia, 2022, pp. 184-190.

2.Poli ć, M., Car, M., Tabak, J. and Orsag, M., "Robotic Irrigation Water Management: Estimating Soil Moisture Content by Feel and Appearance," 2022 19th International Conference on Ubiquitous Robots (UR), Jeju, Korea, Republic of, 2022, pp. 16-22.

3.Markovi ć, L., Car, M., Orsag, M. and Bogdan S., "Adaptive stiffness estimation impedance control for achieving sustained contact in aerial manipulation," 2021 IEEE International Conference on Robotics and Automation (ICRA), Xi'an, China, 2021, pp. 117-123.

4.Poli ć, M., Car, M., Petric, F. and Orsag, M., "Compliant Plant Exploration for Agricultural Procedures With a Collaborative Robot," in IEEE Robotics and Automation Letters, vol. 6, no. 2, pp. 2768-2774, April 2021.

5.Ivanovi ć, A., Car, M., Orsag, M. and Bogdan, S., "Exploiting Null Space in Aerial Manipulation through Model-In-The-Loop Motion Planning," 2020 International Conference on Unmanned Aircraft Systems (ICUAS), Athens, Greece, 2020, pp. 686-693.

6.Bariši ć, A., Car, M. and Bogdan, S., "Vision-based system for a real-time detection and following of UAV," 2019 Workshop on Research, Education and Development of Unmanned Aerial Systems (RED UAS), Cranfield, UK, 2019, pp. 156-159.

7.Turkovi ć, K., Car, M. and Orsag, M., "End-effector force estimation method for an unmanned aerial manipulator," 2019 Workshop on Research, Education and Development of Unmanned Aerial Systems (RED UAS), Cranfield, UK, 2019, pp. 96-99.

8.Markovi ć, L., Ivanović, A., Car, M., Orsag, M. and Bogdan, S., "Geometric Tracking Control of Aerial Robots Based on Centroid Vectoring," 2019 18th European Control

Conference (ECC), Naples, Italy, 2019, pp. 2701-2706.

9.Ivanovi ć, A., Car, M., Orsag, M. and Bogdan, S., "Centroid vectoring control using aerial manipulator: Experimental results," 2019 International Conference on Unmanned Aircraft Systems (ICUAS), Atlanta, GA, USA, 2019, pp. 372-377.

10.Car, M., Ivanovi ć, A., Orsag, M. and Bogdan, S., "Impedance Based Force Control for Aerial Robot Peg-in-Hole Insertion Tasks," 2018 IEEE/RSJ International Conference on Intelligent Robots and Systems (IROS), Madrid, Spain, 2018, pp. 6734-6739.

11.Haus, T., Ivanovi ć, A., Car, M., Orsag, M. and Bogdan, S., "Mid-Ranging Control Concept for a Multirotor UAV with Moving Masses," 2018 26th Mediterranean Conference on Control and Automation (MED), Zadar, Croatia, 2018, pp. 339-344.

12.Car, M., Ivanovi ć, A., Orsag, M. and Bogdan, S., "Position-based adaptive impedance control for a UAV," 2018 International Conference on Unmanned Aircraft Systems (ICUAS), Dallas, TX, USA, 2018, pp. 957-963.

13.Haus, T., Car, M., Orsag, M. and Bogdan, S., "Identification results of an internal combustion engine as a quadrotor propulsion system," 2017 25th Mediterranean Conference on Control and Automation (MED), Valletta, Malta, 2017, pp. 713-718.

14.Orsag, M., Haus, T., Toli ć, D., Ivanović, A., Car, M., Palunko, I. and Bogdan, S., ”Human-in-the-loop Control of Multi-agent Aerial Systems”, in IEEE European Control Conference (ECC), Aalborg, Denmark, June 2016, pp. 2139-2145.

15.Arbanas, B., Ivanovi ć A., Car, M., Haus, T., Orsag, M., Petrović, T. and Bogdan, S., ”Aerial-ground Robotic System for Autonomous Delivery Tasks”, in IEEE International Conference on Robotics and Automation (ICRA), Stockholm, Sweeden, May 2016, pp. 5463-5468.

16.Toli ć, D., Palunko, I., Ivanović, A., Car, M. and Bogdan, S., "Multi-agent control in degraded communication environments," 2015 European Control Conference (ECC), Linz, Austria, 2015, pp. 404-409.

Životopis

Marko Car je diplomirao na Fakultetu elektrotehnike i računarstva (UNIZG-FER) Sveučilišta u Zagrebu 2015. godine. Od tada radi kao istraživač i asistent u Laboratoriju za robotiku i inteligentne sustave upravljanja (LARICS) pod vodstvom prof. Stjepana Bogdana. Tijekom preddiplomskog studija dobio je Rektorovu nagradu za projekt "Prošireno korisničko sučelje za upravljanje robotskim manipulatorom u letu". Njegovi istraživački interesi su u području robotike, bespilotnih letjelica, zračne manipulacije i podatnog upravljanja. 2018. godine kao gostujući istraživač radio je na Vojnoj akademiji Sjedinjenih Država u West Pointu na heterogenom robotskom sustavu (UAV-UGV) za koordinirani prijevoz tereta. Godinu dana kasnije, 2019. proveo je nekoliko tjedana kao gostujući istraživač na Imperial College London, gdje je radio na razvoju origami strukture za upravljanje bespilotnom letjelicom u slučaju kontakta s okolinom. Kao istraživač, radio je na različitim međunarodnim, nacionalnim i industrijskim istraživačkim projektima. Osim toga, bio je član tima LARICS-a koji je sudjelovao u natjecanjima European Robotics Challenge (EuRoC), ERL Emergency Robots 2019 i MBZIRC 2020. Autor je 16 radova na konferencijama, 3 znanstvena rada u časopisima te 2 poglavlja u knjigama.